

# **Extensional deformation and landscape evolution of the Central Andean Plateau**

---

DISSERTATION

von

**Gregor Lauer-Dünkelberg**

zur Erlangung des akademischen Grades

DOCTOR RERUM NATURALIUM

(Dr. rer. nat.)

in der Wissenschaftsdisziplin Geologie

eingereicht an der

Mathematisch-

Naturwissenschaftlichen Fakultät,

Institut für Geowissenschaften der Universität Potsdam

Potsdam, 17.04.2023

Datum der Disputation: 18.10.2023

This work is protected by copyright and/or related rights. You are free to use this work in any way that is permitted by the copyright and related rights legislation that applies to your use. For other uses you need to obtain permission from the rights-holder(s).  
<https://rightsstatements.org/page/InC/1.0/?language=en>

#### **Supervisors**

**Prof. Dr. Manfred Strecker**

**Dra. Carolina Montero Lopez**

#### **Mentor**

**apl. Prof. Dr. Frank Krüger**

#### **Reviewers**

**Prof. Dra. Laura Giambiagi**

**Prof. Dr. Gregory D. Hoke**

#### **Members of the examination board**

**Prof. Dr. Bodo Bookhagen**

**Prof. Dr. Peter van der Beek**

**apl. Prof. Dr. Edward Sobel**

**Prof. Dra. Laura Giambiagi**

**Prof. Dr. Gregory D. Hoke**

**Prof. Dr. Manfred Strecker**

Published online on the  
Publication Server of the University of Potsdam:  
<https://doi.org/10.25932/publishup-61759>  
<https://nbn-resolving.org/urn:nbn:de:kobv:517-opus4-617593>

# **Eigenständigkeitserklärung**

Hiermit bestätige ich, dass die vorliegende Forschungsarbeit mit dem Titel: „Extensional deformation and landscape evolution of the Central Andean Plateau“ selbstständig und ohne Benutzung anderer als der angegebenen Quellen verfasst wurde. Jegliche Verwendung von Arbeiten anderer Autoren ist an der Stelle, an der sie verwendet wurden, gekennzeichnet. Diese Arbeit wurde im Rahmen des Promotionsverfahrens und der Prüfung im internationalen Graduiertenkolleg IGK2018 „StRATEGy“ an der Universität Potsdam in Deutschland angefertigt. Ich erkläre, dass ich diese Arbeit an keiner anderen Einrichtung als der Universität Potsdam eingereicht habe.

Gregor Lauer-Dünkelberg

Potsdam, den 07.12.2023

This thesis was carried out within the framework of the International Research Training Group “SuRfAce processes, TEctonics and Georesources: The Andean foreland basin of Argentina (StRATEGy)“, funded by the German Research Foundation (DFG) and carried out at the University of Potsdam; the project was co-supervised and supported by collaborating institutions in Argentina (Consejo Nacional de Investigaciones Científicas y Técnicas (CONICET), Universidad Nacional de Tucumán (CUAA-DAHZ binational doctorate program).

The principal goal of the project was to better understand the coupled evolution of landscapes and georesources in the Andean orogen, in its foreland and intermontane basins, with the aim to decipher the underlying causal mechanisms, feedbacks and rates of tectonic, climatic, hydrologic and erosional/depositional processes over multiple timescales. Therefore, a broad spectrum of methodologies was used to retrieve data from various geological archives and present-day/historical observations. In this context, this thesis addresses the young tectonic history of the southern part of the Andean Plateau region (Puna) of north-western Argentina.

## Acknowledgement

First and foremost, I want to thank my supervisors Prof. Manfred Strecker and Dra. Carolina Montero-López for their continuous support, encouragement, and scientific guidance during all phases of this thesis, which is also why I never felt left-alone, even while staying in quarantine during the times of the global pandemic. Manfred, I am really grateful for always having an open door and showing me, that the data I got is ‘gold’ when I was in disbelief of the outcome of the research! Thanks also to Angela Landgraf, who was unfortunately not involved in the project, but who was responsible for my interest in quaternary tectonics and paleoseismology and to whom I felt mentally connected whilst working on most of the paleoseismological parts of this thesis. Furthermore, I want to thank Dr. Mitch D’Arcy for giving me professional advice on dating fluvial landforms, especially alluvial fans, during the early stages of my research. Moreover, I had unmissable assistance (and entertainment) during the field work from my friends and colleagues María Johanna Diácono and Elisabeth Schönfeldt. Whilst working in the field, in the labs and during the data processing I was mainly supervised by Prof Dr. Bodo Bookhagen and Dr. Heiko Pingel, who I want to thank for their tireless perseverance concerning my questions and concerns, while working on the geochemical and remote sensing data. The chemical separation in the labs of the university of Potsdam was furthermore guided by Julia Artel, whose continuous optimism could change every frustration into forward-thinking. At this point I want to also mention my colleague and friend Sohini Bhattacharjee, who went through the whole emotional rollercoaster of radionuclide dating with me. Ultimately, when it comes to the radionuclide dating and data processing thereof, I want to thank Samuel Niedermann, who analyzed the  $^{21}\text{Ne}$  samples in the labs of the GFZ Potsdam and who guided me in processing the analyzed data, helped when questions aroused and always found time for a skype-meeting.

As this work was part of a binational graduate school, I stayed quite some time abroad in Argentina. During the first weeks, I was staying with my friend Elisabeth Schönfeldt, who also guided me through Buenos Aires and showed me some of the Argentine lifestyle and I am really grateful that I was with her and not alone during these first weeks. Together we went to a field trip with Prof. Dr. Fernando Hongn and Dr. Adolfo Antonio Gutierrez who

I have to thank for introducing me for the first time to the beautiful geology of NW-Argentina. During these stays abroad, I experienced some of the most welcoming people in my life, which is the family of my co-supervisor Carolina Montero-Lopez. I am really thankful for the possibility to stay in a foreign country with such wonderful human beings, who took me as a part of their own family and incorporated me into their daily and social life, who gave me a feeling of not being a foreigner but a friend, without even knowing me. Much of this experience is also due to my friend Virginia Montero, who lend me a room in her house and showed me the cultural and nightlife of Salta. May our paths cross more often in the future! Many thanks also to my friend Germán Aranda Viana for spending so much time with me in the field and in Salta in general. Moreover, thanks to Emilio Sutti and his amazing family for the best Asado nights you could imagine. Finally, I want to thank the whole staff of the IBIGEO in Rosario de Lerma for having me as a guest scientist. Many thanks also to my office mates who endured me during the 3-4 years we have spend so much time together and had some amazing Weißwurst breakfasts together. Here I would namely like to thank Willemeijn van Kooten, Sohini Bhattacharjee and Nikolaus Rein. Also thanks to the colleagues outside my office, which are the other students from the graduate school who joined me on this journey.

I would like to give some of the most special thanks my dearest friend and best office mate Enrico Ribacki for being my constant since I moved to Potsdam in 2014 and, who luckily joined the same graduate school and later, rather involuntary, even the same office as me. It's been a great time, having our common daily routines and coffee breaks, as well as the frustration sweets from your drawer when everything appeared to fall apart once more. Not to mention the amazing time during the field schools in Argentina, the Humboldt Symposium in Halle and all the other moments that we shared. Those are the things that will definitely be missed and I would happily share another office with you!

Lastly, I want to thank all my friends and my family outside the academic life who always supported me and believed in me, even when times were difficult. Special thanks to my mum, who took the time and effort to visit me in Argentina for my birthday, crossed the Andes with me and even brought me some good old German bread. Thanks also to my father Uwe, my brother Nicolas, my sister Josefa and my grandma Ella for supporting me throughout this journey, although not really getting what I am doing at work.

Last but not least, I want to thank my partner in crime Carolin Reger for always being present, supportive, listening when I bothered you with my sorrows, concerns and questions

and for always being understanding when I was either mentally and/or physically not available. You have been my mental spa during the last years!

## **Abstract**

Mountain ranges can fundamentally influence the physical and chemical processes that shape Earth's surface. With elevations of up to several kilometers they create climatic enclaves by interacting with atmospheric circulation and hydrologic systems, thus leading to a specific distribution of flora and fauna. As a result, the interiors of many Cenozoic mountain ranges are characterized by an arid climate, internally drained and sediment-filled basins, as well as unique ecosystems that are isolated from the adjacent humid, low-elevation regions along their flanks and forelands. These high-altitude interiors of orogens are often characterized by low relief and coalesced sedimentary basins, commonly referred to as plateaus, tectono-geomorphic entities that result from the complex interactions between mantle-driven geological and tectonic conditions and superposed atmospheric and hydrological processes. The efficiency of these processes and the fate of orogenic plateaus is therefore closely tied to the balance of constructive and destructive processes – tectonic uplift and erosion, respectively. In numerous geological studies it has been shown that mountain ranges are delicate systems that can be obliterated by an imbalance of these underlying forces. As such, Cenozoic mountain ranges might not persist on long geological timescales and will be destroyed by erosion or tectonic collapse. Advancing headward erosion of river systems that drain the flanks of the orogen may ultimately sever the internal drainage conditions and the maintenance of storage of sediments within the plateau, leading to destruction of plateau morphology and connectivity with the foreland. Orogenic collapse may be associated with the changeover from a compressional stress field with regional shortening and topographic growth, to a tensional stress field with regional extensional deformation and ensuing incision of the plateau. While the latter case is well-expressed by active extensional faults in the interior parts of the Tibetan Plateau and the Himalaya, for example, the former has been attributed to have breached the internally drained areas of the high-elevation sectors of the Iranian Plateau.

In the case of the Andes of South America and their internally drained Altiplano-Puna Plateau, signs of both processes have been previously described. However, in the orogenic collapse scenario the nature of the extensional structures had been primarily investigated in the northern and southern terminations of the plateau; in some cases, the extensional faults were even regarded to be inactive. After a shallow earthquake in 2020 within the

Eastern Cordillera of Argentina that was associated with extensional deformation, the state of active deformation and the character of the stress field in the central parts of the plateau received renewed interest to explain a series of extensional structures in the northernmost sectors of the plateau in north-western Argentina. This study addresses (1) the issue of tectonic orogenic collapse of the Andes and the destruction of plateau morphology by studying the fill and erosion history of the central eastern Andean Plateau using sedimentological and geochronological data and (2) the kinematics, timing and magnitude of extensional structures that form well-expressed fault scarps in sediments of the regional San Juan del Oro surface, which is an integral part of the Andean Plateau and adjacent morphotectonic provinces to the east.

Importantly, sediment properties and depositional ages document that the San Juan del Oro Surface was not part of the internally-drained Andean Plateau, but rather associated with a foreland-directed drainage system, which was modified by the Andean orogeny and that became successively incorporated into the orogen by the eastward-migration of the Andean deformation front during late Miocene – Pliocene time. Structural and geomorphic observations within the plateau indicate that extensional processes must have been repeatedly active between the late Miocene and Holocene supporting the notion of plateau-wide extensional processes, potentially associated with  $M_w \sim 7$  earthquakes. The close relationship between extensional joints and fault orientations underscores that  $\sigma_3$  was oriented horizontally in NW-SE direction and  $\sigma_1$  was vertical. This unambiguously documents that the observed deformation is related to gravitational forces that drive the orogenic collapse of the plateau. Applied geochronological analyses suggest that normal faulting in the northern Puna was active at about 3 Ma, based on paired cosmogenic nuclide dating of sediment fill units. Possibly due to regional normal faulting the drainage system within the plateau was also affected, promoting fluvial incision.

## Zusammenfassung

Gebirge beeinflussen grundlegend die physikalischen und chemischen Prozesse, die die Oberfläche der Erde formen. Mit Höhen von bis zu mehreren Tausend Metern können sie als topografische Barrieren fungieren, die die Verbreitung von Flora und Fauna einschränken und durch Wechselwirkungen mit atmosphärischen Zirkulationen und hydrologischen Systemen klimatische Enklaven schaffen. Infolgedessen sind die inneren Teile vieler känozoischer Gebirge durch intern entwässerte Becken gekennzeichnet, die einzigartige, von den umgebenden, niedriger gelegenen Bereichen des Vorlands isolierte Ökosysteme beherbergen. Diese durch niedriges Relief geprägte orographische Sektoren werden als Plateaus bezeichnet - das Ergebnis komplexer Wechselwirkungen zwischen geologischen, hydrologischen und atmosphärischen Prozessen. Die Effizienz dieser Prozesse und das Schicksal solcher orogenen Plateaus ist daher an das Gleichgewicht der konstruktiven und destruktiven Prozesse, der tektonischen Hebung und Erosion gebunden. Aus geologischen Studien geht hervor, dass Gebirgszüge fragile Systeme sind, die durch ein Ungleichgewicht dieser zugrunde liegenden Kräfte kollabieren können. Daher erscheint es unumgänglich, dass moderne Gebirgszüge auf geologischen Zeitskalen nicht überdauern werden und voraussichtlich dem Zahn der Zeit zum Opfer fallen. Aufgrund dieser Beobachtungen haben sich bereits viele Studien mit der Aufgabe befasst, den momentanen Zustand känozoischer Gebirge zu erforschen, um zu entschlüsseln, ob sie bereits in eine Einebnungsphase übergegangen sind. Einw solche Einebnung kann auf zwei oberflächliche Anzeichen zurückgeführt werden: i) die fortschreitende Erosion durch Flusssysteme und ii) das Vorhandensein von Extensionstrukturen, die sich entgegen des kompressiven Stressfelds formen und einen gravitativen Kollaps widerspiegeln. Solche Strukturen sind im Inneren des tibetischen Plateaus des zentralasiatischen Himalaya deutlich ausgeprägt, während ein plateauweite Einschneidung durch Flusssysteme die intern entwässerten Gebiete der hoch gelegenen Sektoren des iranischen Plateaus betroffen haben soll.

Im Falle der südamerikanischen Anden und ihres intern entwässerten Altiplano-Puna Plateaus wurden bisher Anzeichen für beide Prozesse beschrieben. Im Szenario des orogenen Kollapses wurde die Art der Dehnungsstrukturen jedoch hauptsächlich an den nördlichen und südlichen Grenzen des Plateaus untersucht; in einigen Fällen wurden die tektonischen Verwerfungen sogar als inaktiv angesehen. Nach einem flachen Erdbeben im Jahr 2020 in der Ostkordillere Argentiniens, das mit Extensionsverformung in Verbindung

gebracht wurde, weckte die Frage nach dem Zustand des Spannungsfeldes und der damit einhergehenden aktiven Deformation in den zentralen Teilen des Plateaus wieder neues Interesse. Daraus resultierende Erkenntnisse würden helfen eine Reihe von Extensionsstrukturen in den nördlichsten Sektoren des Plateaus im Nordwesten Argentiniens zu erklären.

Diese Dissertation befasst sich daher mit (1) der Frage des tektonisch-orogenen Zusammenbruchs der Anden und der Einschneidung in die Plateaumorphologie, indem die Auffüllungs- und Erosionsgeschichte des zentralen östlichen Andenplateaus anhand von sedimentologischen und geochronologischen Daten untersucht wird, und (2) mit der Kinematik, dem zeitlichen Ablauf und dem Ausmaß von Dehnungsdeformation, die gut ausgeprägte Geländestufen in den solig gelagerten Sedimenten der regionalen San Juan del Oro-Oberfläche formte, die wiederum ein integraler Bestandteil des Andenplateaus und der angrenzenden morphotektonischen Provinzen im Osten ist.

Die Sedimenteigenschaften und das bereitgestellten Ablagerungsalter belegen, dass die San Juan del Oro-Oberfläche nicht Teil des intern entwässerten Andenplateaus ist, sondern vielmehr mit einem vorgelagerten Entwässerungssystem verbunden ist, das durch die Anden-Orogenese und die Ostwärtsbewegung der Deformationsfront im späten Miozän bis Pliozän sukzessive in das Orogen integriert wurde. Strukturelle und geomorphologische Beobachtungen innerhalb des Plateaus deuten darauf hin, dass Dehnungsprozesse zwischen dem späten Miozän und dem Holozän wiederholt aktiv gewesen sein müssen, was die Theorie plateauweiter Dehnungsprozesse stützt, die möglicherweise mit Erdbeben der Stärke  $M_w \sim 7$  in Verbindung standen. Die enge Beziehung zwischen Dehnungsklüften und dem Streichen der beobachteten Verwerfungen deutet darauf hin, dass die geringste Normalspannung ( $\sigma_3$ ) horizontal in NW-SE-Richtung und die maximale Normalspannung ( $\sigma_1$ ) zu Zeiten der Deformation vertikal orientiert war. Dies belegt eindeutig, dass die beobachtete Deformation mit Gravitationskräften zusammenhängt, die den orogenen Kollaps des Plateaus vorantreiben. Angewandte geochronologische Analysen deuten darauf hin, dass die Abschiebungen in der nördlichen Puna vor ca. 3 Ma aktiv waren, basierend auf der Expositionsaltern von Sedimentfüllungseinheiten. Möglicherweise wurde durch die regionalen Abschiebungen auch das Entwässerungssystem innerhalb des Plateaus beeinflusst, was die fluviale Einschneidung begünstigte.

## Resumen

Las cadenas montañosas pueden influir de manera fundamental en los procesos físicos y químicos que conforman la superficie terrestre. Con elevaciones de hasta varios kilómetros, crean enclaves climáticos al interactuar con la circulación atmosférica y los sistemas hidrológicos, lo que da lugar a una distribución específica de la flora y la fauna. Como resultado, los interiores de muchas cordilleras cenozoicas se caracterizan por un clima árido, cuencas internamente drenadas y llenas de sedimentos, así como ecosistemas únicos que están aislados de las regiones adyacentes húmedas y de baja altitud a lo largo de sus flancos y antepaíses. Estos interiores de gran altitud de los orógenos se caracterizan a menudo por un relieve bajo y cuencas sedimentarias coalescentes, comúnmente denominadas mesetas, entidades tectono-geomórficas que resultan de las complejas interacciones entre las condiciones geológicas y tectónicas impulsadas por el manto y los procesos atmosféricos e hidrológicos superpuestos. La eficacia de estos procesos y el destino de las mesetas orogénicas están, por tanto, estrechamente ligados al equilibrio de los procesos constructivos y destructivos: el levantamiento tectónico y la erosión, respectivamente. En numerosos estudios geológicos se ha demostrado que las cadenas montañosas son sistemas delicados que pueden quedar arrasados por un desequilibrio de estas fuerzas subyacentes. Por ello, es posible que las cordilleras cenozoicas no persistan a largo plazo y sean destruidas por la erosión o el colapso tectónico. El avance de la erosión retrocedente (i.e. aguas arribas) de los sistemas fluviales que drenan los flancos del orógeno puede acabar cortando las condiciones de drenaje interno y el mantenimiento del almacenamiento de sedimentos en el interior de la meseta, provocando la destrucción de la morfología de la meseta y la conectividad con el antepaís. El colapso orogénico puede estar asociado con el cambio de un campo de tensión compresional con acortamiento regional y crecimiento topográfico, a un campo de tensión tensional con deformación extensional regional y la consiguiente incisión de la meseta. Mientras que este último caso está bien expresado por las fallas extensionales activas en los sectores interiores de la meseta tibetana y el Himalaya, por ejemplo, al primero se le atribuye haber abierto brechas en las zonas internamente drenadas de los sectores de gran altitud de la meseta iraní.

En el caso de los Andes de Sudamérica y su meseta Altiplano-Puna, drenada internamente, se han descrito anteriormente indicios de ambos procesos. Sin embargo, en el escenario de colapso orogénico, la naturaleza de las estructuras extensionales se había investigado

principalmente en las terminaciones norte y sur de la meseta; en algunos casos, las fallas extensionales se consideraban incluso inactivas. Tras un terremoto de poca profundidad ocurrido en 2020 en la Cordillera Oriental de Argentina, asociado a una deformación extensional, el estado de la deformación activa y el carácter del campo de esfuerzos en los sectores centrales de la meseta recibieron un renovado interés para explicar una serie de estructuras extensionales en los sectores más septentrionales de la meseta en el noroeste de Argentina. Este estudio aborda (1) la cuestión del colapso tectónico orogénico de los Andes y la destrucción de la morfología de la meseta mediante el estudio de la historia de relleno y erosión de la meseta andina central oriental utilizando datos sedimentológicos y geocronológicos y (2) la cinemática, cronología y magnitud de las estructuras extensionales que forman escarpas de falla bien expresadas en los sedimentos de la superficie regional de San Juan del Oro, que es parte integrante de la meseta andina y de las provincias morfotectónicas adyacentes al este.

Es importante destacar que las propiedades de los sedimentos y las edades deposicionales documentan que la Superficie de San Juan del Oro no formaba parte de la Meseta Andina drenada internamente, sino que estaba asociada a un sistema de drenaje dirigido por el antepaís, que fue modificado por la orogenia andina y que se incorporó sucesivamente al orógeno por la migración hacia el este del frente de deformación andino durante el Mioceno tardío - Plioceno. Las observaciones estructurales y geomórficas dentro de la meseta indican que los procesos extensionales deben haber estado repetidamente activos entre el Mioceno tardío y el Holoceno, apoyando la noción de procesos extensionales a lo largo de toda la meseta, potencialmente asociados con terremotos de  $M_w \sim 7$ . La estrecha relación entre las juntas extensionales y las orientaciones de las fallas subraya que  $\sigma_3$  estaba orientada horizontalmente en dirección NO-SE y  $\sigma_1$  era vertical. Esto documenta inequívocamente que la deformación observada está relacionada con fuerzas gravitatorias que impulsan el colapso orogénico de la meseta. Los análisis geocronológicos aplicados sugieren que el fallamiento normal en la Puna septentrional estuvo activo en torno a los 3 Ma, basándose en la datación por pares de nucleidos cosmogénicos de las unidades de relleno sedimentario. Posiblemente, debido a las fallas normales regionales, el sistema de drenaje de la meseta también se vio afectado, favoreciendo la incisión fluvial.

# Contents

Eigenständigkeitserklärung	iii
Acknowledgement	v
Abstract	viii
Zusammenfassung	x
Resumen	xii
Contents	xiv
List of figures	xvi
List of tables	xviii
1 Introduction	1
1.1 Motivation .....	1
1.2 The formation of mountain ranges .....	4
1.3 Orogenic plateaus through time.....	5
1.4 Plateau uplift in the Andes .....	8
1.5 Extensional tectonic processes in the interior of the Andean orogen.....	11
1.6 Hypothesis and research questions .....	14
1.7 Study area and geological setting .....	15
2 Methods	28
2.1 Geological framework .....	28
2.2 Remotely-sensed characterization of faulting .....	42
2.3 On-site quantification of vertical displacement values .....	50
3 Results	54
3.1 Geological framework .....	54
3.2 Depositional and exposure ages .....	60

3.3 Fault morphology.....	70
3.4 Drainage-basin morphometries.....	71
3.5 Fault scarp profiling .....	73
3.6 Pumahuasi Fault.....	76
3.7 Yavi Fault .....	84
3.8 Joint measurements.....	90
4 Interpretation & Discussion	92
4.1 Landscape evolution of the central sector of the north-eastern Puna Plateau .....	93
4.2 Extensional tectonic activity.....	111
4.3 Implications for an orogenic collapse .....	133
5. Conclusion	135
6. References	137
7. Appendix	175
Data Tables.....	175

## List of figures

<b>Figure 1:</b> Overview of the Central Andes. ....	3
<b>Figure 2:</b> Earthquake distribution in the Central Andes.....	13
<b>Figure 3:</b> Geological setting of the study area. ....	25
<b>Figure 4:</b> Sampling sites for U-Pb dating.....	32
<b>Figure 5:</b> Sampling sites for surface exposure dating .....	35
<b>Figure 6:</b> Ne 3-isotope diagram for all samples.....	37
<b>Figure 7:</b> Methodological workflow for the processing of the TanDEM-X data set.....	46
<b>Figure 8:</b> Workflow of fault scarp vertical displacement measurements applied to .....	48
<b>Figure 9:</b> Elevation profile extraction at the two study sites. ....	50
<b>Figure 10:</b> Outcrops exposing the stratigraphy of the basin-fill units.....	55
<b>Figure 11:</b> Simplified stratigraphic sections.....	57
<b>Figure 12:</b> Slope map of the study area.....	59
<b>Figure 13:</b> Two-isotope plot showing $^{10}\text{Be}$ concentration in at/g vs $^{26}\text{Al}$ - $^{10}\text{Be}$ ratios of the measured concentrations. ....	62
<b>Figure 14:</b> Two-isotope plot showing $^{10}\text{Be}$ concentration in at/g vs $^{21}\text{Ne}$ - $^{10}\text{Be}$ ratios of the measured concentrations .....	63
<b>Figure 15:</b> Modeled (dashed lines) and measured (prisms) $^{21}\text{Ne}$ concentrations .....	64
<b>Figure 16:</b> Modeled depth profiles.....	65
<b>Figure 17:</b> Calculations of erosion-rate thresholds .....	69
<b>Figure 18:</b> Hillshades and slope maps.....	70
<b>Figure 19:</b> Drainage basin morphometric analysis of the Pumahuasi fault.....	71
<b>Figure 20:</b> Drainage-basin morphometric analysis of the faults at Cordillera de Sama ..	72
<b>Figure 21:</b> Data compilation from the fault-scarp measurements .....	75
<b>Figure 22:</b> Photomosaic.....	80

<b>Figure 23:</b> Road outcrop.....	81
<b>Figure 24:</b> Subvertical and horizontal sheets of sediment layers cemented by ores .....	82
<b>Figure 25:</b> Outcrops of the manganese and iron-ore deposits .....	83
<b>Figure 26:</b> Fault outcrop of the road cut exposure east of Yavi.....	86
<b>Figure 27:</b> Faulted layers at the sand pit east of Yavi. ....	87
<b>Figure 28:</b> Major displacement .....	88
<b>Figure 29:</b> Fault outcrop east of Yavi chico. ....	89
<b>Figure 30:</b> Rose diagrams of joint orientations.....	91
<b>Figure 31:</b> Pilcomayo drainage system and knickpoints .....	109
<b>Figure 32:</b> Late Miocene to Quaternary landscape-evolution model.....	120
<b>Figure 33:</b> Tectonic overprint of sedimentary fill units .....	123
<b>Figure 34:</b> Structural data compilation of the conjugated joints.....	127
<b>Figure 35:</b> Magnitudes of possible paleo-earthquake events.....	130

## List of tables

<b>Table 1:</b> Summary of U-Pb age constraints from the different volcanic ash samples. Grey samples are from the sector west of La Quiaca, associated to the Tafna Formation and the superimposed alluvial fan deposits. Samples Arg21-xx (except Arg21-Ash03) were taken from the sector east of La Quiaca. All errors are 2se.....	60
<b>Table 2:</b> Summary of the measured nuclide concentrations of $^{10}\text{Be}$ , $^{26}\text{Al}$ and $^{21}\text{Ne}$ . .....	61
<b>Table 3:</b> Calculated measured and inheritance corrected exposure ages of the two different surface levels in Ma. Note the corrected ages agreeing within error bounds.....	66
<b>Table 4:</b> Calculated measured and inheritance corrected exposure ages of the two different surface levels in Ma using CRONUS-Earth calculator.....	67
<b>Table 5:</b> Calculated measured exposure ages in Ma and erosion rate estimates of the two different surface levels using CosmoCalc calculator. ....	67
<b>Table 6:</b> Calculated measured exposure ages in Ma and erosion rate estimates of the two different surface levels using CREp online calculator ( $^{10}\text{Be}$ only).....	68

# 1 Introduction

## 1.1 Motivation

Earthquakes generally reflect a sudden response of the Earth's crust to release the build-up of stresses along plate boundaries accrued during the motion of interacting tectonic plates (Kanamori & Brodsky, 2004). Earthquakes manifest themselves by irreversible crustal deformation and topographic changes, which is an integral part of orogenic processes (Brooks *et al.*, 2011; Whipple *et al.*, 2016). In the case of the Andes of South America such deformation and vertical changes of the crust take place in the South American continental plate, contrasting the deep-seated Benioff-zone earthquakes of the subducting Nazca Plate (Jordan *et al.*, 1983; Isacks, 1988) (Figure 1). The foci of frequent shallow crustal earthquakes and related deformation phenomena are primarily found at the interface of the Nazca and South American tectonic plates and within the sub-Andean thrust belts (Cortés & Angelier, 2005; Schurr *et al.*, 2006; Mulcahy *et al.*, 2014) and the broken foreland sectors (Figure 1b) (Costa *et al.*, 2006; Hain *et al.*, 2011; Arnous *et al.*, 2020). In contrast, the lack of instrumentally recorded seismicity in the central sectors of the mountain range, particularly within the orogenic Andean Plateau, has led to the hypothesis of protracted tectonic quiescence in the sectors of the northern Puna Plateau of Argentina (Schurr *et al.*, 1999), although Quaternary deformation structures and tectonically overprinted landforms suggest that this region is or at least was recently also tectonically active (Mon *et al.*, 1988; Allmendinger *et al.*, 1989; Cladouhos *et al.*, 1994; Schoenbohm & Strecker, 2009).

The present-day character of regional seismicity in the plateau and adjacent tectonic provinces is emphasized by a recent shallow crustal earthquake that struck the area of the Quebrada de Humahuaca in the Eastern Cordillera of north-western Argentina on November 20, 2020 (Colavitto *et al.*, 2021). This  $M_w = 5.8$  (USGS 2021) event destroyed local infrastructure and triggered landslides within the Eastern Cordillera. Subsequently, several earthquakes with minor magnitudes ( $M_w \sim 3$ ) occurred in the adjacent area. Two aspects are particularly quite atypical about these events: 1) shallow seismicity had not been recorded previously in this part of the mountain range, and 2) the focal mechanism of the major event indicated N-S-directed extension (Colavitto *et al.*, 2021) and thus reflects a tensional stress field in this part of the mountain range; this kinematic style is contrary to the character of the regional compressional stress field and the well-known, E-W-directed

compressional, crustal deformation in the Andes at lower elevations (Cahill *et al.*, 1992; Schurr *et al.*, 1999; Audin *et al.*, 2006; Mulcahy *et al.*, 2014). Up to now, these young normal-faulting events have not been analyzed in detail, although extensional deformation appears to be an ubiquitous and intrinsic part of the Andean tectonism, especially in the central, high-elevation sectors of the Andean Plateau and the adjacent mountain ranges to the east (Cladouhos *et al.*, 1994; Giambiagi *et al.*, 2003; Schoenbohm & Strecker, 2009; Montero-López *et al.*, 2010; Zhou *et al.*, 2016; Tibaldi & Bonali, 2018; Wimpenny *et al.*, 2018). Extensional surface deformation in some of these areas has been a recurring phenomenon during the Quaternary, and in the southern Puna Plateau of Argentina extensional deformation may have already started during the Late Miocene - Early Pliocene (Montero-López *et al.*, 2010) leading to numerous fault scarps and associated mafic volcanism (Allmendinger, 1986). In the northern sectors of the Puna Plateau, fault scarps cutting sedimentary fill units of inferred Quaternary age might represent one of the youngest vestiges of such deformation processes that appear to be more common at the southern plateau margin (Cladouhos *et al.*, 1994). However, in the northern Puna, there has been a lack of instrumentally recorded seismic activity and a detailed geochronological analysis on the timing and potential magnitudes of fault offsets affecting Quaternary sedimentary valley fills has not been done after the initial recognition by Cladouhos *et al.* (1994). This is surprising since such an analysis could provide crucial data for a more profound understanding of the spatial and temporal distribution of extensional tectonism in the Central Andes and its impact on erosion and sedimentation processes within the intermontane sedimentary basins. Gaining such knowledge would be furthermore helpful to retrieve information on the possible future hazards of seismogenic deformation processes as well as the spatiotemporal transition from long-term shortening to neotectonic extension, which may be similar in character to orogenic collapse processes that have been inferred for other Cenozoic mountain belts, such as within the Anatolian Plateau (e.g. Göğüş & Pysklywec, 2008; Koçyiğit, 2013; Özsayin *et al.*, 2018; Krystopowicz *et al.*, 2020) or the Tibetan Plateau (Armijo *et al.*, 1986; Liu, 2003; Kapp *et al.*, 2008; Guo *et al.*, 2018).

In light of recent normal faulting in the north-eastern Eastern Cordillera, this study aims at addressing the extent and timing of extensional faulting in the northern sector of the neighbouring Puna Plateau, thereby contributing data needed for a better understanding of the geodynamic implications, the structural context, and the overall late Cenozoic tectonic evolution of the north-western Argentine Andes. In addition, the deformation and

sedimentary depositional history of the north-western Argentine Andes will be analyzed in the context of landscape-evolution processes, particularly with respect to the fluvial evolution within the plateau and the possible changeover from internal or severed drainage conditions during the early plateau-forming processes to full fluvial connectivity with the intermontane basins of the eastern bounding ranges and the undeformed foreland.

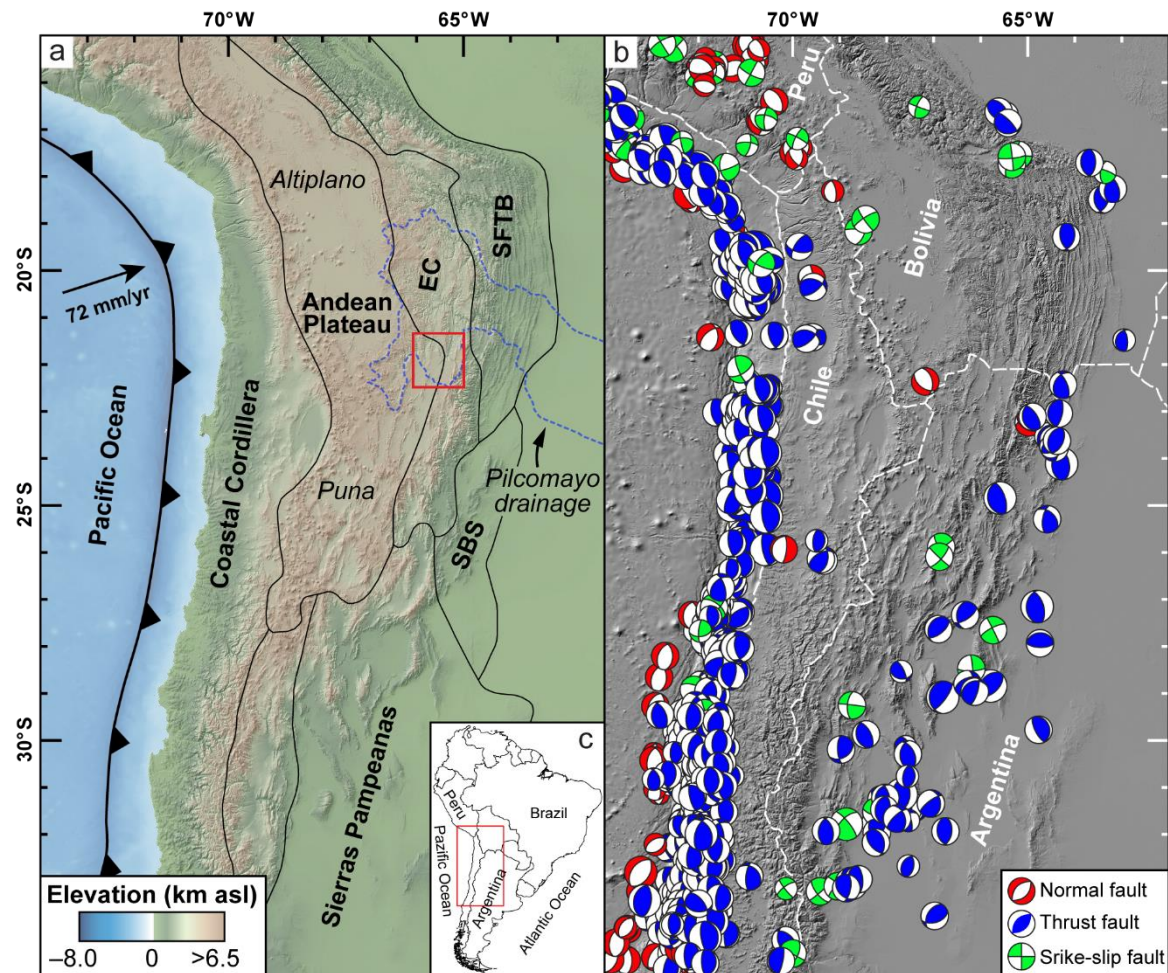


**Figure 1:** Overview of the Central Andes. **a)** Digital elevation model of central South America (SRTM) showing subduction interface in the Pacific Ocean and the morpho-tectonic provinces of the Central Andes bounded by thin black lines (SBS = Santa Barbara System, EC = Eastern Cordillera, SFTB = Subandean Fault and Thrust belt) (Modified after (Jordan et al., 1983; Horton & DeCelles, 2001)). The subduction related deep sea trench is outlined parallel to the western coast of South America, velocity data was taken from Maloney et al. (Maloney et al., 2013). The catchment of the Río Pilcomayo is delineated by a dashed blue line. The red square highlights the location of the study area in the transition zone of the Andean Plateau and the Eastern Cordillera, as part of the Río Pilcomayo drainage system. **b)** Hillshade of central South America. International borders are outlined by white dashed lines. Focal mechanism solutions represent the distribution of shallow earthquakes (hypocenter depth < 50 km) of intermediate to high magnitudes ( $M_w > 4.5$ ) taken from the Global CMT catalog (<https://www.globalcmt.org/>). The three types of fault mechanisms are displayed in different colors (red = normal fault, blue = thrust fault, green = strike-slip fault). The distribution shows a clear trend of shallow seismicity along the western subduction interface, the central sectors of the mountain range only experienced low crustal seismicity dispersed in time and space, while the broken foreland of the Sierras Pampeanas, the Santa Bárbara System and the Subandean Fold-and-Thrust Belt show intermediate seismic activity. Most of the fault plane solutions show thrust and strike-slip faulting mechanisms. Normal faulting is scarce and, for the Andean Plateau, appears to be concentrated in the northern sectors of the Altiplano of Peru. **c)** Location of Figure 1 a and b within South America.

### **1.2 The formation of mountain ranges**

Tectonically active mountain ranges such as the Andes are monumental expressions of the dynamics of subduction and/or collisional processes, shaping Earth's surface along plate boundaries (Avouac, 2015). Mountain ranges may develop in a variety of geodynamic settings that include i) two continental plates in collision, as it is seen in the Himalayas, where the Eurasian and Indian tectonic plates collide and deform; ii) a continental and an oceanic plate, represented by the Andes of South America, where the subduction of the oceanic Nazca plate beneath the South American plate has been generating compressional stresses that ultimately caused shortening and uplift of rocks of the South American Plate; or iii) even far away from active plate boundaries, as shown by the formation of the Tien Shan mountains in Central Asia (Hendrix *et al.*, 1992; Avouac & Tapponnier, 1993) or the Sierras Pampeanas and the ranges of the Santa Bárbara System of western and north-western Argentina, respectively (Jordan *et al.*, 1983; Ramos & McNulty, 2002). Some mountain ranges that were active in the past were able to maintain high topography on geological timescales and under changing tectonic regimes, while continuous erosion fed adjacent sedimentary basins with large amounts of detritus (Einsele, 2000). These examples illustrate, how the underlying tectonic forces can cause sustained deformation and uplift of continental crust, which creates pronounced contrasts in relief that in turn enable efficient erosional regimes and sedimentary processes that result in thick sedimentary strata and potentially change the tectonic stress field (Liu *et al.*, 2016; Allen, 2017; Ballato *et al.*, 2019).

Compressional stresses generated in plate-boundary settings ultimately lead to crustal shortening, large-scale surface uplift, and the formation of efficient orographic barriers (Molnar & Lyon-Caen, 1988; Baby *et al.*, 1997; Kleinert & Strecker, 2001; Smit *et al.*, 2003; Mulch & Chamberlain, 2006; Allen *et al.*, 2013; Pingel *et al.*, 2014; Avouac, 2015). In these settings thrust faults and folds generally form perpendicular to the orientation of the greatest horizontal stress ( $S_{Hmax}$ ) (Allmendinger, 1986; Victor *et al.*, 2004). Complexly distributed loading of pre-existing crustal heterogeneities and the impact of compression on layered sedimentary strata results in deformation features, which tend to be characterized by parallel belts that incorporate and expose strata of different geological domains (Willis, 1893; Argand, 1922). Paired with superposed and orographically distributed precipitation, disparate erosional forcing will subsequently follow and often lead to highly asymmetric and variable relief development, forming peaks and valleys with

steep topographic gradients that may reach elevations of several thousands of meters. In extreme cases, these combined effects of range uplift, the migration of thrusting and uplift toward the foreland, and ensuing changes in topographic-atmospheric interactions may result in the hydrologic isolation of the interior sectors of mountain ranges; in these settings dry conditions with transport-limited and sometimes endorheic fluvial systems prevail, while the windward, humid flanks, evolve toward highly efficient erosion and transport systems that are connected with the undeformed foreland (Ruddiman & Kutzbach, 1991; Sobel *et al.*, 2003). As a result, the sedimentary basins in the orogen interiors will receive large amounts of detritus and chemical precipitates may form in the center of the basins over time (Alonso *et al.*, 1991). Moreover, the relief contrasts between the basins and ranges will be successively reduced in these environments, because sediments will continue to accumulate within the orogen and not be transported toward the foreland (Sobel *et al.*, 2003; Strecker *et al.*, 2007). This reduction in relief and the internal drainage conditions are typical of orogenic plateaus and the process of protracted sediment accumulation may contribute toward the attainment of a plateau-like topography by coalesced intermontane basin formation (Sobel *et al.*, 2003; Sobel & Strecker, 2003; Zhu *et al.*, 2006; Liu-Zeng *et al.*, 2008; Cheng *et al.*, 2018). In the past three decades, the evolution of orogenic plateaus has therefore been a major focus of studies aimed at unraveling the relationship between tectonics, topography, climate, surface processes, and biodiversity (Smith & Foggin, 1999; Bai-ping *et al.*, 2002; Alonso *et al.*, 2006; Croft, 2007; Barnes, 2008; Lease & Ehlers, 2013; Strecker *et al.*, 2016; Amidon *et al.*, 2017; Quiñones *et al.*, 2019; Perrigo *et al.*, 2020).

### **1.3 Orogenic plateaus through time**

Present-day orogenic plateaus are first-order tectonic and topographic features found in many Cenozoic mountain belts on Earth. However, their existence has also been documented in similar paleo-tectonic settings in deep geological time, such as the late Mesozoic Nevadoplano in the western United States (Zandt *et al.*, 1995; Best *et al.*, 2009; Levander & Miller, 2012) or the Variscan orogenic plateau in central Europe (Murawski *et al.*, 1983; Vacek & Žák, 2019). Plateaus define the character of the North American Cordillera (Schmidt, 1988; McQuarrie & Chase, 2000; Karlstrom *et al.*, 2022), the India-Eurasia collision zone (Tibet and eastern Pamir) (Dewey & Burke; Rothery & Drury, 1984; Allen *et al.*, 2013; Zuza, 2016), the South American Andes (Allmendinger & Gubbels; Allmendinger & Gubbels, 1996; Garziona *et al.*, 2017; Tapia *et al.*, 2019), and the highlands of Turkey and Iran (Schildgen *et al.*, 2012; Allen *et al.*, 2013; Krystopowicz *et*

*al.*, 2020). Although they may have developed under a variety of geodynamic conditions, orogenic plateaus share common characteristics; these include low relief at high elevations, semiarid to arid interiors, as well as steep topographic and climatic gradients at their margins, especially if the orientation of the bounding ranges is perpendicular to with respect to the regional wind- and moisture-transport pattern (Ruddiman & Kutzbach, 1991; Allmendinger *et al.*, 1997; Alonso *et al.*, 2006; Schildgen *et al.*, 2007; Strecker *et al.*, 2009; Allen *et al.*, 2013; Rohrmann *et al.*, 2016; Pingel *et al.*, 2019).

Much effort has already been put into unraveling the formation, protracted uplift and morphological evolution of orogenic plateaus. The current theories can be broadly grouped into structural and thermo-mechanical processes, ranging from commonly described mechanisms such as bulk crustal shortening and distributed shortening of the upper crust (Isacks, 1988; Allmendinger & Gubbels, 1996), over partial subduction of buoyant continental crust (Pope & Willett, 1998), and lower crustal flow (Husson & Sempere, 2003; Rey *et al.*, 2010) to lithospheric delamination (Garzione *et al.*, 2008; Perkins *et al.*, 2016). A theory linking tectonic activity of developing plateau areas with the effects of arid climatic conditions and the properties of rock erodibility was presented by Sobel *et al.* (2003). This hypothesis claims that foreland-basin areas are successively incorporated and transformed into intermontane sedimentary basins by foreland-directed migration of orographic-barrier uplift and ensuing aridification of the orogeny interior. As a result, these basins will be hydrologically isolated and subsequently infilled with sediment, thus leading to a reduction in relief. In combination with the leeward aridification of the orogen's interior, this may lead to a defeat of the drainage network with a changeover from externally to internally drained basins. Continuously infilled basins will ultimately become overfilled and coalesce, leading to equal-elevation basin surfaces, reduced relief contrasts, and lateral growth of the developing plateau area as the structures that bound these sectors of the orogen will continue to migrate toward the foreland (Métivier *et al.*, 1998; Sobel *et al.*, 2003; Strecker *et al.*, 2009). Although single mechanisms as briefly described above can be quite effective in themselves, a combination of different mechanisms, which are not mutually exclusive, should always be considered to find a plausible explanation for the formation of orogenic plateaus as well as their late-stage tectonic evolution.

Regardless of the mechanisms responsible for plateau formation, in order to maintain the character of internal drainage and severed, external sediment transport in these high-elevation sectors, either uplift rates of the plateau and its bounding ranges must be relatively

high or range-perpendicular precipitation must be low. Such a scenario would prevent headward erosion, which, under humid conditions, would tap the internally drained basins in the orogen's interior, cause plateau-wide incision and sediment evacuation towards the foreland, thus destroying plateau morphology. Deeply incised sedimentary fill units associated with formerly internally drained intermontane basins might represent the vestiges of such processes. Examples have been described along the Yellow River of Tibet (Liu-Zeng *et al.*, 2008; Craddock *et al.*, 2010), the Colorado Plateau (Schmidt, 1988; Meek & Douglass, 2001) or along the north-western margin of the Iranian Plateau (Heidarzadeh *et al.*, 2017). Conversely, under a tectonic regime of progressively advancing foreland-directed tectonism, the plateau realm will prevail as a topographic, sedimentologic, and geomorphic entity due to the inability of erosion to keep pace with the uplifting plateau flanks.

Theories explaining the underlying mechanisms of lowering plateau topography and increasing relief by fluvial incision propose either tectonic processes, such as gravitational collapse that in turn will facilitate pathways for subsequent incision (Dewey, 1988; Rey *et al.*, 2001; Jadamec *et al.*, 2007) or incision by rivers draining the steep flanks of the plateaus that might follow over-spilling of the endorheic plateau basins due to progressive infilling, barrier incision, and headward erosion (Clark *et al.*, 2006; Montero-López *et al.*, 2014; Heidarzadeh *et al.*, 2017). In the Andes such plateau-wide destructional processes of river systems are still areally limited. In the central Altiplano of Bolivia, the Río La Paz, the Río Grande and the Río Consata traversing the Eastern Cordillera have tapped into the Andean Plateau and thus may represent such a stage in plateau evolution (Zeilinger & Schlunegger, 2007). Similarly, in the northeastern sectors of the Argentine Puna and the southernmost Altiplano of Bolivia, widespread incision has formed steep canyons along the catchment of the Río Pilcomayo drainage system that contributes sediment to the foreland (Kennan *et al.*, 1997). In the Peruvian sectors of the Altiplano, the internal drainage character of the plateau has partly been breached by Pliocene incision of the Urubamba drainage system (Gérard *et al.*, 2021). Moreover, recent studies focusing on the possible migration of drainage divides in the eastern Andes of Argentina present geomorphic evidence of westward directed migration of the drainage divide between externally and internally draining regions in the orogen, leading to minor area losses for the Andean Plateau (Seagren & Schoenbohm, 2021). Continued headward erosion by these river systems could

potentially lead to widespread incision and erosional exhumation resulting in the progressive demise of the plateau.

### **1.4 Plateau uplift in the Andes**

The Andes are the largest non-collisional mountain belt on Earth, straddling the N-S-oriented western continental margin of South America for more than 7000 km, reaching peak elevations of up to 7000 m above sea level (a.s.l.). The main topographic feature of the Central Andes is the Andean Plateau, also known as the Altiplano (Peru, Bolivia)-Puna (Argentina) Plateau, which is the second largest plateau on Earth (Isacks, 1988). With an average elevation of around 4000 m a.s.l. the plateau extends from north to south for approximately 1800 km (13°S to 27°S), spanning southern Peru, Bolivia, and north-western Argentina. In an east-west direction the plateau extends up to 400 km in the Bolivian Andes, but towards the northern and southern margins the plateau width becomes increasingly smaller (Coutand *et al.*, 2001). The plateau is structurally bounded by the Eastern and Western Cordillera morphotectonic provinces that reach peak elevations over 6000 m a.s.l. (Figure 1a) (Jordan *et al.*, 1983; Schoenbohm & Strecker, 2009). While the Western Cordillera comprises the modern Andean magmatic arc, the Eastern Cordillera and the Altiplano-Puna record a complex history of folding and faulting, and potentially wholesale uplift related to upper-mantle processes (Garzzone *et al.*, 2008).

The formation of the Andes is the result of the ongoing oblique subduction of the oceanic Nazca Plate beneath the South American Plate and the Brazilian Shield, respectively (Ramos, 2018). Protracted crustal shortening has been active over the last 50 million years (McQuarrie *et al.*, 2005), resulting in a crustal thickness of up to 70 km (Beck & Zandt, 2002). Despite crustal shortening being a key mechanism for thickening of the crust, balanced cross sections at different latitudes of the Central Andes have shown that shortening estimates alone cannot account for the observed crustal thickness (Roeder, 1988; Schmitz, 1994; Baby *et al.*, 1997; Kley & Monaldi, 1998). This missing link led to the search for additional mechanisms, capable of generating topography by processes of mantle-driven surface uplift. Geophysical studies suggested the absence of an eclogitic lower crust underneath the plateau area (Beck & Zandt, 2002), a hypothesis, supported by earlier observations on strikingly low P-wave velocities below the plateau that may indicate the delamination of mantle lithosphere between 16° and 20°S (Wigger *et al.*, 1994; Dorbath & Granet, 1996; Myers *et al.*, 1998). Additionally, high He-isotope ratios of hydrothermal

fluids measured across the plateau and the Eastern Cordillera imply degassing of magmas derived from the upper mantle, rather than a more crustal isotopic signature (Hoke *et al.*, 1994).

In combination with the geophysical studies, these findings point towards a deep-seated substitution of lower crust with mantle material underneath the plateau. Possible processes responsible for this may thus either include rapid delamination and convective removal of the lower crust (Bird, 1979; Houseman *et al.*, 1981; Göğüş & Pysklywec, 2008; Garzione *et al.*, 2017; Gao *et al.*, 2021) or gradual ablative subduction of foreland cratonic lithosphere (Tao & O'connell, 1992; Pope & Willett, 1998; Ramos, 2018). In either case, this would have generated accommodation space facilitating the emplacement of asthenosphere-derived material. Buoyancy-force gradients between the two different materials would ultimately lead to additional surface uplift (Levandowski *et al.*, 2018; Evans *et al.*, 2021). These models could explain uplift of the Andean interior, which was temporally partially decoupled from processes of crustal shortening. As these mantle-driven processes do not directly provide information on the pace of mountain building, the question remains as to how fast or slow the uplift occurred and what its relationship with crustal shortening was. In this context, regionally extensive geomorphic paleo-surfaces either related to the emplacement of ignimbrites or erosional and depositional processes may constitute excellent archives that yield information on paleo-elevations, but may also be used as strain markers that potentially provide data on the timing of deformation and uplift, if they can be dated radiometrically.

Fossil leaves in sediments deposited in the Bolivian Altiplano areas indicate paleo-elevations of less than 1300 m for the timeframe between 15-20 Ma (Gregory-Wodzicki, 2000). This observation is in agreement with earlier studies suggesting that the plateau did not reach its present elevation prior to 10 Ma (Gubbels *et al.*, 1993), and more recent studies on mammal fossils in southern Bolivia suggest that sedimentary fill units from the middle Miocene (13-12 Ma) were deposited in a paleo-topographic setting above 2000 m a.s.l., but below the current elevation of 3700 m a.s.l. (Gibert *et al.*, 2020). These findings are further supported by other studies of paleo-environmental conditions based on the existence of various fossils (Cadena *et al.*, 2015; Catena *et al.*, 2017; Quiñones *et al.*, 2019), which were recently discussed in light of the uplift history of the central-eastern Andes (Pingel *et al.*, 2020; Montero-López *et al.*, 2021).

According to these analyses, the final uplift of the Andean interior must be a relatively young phenomenon, which had also been suggested earlier by Gubbels (1993) and Garzzone *et al.* (2006; 2008). Incision into plateau-wide paleo-surfaces and associated base-level lowering was used to further delimit timing and rates of uplift. For example, low-relief drainage networks associated with some of these paleo-surfaces existed between 7 and 12 Ma along the eastern flanks of the Andes (Gubbels *et al.*, 1993; Kennan *et al.*, 1997) and until ~10 Ma at the western flanks (Hoke *et al.*, 2007). Relief reconstructions of incised valleys provided surface-uplift estimates of approximately 2 km for the Eastern Cordillera (Barke & Lamb, 2006) and 1 to 2.5 km for the Western Cordillera (Schlunegger *et al.*, 2006; Hoke *et al.*, 2007; Schildgen *et al.*, 2007; Jordan *et al.*, 2010). Despite different climatic settings, contemporaneous uplift at the eastern and western flanks was interpreted to have generated regional high topography, which may have driven widespread incision processes (Garzzone *et al.*, 2017).

A synthesis of different studies on the uplift history suggests a two-stage model of surface uplift in the Andes (Garzzone *et al.*, 2008): while initial uplift was driven by crustal shortening, a dense, eclogitic root of the mountain range limited uplift and therefore elevations were maintained at around 2000 m a.s.l. Between 10-6 Ma, the lithospheric character of the Andes must have changed, possibly due to the removal of the dense root of the orogen, leading to wholesale uplift associated with an additional 1.5-2 km (Garzzone *et al.*, 2008). An absence of compressional features within the ubiquitous paleo-surfaces in the realm of the Andean Plateau indicates that crustal shortening in the central sectors of the Andes ceased and migrated eastward toward the Subandean region, where a fold-and-thrust belt and broken-foreland uplifts developed (Gubbels *et al.*, 1993; Echavarría *et al.*, 2003). The latter was facilitated by the compressional reactivation of Cretaceous normal faults, leading to disparate foreland uplifts, while the former was associated with deformation along a westward-dipping décollement and the systematic eastward migration of deformation (Mon & Salfity, 1995; Arnous *et al.*, 2021). An associated change in the distribution of deviatoric stresses within the high-elevation sectors at a later stage have set the conditions for the onset of extensional deformation along and within the interior of the Andean Plateau, which triggered an orogenic-collapse process that has been active until the present-day (Froidevaux & Isacks, 1984; Giovanni *et al.*, 2010; Giambiagi *et al.*, 2016).

## 1.5 Extensional tectonic processes in the interior of the Andean orogen

Extensional structures within orogenic plateaus are a frequently observed phenomenon in advanced stages of orogenic cycles (Mercier, 1981; Dewey, 1988; Liu, 2003; Madarieta-Txurruka *et al.*, 2021; Wang *et al.*, 2021). Normal faults suggest the existence of extensional forces acting on the thickened crust, potentially compensating the weight of the accumulated mass through processes of gravitational spreading (Dewey *et al.*, 1993; Liu *et al.*, 2000; Rey *et al.*, 2001). However, the origin and particularly the geodynamic implications in the context of the force-balance of mountain ranges is still not well understood, as implied by numerous studies on the topic (Dewey, 1988; Dewey *et al.*, 1993; Liu *et al.*, 2000; Rey *et al.*, 2001; Vanderhaeghe & Teyssier, 2001; Jadamec *et al.*, 2007; Folguera *et al.*, 2008). This is especially the case in the Central Andes of South America, where seismically active zones of extension exist (Cladouhos *et al.*, 1994; Schoenbohm & Strecker, 2009; Wimpenny *et al.*, 2018); however, the timing and possible spatial changes in the distribution of this extensional tectonism as well as reliable seismological observations of this phenomenon are limited (Schurr *et al.*, 1999; Beck & Zandt, 2002; Mulcahy *et al.*, 2014). Conversely, on the Tibetan Plateau, at least six  $M_w > 6$  dip-slip events occurred along previously unknown normal faults (Elliott *et al.*, 2010) and extensional processes in this region have been the focus of protracted research projects (Armijo *et al.*, 1986; Liu *et al.*, 2000; Liu, 2003; Kapp *et al.*, 2008; Chevalier *et al.*, 2020; Burke *et al.*, 2021; Xu *et al.*, 2021). Regional studies in the Himalayan-Tibetan realm indicate that active N-S to NW-SE-striking normal faults and predominantly E-W-striking strike-slip faults are currently accommodating extension in the high-elevation sectors of this collisional setting. These studies suggest that Tibet is extending in approximately E-W direction while shortening prevails at the plateau margins and the peripheral sectors of the mountain range (Rothery & Drury, 1984; Armijo *et al.*, 1986).

In the Andes, seismicity is primarily associated to the subducting Nazca slab, reflected by east-directed increase of hypocenter depths beneath the central sectors of the mountain range (Figure 2). Shallow crustal seismic events occur in the eastern fold-and-thrust belt (Subandean ranges) and the broken-foreland sectors of the Sierras Pampeanas and the Santa Bárbara System (Cahill *et al.*, 1992) (Figure 1 and Figure 2). More recent local seismic experiments in the Central Andes of Argentina revealed crustal micro-seismicity ( $M_w < 4$ ) in the plateau, located preferably along and south of the inferred 'Calama-Olacapato-El

Toro (COT)-Lineament' (Schurr *et al.*, 1999). No seismic events were recorded north of this lineament, suggesting a structural boundary to these authors. Schurr *et al.* (1999) concluded that the southern section of the plateau is internally deforming, associated with extensional processes that enable the ascent of mafic magmas that are geochemically similar to ocean-island basalts (Coira & Koukharsky, 1991; Allmendinger *et al.*, 1997). In contrast, the northern Puna was thought to deform as a stable block without such zones of weakness. This behavior is also reflected in measured ground acceleration values: velocity fields calculated from continuous GPS data exhibit a systematic decrease in horizontal velocities from West to East from  $\sim 35$  mm/yr at the Nazca-South America plate intercept to  $<1$  mm/yr at the eastern boundary of the orogen (McFarland *et al.*, 2017). The strongest gradients can be found in the Precordillera and the Eastern Cordillera and the isolated foreland uplifts of the Santa Bárbara System, which could indicate a potential locked zone along the deformation front of the orogen. However, on satellite imagery and digital elevation models of the north-eastern Puna Plateau surface-deformation features affecting deposits younger than the late Miocene to Pliocene can be identified. More specifically, fault scarps with a throw of several meters to tens of meters cut through alluvial sediments that were probably deposited during the Quaternary (Cladouhos *et al.*, 1994). Based on relative age relationships, these structures must be younger than the affected morphological features with activity during the latest stages of the Andean orogeny. Active extensional structures were documented in recent studies, virtually affecting the entire plateau interior and the plateau margins in the southern sector of the Puna, and often associated with orogen-parallel extension and strike-slip motion (Schoenbohm & Strecker, 2009; Montero-López *et al.*, 2010; Zhou *et al.*, 2016). Similar phenomena have been observed at the northern margins of the Altiplano Plateau in southeastern Peru, where a  $M_w \sim 6.1$  dip-slip earthquake along a normal fault occurred in 2016 (Wimpenny *et al.*, 2018), and at the western transition from the Puna Plateau to the Atacama Basin of Chile (Tibaldi & Bonali, 2018). These studies contributed to the notion that extensional structures are mainly distributed along the margins of the plateau, thus supporting a concept that incorporates topographic edge-effects in explaining the collapse of the orogen's margins, where either (1) narrowing topography and decreasing crustal thickness at the northern and southern margins (Allmendinger *et al.*, 1989; Marrett *et al.*, 1994), (2) a decrease of shortening rates along strike of the plateau (Allmendinger *et al.*, 1989), or (3) variations in subduction angles of the Nazca slab might have played a major role in driving extensional processes (Allmendinger, 1986). A more recent modified concept describes the Miocene onset of

extension at high altitudes of the Andes as a result of varying lateral contrasts in gravitational potential energy (Wimpenny *et al.*, 2018).

However, since a definitive, unambiguous mechanical explanation for extensional forces acting on the Andean Plateau does not yet exist, it is important to identify, map, kinematically characterize, and date extensional structures in other sectors of the plateau and view them in light of earlier reports from the plateau region. The early studies by

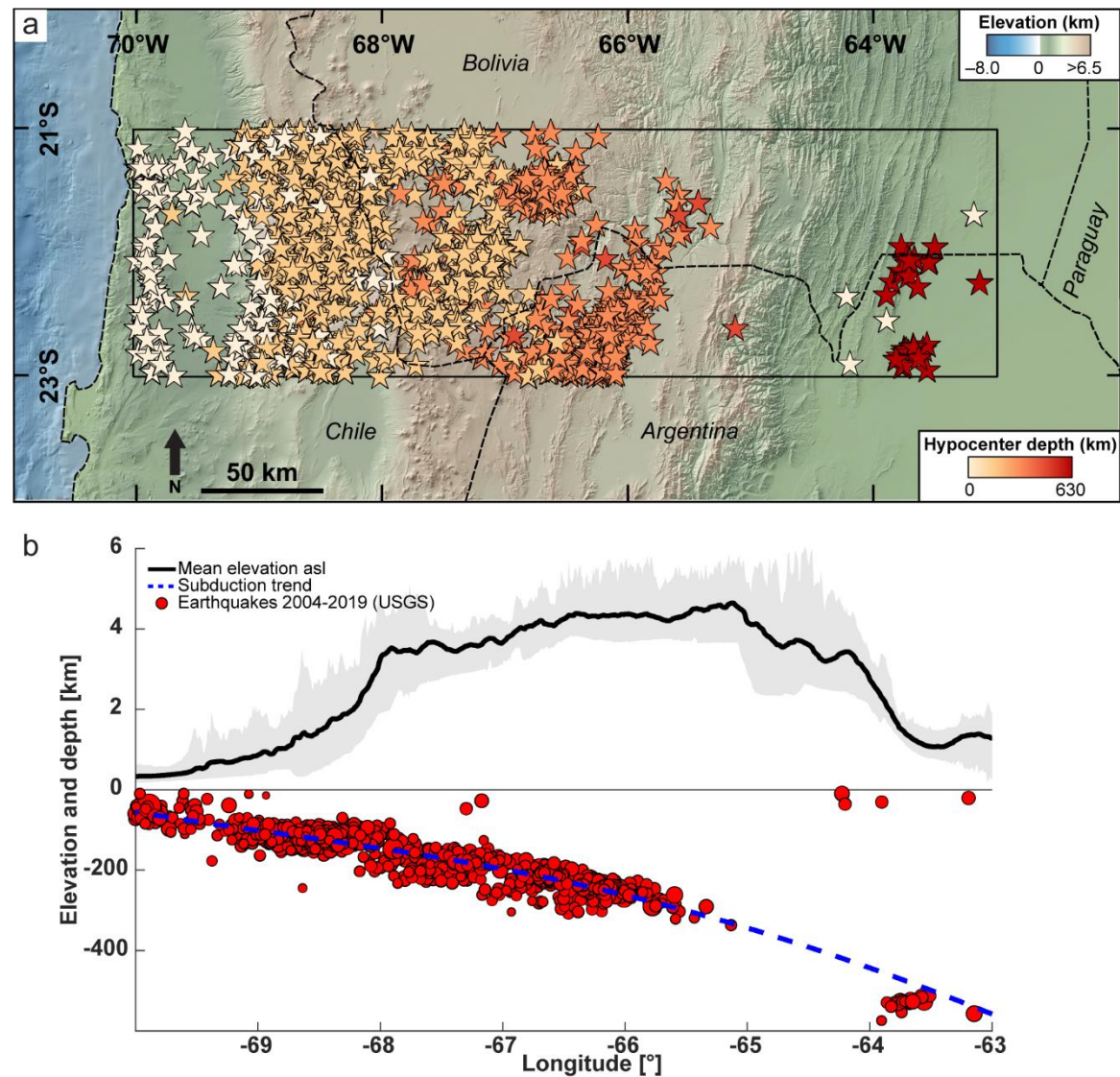


**Figure 2:** Earthquake distribution in the Central Andes between 21°-23°S and 63°-70°W based on data from 2004 to 2019 published by the United States Geological Survey (USGS). **a)** Earthquake hypocentral depths and location in the central Andes of Argentina, Bolivia and Chile. Single events are marked by stars; color coding displays the depth of the hypocenter. Note the gap of seismic events between 65° and 64°W. Shallow earthquakes (<50 km depth) occur preferably along the eastern and western margins of the mountain range. **b)** Swath-elevation data of the Central Andes (upper figure, mean in black, min and max elevations in grey) against hypocenters (red circles) and moment magnitudes (circle size). W-E increasing hypocenter depths allow to interpolate the trend of the subducting Nazca Plate. Shallow crustal earthquakes are sporadically distributed in the central and eastern section. No crustal earthquakes were recorded at peak elevations within the Andean Plateau.

Cladouhos et al. (1994) were a first attempt to shed light on these processes, and the results of these authors constitutes a valuable basis for additional follow-up studies as proposed in this thesis. In addition, potentially ongoing extension in other parts of the Puna Plateau could lead to more organized and pronounced fault patterns, comparable to the zones of active normal faulting on the Tibetan Plateau and hence, result in greater seismic hazard and risk (Schoenbohm & Strecker, 2009). In consideration of the economic development of the Puna Plateau as a major source for lithium (Dorn, 2021), other strategic resources, and increasing demographic change associated with resource-exploration efforts, this regions' population and infrastructure will be subjected to geological hazards and thus be more vulnerable. It is therefore important to better understand the neotectonics and potentially active geological structures of the plateau region and its transitional geologic provinces.

### **1.6 Hypothesis and research questions**

This study is based on two related hypotheses. First, while the early plateau stages were characterized by internally draining basins that successively received substantial amounts of detritus, this phase of plateau aggradation ended with the reduction of uplift processes and the changeover to extensional tectonic activity. The change in kinematic conditions subjected the plateau margins to fluvial processes promoting downcutting, headward erosion, and plateau incision. This phase of incision is still ongoing and responsible for the adjustment of the plateau morphology and the active fluvial evacuation of sedimentary fill units on the plateau, which may result in the demise of the overall plateau area. Second, neotectonic activity along extensional structures in the Andean Plateau is related to gravitational potential energy reflecting an ongoing orogenic collapse that initiated during the Pliocene after major plateau uplift had occurred. This phase of orogenic evolution is expressed by young normal-fault scarps that may have a similar history as their counter parts in the southern plateau and within the Altiplano of Bolivia and Peru.

The following research questions will form the basis to adress this hypothesis and guide the approach to test both hypotheses:

- 1) What is the geological and geochronological context of the deformed sedimentary strata in the north-eastern Puna, and were these deposits formed as a part of the internally drained basins associated with the Andean Plateau?*

- 2) *Is the present-day incision into these deposits part of an ongoing process of fluvially-driven plateau destruction?*
- 3) *What is the spatial and temporal distribution of normal faults in the central north-eastern part of the Argentine Puna Plateau and what are the characteristics of fault kinematics, displacement values and the timing of tectonic activity along the identified structures?*
- 4) *Are these normal faults related to a gravitationally driven collapse of the high elevation areas of the Andes, as already proposed by previous studies in the Andes and elsewhere?*

In order to answer these questions, faulted landscapes in the central north-eastern sector of the Puna Plateau were analyzed by morphometry, sedimentology, geochronology, and structural observations. In particular the focus of this study is on i) using geomorphic analysis of high-resolution digital elevation data (TanDEM-X) to characterize the degree of surface deformation and maintenance of morphological characteristics over time; ii) presenting new field data of faulted sedimentary strata to quantify the amount and type of displacement; and iii) determining the maximum depositional and surface-exposure ages of gently sloping transport surfaces overlying basin-fill units to identify the timing of past surface ruptures and the onset of incision processes that were linked to fluvial connectivity with the foreland.

The results will add valuable information to the understanding of the overall tectonic evolution of the central Andean Plateau region and it is hoped that the analysis of faults and the new geochronology of offset Plio-Pleistocene strata will provide insight into the timing of tectonic activity and help to bridge the temporal gap between deformation phenomena on a variety of timescales. Moreover, it is expected that the results will shed light on the spatiotemporal transition between regional shortening and extension within the high plateau and within the context of larger plate-boundary processes.

## **1.7 Study area and geological setting**

The area analyzed in this study is located within the transition between the north-eastern Puna Plateau and the Eastern Cordillera, between approximately 21 and 23°S (Figure 1a). The Puna Plateau in Argentina is the southern continuation of the Peruvian-Bolivian Altiplano, whose uplift is intimately coupled with the Cenozoic Andean orogeny and

inferred mantle processes. Plateau uplift of the central Altiplano peaked at about 25 Ma and probably initiated as early as between 53 and 34 Ma (Allmendinger *et al.*, 1997). It is thought that the Puna began to be uplifted later, between about 15 and 20 Ma (Coira *et al.*, 1993; Kay *et al.*, 1995; Perkins *et al.*, 2016; Henríquez *et al.*, 2020). While the Altiplano is characterized by low internal topographic relief and hosts some of the world's widest intermontane depressions, such as the Lake Titicaca basin and the Salar de Uyuni, the Puna is characterized by more pronounced relief and smaller intermontane, high-elevation basins. The Puna is compartmentalized by complex reverse-fault systems that have generated an alternation of Precambrian to Paleozoic basement ranges and arid to semi-arid Cenozoic basins (Jordan & Alonso, 1987; Alonso *et al.*, 1991). In the basins, the exposed stratigraphy includes Paleogene to Quaternary sedimentary fill units, whereas in the intervening ranges late Cambrian basement rocks dominate (Alonso & Viramonte, 1987; Bahlburg *et al.*, 1990; Ledesma *et al.*, 2019). Although virtually all of the Puna region is internally drained, the study area is part of the headwaters of the Río Pilcomayo that is adjusted to the eastern foreland in Argentina and Bolivia. The Río Pilcomayo flows south-eastward from the Bolivian Andes to the Chaco Plains, where it forms the border between Argentina and Paraguay; it ultimately joins the Paraguay River close to the city of Asunción, Paraguay, and thus is connected with the Atlantic Ocean. The drainage basin of the Río Pilcomayo includes the southern Andean ranges of Bolivia and the northern parts of Argentina, constituting a catchment area of approximately 81.300 km<sup>2</sup>. The measured sediment load reaches up to 140 million tons per year (Martín-Vide *et al.* 2014), feeding a megafan at the intersection between the sub-Andean fold-and-thrust belt and the undeformed foreland; the lateral extent of the fan is approximately 223.000 km<sup>2</sup>, making it one of the largest megafan systems in South America (Horton & DeCelles, 2001; Latrubesse, 2015).

Within the plateau, the Cenozoic sedimentary fill units form a low-slope surface, which has been deeply incised by the Río Pilcomayo and its tributaries. The sediments of the paleo-surface cover extensive parts of the high-elevation regions and constitute a pronounced morphologic contrast between the deeply incised canyons and the elevated basement ranges. Sedimentary transport processes associated with these surface remnants must have ceased with the onset of the externally draining fluvial system, which was coupled with a decrease in base level. Therefore, these gently inclined surface remnants are not only ideal strain and sedimentologic markers that record fluvial transport processes in piedmont

regions toward the low-lying basin centers of the Puna, but they are also well-suited to help constrain subsequent deformation events. Indeed, past surface deformation events are expressed by various fault scarps that cut through the sedimentary fill units and these tectonic processes have influenced the fluvial network. While the underlying mechanism responsible for normal faulting in these high-elevation sectors may reflect gravitational collapse, a rigorous chronology of faulting and an assessment of the different processes linking gravitational collapse and incision of the plateau has not been done in the context of the regional structural and stratigraphic framework. For this reason, it is important to first review the stratigraphic characteristics of the north-eastern Puna region with a particular emphasis on the basin-fill history. The stratigraphic synthesis in the following sections forms the basis for additional geochronological work with the aim to refine the characteristics of the late Neogene and Quaternary fill deposits in light of different deformation events that have impacted these strata and ensuing landscape-evolution processes in the high-elevation plateau region.

Most of the following stratigraphic and structural description was adapted from the “Programa Nacional de Cartas Geológicas de la República Argentina” by Rubiolo (2003). Additional information was taken from Turner (1964b), who published the geological map of the area, and several case studies by various authors that are referred to in the text. Again, a brief discussion of the overall stratigraphy of the region’s basin fills is relevant because it will help to understand the compositional variations and provenance signals recorded in the valley fills and alluvial-fan strata of the study area.

### ***1.7.1 Stratigraphy***

The study area is bordered by N-S-oriented, reverse-fault bounded basement ranges comprised of Precambrian to Ordovician rocks, but it also includes Neogene to Quaternary sedimentary fill units that onlap paleo-topography developed in older, deformed sedimentary strata in the intervening intermontane basins. In different places, the older deformed units protrude from the sedimentary basin fill strata, creating a patchwork of medium-elevation ranges within the generally low-relief basin interiors (Figure 3).

#### ***Late Precambrian – early Cambrian***

The eastern margin of the study area is bounded by ranges that are an integral part of the thick-skinned Eastern Cordillera thrust belt. The exposed low-grade metamorphic basement rocks within the Eastern Cordillera are part of the late Precambrian – early

Cambrian Puncoviscana Formation (Escayola *et al.*, 2011). K-Ar radiometric dating of intercalated volcanic deposits provided ages between 545 and 530 Ma (Do Campo *et al.*, 1994) which is in agreement with more recent studies that generated protolithic depositional ages between 560 and 534 Ma (González *et al.*, 2009). The Puncoviscana Formation is ubiquitous in north-western Argentina and mainly constitutes metamorphosed sedimentary rocks of alternating sandstones, siltstones and mudstones, including turbidites, quartzites and wackestones of dark, olive-green, rarely violet color, and bedding-parallel, undulating lamination and other preserved primary sedimentary structures (Turner, 1964b; Do Campo *et al.*, 2017). The base of this unit is unknown, but its thickness is inferred to be on the order of 2000 m (Rubiolo, 2003). The thickness of individual layers varies between 30 and 50 cm of sandstone with intercalated claystone lenses and quartzite (Rubiolo, 2003). Large- and small-scale folding indicates at least two phases of deformation, creating WNW-vergent, asymmetric folds of varying amplitude (cm- to m-scale). The abundance of small volumes of early Cambrian felsic to mafic volcanic rocks and the composition of the turbidites implies that these sediments must have been deposited adjacent to an approximately contemporaneous arc terrane at the western Gondwana margin (Adams *et al.*, 2011; Escayola *et al.*, 2011)

### ***Late Cambrian - early Ordovician***

Separated by an angular unconformity, the Puncoviscana Formation is overlain by late Cambrian to early Ordovician strata of the Mesón Group, including the Lizoite, Campanario and Chalhualmayoc Formations (Rubiolo, 2003). This unconformity is assigned to the Tilcaric orogenic phase (Turner, 1975), followed by three different sequences. The oldest unit consists of a basal conglomerate with cherts, quartzites, and lithic fragments from the Puncoviscana Formation; this unit reaches a thicknesses of approximately 10 m of up to 1000 m (Sánchez & Salfity, 1999). These strata are superseded by green and purple, medium- to fine-grained sandstones with *skolithos* tubes, ripple marks, mud cracks, and load casts. The youngest, third sequence, is formed by a coarsening-upward sequence of medium- to fine-grained, well-stratified, silicified, white to yellowish sandstones with cross-bedding (Franceschinis *et al.*, 2020). The depositional environment is described to reflect shallow-marine, tide-dominated conditions reflected by the lower units, with a transition to intertidal flat-channel facies in the upper section (Such *et al.*, 2007). During the time of deposition, these strata formed the western margin of Gondwana,

which was controlled by subduction and accretion of small terranes during the Neoproterozoic-early Paleozoic.

### ***Late Cambrian – late Ordovician***

The late Cambrian to late Ordovician rocks of the region are represented by the Santa Victoria Group (Turner, 1964), which is subdivided into two main units. The up to 2300-m-thick lower Santa Rosita Formation mainly consists of light grey to white, medium- to fine-grained sandstones and mudstones showing a variety of sedimentary structures, including cross bedding, ripple lamination and hummocky cross stratification. These characteristics point toward a tide-, estuarine- to wave-dominated, shallow-marine depositional environment, ranging from upper shoreface to lower offshore (Such *et al.*, 2007). Paleontological evidence points to a late Cambrian to early Ordovician age (Buatois *et al.*, 2006). These units are overlain by the Acoite Formation, a succession of black shales, greenish mudstones, and mudstones with interbedded sandstones of up to 1000 m thickness. These strata were deposited in shelf to offshore areas recording a basin-wide transgressive phase (Such *et al.*, 2007). In contrast to the Mesón Group, the Santa Victoria Group is exposed in the Eastern Cordillera as well as in the sectors of the Puna Plateau, such as in the Cochinoa-Escaya Complex (Figure 3) and in isolated exposures within the sedimentary basins. There also magmatic, predominantly intrusive rocks, forming a narrow belt of granitoids with approximately 400-km long N-S extension, which is called the ‘Faja Eruptiva de la Puna Oriental’ (Schwab, 1973; Lork *et al.*, 1989; Bahlburg *et al.*, 2016). Recent age determinations for the intrusion of the granites and granitoids have resulted in an age of 444 Ma (Bahlburg *et al.*, 2016). In the study area, these magmatic rocks crop out in the Cochinoa-Escaya Complex.

### ***Cretaceous***

In the study area, the approximately 5000-m thick Salta Group (Moreno, 1970; Marquillas *et al.*, 2005) of cretaceous-paleogene age is restricted to a limited number of outcrops, most of which are located at the central sectors along a NNE-SSW-trending range (Figure 3). The Pirgua Subgroup defines the oldest deposits of the Cretaceous syn-rift sequence and consists of red to violet, matrix-supported conglomerates, partly with angular clasts; these units are followed by a succession of reddish to brown, fine-grained sandstones, with intercalated claystone. Locally this unit reaches a thickness of 30 m. Cross bedding is well established in the upper sandstone layers. Sporadically distributed secondary bleaching

generated beige-whitish colors in the sandstones, possibly indicating decay of organic matter (Turner, 1964b). Dating of interstratal rhyolites and basalts yielded lower Cretaceous ages (Marquillas *et al.*, 2005). These units are conformably overlain by approximately 15 m of greenish pelites and sandstones, followed by brighter-colored, whitish-beige sandstones to carbonate-bearing sandstones and dolomitic chalks with increasing carbonate components; these units transition into well-stratified, massive, oolitic limestone beds at the top, more than 50 m thick (Astini *et al.*, 2020), that define the post-rift Balbuena Subgroup. All sandstone components exhibit cross-stratification and partly ripple lamination. The pelitic to sandy layers constitute the Lecho Formation, whilst the following massive limestone banks constitute the marine to lacustrine Yacoraite Formation (Mutti *et al.*, 2023). The entire succession was deposited during and after the activity of the intracontinental Salta Rift. The Salta Rift is subdivided into several smaller basins; for example, the study area in northern Argentina and southern Bolivia is part of the Tres Cruces sub-basin.

### ***Oligocene***

The Oligocene - Miocene strata of the 750-m-thick Moreta Formation (Coira, 1979) crop out in the south-western Sierra de Escaya and along its northern extension in Bolivia. These units contain sandstones and tuffaceous sandstones developed in banks of 10-30 cm at the base; these are followed by sandstones and andesitic volcanoclastics with clast sizes of up to 25 cm in diameter and a total thickness of 500 m. The upper deposits include reddish, polymictic conglomerates with pebbles and boulders from Ordovician and Cretaceous sources (Soler & Coira, 2002). K/Ar dating of the volcanic material from the Moreta Formation resulted in an age range between 28 and 20 Ma (Coira, 1979). The sediment succession reflects continental deposits, accumulated in a fluvial-alluvial depositional system, accompanied by intercalated andesitic and dacitic rocks.

### ***Miocene***

Miocene strata were described in southern Bolivia, in the central eastern section of the study area, in the vicinity of the Cordillera de Sama (Figure 3). Fine-grained, reddish-brown to yellowish-green fluvial silty clays, silts and fine sands form the Honda and Río Rosario formations of up to 300 m thickness (MacFadden *et al.*, 1990). Local, coarser grained lenticular channel deposits consist of sands and gravels. Occasionally interbedded tuffaceous horizons occur within both formations. The base of the stratigraphic succession

comprises 50 to 100 m of gravels that unconformably overlie basement rocks. A shallow cover of Quaternary, fine- to coarse-grained alluvial and fluvio-glacial deposits overlie the Honda and Río Rosario formations (MacFadden *et al.*, 1990). Locally, these formations constitute some of the richest mid-Miocene fossil localities in South America (Croft, 2007). Around 30 species of non-volant mammals were described in this area. Based on modern analogs, it was proposed, that the fossil-bearing strata were deposited at elevations of  $\geq 2000$  m a.s.l. Magnetostratigraphy and  $^{40}\text{Ar}/^{39}\text{Ar}$ -dating provided depositional ages between 13 and 12 Ma (Gibert *et al.*, 2020). Although compressional structures are absent, Gibert *et al.* (2020) postulate a late Miocene regional uplift as an explanation for their findings that would post-date the sedimentation of the fossil bearing units.

### ***Plio - Pleistocene***

Plio-Pleistocene deposits within the study area include horizontally layered clastic sediments, mainly comprised of gravels, sands and silts, partly including volcanic ashes (Rubiolo, 2003). These deposits form continuous fill units between the ranges of the Eastern Cordillera and the Sierra de Escaya (Figure 3). Locally, a maximum thickness of up to 200 m is reached and the strata are exposed in deeply incised canyons that are currently adjusted to the Río Pilcomayo drainage system. The sediments were deposited in alluvial, glacio-fluvial and restricted fluvial environments (Kulemeyer, 2005).

A separately described section (see below) of these sedimentary deposits is the Tafna Formation (Turner, 1964b). The weakly lithified Tafna Formation is a well-stratified, sandy to silty succession exposed in the central-western sectors of the study area. Permeable volcanic ash layers of 20-40 cm thickness, and beige to white color are intercalated in this sedimentary succession. About 45% of quartz and 11% of kaolinite content are characteristic for this deposit (Kröger, 1956). The origin of the volcanic ash is debated but it has been proposed earlier that they were associated with volcanic centers, active during the Tertiary (Turner, 1959). Within the study area, the Tafna Formation is limited to outcrops along the foothills of the Sierra de Escaya reaching a maximum thickness of 30 m. The formation is areally more distributed in the West, outside the study area. The overall appearance of the sedimentary strata points toward a fluvial origin with episodes of laharc activity, which caused sedimentation in small depressions of the paleo-topography. The Tafna Formation and the other fill units overlie unconformably Ordovician basement and are covered by alluvial fan deposits.

### ***Holocene (unspecified Quaternary)***

Holocene strata within the study area are mainly associated with active surface processes; for example, these units are found along the perennially active channels and rivers that drain the highlands of the plateau and in local depressions, capable of storing meteoric waters (Figure 3). Among the deposits are coarse- to medium-grained fluvial gravels and sands, and medium- to fine-grained lacustrine and eolian deposits of sands, silts and clays, comparable to the Holocene deposits in the Pozuelos Basin west of the study area (Camacho & Kulemeyer, 2017). In areas of stagnant water, salt crusts are common (Rubiolo, 2003). South of the watershed of the Río Pilcomayo catchment, deposition of Holocene sediments is associated with floodplains within the internally drained sectors of the plateau.

### ***1.7.2 Physiography and Geomorphology***

#### ***Sierra de Escaya***

Uplifted Ordovician metasedimentary rocks of the Acoite Formation (Upper Santa Victoria Group) and associated syn-sedimentary volcanic rocks and dikes of the ‘Faja Eruptiva de la Puna Oriental’ constitute the ‘Cochinoca-Escaya-Complex’ in the west of the study area (Coira & Koukharsky, 1991; Rubiolo, 2003). As part of this complex, the Sierra de Escaya locally forms the western border of the study area and separates it from the higher elevated, internally drained basins such as the Pozuelos Basin in the West (Figure 3).

#### ***Sierra de Santa Victoria***

The eastern margin of the study area is bounded by the Sierra de Santa Victoria of the Eastern Cordillera (Figure 3), which reaches elevations of about 5000 m. The range forms an important orographic barrier for easterly moisture-bearing winds. At this latitude, the Eastern Cordillera comprises rock formations of the Ordovician Santa Victoria Group (Rubiolo, 2003; García *et al.*, 2013).

#### ***Siete Hermanos***

In the center of the basin, west of the town of Yavi, a range comprised of the Cretaceous-Paleogene Salta Group is exposed and forms a prominent northeast- to southwest-oriented area of high topography. The triangular-shaped strata are composed of westward-tilted carbonates and mudstones of the Balbuena Subgroup and sandstones of the Pirgua Subgroup.

### *San Juan de Oro Surface*

The low-slope areas of the basin comprise alluvial-fan and floodplain deposits, including lacustrine, eolian, and fluvial sediments of up to 250 m thickness, truncating and onlapping low-relief areas of deformed bedrock (Rubiolo, 2003; Barnes, 2008). These low-relief areas were described as the regional San Juan de Oro Surface (Servant *et al.*, 1989). Gubbels *et al.* (1993) recognized this surface in central to southern Bolivia as a composite landform of three discrete surface types: low-relief erosional uplands of deformed bedrock (type 1), coalesced pediments (type 2), and a prominent unconformity beneath undeformed, Tertiary clastic deposits and ignimbrite sheets (type 3). Age controls of this unconformity were provided by  $^{40}\text{Ar}$ - $^{39}\text{Ar}$  dates: at 18°S the surface was dated to be between 18 to 8 Ma, farther south, at about 21°S, the age was bracketed between 13 to 9 Ma (Gubbels *et al.*, 1993). Following the previous authors' interpretation, these ages postdate compressional deformation and predate regional incision. Sheets of volcanic deposits that lack a proper stratigraphic classification, lie with an unconformity over an area of around 10,000 km<sup>2</sup> and were dated at 8 to 5 Ma. Where these deposits are absent, an up to 250-m-thick succession of conglomerates, sandstones, and claystone beds mantles the unconformity. In the higher-elevated parts of the basin, the type 2 surface transitions into the type 1 surface of gently rolling topography that is characterized by relatively smooth and rounded slopes. This composite landform must be the product of concomitant erosional down-wearing and aggradation processes that followed the cessation of compressive deformation in this part of the plateau region. Uplands were erosionally smoothed, pediments expanded, and erosion processes beveled the uplands while basins expanded, coalesced, and ultimately buried the pediments. This evolutionary sequence of sedimentary units started after 10 Ma and lasted until the headward erosion of the Río Pilcomayo and tributary rivers tapped these basins and started to carve deep canyons into the strata (Gubbels *et al.*, 1993).

Another study, which was conducted by Kennan *et al.* (1997) suggested that the San Juan de Oro surface is considerably older than late Miocene, as proposed by Gubbels *et al.* (1993). A single radiometric age on ignimbrites that cover low-gradient topography at around 4000 m of 21 Ma, supports this claim (Schneider 1985 in GEOBOL-SGAB 1992 - not accessible), suggesting the onset of planation as early as early Miocene (Kennan *et al.*, 1997). Additionally, these authors argued that in Bolivia several other widespread surface remnants as low as 2000 m had formed within the same drainage system. Following their arguments and other studies on the more western San Juan de Oro Basin (Caffe & Coira,

2002; Prezzi *et al.*, 2004), the drainage systems must have been active prior to the ultimate rise of the Andean plateau and the paleo-surfaces have been gradually uplifted since then. This argument is supported by studies on paleo-elevations of orogen-wide surfaces using fossil leaf-physiognomy (Gregory-Wodzicki, 2000), stable isotope paleo-altimetry of soil carbonates and palustrine carbonates (Garziona *et al.*, 2006), and stream profile and knickpoint analysis, respectively (Barke & Lamb, 2006), all of which agree that these surfaces were uplifted and incised after 10 Ma. While the uplift did not deform the sediments in study area, more western Neogene (20-10 Ma) valley fill deposits of the San Juan de Oro Basin must have experienced deformation as suggested by Caffè & Coira (2002).

The youngest alluvial fan and floodplain deposits mantling the valley fill have been proposed to be of Quaternary age (Cladouhos *et al.*, 1994), but no unambiguous age information for these deposits has been available, an important issue that will be addressed in this thesis.

### ***1.7.3 Structural setting***

While the basement ranges in the study area are associated with large-scale compressional tectonic features that used to guide shortening and uplift processes during the rise of the Andes, several faults, expressed by clear morphological normal fault scarps, deform the sedimentary valley fill strata. These structures clearly accommodated post-depositional deformation within the area. Understanding their mechanical behavior will help to evaluate the state of the regional stress field and its geodynamic implications.

The section below summarizes the work of previous studies on these structures and provides an assessment of relative ages of the affected sedimentary deposits. A detailed analysis of these faults and the involved deposits, however, constitutes the core of this thesis and will be presented in detail in chapters 3 and 4.

#### ***Pumahuasi Fault***

West of the city of La Quiaca, in the foothills of the Sierra de Escaya, a 40-km-long, N-S-striking linear fault zone crosses and offsets alluvial fan surfaces in Argentina and Bolivia (Figure 3). This structure has been described by Cladouhos *et al.* (1994) as the Pumahuasi fault, interpreted to be a single-strand, right-lateral strike-slip fault with a minor dip-slip component. It is characterized by a 10 to 15-m-high, west-facing fault scarp and an alignment of ponds in the hanging wall. In its central sectors, the fault crosses the Bolivian-

Argentine border along the Río La Quiaca. Areal limited outcrops of basement rocks are sporadically exposed along the footwall. Fault-associated lateral and vertical displacement dissects the low relief areas of the piedmont, indicating subsidence of the range relative to the basin floor (Cladouhos *et al.*, 1994).

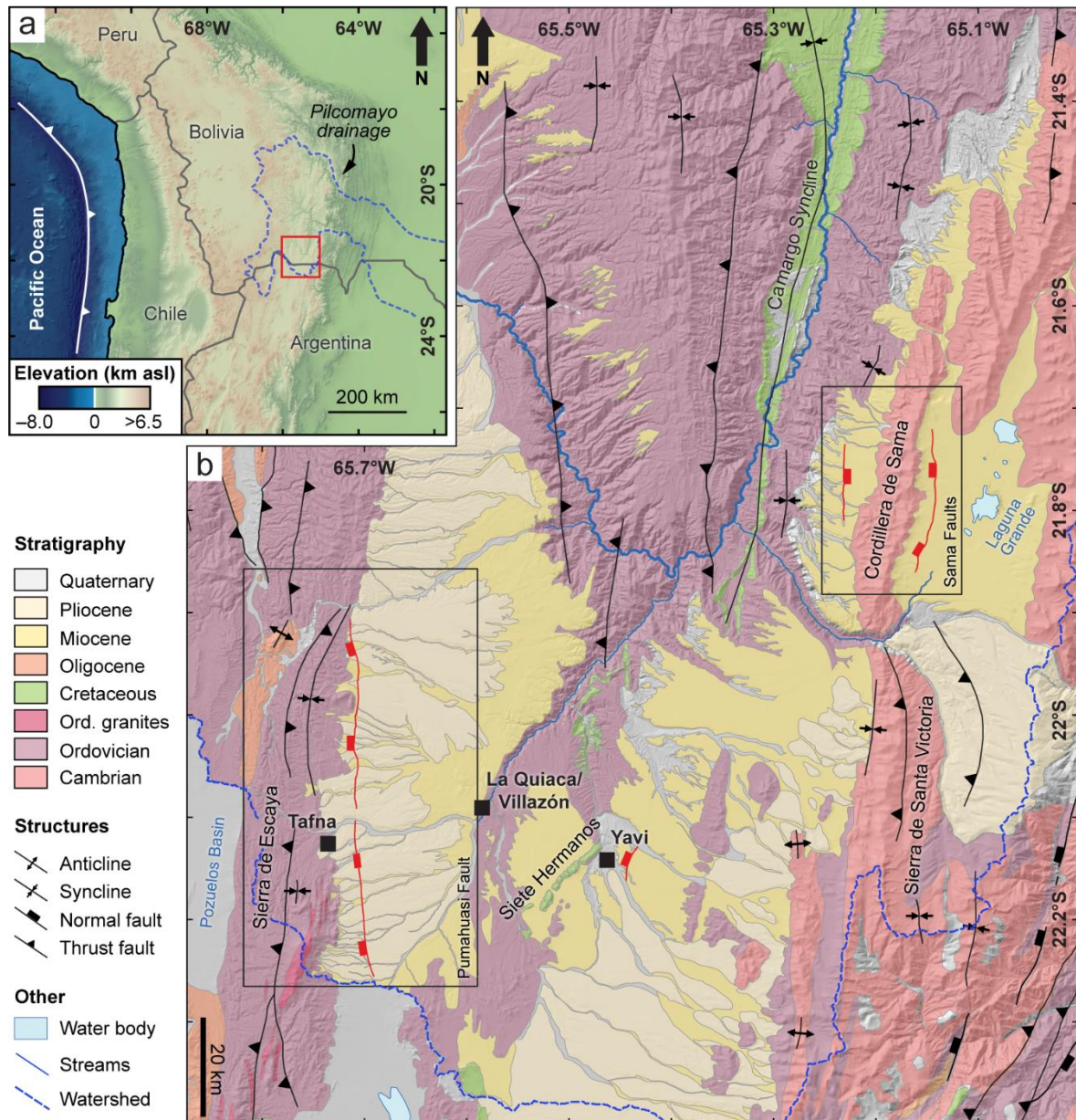


**Figure 3:** Geological setting of the study area. a) Location of the study area within the realm of the Central Andes in the border area between Argentina and Bolivia. The study area is situated within the catchment of the Río Pilcomayo drainage basin. b) The geologic map shows the stratigraphy and tectonic structures of the study area. The faults analyzed in this study are outlined in red. Black boxes correlate with cropped study site for the remote-sensing analysis of the studied faults and sedimentary basin units.

### ***Cordillera de Sama***

Similar to the Pumahuasi Fault, linear structures exist in the northern continuation of the basin in Bolivia, they are located within the Cordillera de Sama (Figure 3). The structures border the southern part of the range. In the west, a well-defined fault scarp of 15 km length strikes N-S. This fault was also mentioned by Cladouhos *et al.* (1994). These authors stated that similar to the Pumahuasi Fault, the fault kinematics is dominated by strike-slip motion, with a minor dip-slip component. Right lateral offsets of approximately 700 m have been documented and a vertical fault scarp recording a throw of approximately 10 m were reported (Cladouhos *et al.*, 1994). On the opposing, eastern side of the range, a similar feature can be observed, which, however, was not described by these authors. This structure is located between the range and the Laguna Grande salt pan. It bends parallel to the outline of the range and offsets the sedimentary deposits in the piedmont.

### ***Linear features of inferred tectonic origin***

Additional well-expressed N-S trending linear features, some of which were already described as the Yavi Fault East and West (Cladouhos *et al.*, 1994) cut through the sediments in the central sectors of the study area. Their origin and significance will be discussed later (see chapter 3.1.2 and chapter 4.1.2) in the context of the observations made in this study.

### ***1.7.4 Climate***

The study area is located near the Tropic of Capricorn, within the realm of the subtropical anticyclone and the subtropical monsoonal system (Kulemeyer, 2005; Castino *et al.*, 2017; Ferrero & Villalba, 2019). Precipitation is limited to the southern-hemisphere summer months and tied to the southward shift of the Intertropical Convergence Zone (ITCZ). Following Weischet (1996), the entire Puna Plateau is considered arid, but aridity increases from north to south, and from east to west (Weischet & Endlicher, 1996). The orographic barrier of the Eastern Cordillera prevents humid air masses to enter from the wetter foreland areas, resulting in dry leeward winds entering the high-altitude plains.

The local climate of the study area was characterized by Kröger (1956) to be of continental type, cold and dry, and with strong temperature amplitudes between day and night. Precipitation is limited to the summer months and rarely exceeds 350 mm/yr. During winter, frequent snowfall is common and accompanied by strong winds from NNW (Kröger, 1956). These climatic conditions have a strong impact on the erosive capacity of

the local drainage systems and in turn on the landscape preservation potential in the study area.

## **2 Methods**

To address the research questions on the geomorphological, sedimentological and structural aspects of the late Cenozoic evolution of the northern Puna Plateau, a multi-disciplinary workflow with different methodological foci was established. Therefore, the method section is divided into three subchapters:

The first subchapter focuses on elaborating a consistent geological framework for the analysis of the tectonic structures in light of the Quaternary landscape evolution. This includes a detailed description of the basin-fill strata, the delineation of geomorphological features and developing a geochronological fabric to establish timing constraints of depositional and erosional relief-forming processes by means of radiometric (U-Pb) and cosmogenic radionuclide (CRN) dating.

The second subchapter focuses on the quantification of faulting, its morphological expression in the landscape and imprint on the local drainage systems. Remotely sensed data and digital data analysis were used to identify and distinguish between lateral and vertical tectonic displacements and to assess the recency of deformation, especially by documenting the degree of tectonic overprint of the drainage system. Finally, the displacement values along the identified fault scarps were measured on elevation profiles across the identified faults that had affected gently inclined alluvial fan surfaces.

The third subchapter quantifies and documents displacement values of possible seismogenic origin within the local basin-fill strata, the identification of structural features associated with faulting and the determination of the tectonic stress field by inversion of the observed structural measurements.

### **2.1 Geological framework**

#### ***2.1.1 Stratigraphy***

The stratigraphy of the study area has previously been described at regional scale by several authors (Turner, 1964b; Coira, 1979; Rubiolo, 2003). However, most of the younger sedimentary deposits have been typically summarized as valley fill, characterized by intercalated tuffs and conglomerates, and onlapping onto the paleo-topography. More detailed descriptions of the sedimentary successions are available from adjacent, possibly

correlative sites in Bolivia (Croft, 2007; Gibert *et al.*, 2020). As variations in sediment properties and provenance provide information on possible changes in energetic, climatic and/or tectonic conditions, detailed sections of the sequences have been recorded in this thesis to help elucidate the overall characteristics of landscape evolution. This was conducted by stratigraphic analysis, flanked by structural studies, as well as detailed geological mapping of exposed units, regional unconformities and lateral pinch-outs and lithological contacts. Grain size variations and provenance differences were recorded where possible.

### **2.1.2 Morphology**

A regional geomorphic analysis of the landscape adds supplementary information on the geological framework of the study area, improving landscape evolution models and helps to discriminate structural features (degraded fault scarps) from linear features formed by surface processes. This analysis was carried out by visual inspection of slope maps and elevation profiles of the basin-fill strata derived from a TanDEM-X data set provided by the German space agency (DLR).

### **2.1.3 Depositional ages**

Although the timing of many regional geologic processes within the Andean Plateau can be constrained by relative age relations, efforts to define an unambiguous Quaternary history suffers from the lack of adequate geochronological data sets. Sedimentary fill units were dated in Bolivia in the past, often without a proper description of the location, stratigraphic position or altitude (Gubbels *et al.*, 1993). More recent data is mainly based on fossil occurrences within sediment sequences of the Quebrada Honda formation in southern Bolivia (Croft, 2007; Gibert *et al.*, 2020). Without questioning the usefulness of these datasets in terms of depositional environment and paleo-elevation interpretations, these studies unfortunately do not address the timing of the principal geomorphic evolutionary steps that are needed to unravel the tectono-sedimentary history of the area; yet, such processes may indicate a shift in tectono-climatic conditions that accompany regional geodynamic adjustments and possible feedback mechanisms between climatic and tectonic forcing (Ruddiman & Kutzbach, 1991; Ruddiman, 1997; Alonso *et al.*, 2006; Willett, 2006; Strecker *et al.*, 2009; Whittaker & Boulton, 2012; D'Arcy & Whittaker, 2014). To close the gap in age information especially with regards to the evolution of the study area in the north-eastern Puna, two different dating methods were used to decipher

1) the timing of deposition of the exposed sediment strata by dating incorporated volcanoclastic deposits using U-Pb isotope geochronology, and 2) the timing of major incision phases on the plateau by dating the elapsed exposure of geomorphic surfaces with isotopes generated by cosmic rays. Apart from helping to bracket the timing of documented tectonic activity in the study area, the expected ages will therefore also help improve our understanding of landscape-evolution processes in the Central Andes and comparable tectonic and climatic settings elsewhere.

### *U-Pb dating of volcanoclastics*

Samples of volcanic ashes intercalated in the sedimentary fill units were extracted from different layers at various sites within the study area (Figure 4). Approximately 1-3 kg of material was sampled for the separation of zircons needed for the radioisotopic analysis. Assuming a relatively brief time between eruption and deposition of the volcanic ashes, ages associated with the U-Pb ratios of zircon minerals are considered to reflect the time of deposition of the sedimentary sequence. Since these deposits are clearly affected by tectonic processes, the moment of their deposition implies a maximum age of the tectonic activity of the associated sedimentary strata. Moreover, these ages also predate the onset of basin incision and the establishment of fluvial connectivity with the foreland.

Zircon minerals were extracted from the ash samples following standard magnetic and heavy liquid mineral-separation techniques. Approximately 80-130 grains per sample were handpicked, mounted in epoxy, and polished for isotope analysis of U, Th, and Pb using a Laser Ablation Multi-Collector Inductively Coupled Plasma Mass Spectrometer (LA-MC-ICPMS) at the University of California, Santa Barbara. Samples were measured during one analytical session. The instrumentation consists of a Nu Plasma MC-ICPMS and a 193 nm ArF laser ablation system. The process followed the analytical protocol described in Cottle *et al.*, (2013) (Cottle *et al.*, 2013) and Cottle *et al.*, (2014) (Cottle *et al.*, 2013; Cottle, 2014). U-Th-Pb analysis were conducted for an average of 17 seconds using a spot diameter of 24 to 35  $\mu\text{m}$ , a frequency of 4 Hz and 1.2 J/cm<sup>2</sup> fluence. The 91500-reference zircon ( $1065.4 \pm 0.6 \text{ Ma } ^{207}\text{Pb}/^{206}\text{Pb}$  ID-TIMS and  $1062.4 \pm 0.8 \text{ Ma } ^{206}\text{Pb}/^{238}\text{U}$  ID-TIMS) (Wiedenbeck *et al.*, 1995) was used to monitor and correct for mass bias as well as Pb/U and fractionation. Data accuracy was monitored using secondary reference zircons of 'GJ-1' ( $601.7 \pm 1.3 \text{ Ma } ^{206}\text{Pb}/^{238}\text{U}$  ID-TIMS age,  $608.5 \pm 0.4 \text{ Ma } ^{207}\text{Pb}/^{206}\text{Pb}$  ID-TIMS age) (Jackson *et al.*, 2004), which were analyzed once every ~18 unknowns and mass bias- and fractionation-corrected based on measured isotopic ratios of the primary reference zircon.

Repeat analyses of GJ-1 during the session yield a weighted mean  $^{206}\text{Pb}/^{238}\text{U}$  age of  $598 \pm 2$  Ma, MSWD = 0.5 (N = 36/36); Data reduction, including corrections for baseline, instrumental drift, mass bias, down-hole fractionation and uncorrected age calculations were carried out using Iolite version 2.5 (Paton *et al.*, 2010). Data were corrected for common lead using the method of (Andersen, 2002). The uncertainty on the  $^{207}\text{Pb}$ -corrected age incorporates uncertainties on the measured  $^{206}\text{Pb}/^{238}\text{U}$  and  $^{207}\text{Pb}/^{206}\text{Pb}$  ratios as well as a 2% uncertainty on the assumed common lead composition. Correction for excess  $^{230}\text{Th}$  follows the method of (Crowley *et al.*, 2007) assuming  $\text{Th}/\text{U}[\text{magma}] = 4 \pm 1$ . All uncertainties are quoted at the 95% confidence or 2 sigma level and include contributions from the external reproducibility of the primary reference material for the  $^{207}\text{Pb}/^{206}\text{Pb}$  and  $^{206}\text{Pb}/^{238}\text{U}$  ratios. Due to potentially significant pre-eruptive residence times and/or post-eruptive reworking, the analyzed samples show a non-uniform pattern of U–Pb zircon age distributions. Therefore, the oldest ages were systematically excluded from calculations of an average zircon crystallization age until near-unity values for the mean square of weighted deviates (MSWD < 2) were achieved. In addition, a generalized Chauvenet Criterion was applied to the remaining grain ages to reject outliers (Vermeesch, 2018).

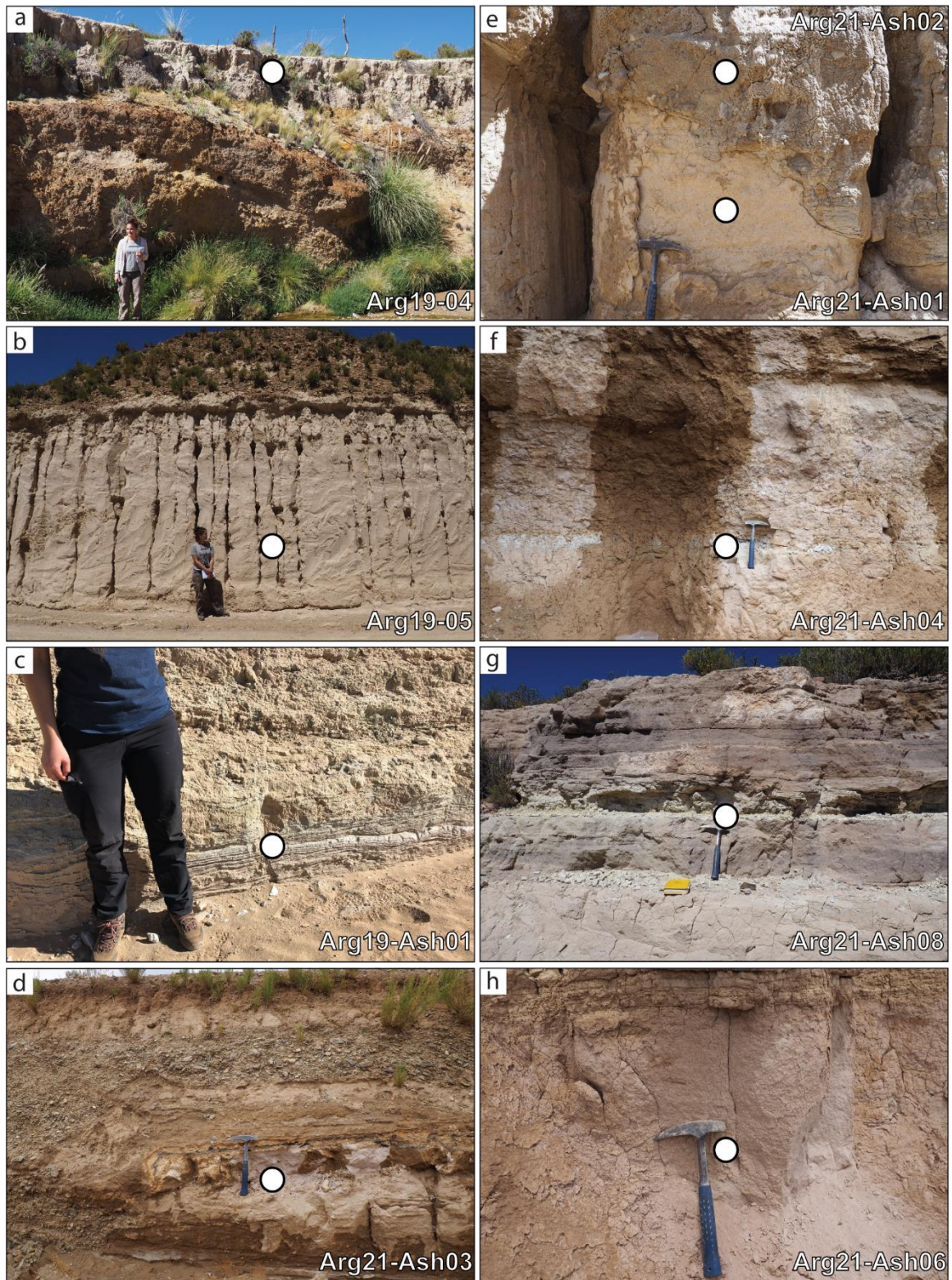


**Figure 4:** Sampling sites for U-Pb dating. **a)** Reworked ashes at river cut along the Pumahuasi Fault, 3489 m a.s.l.; **b)** primary ashes at roadcut within the Tafna Formation, 3592 m a.s.l.; **c)** Roadcut of distal alluvial fan section, 3553 m a.s.l.; **d)** primary ash layer at Pumahuasi Fault, 3610 m a.s.l.; **e)** secondary (lower, white) and primary (upper, grey) ash layers with erosional contact at roadcut close to the Yavi fault, 3525 m a.s.l.; **f)** thin layer of primary ashes close to Yavi, 3498 m a.s.l.; **g)** secondary ash layer at Sansana, 3504 m a.s.l.; **h)** primary ash layer at Yavi Chico, 3493 m a.s.l..

### ***2.1.4 Paired cosmogenic radionuclide exposure ages***

#### ***Background***

With the aim of determining the duration of exposure of the different geomorphic surfaces, samples were taken for exposure dating, using paired cosmogenic radionuclides at two sites with different elevations.

The use of cosmogenic radionuclides (from here on referred to as CRN) has been proven to be applicable in a wide range of scientific issues related to surface processes such as glacial chronology (Wüthrich *et al.*, 2017; Luna *et al.*, 2018), fluvial sedimentation processes (Tofelde *et al.*, 2018; D'Arcy *et al.*, 2019) and burial dating (Granger, 2006; Balco & Shuster, 2009). The datable timeframe stretches from 1 ka up to 10 Ma depending on the types of isotopes used. The CRN-method therefore bridges the gap between radiocarbon dating and U-series dating methods, covering either shorter or longer time spans. Moreover, it is especially well-suited in areas, where a lack of organic material or a generally poor preservation potential exists and where landforms of late Miocene to Pliocene age exist. All of these criteria match the setting of the study area.

In situ CRNs are accumulated in target minerals interacting with neutrons and muons of secondary cosmic rays (Lal & Peters, 1967). The primary production pathway is considered to be spallation of high-energy neutrons, accompanied by a small amount of negative and low-energy muon capture. (Gosse & Phillips, 2001). Their concentrations in rock material scales with exposure duration and denudation rates of the sampled material. Besides the advantages of this method, many factors must be considered while applying to problems in fluvial and alluvial contexts. This includes soil-mixing, post-depositional erosion, sediment burial and the accumulated concentration of CRNs prior to the final deposition of sediments (Gosse & Phillips, 2001). The latter issue being one of the major limitations in calculating a precise exposure age.

As rocks are exposed, they will accumulate CRNs, whilst being transported close to or at the surface until the material reaches its destination where it is being deposited. The pre-depositional concentration is referred to as the inherited concentration (Anderson *et al.*, 1996). In sedimentary regimes, the measured concentration of CRNs usually needs to be corrected for the inheritance in order to avoid overestimating the calculated exposure ages. This can be achieved by sampling along a depth profile and measuring the consecutive concentrations at depth (Anderson *et al.*, 1996). These concentrations will decrease with depth, as the cosmic rays are being attenuated by the sedimentary strata (Brown *et al.*,

1992), until a distinct value is reached, which must have been accumulated as the sample was close to, or directly at the surface. Assuming a constant deposition rate, all samples along such a profile will share a comparable inherited concentration for which the samples will be corrected. The resulting surface concentration will solely be the product of in situ production and hence, represent the time since surface exposure.

### ***Sampling***

Samples were taken at two surface levels from different elevations, here referred to as “upper surface level” (S1) and “lower surface level” (S2) (Figure 5b). Clasts of 2-5 cm in diameter were taken from the first 5-10 cm below the surface (Figure 5a). A depth profile was sampled in an open pit that exposed an approximately 4 m high wall of conglomeratic fill on the lower surface level S2 (Figure 5c, d, e). Although the individual sediment layers were partly separated by erosional contacts associated with paleosol formation and chemical weathering, sampling of the depth profile was carried out under the assumption, that transient times might have been short enough to not have strongly influenced the concentration of CRNs. Samples primarily consisted of amalgamated, well rounded conglomerate clasts of quartzitic composition, deposited in a sandy matrix. Clast sizes varied between 2-10 cm accumulated in lenses and layers between finer grained material. The target material to be extracted for the analysis was quartz. As the sampled lithology mainly consisted of quartzitic pebbles, sample sizes of 1-3 kg were sufficient for later mineral extraction.

### ***Sample preparation and measuring***

Quartz was separated using standard mineral-separation techniques including crushing, grinding, sieving as well as magnetic and density-based separation methods (Kohl & Nishiizumi, 1992). Organic contaminants were dissolved using dilute HCl and Hexafluoroantimonic acid ( $\text{H}_2\text{SiF}_6$ ) was used to dissolve feldspar-rich minerals (Brown *et al.*, 1991). In order to remove meteoric components of Be and Al, samples were leached in 1% HF. Sample purity was measured in part sample aliquots (PSA) using inductively coupled plasma optical emission spectrometry (ICP-OES). Except for one sample that did not contain enough cleaned material, small fractions of ~2 g were excluded for  $^{21}\text{Ne}$  analysis. Be and Al were extracted following the modified version of Merchel and Herpers (Merchel & Herpers, 1999), described by Luna *et al.* (Luna *et al.*, 2018). A blank sample containing both, ~330  $\mu\text{g}$  of  $^9\text{Be}$  and ~1 mg of  $^{26}\text{Al}$  carrier was processed accordingly. Approximately 20 g of each cleaned sample were dissolved in conc. HF, and approximately 330  $\mu\text{g}$  of  $^9\text{Be}$

carrier of known concentration was added. Due to the high concentrations of Al, no additional carrier was needed. After digestion of the sample material, HF was evaporated with added HClO<sub>4</sub>. The product was subsequently dissolved in HCl to be further processed. Be and Al were separated from each other using ion-exchange column chemistry. The

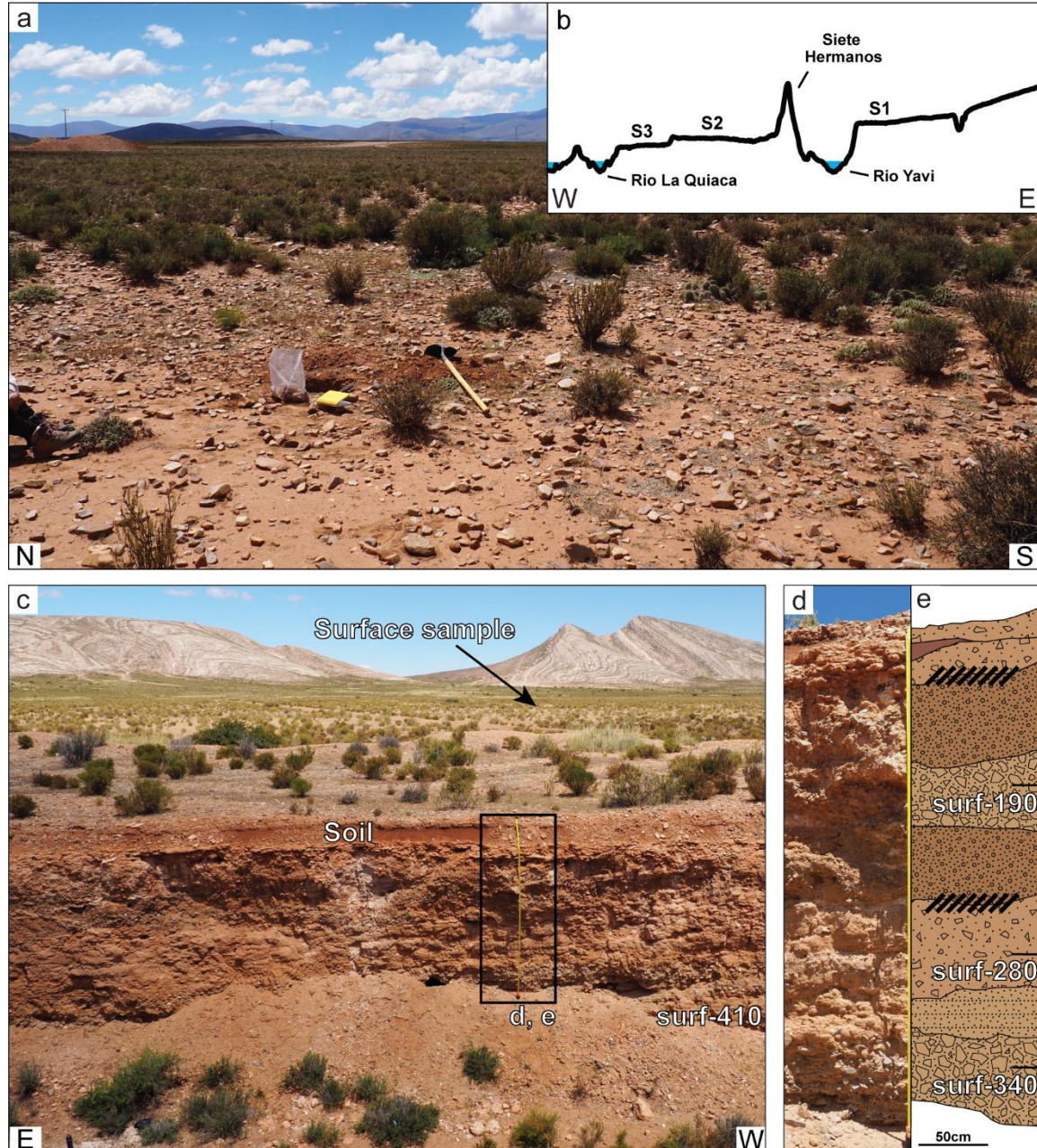


**Figure 5:** Sampling sites for surface exposure dating. **a)** Sampling site on upper surface level S1. **b)** Simplified topographic profile of the sampled surfaces between Río La Quiaca and Río Yavi. Surfaces S1 and S2 were sampled for the analysis of CRNs. **c)** Open pit used for sampling a depth profile at lower surface level S2. Associated surface sample was taken at around 100 m distance to avoid sampling excavated material from the pit. Depth sample at 410 cm below the surface was taken approximately 2 m west of the sampled profile as indicated by '-410'. Siete Hermanos range in the background, view SE. **d)** Close up of sampled depth profile with yellow measuring tape, and, **e)** sketch of the sampled units along the depth profile with indicated sample depth in cm. Black dashed areas indicate erosional contacts between the different units.

separated solutions were then precipitated as hydroxides. Purity of the samples and therefore success of the separation was checked again with ICP-OES measurements. Some samples contained high amounts of Ti, which made chemical separation difficult and multiple steps were necessary to clean the Al-separates. During different runs of sequential precipitation of Al and Ti at different pH values using NH<sub>3</sub>, some of the Al was lost and could not be recovered. After the cleaning, samples were exposed to temperatures of >1000° C forming BeO and Al<sub>2</sub>O<sub>3</sub>. Oxides were ground and transferred into copper targets with a 4:1 weight ratio of Nb:BeO and 1:1 ratio of Ag:Al<sub>2</sub>O<sub>3</sub>, respectively. During loading, two Be samples broke due to handling issues and had to be redone. The Be and Al isotope measurements were performed at the DREAMS facility of HZDR, Germany, using Accelerator Mass Spectrometry (AMS). Ne isotopes were measured by noble gas spectrometry at the GFZ Potsdam. Gases were extracted by stepwise heating at 400°C, 600°C, 800°C and 1200°C in a resistance heated furnace. Ne was admitted separately into a VG5400 noble gas spectrometer. Aliquots from all samples were crushed in vacuo to determine the isotopic composition of trapped Ne.

### ***Isotope concentration conversion***

Be and Al ratios were converted into concentrations of atoms per gram following the AMS data-reduction guide provided by Balco (Balco, 2006). The equation used to calculate the concentration of <sup>10</sup>Be is:

$$(1) N_{10} = \frac{1}{M_q} \left( \frac{R_{10/9} M_C N_A}{A_{Be}} - n_{10.B} \right)$$

where  $N_{10}$  is the desired <sup>10</sup>Be concentration (at/g),  $M_q$  is the mass of pure, dissolved quartz sample (g),  $R_{10/9}$  is the measured isotope ratio of <sup>10</sup>Be/<sup>9</sup>Be,  $M_C$  is the mass of Be added as carrier (g),  $N_A$  is Avogadro's number ( $6.022 \times 10^{23}$  at/mol),  $A_{Be}$  is the molar weight of Be (9.012 g/mol) and  $n_{10.B}$  is amount of <sup>10</sup>Be isotopes in the blank.

The <sup>26</sup>Al concentrations were calculated following a comparable scheme, the equation is slightly different due to the lack of Al carrier in the samples.

$$(2) N_{26} = \frac{1}{M_q} \left( \frac{R_{26/27} N_A}{A_{Al}} - n_{26.B} \right)$$

where  $N_{26}$  is the desired <sup>26</sup>Al concentrations,  $R_{26/27}$  is the measured <sup>26</sup>Al/<sup>27</sup>Al isotope ratio,  $A_{Al}$  is the molar weight of Al (26.98 g/mol) and  $n_{26.B}$  is the is amount of <sup>26</sup>Al isotopes in the blank.

The total amount of excess  $^{21}\text{Ne}$  was calculated using the combined Ne ratio data from the 400° C, 600° C and 800° C steps (Niedermann, 2002) using the following equation:

$$(3) \ ^{21}\text{Ne}_{ex} = \left[ \left( \frac{^{21}\text{Ne}}{^{20}\text{Ne}} \right)_m - \left( \frac{^{21}\text{Ne}}{^{20}\text{Ne}} \right)_{tr} \right] ^{20}\text{Ne}_m$$

where ex = excess, m = measured, and tr = trapped, and assuming that  $^{20}\text{Ne}_{ex}$  can be ignored.  $(^{21}\text{Ne}/^{20}\text{Ne})_{tr}$  was taken to be  $0.00319 \pm 0.00008$ , the error-weighted mean of the crushing measurements. Measured  $^{21}\text{Ne}/^{20}\text{Ne}$  and  $^{22}\text{Ne}/^{20}\text{Ne}$  ratios plot very close to the spallation line, indicating a two-component mix between cosmogenic and atmospheric components (Figure 6).

### *Isotope ratios and burial signal*

The concentration of cosmogenic nuclides within a mass of rock is governed by the balance of production rates and, for unstable nuclides, radioactive decay (Granger, 2006). Cosmogenic nuclides of different nuclide series accumulate according to intrinsic production rates. Ratios between the production rates of different nuclide series have been established at various sites all over the world (Goethals *et al.*, 2009; Kober *et al.*, 2011; Kelly *et al.*, 2015; Luna *et al.*, 2018). Based on these ratios and measured nuclide concentrations, statements about the continuity and the duration of the exposure can be made. When material is exposed for a long time, or when it is shielded from cosmic rays

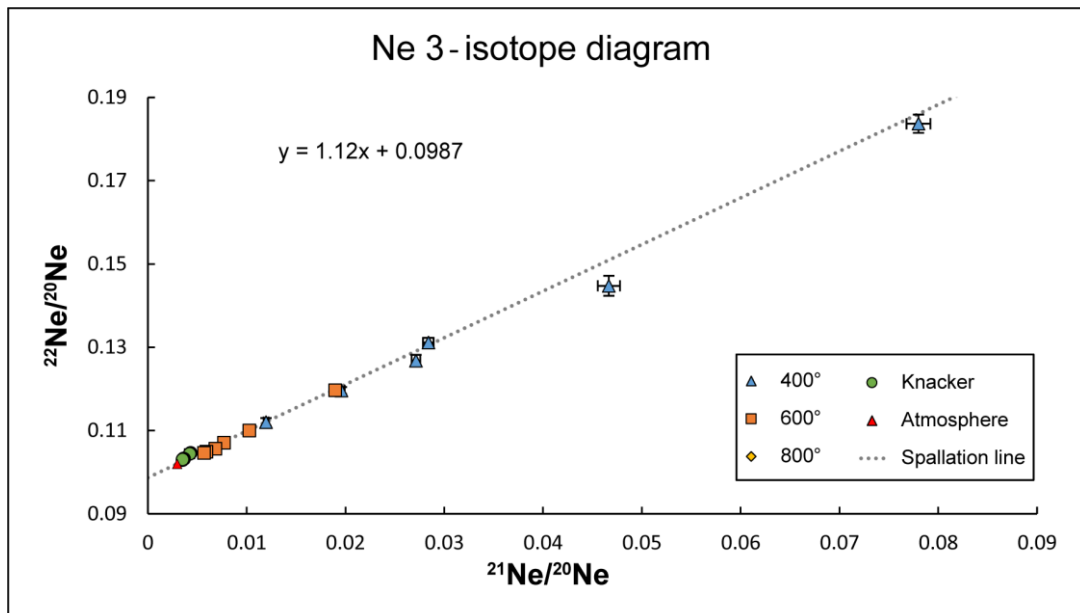


**Figure 6:** Ne 3-isotope diagram for all samples. Temperature steps are plotted with different markers and colors. Low-temperature crusher measurements are plotted in green. Atmospheric composition is marked by red triangle. Blue dotted line represents the spallation line – atmospheric composition. Low to mid-temperature measurements plot close to the spallation line. Most Ne-compounds are being released below 800°C; hence, this data can be regarded as representative for the samples.

by sediment or ice, radioactive decay of the shorter-lived nuclide series starts to change the nuclide ratios to values that deviate from the production rate ratios (Balco *et al.*, 2008). This signal can be used to infer the duration of burial of a previously exposed rock sample (Granger & Muzikar, 2001; Granger, 2006; Balco & Shuster, 2009; Dehnert *et al.*, 2011). When determining the age of a surface sample, ratios of the measured isotope concentrations should be examined, to ensure a simple deposition-exposure history of the sample. As a long-time exposure will create a comparable signal to that of burial, the nuclide concentrations will ultimately help to differentiate between the two mechanisms. The ratios of two nuclides (including at least one radionuclide) are plotted against the concentration of the stable nuclide in two-isotope diagrams, also known as ‘banana plots’ (Lal, 1991). Samples subjected to continuous exposure or steady-state erosion, will plot within the steady-state erosion island. Hence, these samples are useful to calculate exposure ages (Balco & Shuster, 2009). Samples that plot outside of the steady-state erosion island are either in the ‘forbidden zone’, an area of non-realistic concentrations that likely indicates problems during the separation or measurements, or they plot in the zone of burial, implying burial and/or shielding of the sample from cosmic rays (Granger & Muzikar, 2001; Dehnert *et al.*, 2011).

The three nuclide series analyzed in this study are displayed in two-isotope plots using the Excel plugin ‘CosmoCalc’ (Vermeesch, 2007).

### ***Production rate scaling and preliminary exposure ages***

The final step in calculating the exposure ages based on the isotope concentrations requires the implementation of site-specific production rates (Dunai, 2000). Reference production rates for individual study sites were determined by means of independent age data (Kelly *et al.*, 2015; Martin *et al.*, 2015) or cross-calibrated using various nuclide systems and within different minerals (Luna *et al.*, 2018). Production rate databases are published in open-access outlets and can be obtained from various sources (Balco *et al.*, 2008; Jones *et al.*, 2019).

Production rates are commonly scaled to mean sea-level-high latitude (SLHL) position to ensure comparability. To correctly apply a reference production rate to a study site, it needs to be scaled to the specific location. For the calculation of exposure ages, a reference production rate of  $4.02 \pm 0.12$  at/g/yr SLHL for  $^{10}\text{Be}$  was used (Kelly *et al.*, 2015; Martin *et al.*, 2015). The production rates for  $^{26}\text{Al}$  and  $^{21}\text{Ne}$  were calculated based on the production rate ratios of  $^{26}\text{Al}:^{10}\text{Be} = 6.74 \pm 0.34$  and  $^{10}\text{Be}:^{21}\text{Ne} = 0.232 \pm 0.009$  documented by

Goethals et al. (2009). The resulting production rates are  $27.1 \pm 1.6$  at/g/yr SLHL for  $^{26}\text{Al}$  and  $17.33 \pm 0.85$  at/g/yr SLHL for  $^{21}\text{Ne}$  respectively. These production rates were ultimately scaled to the study site following the scaling scheme of Dunai (2001) for a mean elevation of 3550 m a.s.l. The site-specific production rates are  $29.23 \pm 0.87$  at/g/yr for  $^{10}\text{Be}$ ,  $197.04 \pm 11.63$  at/g/yr for  $^{26}\text{Al}$  and  $126.01 \pm 6.18$  at/g/yr for  $^{21}\text{Ne}$ . The depth shielding of the production rate for the samples taken from beneath the surface was calculated with an attenuation length of  $160 \text{ g/cm}^2$  (Farber *et al.*, 2008) and a bulk density of  $1.8 \text{ g/cm}^3$  (Manger, 1963). Finally, the duration of exposure to cosmic rays was calculated for each individual sample and isotope system.

The exposure ages depending on production rate, radioactive decay, erosion rate, attenuation length, and depth of the sample can be calculated using the equation:

$$(4) N(z, \varepsilon, t) = \sum_i \frac{P(0)_i}{\varepsilon * \rho_z + \lambda} * e^{\left(\frac{-z * \rho_z}{\Lambda_i}\right)} * \left[ 1 - e^{\left(-1 \left(\frac{\varepsilon * \rho_z + \lambda}{\Lambda_i}\right) t\right)} \right] + N_{inh} * e^{-\lambda * t}$$

where  $N$  is the concentration (at/g),  $z$  is the depth (cm),  $t$  is time (years),  $\varepsilon$  is erosion rate (cm/yr),  $N_{inh}$  is the inherited concentration (at/g),  $P(0)_i$  is the site-specific production rate via production pathway  $i$ ,  $\rho_z$  is the cumulative bulk density ( $\text{g/cm}^3$ ) and  $\Lambda_i$  is the attenuation length of pathway  $i$  ( $\text{g/cm}^2$ ).

For the calculation of a preliminary exposure duration without including information on erosion rates or inherited concentration the equation for  $^{10}\text{Be}$  simplifies to:

$$(5) t_{exp10} = -\frac{1}{\lambda_{10}} \ln \left[ 1 - \left( \frac{N_{10} \lambda_{10}}{P_{Be}} \right) \right]$$

where  $\lambda_{10}$  is the decay constant of  $^{10}\text{Be}$  of  $4.9856 \times 10^7$ ,  $N_{10}$  is the calculated concentration of  $^{10}\text{Be}$  and  $P_{Be}$  is the production rate of  $^{10}\text{Be}$  scaled for the study area.

The same equation was used for  $^{26}\text{Al}$  with adjusted constants:

$$(6) t_{exp26} = -\frac{1}{\lambda_{26}} \ln \left[ 1 - \left( \frac{N_{26} \lambda_{26}}{P_{Al}} \right) \right]$$

where  $\lambda_{26}$  is the decay constant of  $^{26}\text{Al}$  of  $9.6653 \times 10^7$ ,  $N_{26}$  is the calculated concentration of  $^{26}\text{Al}$  and  $P_{Al}$  is the production rate of  $^{26}\text{Al}$  scaled for the study area.

For  $^{21}\text{Ne}$  a simpler equation was used, due to the absence of radioactive decay:

$$(7) t_{exp21} = \frac{N_{21}}{P_{21}}$$

where  $N_{21}$  is the calculated concentration of  $^{21}\text{Ne}$  and  $P_{Ne}$  is the production rate of  $^{21}\text{Ne}$  scaled for the study site (Ma & Stuart, 2018).

### ***Inheritance correction***

Inheritance correction was performed using a modeled depth profile of nuclide concentrations of the measured surface concentrations of  $^{21}\text{Ne}$ , because this isotope system does not suffer from radioactive decay. Hence, the pre-depositional accumulated concentration will be fully stored in the samples. Therefore, a modeled depth profile reflects the distribution of concentrations under undisturbed conditions, such as a simple deposition-exposure history, neglecting major post-depositional surface processes, and burial effects from sediment or snow cover. Profile concentrations will asymptotically approach a value at depth that reflects the amount of CRNs produced during transport, as the deepest sample is assumed to be completely shielded from cosmic rays by the time of surface exposure.

The modeled depth profile was calculated using the equation:

$$(8) N_{21}(z) = N_{21}inh + N_{21}0 * e^{(-\rho\lambda z)}$$

where  $N_{21}(z)$  is the concentration of  $^{21}\text{Ne}$  at depth ( $z$ ),  $N_{21}inh$  is the inherited concentration of  $^{21}\text{Ne}$ ,  $N_{21}0$  is the inheritance-corrected surface concentration of  $^{21}\text{Ne}$ ,  $\rho$  is the bulk density of the sampled material,  $\lambda$  is the attenuation length for cosmic rays ( $160 \text{ g/cm}^2$ ) and  $z$  is the depth (cm) (Anderson *et al.*, 1996).

The measured  $^{21}\text{Ne}$  concentrations, however, did not fit the depth profile using empirical parameters such as an attenuation length of  $160 \text{ g/cm}^2$  and a bulk density of  $1.8 \text{ g/cm}^3$ . As sample concentrations exceed the modeled concentrations, a Chi<sup>2</sup>-inversion was used to find the minimum misfit between the theoretical profile and the measured data with the bulk density and the inherited concentration as the main variables. The best fit of the data was generated by using unrealistically low bulk density values of  $\sim 1 \text{ g/cm}^3$ . After several approaches with varying parameters, an accurate inheritance calculation could not be carried out, due to the lack of density measurements of the material and the possibility, that the deposits do not have a simple deposition-exposure history. As a result of this, the concentration of the deepest  $^{21}\text{Ne}$  sample was assumed to reflect the inherited concentration and was subtracted from the measured concentrations of the upper  $^{21}\text{Ne}$  concentrations. For the remaining two isotope systems, the assumed inherited  $^{21}\text{Ne}$  concentration and the production-rate ratios were used to scale the inherited concentrations of  $^{10}\text{Be}$  and  $^{26}\text{Al}$

relative to  $^{21}\text{Ne}$ . The radioactive-decay correction of the inherited concentrations was performed by iteratively correcting the measured surface concentration for the relative inherited concentrations decayed over the time since the uncorrected surface exposure. After five steps, the inheritance values stagnated. These values were ultimately subtracted from the measured  $^{10}\text{Be}$  and  $^{26}\text{Al}$  concentrations. The complications while calculating and the deviations from the ideal depth profiles were investigated and interpreted according to the history and properties of the sediment deposits.

Additional tools for exposure-age calculation (Vermeesch, 2007; Balco *et al.*, 2008) were tested to benchmark the calculations carried out. Many of these tools are not fully transparent as the distinct equations, parameters and workflows are not completely comprehensible. The results of these tools are displayed for comparison and validation of the calculations carried out in this study.

### ***Erosion-rate estimates***

Erosion rates play a significant role in the accumulation of surface concentrations of CRNs, as erosion limits the maximum isotope concentrations by rejuvenating target surfaces. Depending on erosion rates and production rates (and for  $^{10}\text{Be}$  and  $^{26}\text{Al}$  nuclide specific half-lives), a secular equilibrium of the specific isotope system is reached after distinct time (Granger & Muzikar, 2001). As the production rates, half-lives, and maximum depositional ages (see chapter 3.2.1) are known, erosion-rate thresholds were calculated by solving equation (1) for the erosion rate, using the previously uncorrected and corrected concentrations of the surface samples of all three nuclide systems and maximum depositional ages of the youngest U-Pb sample. Additionally, these rates will be compared with respect to erosion rates calculated by common CRN calculators (CRONUS, CosmoCalc) and regionally established erosion rates for the Puna-Altiplano-Puna Plateau.

### ***Corrected exposure ages***

Following the calculations of inherited concentrations and maximum erosion rate thresholds, the corrected exposure ages were calculated using equation (1). As the erosion rate thresholds were interpreted to be boundary conditions instead of precise values, and the final exposure ages were only calculated based on the measured and inherited concentrations. Thus, the resulting values are minimum ages and might as well be older, if distinct erosion rates would be included in the calculations. Exposure ages including erosion rates are provided by the previously mentioned calculators and will be included in the discussion chapter.

## **2.2 Remotely-sensed characterization of faulting**

### **2.2.1 Background**

Characterizing the geometric and mechanical properties of faults helps to evaluate their relationship with the regional stress field. This requires a meticulous, multi-scale analysis of individual faults and the affected geological framework. Surface-rupturing earthquakes along tectonic faults can break through river channels, river terraces, alluvial fans and other geomorphological features that serve as excellent strain markers (Hodge *et al.*, 2019). Aerial and satellite imagery allows to remotely identify tectonically overprinted landforms, and hence, active faults (Ramasamy, 2006; Funk *et al.*, 2009). The dimensions of the identifiable structure scales with the ground resolution of the available data sets. While in the past, faults with minimum lengths of several kilometers could be delineated, technical progress in aerial and satellite-image acquisition has reduced this threshold, allowing the identification of smaller structures, thus unravel the complexity of surface deformation features (Thomas *et al.*, 2021). Moreover, the remotely sensed analysis of fault scarps and offsets enables measuring their cumulative, vertical displacement. If this information exists, estimates on earthquake magnitudes can be retrieved and analyzed in the context of empirical data on fault length, displacement, and magnitude relations (Wells & Coppersmith, 1994; Gudmundsson, 2000).

### **2.2.2 Topographic data**

Topographic analysis was carried out using the TanDEM-X “© DLR 2018” digital elevation model (DEM), provided by the German Aerospace Center (DLR) and Landsat composite satellite imagery (U.S. Geological Survey) in combination with the TopoToolbox 2 Matlab functions (Schwanghart & Kuhn, 2010; Schwanghart & Scherler, 2014) and spatial analysis-tools in Quantum GIS (QGIS.org, 2021. QGIS Geographic Information System. QGIS Association. <http://www.qgis.org>).

With a spatial resolution of 10 m per pixel (absolute vertical and horizontal spatial resolution) and a relative accuracy of 2 m per pixel (in areas with less than 20° of slope) (Zheng *et al.*, 2010), the TanDEM-X data set is a state-of-the-art, non-commercial, digital elevation model with global coverage. For the analysis performed here, the DLR provided two tiles of the TanDEM-X data covering the area between 21°S-65°W and 22°S-66°W. In order to calculate derivatives from the GIS project was set to the World Geodetic System

1984 (WGS84), Universal Transverse Mercator (UTM) zone 20S. Additionally, several sites were surveyed using a DJI Mavic 2 Pro unmanned aerial vehicle (UAV), equipped with a 12-megapixel camera. The stereoscopic imagery, acquired by the UAV was used to generate digital elevation models based on structure from motion (sfm) methods (Westoby *et al.*, 2012). The image stitching and subsequent point-cloud generation was carried out in AgiSoft Metashape. These models were georeferenced using meter-by-meter-sized targets, or ground control points (GCPs), whose locations were measured using a Leica real-time kinematic global positioning system (RTK-GPS). The resulting models were exported in GeoTIFF (.tif) format for further use in QGIS.

### ***2.2.3 Visual inspection of DEMs - morphology and slope***

Digital elevation models are grids of elevation data, equally sampled in georeferenced x- and y-space (Maune *et al.*, 2001; Maune, 2007). To visually analyze the elevation data, a shaded relief effect can be applied, referred to as a hillshade. This technique generates a realistic terrain view by creating a three-dimensional surface from 2-dimensional data. During the calculation of the hillshade, it is possible to specify an azimuth and an altitude of synthetic illumination, a vertical exaggeration factor, and a scaling factor to account for differences between vertical and horizontal units. Draping a color-coded, semi-transparent set of the elevation data over a hillshade creates a vivid visualization of the landscape.

The analysis of slope maps in the context of tectonic geomorphology can be useful to visualize disturbances in generally continuously sloping surfaces, such as alluvial-fan surfaces or river terraces. Slope values can be extracted from a DEM by calculating the first derivative of the elevation data of each pixel. This way, high-relief areas can be distinguished from low-relief areas. Modern GIS software solutions commonly include dedicated functions, such as roughness and aspect functions, among others. Previous studies, however, have found, that hillshades are the most effective tool for identifying surface faults (Ganas *et al.*, 2005; Engelkemeir & Khan, 2008).

For the geomorphological analysis with respect to a tectonic overprint of the landscape, hillshades and slope maps were used in the study area. The hillshades were generated using an ‘azimuth of the light’ value of 315° and an altitude of the light of 45°. During the process of hillshade generation, scaling was set to 111120 to convert the elevation data of the DEM from decimal degrees to meters. No additional vertical exaggeration was applied. Slope maps were calculated using the terrain-analysis slope function of QGIS. The resulting data

was draped over the hillshade and displayed in a spectral-color scheme with a transparency of 50%. The color-scheme was limited to slope values of 0-5°, in order to distinguish disturbances in the low-slope surfaces.

### ***2.2.4 Drainage-basin morphometry***

Analysis of river networks and drainage-basin morphometry have become widely used methods in neotectonic studies. Drainage networks in particular are sensitive to tectonic perturbations (Queiroz *et al.*, 2015). Common responses can reach from large scale modifications, such as long-wavelength changes in longitudinal river profiles (Mudd *et al.*, 2018), over small-scale changes like variations in stream sinuosity and steepness (Zámolyi *et al.*, 2010; Gallen & Wegmann, 2017; Mudd *et al.*, 2018), to local knickpoint formation (Crosby & Whipple, 2006; Berlin & Anderson, 2007; Boulton *et al.*, 2014; Babaei *et al.*, 2020) and beheaded river channels (Walker & Allen, 2012). In tectonically active areas, surface-rupturing earthquakes can be a common cause for such perturbations. However, over time, drainage systems tend to reverse this modification through sustained erosion. Therefore, analyzing the morphometric properties mentioned above can be useful to emphasize the possible recency of tectonic activity in areas with morphological evidence of surface faulting and a lack of instrumentally recorded seismic activity. In this study, variations in normalized channel steepness index ( $k_{sn}$ ) and the spatial distribution of knickpoints and associated magnitudes are used as proxies for vertical displacement; lateral displacement will be examined by the analysis of offset drainage divides and streams.

#### ***Stream network***

The analysis of the digital elevation model was performed in QGIS and Matlab following a stepwise approach in both software environments (Figure 7). Drainage parameters such as flow directions and flow accumulation were calculated using the dedicated functions in TopoToolbox. The DEM was pre-processed using the ‘carving’-function instead of the commonly used ‘fill’-function. The advantage of carving is that the algorithm does not seek the best path along center lines of flat sections, but tries to find a path through sinks that runs along the deepest path (Schwanghart & Scherler, 2014); this is the preferable way to avoid unrealistically straight sections through topographic depressions. Based on this data, a stream network was generated, limiting streams to a minimum upstream area of 1000 pixels, thereby reducing the computational load of the analysis to a manageable number of

streams. Based on the stream network, drainage basins were delineated. The DEM and the stream network were cropped to the largest drainage basin.

For a more detailed overview of the tectonically influenced patterns and a less time- and resource-consuming processing, more detailed analysis was further restricted to the identified structures and surrounding features. Ultimately, stream networks were visually inspected for a tectonic overprint.

### ***Drainage basins***

Tributary drainage basins were delineated for the selected sites in the same way as the larger basins. As for the stream networks, drainage divides were visually inspected for perturbations that coincide with the tectonic structures.

### ***Normalized channel steepness index and knickpoints***

Analysis of normalized channel steepness is based on the empirical relationship that describes local channel slope ( $S$ ) as a function of channel steepness ( $k_s$ ), contributing drainage area ( $A$ ) and the concavity index ( $\theta$ ) (Flint 1974).

$$(9) S = k_s A^{-\theta}$$

An undisturbed stream profile at steady-state conditions has a concave upward profile in elevation vs downstream-distance space, with typical values of the concavity index ranging from 0.35 to 0.6 (Boulton *et al.*, 2014; Lague, 2014). Discontinuities in channel profiles are commonly expressed by convexities and indicate a transient response to a perturbation, referred to as a knickpoint or knickzone (Crosby & Whipple, 2006). Knickpoints correlate with sudden changes in channel steepness, where steepness values suddenly increase along profile instead of following an expected continuous decrease. The reason for such perturbations can be of different nature, including, but not limited to structural and mechanical properties of the riverbed, climatic fluctuations, and human modifications (Burbank & Anderson, 2012). Two end members of knickpoints have been described in geomorphological studies: vertical-step and slope-break knickpoints (Kirby & Whipple, 2012). The former is expressed by a spike in slope values on a slope-area plot, anchored in space due to locally resistant substrate. The latter is expressed by a break in the slope-area plot that can be forced by persistent changes such as the initiation of faulting or a change

in slip rate along a fault. As such, this type of knickpoint was used for tectonic interpretations in erosional landscapes.

Linear alignments of slope-break knickpoints allowed the identification of previously unknown tectonic structures (Bhosle *et al.*, 2009) and the quantification of recent fault activity (Marliyani *et al.*, 2016; Gallen & Wegmann, 2017; Babaei *et al.*, 2020). In case of episodic fault activity, knickpoints tend to migrate upstream during interseismic phases,

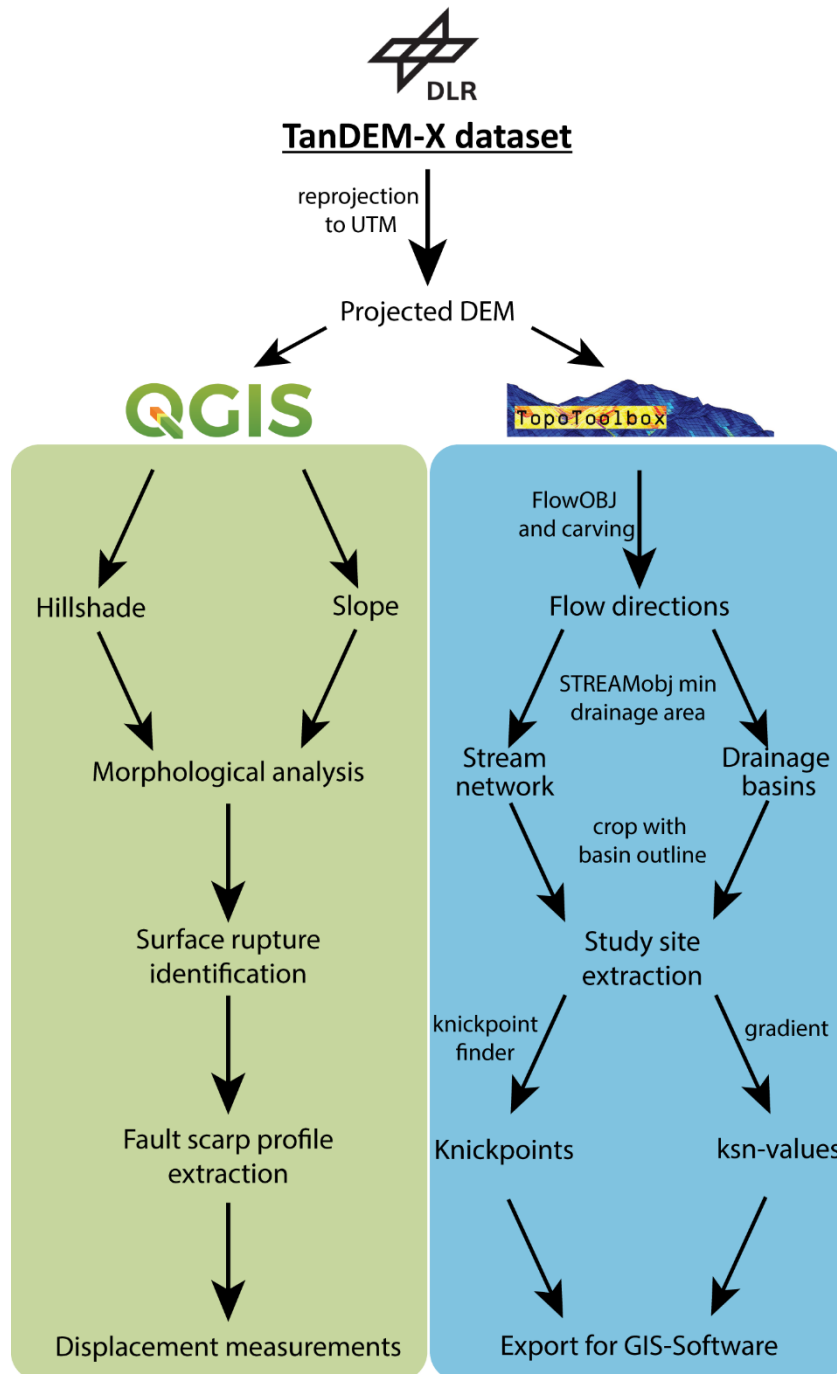


**Figure 7:** Methodological workflow for the processing of the TanDEM-X data set. Analysis was carried out in QGIS using terrain analysis functions (green) and TopoToolbox functions in Matlab (blue).

where the celerity of the horizontal migration rate is a function of drainage area and climate. At the same time, channels will tend to eradicate the steepness perturbation by sequential erosion, leading to the pre-deformed, steady-state, concave-up longitudinal profile.

Based on these observations, the recency of deformation along the identified faults was tested, by analyzing their impact on the local drainage system using the normalized river steepness index and knickpoints. River-steepness indices were calculated using the previously extracted stream network. The relative  $k_s$ -values strongly depend on the chosen concavity index ( $\theta$ ). The higher the values, the faster the channel gradient decreases downstream (Mudd *et al.*, 2018). Hence, this parameter may vary with tributary drainage basin and/or stream order. Concavity indices were calculated for every trunk stream and tributary drainage basin using a slope-area approach and a  $\chi$ -based method, without finding an overall applicable trend. Values scatter over a wide range. Therefore, calculations were carried out using a common reference value of  $\theta_{ref} = 0.45$ , which is commonly used as a normalization and delivers  $k_{sn}$ -values respectively. The resulting steepness values were aggregated into stream segments of 1000 m length and ultimately exported for further use in GIS software.

Knickpoints were calculated using the ‘knickpointfinder’-function implemented in TopoToolbox (Schwanghart & Kuhn, 2010). This function uses the previously extracted stream network and the DEM to reconstruct the actual longitudinal river profiles by iteratively removing curvature constraint at locations of maximum vertical offset to the actual profile. To avoid knickpoint detection based on the digital elevation models’ inherited resolution, the algorithm was set to a tolerance of 3 m, hence only detecting knickpoints offsetting the longitudinal river profile by more than 3 m.

### ***2.2.5 Fault-scarp profiling***

Topographic profiling of fault scarps is a major data source on vertical displacement of surface-rupturing dip-slip faults (McCalpin, 2009). Fault scarps are the topographic expression of fault displacement at the surface, indicated by a step in the landscape. Repeated fault activity accumulates displacement at the scarp. If the displacement was distributed over several fault branches in a wider fault zone, this will be expressed by distinct slope breaks, indicating multiple fault scarps. Either way, the total amount of displacement can be determined by measuring the vertical separation of the undisturbed hanging- and footwall surfaces. This works exceptionally well in areas of steady and low-

slope angles. Using the TanDEM-X data and the previously calculated slope maps, alluvial-fan surfaces were distinguished from the basement rocks and fluvially overprinted sections by delineating undisturbed low-slope areas. By applying the ‘cross profiles’-tool in QGIS,

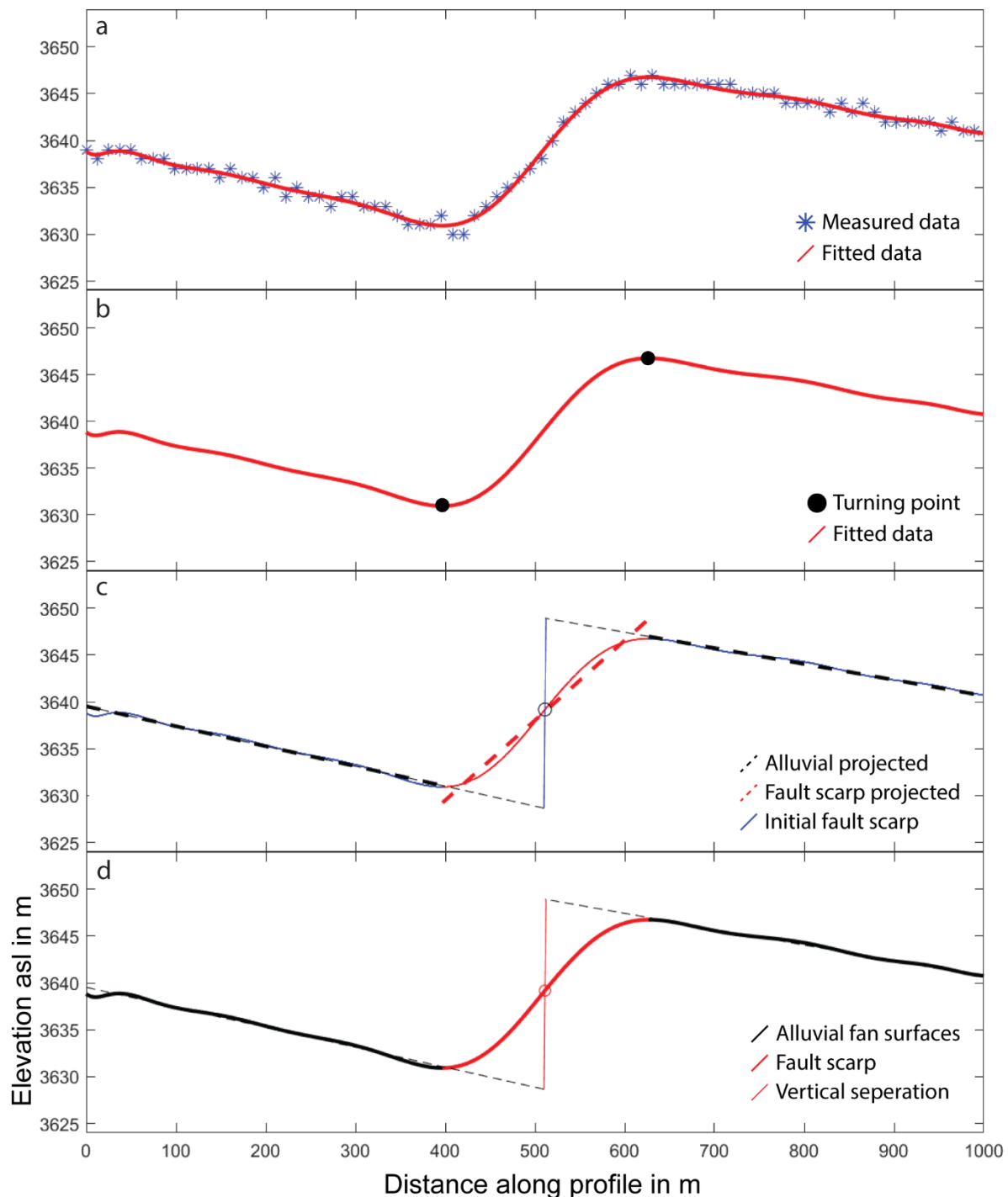
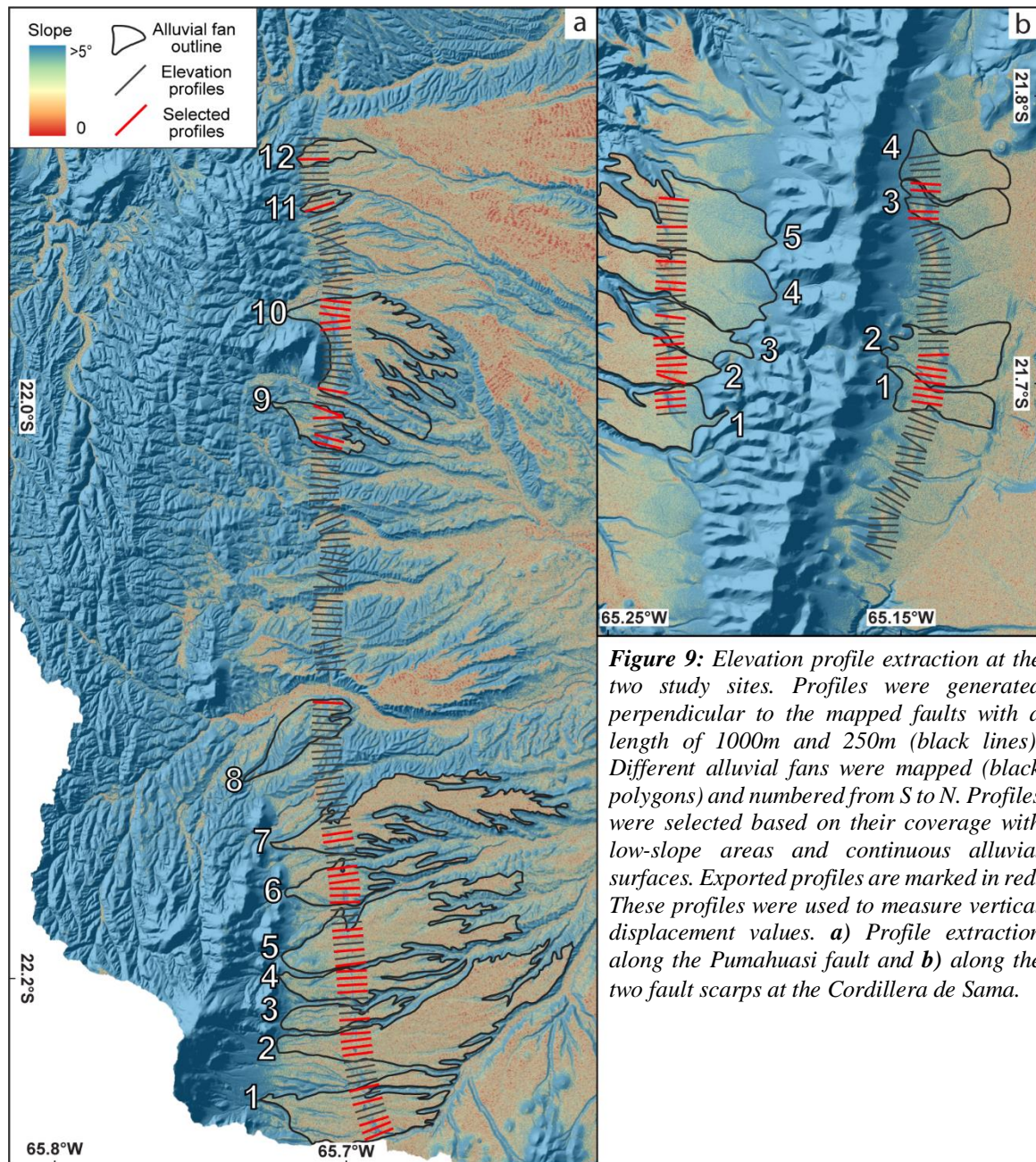


**Figure 8:** Workflow of fault scarp vertical displacement measurements applied to an exemplary profile. **a)** Extracted elevation values from the TanDEM-X dataset (blue stars) and fitted data using a Savitzky-Golay filter (red line). **b)** Fitted data (red line) and the calculated turning points in slope (black circles) that represent the limits of the fault scarp. **c)** linear fits of the far field slopes (black dashed line) and the fault scarp (red dashed line). The simplified fault is set in the center of the scarp with a dip angle of  $80^\circ$  towards the West. Due to the exaggeration of the elevation to distance ratio, the fault inclination is barely visible. **d)** Final model of the fault scarp profile (continuous lines) and the initial scarp (dashed lines). The calculated vertical displacement is the offset of the far field alluvial surfaces along the synthetic fault plane.

fault-perpendicular elevation profiles of 1000 m length were generated, every 250 m along the faults (Figure 9). Profiles were visually inspected for their morphological overprint and only the ones that appeared to be solely affected by primary tectonic processes were selected for further processing. Additionally, profiles not crossing isolated, low-slope surfaces were discarded. To reduce unwanted noise, these profiles were smoothed using a  $15^\circ$  Savitzky-Golay filter applied to the entire data set (Figure 8a). The filtered data was resampled using a spline interpolation (Figure 8b). Subsequently, the profiles were split into three segments, the hanging wall, the footwall and the fault “free face” or colluvium, along the most prominent local maxima and minima of the elevation data, representing the points of most prominent slope changes and therefore, the section of the surface that was faulted. Every segment was subsequently fitted using a linear regression to reconstruct the initial, fault-scarp morphology prior to degradation (Figure 8c). The fault was assumed to be in the central part of the fault-scarp segment with a steep westward dip of  $80^\circ$ , as observed in the field (see chapter 3.5). Vertical displacement was finally calculated by measuring the vertical distance between the linear fits of the hanging- and footwalls. Fault-scarp width was measured by calculating the distance between the most prominent local maxima and minima (Figure 8d). In order to ensure reproducibility and provide automation, all steps of the calculations were compiled in a Matlab-script.



### 2.3 On-site quantification of vertical displacement values

Remote-sensing analysis of faults can be ambiguous as vertical displacement do not always directly imply an explicit kinematic behavior. At first sight two opposing styles of deformation may be derived because compressional and tensional stresses might result in similar surface expressions of deformation. To unravel a proper kinematic solution, it is important to provide data on faulting in the subsurface by analyzing the affected strata. This can only be achieved by detailed fieldwork. In the scope of the analysis conducted in this study, field work was carried out in the central-eastern Puna Plateau of NW-Argentina.

Unfortunately, it was neither possible to visit the study sites in Bolivia in the vicinity of the Cordillera de Sama nor the northern continuation of the Argentine Pumahuasi Fault. Nonetheless, the available data clearly demonstrate the mechanisms of faulting by direct and indirect implications.

Field work included i) structural analysis and mapping of exposed geological units; ii) documentation of geomorphic and geological indicators of faulting; and iii) description of lateral facies variations and regional unconformities of strata associated with faulting. The latter record the tectono-sedimentary history of the headwater region of the Río Pilcomayo. This is essential for the overall understanding of the mountain range along with the tectonic analysis. A change in depositional environments can also reflect either changing energetic conditions or climatic variations and may thus lead to erroneous interpretations concerning the faulting history and ensuing erosional and depositional processes. In the following two sections it is described how key outcrop at the Pumahuasi and Yavi faults were documented, taken these issues into consideration, followed by taking into account diverse types of ore deposits that are linked with the central sectors of the Pumahuasi fault.

### ***2.3.1 Structural data***

#### ***Pumahuasi fault***

Based on the information gathered from the remote-sensing analysis, natural erosional cuts along or across potential faults were analyzed for exposed deformed strata. A key outcrop of the Pumahuasi Fault, described by Cladouhos et al. in 1994, exposing a 12-m-wide fault gouge, was not found. In contrast, one channel cut within an alluvial fan on the eastern foothills of the Sierra de Escaya revealed a natural outcrop of faulted sedimentary strata. To accurately document the deformation of the different strata, paleoseismological methods were applied. The outcrop was cleaned from loose and collapsed material originating from the topsoil. The sedimentary layers, the faults and cracks were subsequently identified and marked with colored flags for better differentiation. A reference grid of 1x1 m was applied to the wall. Afterwards, the marked units, faults and cracks were transferred to graph paper at a scale of 1:25 (1 cm on graph paper = 25 cm of the outcrop wall). Before and after the gridding of the faulted stratigraphic sequence, images of the wall with at least 50% overlap between consecutive images were taken, using an Olympus OM-D E-M10 Mark 2 system camera. One set of images was taken from close distance (~1 m) to the wall and a second set from further distance (~3 m), to ensure proper

resolution of all grain sizes. In total, 293 high-resolution images were taken, 153 close shots, and 86 from further distance. Subsequently, these images were used to create a 3D model and a photomosaic of the outcrop in Agisoft Metashape Professional. The processing followed the method described in the supplementary material of Reitman *et al.* (Reitman *et al.*, 2015). Some deviations from the described method are to be noted: 1) since the outcrop is a natural exposure, the wall is not in a perfectly straight line but shows some curvature in E-W direction, and 2) the grid points were not measured with a differential GPS. The model was scaled using a digital scalebar of 1 m, aligned to the gridlines mounted to the wall. Images were preprocessed by masking areas for essential information and by color correction of shaded and glaring areas. Preprocessed images were aligned, and point clouds were generated by the software. These point clouds were manually cleaned from erroneous points and unaligned images. After proper image alignment had been done, a photomosaic was generated and exported. The result was combined with a scan of the field log and a detailed digital log was generated using graphic software (Adobe Illustrator 2020).

### ***Yavi***

Additional outcrops exposing deformed strata were found in the valley fill in the vicinity of the village of Yavi. These outcrops were documented in a less precise manner due to limited exposure. Therefore, the applied methods were limited to detailed descriptions, displacement measurements, and the generation of photomosaics.

### ***Joint measurements***

Besides major tectonic structures such as faults, crustal stress can manifest itself by the formation of (conjugated) joints within layers of rock and sedimentary deposits. The analysis of these brittle-deformation features can be used to identify the principal tensors of the governing tectonic stress field to first order (Engelder, 1985; Hancock, 1985; Engelder & Gross, 1993; Clark & Leonard, 2003; Whitaker & Engelder, 2005; DeGuidi *et al.*, 2013).

In order to gain information on the orientation of the stress field within the study area, subsequent to the deposition of the sedimentary strata of the basin fill, the strike of systematic vertical joint sets was measured. A minimum of 40 joints was measured per measuring site. This data was imported into the software Stereonet 11 (Cardozo & Allmendinger, 2013; Allmendinger *et al.*, 2020) and plotted as rose diagrams to visualize the main azimuth of joint orientations. In order to infer the orientation of the causative

tectonic stress tensor, the data can be inverted to display the opening direction of the joints (DeGuidi *et al.*, 2013).

### **2.3.2 Ore deposits**

Deposits of ore-bearing rocks close to the national border between Argentina and Bolivia constitute an interesting phenomenon in the geological framework of the area that is intimately linked with the fault zones in the basin in the western sector of the study area. These deposits were extensively mined during the mid-20th century. Precise information about the mining campaign was published shortly afterwards (Kröger, 1956). Following these observations, several types of deposits can be found within the fault zone, but not all of them were mineralized in distinct fault zones. Their formation could be induced by precipitation out of a stagnant water body, or the components of these materials were generated by hydrothermalism that migrated towards the surface along fault planes within the strata. In order to evaluate the formation of these mineral deposits in the context of faulting, old mining pits and trenches were visited, and different phases of mineralization were recorded.

## 3 Results

### 3.1 Geological framework

#### 3.1.1 Stratigraphy

Stratigraphic sections of the Neogene to Quaternary sedimentary fill in the intermontane basin of the study area were recorded at four key sites along an East-West profile between the western Sierra de Escaya and the eastern Sierra de Santa Victoria (for location see Figure 12). Natural erosional cuts in river channels and road sections as well as mining trenches provided insight into the sedimentary deposits. As observed in the stratigraphic sections and already described for equivalent strata in the Bolivian Altiplano (Kennan *et al.*, 1997), the strata were deposited in a braided river system. As such, a basin-wide correlation of the highly variable sediments is difficult. Thickness variations of the sedimentary column at the distinct locations are due to paleo-topographic features and erosive contacts (Figure 11). Below, several sites will be characterized and discussed in light of their geochronology.

#### *Tafna (3510-3570 m)*

A single representative outcrop of the entire succession within the vicinity of Tafna could not be found. As this location is close to the Sierra de Escaya, the thickness of the sediment succession is strongly influenced by the paleo-topographic features of the range. The following description is a compilation of data from different outcrops.

Many river cuts in the alluvial-fan deposits east of the Sierra de Escaya expose the deeply weathered Acoite Formation (Ordovician) in the footwall of the Pumahuasi fault, which is unconformably overlain by conglomerates that vary in thickness between 1 and 2 m, depending on paleo-topographic conditions. The conglomerate clasts are up to 50 cm in diameter and comprise metapelites and rhyolites most probably sourced from the Sierra de Escaya. In the border region between Argentina and Bolivia and along strike of the Pumahuasi Fault, this unit can be observed in many abandoned mining pits. Generally, the sandy to arkosic matrix in the fault zone is cemented by iron- and manganese-ore precipitates. The conglomerates terminate in an erosional unconformity and are followed by horizontally layered sand, silts, and sandy tuffites of the Tafna Formation which was originally proposed to be of Plio-Pleistocene age (Kröger, 1956; Cladouhos *et al.*, 1994).

According to new age data presented in this study (see chapter 3.2.1; Table 1), the age of deposition of the Tafna Formation can be corrected to have initiated by Late Miocene and terminated in the Pliocene. With a maximum thickness of 40 m, the Tafna Formation is mostly exposed in higher sectors of the hanging wall of the Pumahuasi Fault (Figure 10a). On the footwall however, the number of outcrops and the color of the Tafna Formation decreases, i.e., its white-colored character turns into a brownish tone due to mixing with other sedimentary components. Apparently, most of the unit is limited to the western hanging-wall section of the Pumahuasi Fault. In close vicinity to the fault, the sedimentary strata were overprinted by the same iron- and manganese-ore precipitates as the conglomerates, but in this case, the precipitates developed finger- to coral-shaped radial nodules (see chapter 3.6.2). The Tafna Formation is superseded by angular to subangular metapelitic, rhyolitic, and quartzitic clasts, most probably derived from source rocks in the Sierra de Escaya. These gravels are the youngest deposits of this section and form an integral part of wide alluvial fans that cover most of the western part of the study area with a thickness of up to 10 m. While the surface of the alluvial fans is mainly covered by sands

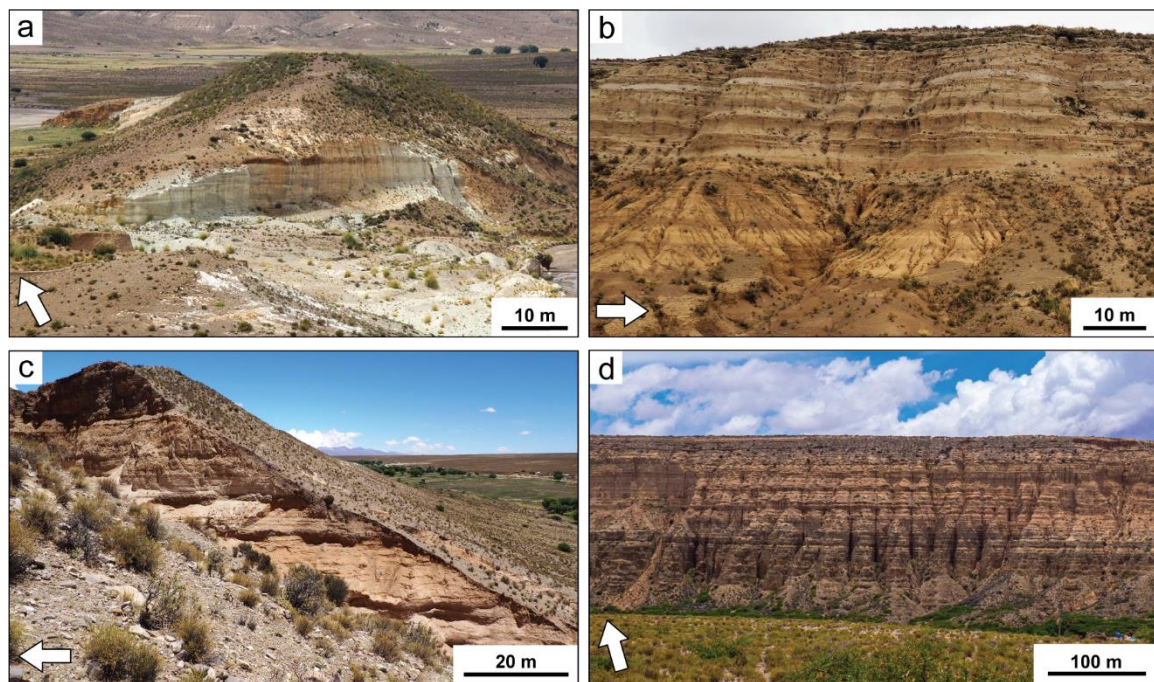


**Figure 10:** Outcrops exposing the stratigraphy of the basin-fill units. North direction indicated by white arrows. **a)** Former kaolinite mine within the Tafna Formation. Bright lacustrine volcanic ash incorporating deposits in contrast to overlying gravels of alluvial-fan deposits. Erosion by the La Quiaca river exposed this outcrop. Basement rocks are exposed along the present-day base level of the river. **b)** Incomplete basin-fill succession at Sansana. Alternating brown gravel and yellowish sand beds at the base are followed by grey to whitish fine sand to silt deposits, including layers of volcanic ash. Basement and recent sedimentary cover units are missing at this site. **c)** Stratigraphy east of the village of Yavi; grey and whitish beds of sandy and silty material at the base, followed by gravels and sands. **d)** Most complete sedimentary succession of the basin-fill units at the river cut north of Yavi Chico. The outcrop exposes a vertical cut of more than 140 m of horizontally layered clastic sediments.

and clasts smaller than 10 cm in diameter, vertical cuts in these deposits also expose clasts reaching a diameter of up to 50 cm alternating with sandy layers, suggesting pronounced weathering effects and size reduction on surface clasts over time. Vertical displacement along the Pumahuasi Fault affected the entire stratigraphic section.

#### *Sansana (3444-3500 m)*

Farther east and west of the settlement of Sansana, an east-directed canyon exposes the sediment-fill strata with a thickness of approximately 62 m (Figure 10b). This succession can be subdivided into four major units based on pronounced breaks in slope that are associated with changes in material properties. Medium to fine-grained brown sands mark the base of this section, including a single, grey-colored, and 30-cm-thick layer of volcanic ash that stands out from the uniform lower succession. The lowest deposits form smooth slopes along the base of the exposure for approximately 20 m of elevation. As the deposits change towards a more yellowish appearance of finer grained sands in beds of approximately 1 to 2 m thickness, the slopes increase. The amount of coarser grained layers changes for a larger amount of the finer grained yellowish layers. This unit reaches a thickness of approximately 15 m, followed by a 10-m-thick layer of grey to white-colored, 1-m-thick beds of predominately silty material. A high content of volcanoclastics causes the bright-colored, tuffaceous appearance of this deposit. Due to the finer grain size, this unit forms an almost vertical wall, which is only interrupted by small steps at the transition between beds of different resistance to weathering. The upper 5-7 m of the outcrop consist of dark grey, thoroughly fractured silts. The thickness of individual beds is within a range of 30-50 cm; the deposit is cross-stratified and load casts form undulating contacts. This unit shows a different weathering behavior with retreating, erosionally resistant steps that are formed at the surface along vertical carbonate-filled fracture planes.

#### *Yavi (3470-3570 m)*

The stratigraphic section at Yavi town and surroundings is discontinuous in the lower parts and was constructed by using a patchwork of different outcrops. In many places, the initial deposits are eroded and are covered by younger conglomerates (Figure 10c). However, the observations that can be made here correlate well with the stratigraphic succession at Sansana. The oldest deposits, exposed approximately at the present-day riverbed, are composed of medium- to fine-grained brownish sands of about 10 m thickness. Sporadically distributed within these beds are lenses of silts and clays. These are followed by brighter colored, alternating, meter-thick beds of sands and gravels that reach a thickness

of approximately 20 m. An erosional contact marks the transition to the whitish to greyish layers that are also well-expressed at Sansana. These layers show different sediment structures, such as load casts, cross bedding, and erosional transitions between beds. This unit reaches an overall thickness of approximately 24 m. A major unconformity marks its upper section and the transition towards coarser grained deposits of alternating beds including sandy and gravelly channel deposits. The entire succession is topped by conglomerates of beige to reddish color, hosting well-established k-horizons. In some of the outcrops, vertical displacement was observed along steeply dipping, N-S-striking fault planes (see section 3.7 Yavi Fault).

### *Yavi Chico (3410-3555 m)*

The most continuous exposure of the fill units exists close to the settlement of Yavi Chico (Figure 10d). A succession of approximately 140 m thickness is exposed at a south-facing canyon wall along a tributary river of the Río Pilcomayo drainage system. As for the other

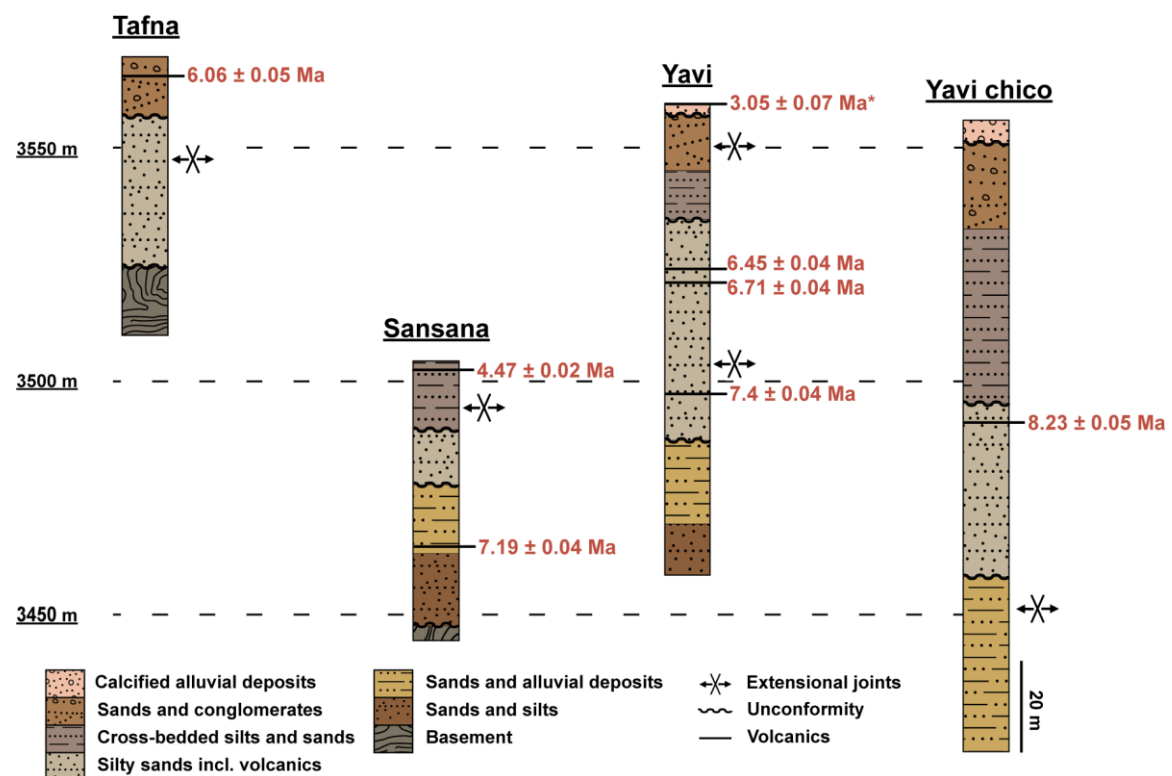


**Figure 11:** Simplified stratigraphic sections from different sites along an E-W-oriented profile, including U-Pb dates (section 3.2.1) and measurements of extensional joints (crosses with arrows). Six major sedimentary units were identified in the field. Deformed basement rocks were only recorded at the westernmost site, close to the settlement of Tafna. These units are overlain by fine sands and silts incorporating volcanoclastics of the Tafna Formation and alluvial gravels. The exposed strata at Sansana involve a more complete succession but lack the upper layers found at Yavi and Yavi chico. The most complete stratigraphic section was found at Yavi chico, constituting sediments of 140 m thickness. The surfaces at Yavi and Yavi chico are continuous paleo-surfaces with a gentle, N-directed slope, explaining the difference in elevation.

sites, the lowermost strata are comprised of alternating beds of sands and gravels. These deposits cover the lower 40 m of the profile. An erosional contact marks the onset of beige to whitish sand deposits, including volcanoclastics. These layers reach a thickness of about 50 m at this site, differing from the lower deposits by a distinct break in slope, creating an almost vertical and inaccessible wall. Therefore, the uppermost section of the outcrop was not directly measured; observations made just below the surface in outcrops east of Yavi, were extrapolated to this site, as the upper strata appeared to follow a similar sequence. Signs of deformation were not visible within the succession.

#### ***3.1.2 Morphology***

The geomorphology of the study area can be divided into three major features: 1) basement ranges, including patches of basement protruding from the basin-fill units, 2) flat-lying, sedimentary basin-fill units, covering the deformed basement and deformed older Tertiary strata, and 3) deep canyons in the valley fill, adjusted to the Río Pilcomayo drainage network. The basement ranges strike predominantly N-S and constitute the high-relief areas of the study area. The western Sierra de Escaya reaches elevations of approximately 4000 m a.s.l., whereas the ranges of the Eastern Cordillera, reach peak elevations of up to 4400 m a.s.l. On the slope map, basement ranges can be identified by intermediate hillslopes of 10-25°, displayed by orange to light red colors (Figure 12). The patchwork of basement rocks that protrudes from the valley fill does only reach low elevations with respect to the flat-lying basin-fill units. In the central sectors of the study area, the Siete Hermanos Range, formed by Cretaceous strata, constitutes an anomaly in the otherwise monotonous basin-fill succession. These hills have an asymmetric shape, with gentle slopes on the NW-facing side that are parallel to the bedding planes and steep slopes on the SE-facing flank that are perpendicular to the bedding planes. The flat-lying basin-fill units that cover wide parts of the study area form a pronounced morphologic contrast with respect to the slopes of the Siete Hermanos and basement ranges. The upper layers of the basin-fill units form an integral part of high surfaces that occur within an elevation range between 3750 m a.s.l. to 3550 m a.s.l. Regionally, the elevations of these surfaces gently decrease northward, and locally toward the canyons. While the western sectors of the study area are dominated by coalesced, incised alluvial fans that form the piedmont of the Sierra de Escaya, the eastern sectors constitute more continuous, flat-lying gravel surfaces. On the slope map, those gentle surfaces can be readily identified by low slope values of less than 5°, displayed in light blue to light green colors (Figure 12). The gently inclined character of these surfaces

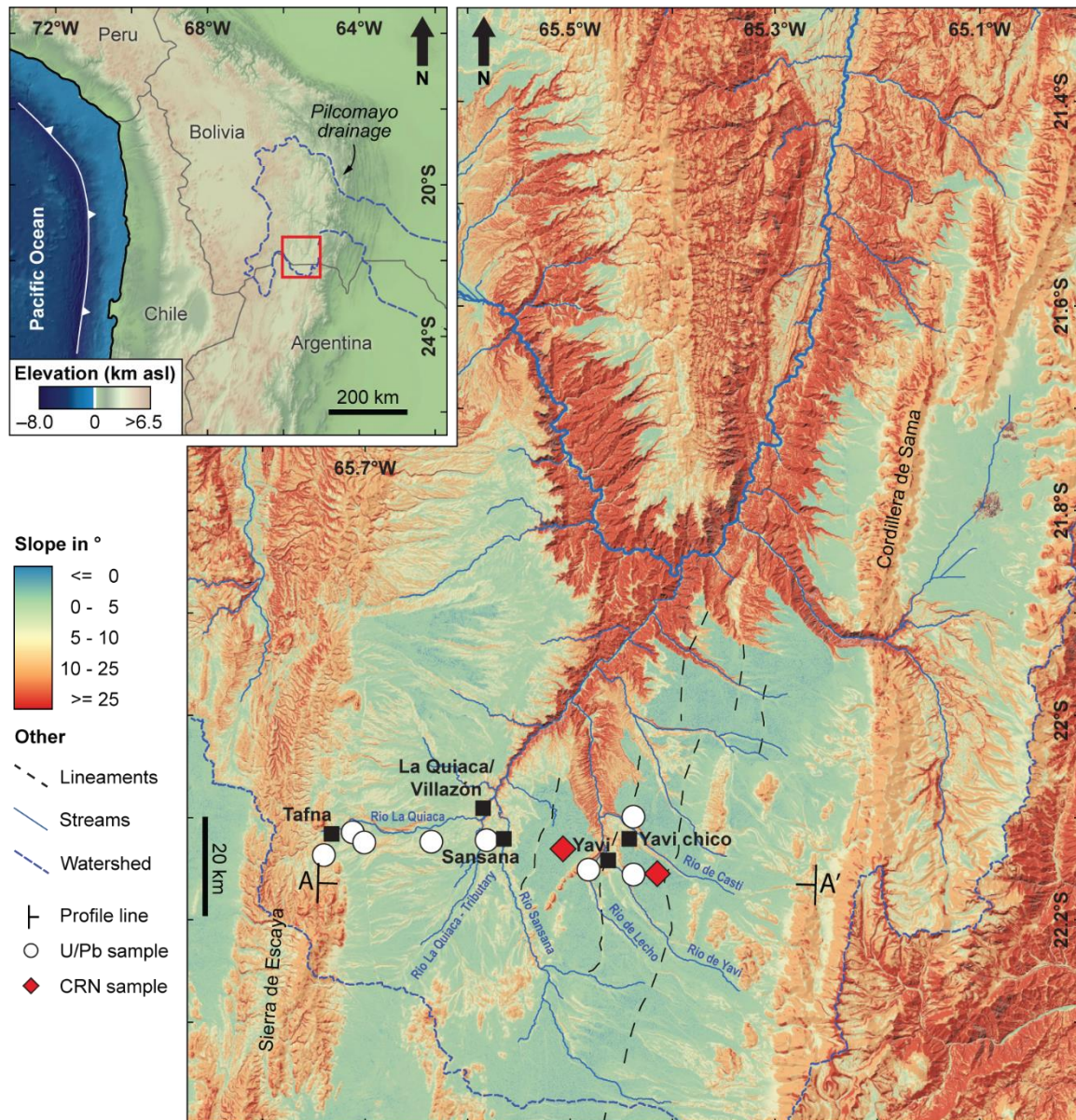


**Figure 12:** Slope map of the study area. Hillslopes are displayed with discrete gradations in spectral color scheme. Gently inclined areas ( $<5^\circ$ ) are displayed in blue to green colors, steeper-inclined areas ( $>5^\circ$ ) in yellow to red colors. Samples for U-Pb dating are marked by white dots, samples for cosmogenic radionuclide dating with red rhombs. Black dashed lines are lineaments inferred to be faults. Flat surfaces of the basin fill strata cover expansive parts of the study area and are only occasionally interrupted by basement outcrops. Deep canyon incision along the major river system takes place along the borders of these surfaces. In the central to western section of the southern study area, around the area of Yavi, well defined, parallel lineaments cut through the low-slope surfaces. In the western section, between Tafna and La Quiaca, these surfaces are covered by alluvial fan sediments. An elevation profile (A-A') displays the morphology in Figure 13.

is interrupted by various N-S-oriented, post-depositional asymmetric ridges and vertical steps that may have been caused by faulting.

In the central sectors of the study area, the gentle slopes of the basin-fill units merge with the steep slopes of the canyons that are adjusted to the major drainage network of the Río Pilcomayo. The slopes of these canyons often reach values of more than  $25^\circ$ , indicated by

dark orange to red colors (Figure 12). Erosion has beveled the valley bottom to elevations of approximately 2700 m in the central sectors of the study area and to about 2300 m a.s.l. farther downstream in the northern sector of the study area. The relief between the highest peaks of the basement ranges and the bottom of the river valleys reaches 2000 m.

## 3.2 Depositional and exposure ages

### 3.2.1 U-Pb ages

14 samples of volcanic ash layers were collected from the basin-fill units at different levels within the stratigraphic sections. Dating of the zircon grains extracted from the volcanic ashes resulted in ages spanning late Miocene to Pliocene. The youngest populations measured, indicating the minimum depositional age, are limited and include two single-grain ages. In the western part of the study area, the ages range from  $6.83 \pm 0.05$  Ma within the faulted strata of the Tafna Formation to  $2.86 \pm 0.02$  Ma in the distal part of the alluvial fan deposits forming the foothills of the Sierra de Escaya. In the East, around the area of Yavi and Sansana, the ages of samples taken from different layers interbedded into the valley fill units, range from  $8.23 \pm 0.05$  Ma to  $3.05 \pm 0.07$  Ma east of the Siete Hermanos range. A small lens of volcanic deposits within tilted gravels that probably originated from this range was dated at  $6.59 \pm 0.07$  Ma.

**Table 1:** Summary of U-Pb age constraints from the different volcanic ash samples. Grey samples are from the sector west of La Quiaca, associated to the Tafna Formation and the superimposed alluvial fan deposits. Samples Arg21-xx (except Arg21-Ash03) were taken from the sector east of La Quiaca. All errors are 2 $\sigma$ .

Sample	Lat (°)	Lon (°)	Elev. (m)	Age (Ma)	Error (Ma)	MSWD	Grains
Arg19-04	-22.1182	-65.7088	3528	3.86	0.09	-	1/40
Arg19-05	-22.1316	-65.7440	3592	5.74	0.09	2.13	3/40
Arg19-06	-22.1428	-65.4810	3526	6.59	0.07	2.10	10/40
Arg19-Ash01	-22.1316	-65.6297	3428	2.86	0.02	0.16	3/40
Arg19-Car01	-22.1270	-65.7059	3573	6.83	0.05	1.67	17/40
Arg21-Ash01	-22.1407	-65.4504	3525	6.45	0.04	1.53	6/50
Arg21-Ash02	-22.1407	-65.4504	3525	6.71	0.04	1.53	12/50
Arg21-Ash03	-22.1269	-65.7057	3571	6.06	0.05	1.76	8/51
Arg21-Ash04	-22.1358	-65.4539	3498	7.40	0.04	1.80	22/50
Arg21-Ash05	-22.1414	-65.4472	3570	3.05	0.07	-	1/40

Arg21-Ash06	-22.1044	-65.4352	3493	8.23	0.05	1.88	22/50
Arg21-Ash07	-22.1138	-65.4358	3479	7.75	0.06	2.03	12/50
Arg21-Ash08	-22.1153	-65.5692	3504	4.47	0.02	0.22	3/50
Arg21-Ash09	-22.1203	-65.5699	3465	7.19	0.04	1.96	29/50

### 3.2.2 Exposure ages

#### *Isotope concentrations*

Isotope concentrations of the different sample sites were determined using the approach described in chapter 2.1.4. The isotope concentrations are displayed in Table 2. The  $^{10}\text{Be}$  concentration of the upper surface level S1 is  $48.34 \pm 0.968 \times 10^6$  at/g. (The other isotope systems were not measured for this site due to material loss.) The  $^{10}\text{Be}$  concentration from the lower surface level S2 is significantly reduced, and in the order of  $32.19 \pm 0.69 \times 10^6$  at/g. The concentrations for  $^{26}\text{Al}$  and  $^{21}\text{Ne}$  are  $163.94 \pm 2.93 \times 10^6$  at/g and  $191.0 \pm 8.8 \times 10^6$  at/g, respectively. Concentrations of the associated depth profile decrease with depth for all three isotope systems as shielding and attenuation increase. The only outlier is the  $^{26}\text{Al}$  from 5 cm below the surface, whose concentration is slightly higher than the surface concentration, but still agrees within error bounds.

**Table 2:** Summary of the measured nuclide concentrations of  $^{10}\text{Be}$ ,  $^{26}\text{Al}$  and  $^{21}\text{Ne}$ .

Sample name	Depth below surface (cm)		Shielding factor	Nuclide concentrations in quartz		
	Top	Bottom		$^{10}\text{Be}$ ( $10^6$ at/g)	$^{26}\text{Al}$ ( $10^6$ at/g)	$^{21}\text{Ne}$ ( $10^6$ at/g)
<b><i>Upper surface level S1</i></b>						
Cos001	0	3	0.99	$48.34 \pm 0.968$	-	-
<b><i>Open gravel pit / Lower surface level S2</i></b>						
surf	0	3	0.99	$32.19 \pm 0.69$	$163.94 \pm 2.93$	$191.0 \pm 8.8$
surf-5	5	15	0.97	$27.43 \pm 0.67$	$166.97 \pm 2.94$	$177.3 \pm 6.7$
surf-190	180	200	0.30	$12.44 \pm 0.27$	-	$83.4 \pm 3.3$
surf-280	270	290	0.17	$7.99 \pm 0.38$	$33.51 \pm 0.71$	$70.3 \pm 2.8$
surf-340	330	350	0.12	$5.61 \pm 0.12$	$26.30 \pm 0.57$	$61.7 \pm 2.6$
surf-410	400	420	0.08	$2.98 \pm 0.07$	$8.13 \pm 0.22$	$45.1 \pm 2.0$

#### *Isotope ratios and burial signal*

The measured, uncorrected concentrations of the three-nuclide series of the samples taken

from lower surface level S2 were plotted in  $^{26}\text{Al}/^{10}\text{Be}$ - $^{10}\text{Be}$  space and  $^{21}\text{Ne}/^{10}\text{Be}$ - $^{10}\text{Be}$  space, respectively (Figure 13 and Figure 14). The surface sample ‘Surf’ and the near-surface sample ‘Surf-5’ plot within the ‘steady-state erosion island’. This implies no burial signal for the upper two samples. The deeper samples, however, follow a distinct burial path that correlates with the deposition rate of the sediments, that is approximately 1-2 m/Ma for the  $^{21}\text{Ne}/^{10}\text{Be}$  nuclide pair (Figure 14). The ratios of the  $^{26}\text{Al}$  and  $^{10}\text{Be}$  surface sample also plot in the steady state erosion island, whereas the near surface sample (Surf-5) plots within the ‘forbidden zone’, outside of what can be realistically produced. Also, the burial path of the lower samples is not as linear as the one for the  $^{21}\text{Ne}$  and  $^{10}\text{Be}$  ratios but also in a range of 1-3 m/Ma (Figure 13). The deviation of the measured surface ratios with respect to the production-rate ratios is due to long-time exposure approaching a secular equilibrium, as seen in the plot by the curvature of the zero-erosion and steady-state erosion concentration lines (solid and dashed black lines in Figure 13 and Figure 14). The ratios of  $^{26}\text{Al}$  and  $^{10}\text{Be}$  follow a comparable pattern, only the sample ‘Surf-5’ plotting within the forbidden zone indicates that the measured concentrations of  $^{26}\text{Al}$  for this sample might not be correct. The

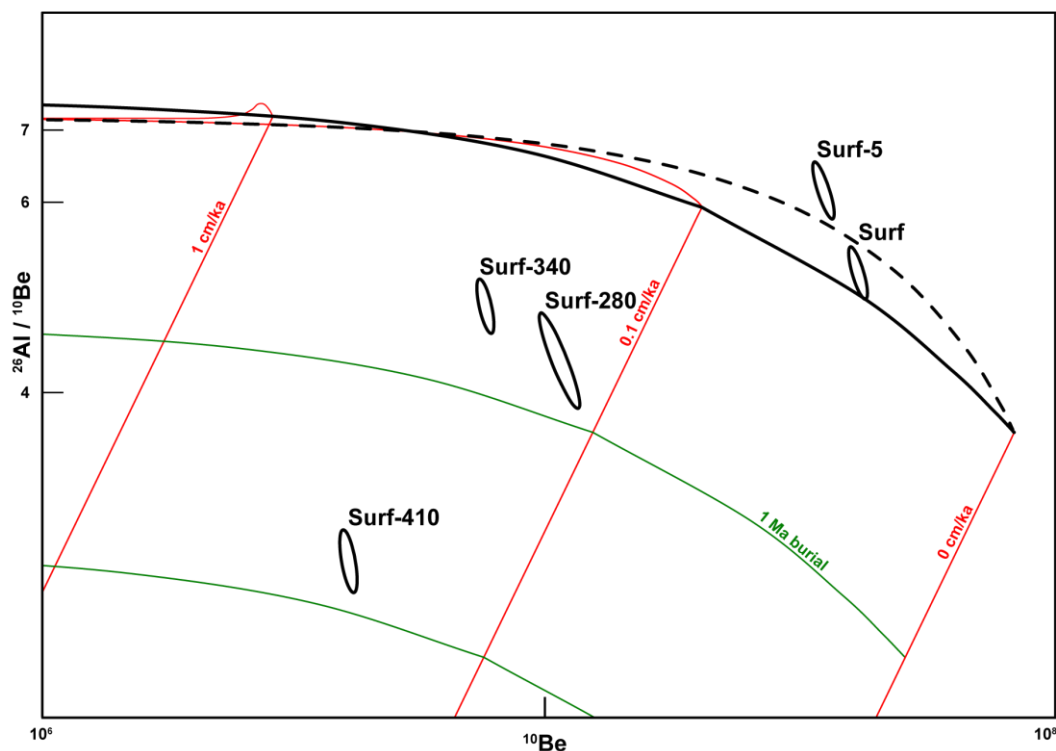


**Figure 13:** Two-isotope plot showing  $^{10}\text{Be}$  concentration in at/g vs  $^{26}\text{Al}$ - $^{10}\text{Be}$  ratios of the measured concentrations. The dashed black line follows a zero-erosion pathway, while the solid black line marks the steady-state erosion pathway. Red lines indicate different erosion pathways as noted along the line. Green lines show burial timeframes. Note that the surface sample plots within the steady-state erosion island, indicating no burial of the surface sample. The sample slightly below the surface plots in the forbidden zone, possibly due to the relatively high Al-concentration. Subsurface samples plot within the zones of burial.

surface sample, however, does not show a burial signal. Again, decreasing ratios are due to the prolonged exposure time of the material. The deeper samples of the  $^{26}\text{Al}$  and  $^{10}\text{Be}$  series do not follow a clear burial path as displayed by the  $^{21}\text{Ne}$  and  $^{10}\text{Be}$ -series.

### *Uncorrected exposure ages*

The single, uncorrected  $^{10}\text{Be}$  exposure age of the upper surface level S1 is  $2.944 \pm 0.149$  Ma (Table 2, Table 3 and chapter 2.1.4). The exposure ages associated with the calculated isotope concentrations for the lower surface level S2 are  $1.518 \pm 0.069$  Ma for  $^{21}\text{Ne}$ ,  $1.602 \pm 0.053$  Ma for  $^{10}\text{Be}$  and  $1.694 \pm 0.079$  Ma for  $^{26}\text{Al}$  (Table 2, Table 3 and chapter 2.1.4).

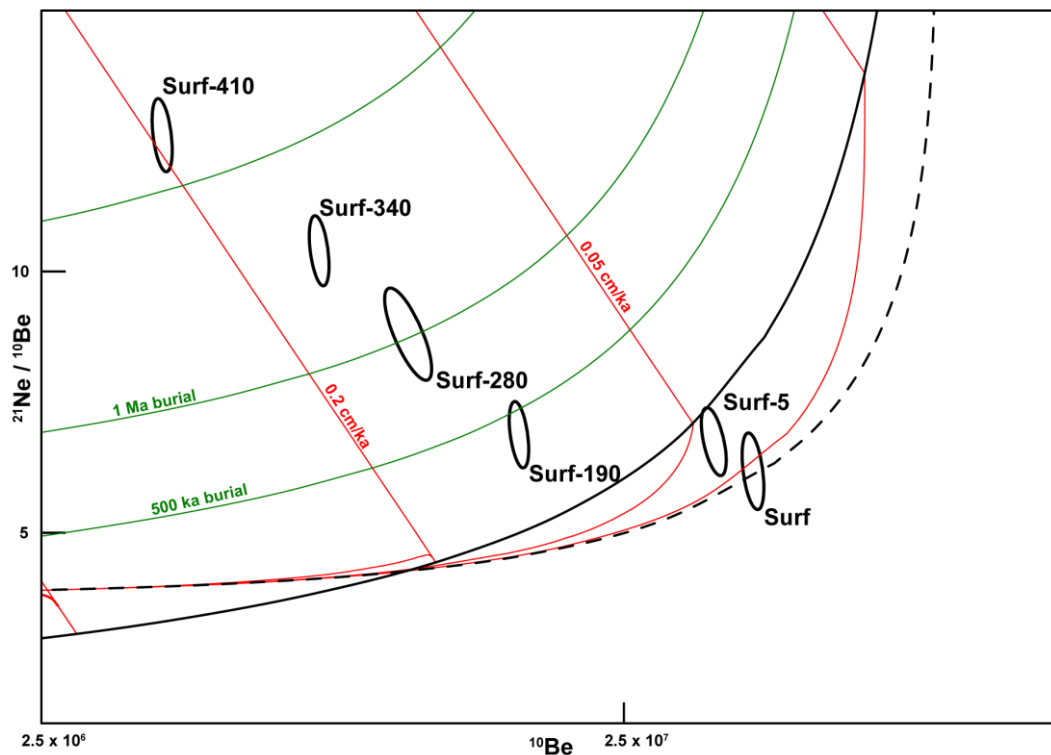


**Figure 14:** Two-isotope plot showing  $^{10}\text{Be}$  concentration in at/g vs  $^{21}\text{Ne}$ - $^{10}\text{Be}$  ratios of the measured concentrations. The dashed black line follows a zero-erosion pathway, while the solid black line marks the steady-state erosion pathway. Red lines indicate different erosion pathways as noted along the line. Green lines show burial timeframes. Note that both, the surface and subsurface samples plot within the steady-state erosion island, indicating no burial. The subsurface samples follow an almost linear path into zones of burial.

As these ages still include the inherited isotope concentration and are calculated without any erosion-rate estimates, they do not reflect the absolute exposure age of the surfaces but are rather overestimated, preliminary values.

***Inheritance correction***

The depth profile was primarily sampled for an inheritance correction of the surface concentrations. However, theoretical concentrations at depth, calculated using the surface concentration and empirical parameters do not match all measured  $^{21}\text{Ne}$  concentrations. For a depth profile following the measured surface concentration of  $^{21}\text{Ne}$  and using a common bulk density of  $1.8 \text{ g/cm}^3$  combined with an attenuation length of  $160 \text{ g/cm}^2$ , the inherited concentration would be  $58 \pm 10 \times 10^6 \text{ at/g}$ , exceeding the concentration of the deepest sample (Figure 15a). The associated surface concentration would be  $130 \pm 12 \times 10^6 \text{ at/g}$ . Applying a  $\chi^2$ -inversion of the data, the best fit parameters delivered an unrealistically low-density value of  $\sim 1 \text{ g/cm}^3$ . This profile would fit all the measured concentrations within error boundaries (Figure 15b). The associated inherited concentration would be  $40 \pm 13 \times 10^6 \text{ at/g}$  and the surface concentrations  $146 \pm 13 \times 10^6 \text{ at/g}$ , respectively. Although the inherited concentration of the  $\chi^2$ -inversion fits the deepest samples' concentration of  $45.1 \pm 2.0 \times 10^6 \text{ at/g}$  within error boundaries, the value cannot be trusted due to the abnormally low bulk density. Hence, the unequal distribution of concentrations at depth might be the result of a non-uniform depositional history. Accordingly, a precise inheritance correction

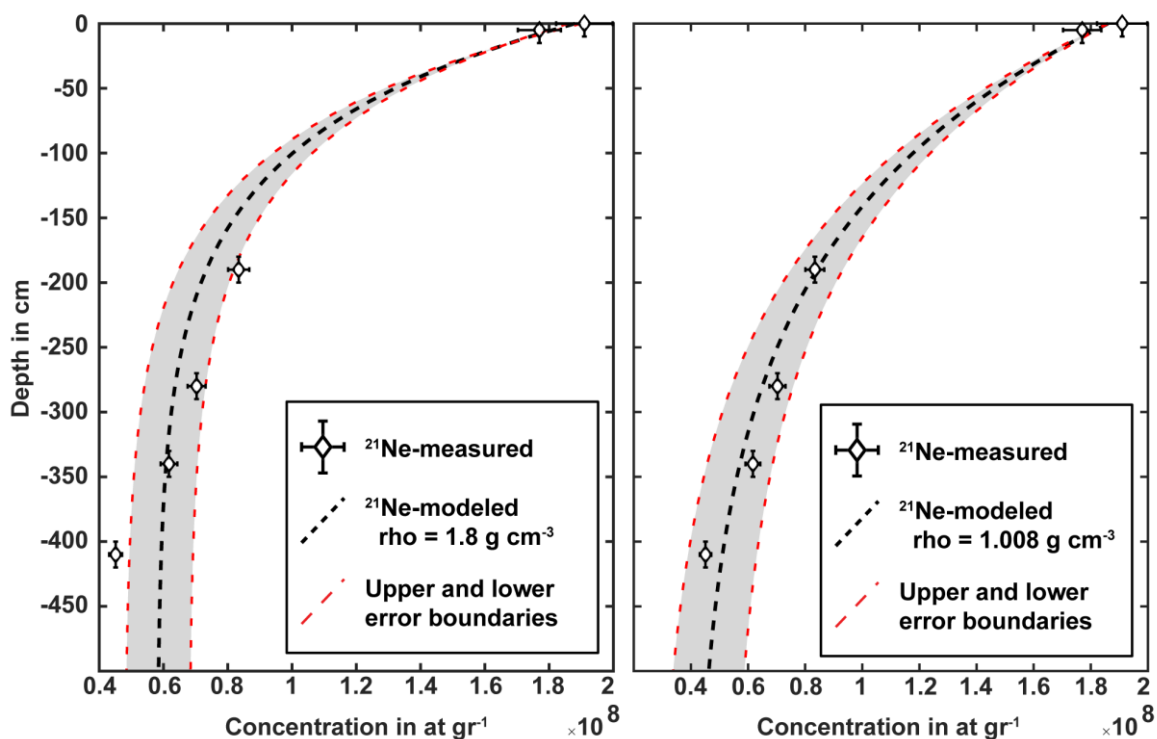


**Figure 15:** Modeled (dashed lines) and measured (prisms)  $^{21}\text{Ne}$  concentrations. **a)** Modeled concentrations based on empirical parameters. **b)** Modeled concentrations using best-fit parameters following a  $\chi^2$ -inversion. A fit of the complete depth profile was achieved with an unrealistically low bulk density of  $1.008 \text{ g/cm}^3$ . A depth profile using empirical values did not fit the measured data at depth.

could not be accomplished, which is why the  $^{21}\text{Ne}$  concentration of the lowest sample in the profile was assumed to reflect the inherited concentrations and was therefore used for a simplified inheritance correction.

Scaling the  $^{10}\text{Be}$  and  $^{26}\text{Al}$  inherited concentrations based on the concentration of the deepest  $^{21}\text{Ne}$  sample and applying an iterative decay correction delivered inheritance values of  $5.731 \times 10^6$  at/g for  $^{10}\text{Be}$  and  $20.97 \times 10^6$  at/g for  $^{26}\text{Al}$ . Correcting the measured surface concentrations from the lower surface with these values delivered concentrations of  $26.469 \times 10^6$  at/g for  $^{10}\text{Be}$  and  $142.927 \times 10^6$  at/g for  $^{26}\text{Al}$ . Subtracting the inherited concentrations from the deeper samples of the profile partly generates negative values, indicating that this approach overestimates the inherited concentration.

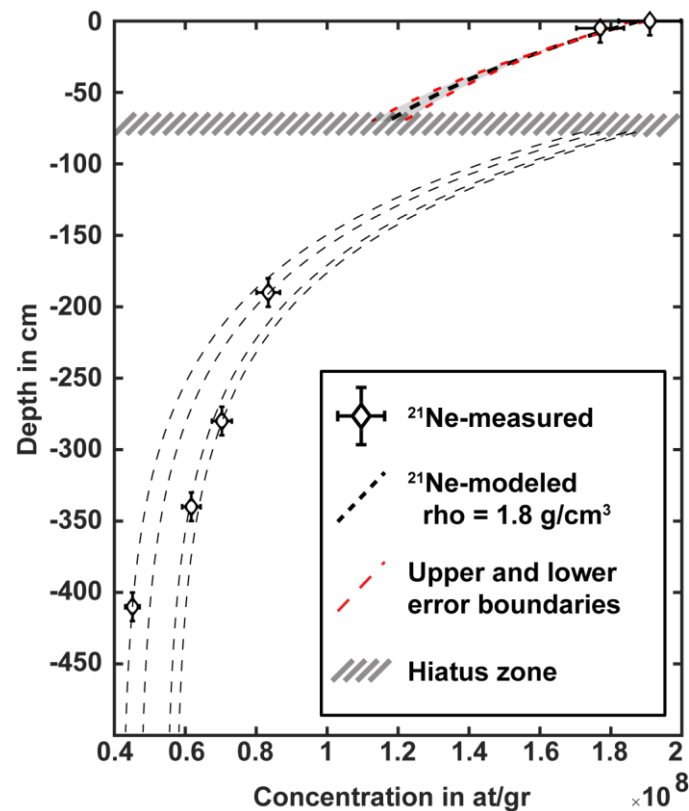


**Figure 16:** Modeled depth profiles for the surface sample up to the observed hiatus zone, formed by a major erosional contact in the depth profile (see Figure 5). Modeled concentration curves for each sample at depth (thin black dashed line) indicate no correlation between the upper and lower samples as well as in between each sample at depth. Only the sample at 280 and 340 cm depth seem to fit on the same concentration curves within error. Non-correlating concentration-curves imply that the deposition of the sampled layers did not progress in a continuous way but was rather interrupted by phases of erosion and soil formation. This conclusion implies that depth-profile based inheritance concentration delivers values of unknown uncertainty.

### **Erosion rates**

The erosion-rate thresholds, i.e., the critical surface rejuvenating rates under which the measured surface concentrations could be generated within the timeframe since the deposition of the youngest and closest zircon grain (3.05 Ma) are 0.47 m/Ma for  $^{21}\text{Ne}$ , 0.29 m/Ma for  $^{10}\text{Be}$  and 0.18 m/Ma for  $^{26}\text{Al}$ . The erosion rates for the inheritance-corrected concentrations are 0.69 m/Ma for  $^{21}\text{Ne}$ , 0.49 m/Ma for  $^{10}\text{Be}$  and 0.34 m/Ma for  $^{26}\text{Al}$  (Figure 17). Under the influence of higher erosion rates, the time since the deposition of the

material, based on the shallowest zircon age, would not be sufficient to accumulate the measured surface concentrations of CRNs. As all concentrations were measured on the same samples, erosion rates should be consistent between the three isotope systems. This implies that the lowest possible value would set the erosion threshold for the sample site, which is 0.18 m/Ma for the measured concentrations following the  $^{26}\text{Al}$  calculations and 0.34 m/Ma for the inheritance-corrected ages following the  $^{26}\text{Al}$  calculations (Figure 17).

### ***Inheritance-corrected surface exposure ages***

Calculating the ages of the inheritance-corrected surface exposure ages without the influence of erosion provided ages of  $1.16 \pm 0.07$  Ma for  $^{21}\text{Ne}$ ,  $1.21 \pm 0.05$  Ma for  $^{10}\text{Be}$  and  $1.25 \pm 0.08$  Ma for  $^{26}\text{Al}$ , all of them agreeing within error boundaries. Assuming a similar inherited concentration for the upper surface level S1 results in an exposure age of  $2.55 \pm 0.20$  Ma. As the effect of erosion has been widely disregarded in the previous calculations, the exposure ages should be viewed as minimum exposure ages that would increase with higher erosion rates up to the calculated erosion threshold. As for the uncorrected concentrations, the ages calculated with the  $^{21}\text{Ne}$  isotope concentrations are younger than those based on  $^{10}\text{Be}$  and  $^{26}\text{Al}$ .

**Table 3:** Calculated measured and inheritance corrected exposure ages of the two different surface levels in Ma. Note the corrected ages agreeing within error bounds.

Sample	Uncorrected exposure age			Inheritance corrected exposure age		
	[ $^{21}\text{Ne}$ ]	[ $^{10}\text{Be}$ ]	[ $^{26}\text{Al}$ ]	[ $^{21}\text{Ne}$ ]	[ $^{10}\text{Be}$ ]	[ $^{26}\text{Al}$ ]
<i>Upper surface level</i>		$2.94 \pm 0.15$			$2.55 \pm 0.20$	
<i>Lower surface level</i>	$1.51 \pm 0.07$	$1.60 \pm 0.05$	$1.69 \pm 0.08$	$1.16 \pm 0.14$	$1.21 \pm 0.08$	$1.25 \pm 0.1$

Ages calculated using calculators from various sources are displayed in Table 4. Due to different scaling models, base equations and scientific aims of the calculators, the results i) were partly calculated with an erosion-rate estimate (CRONUS-Earth - (Balco *et al.*, 2008; Borchers *et al.*, 2016; Marrero *et al.*, 2016), and ii) delivered erosion-rate estimates based on the measured concentrations (CosmoCalc – Vermeesch, 2007). In order to gain a more detailed information on the various applied scaling schemes implemented in these software solutions, please refer to the references within Vermeesch (2007) and Balco *et al.* (2008).

### 3.2 Depositional and exposure ages

**Table 4:** Calculated measured and inheritance corrected exposure ages of the two different surface levels in Ma using CRONUS-Earth calculator.

CRONUS-Earth						
	Uncorrected exposure age			Exposure age assumed erosion of 0.1 m/Ma		
	[ <sup>21</sup> Ne]	[ <sup>10</sup> Be]	[ <sup>26</sup> Al]	[ <sup>21</sup> Ne]	[ <sup>10</sup> Be]	[ <sup>26</sup> Al]
<b>st scaling</b>						
<i>Upper surface level</i>		2.49 ± 0.11			4.43 ± 0.58	
<i>Lower surface level</i>	1.59 ± 0.07	1.45 ± 0.05	1.69 ± 0.08	1.85 ± 0.10	1.74 ± 0.08	2.52 ± 0.3
<b>lm scaling</b>						
<i>Upper surface level</i>		1.56 ± 0.05			1.93 ± 0.08	
<i>Lower surface level</i>	1.29 ± 0.06	1.04 ± 0.03	1.04 ± 0.03	1.46 ± 0.08	1.16 ± 0.04	1.19 ± 0.05
<b>lsd scaling</b>						
<i>Upper surface level</i>		1.63 ± 0.05			2.03 ± 0.09	
<i>Lower surface level</i>	1.24 ± 0.06	1.09 ± 0.04	1.09 ± 0.04	1.41 ± 0.07	1.21 ± 0.05	1.36 ± 0.06

**Table 5:** Calculated measured exposure ages in Ma and erosion rate estimates of the two different surface levels using CosmoCalc calculator.

CosmoCalc						
	Uncorrected exposure age			Calculated erosion rate in m/Ma		
	[ <sup>21</sup> Ne]	[ <sup>10</sup> Be]	[ <sup>26</sup> Al]	[ <sup>21</sup> Ne]	[ <sup>10</sup> Be]	[ <sup>26</sup> Al]
<b>lal scaling</b>						
<i>Upper surface level</i>		2.39 ± 0.06			0.13 ± 0.02	
<i>Lower surface level</i>	1.39 ± 0.13	1.38 ± 0.04	1.22 ± 0.03	0.4 ± 0.04	0.31 ± 0.2	0.26 ± 0.04
<b>stone scaling</b>						
<i>Upper surface level</i>		2.45 ± 0.06			0.13 ± 0.02	
<i>Lower surface level</i>	1.29 ± 0.06	1.40 ± 0.04	1.28 ± 0.03	0.43 ± 0.04	0.30 ± 0.02	0.24 ± 0.02
<b>dunai scaling</b>						
<i>Upper surface level</i>		2.69 ± 0.06			0.11 ± 0.02	
<i>Lower surface level</i>	1.47 ± 0.14	1.51 ± 0.05	1.41 ± 0.03	0.41 ± 0.04	0.27 ± 0.02	0.2 ± 0.02

### 3 Results

**Table 6:** Calculated measured exposure ages in Ma and erosion rate estimates of the two different surface levels using CREp online calculator ( $^{10}\text{Be}$  only).

CREp						
	Uncorrected exposure age			Calculated erosion rate in m/Ma		
	[ $^{21}\text{Ne}$ ]	[ $^{10}\text{Be}$ ]	[ $^{26}\text{Al}$ ]	[ $^{21}\text{Ne}$ ]	[ $^{10}\text{Be}$ ]	[ $^{26}\text{Al}$ ]
<b>lm scaling</b>						
<i>Upper surface level</i>		$2.39 \pm 0.06$			$0.13 \pm 0.02$	
<i>Lower surface level</i>		$1.35 \pm 0.04$			$0.31 \pm 0.02$	

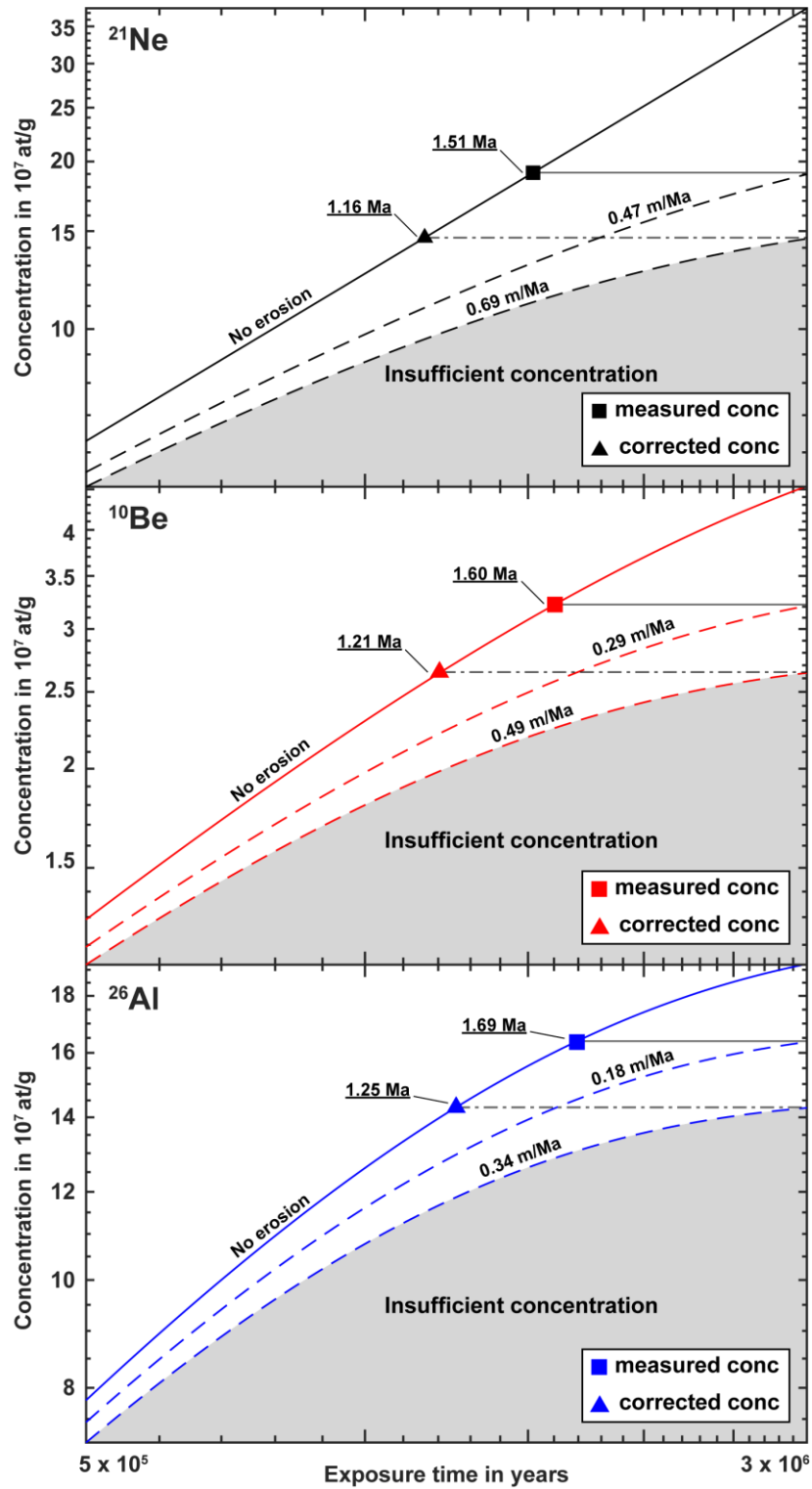


**Figure 17:** Calculations of erosion-rate thresholds and exposure ages of the lower surface level based on the measured and inheritance-corrected concentrations of the three different nuclide systems ( $^{21}\text{Ne}$  upper figure, black lines,  $^{10}\text{Be}$  central figure, red lines and  $^{26}\text{Al}$  lower figure, blue lines). Plots show exposure time in years against nuclide concentrations in  $\text{g}^{-1}$ . Results from the exposure-age calculations are plotted with squares for the measured data and triangles for inheritance-corrected data. Erosion-rate thresholds were calculated by solving equation 8 for the erosion rate with the depositional age of the closest U-Pb age (3.05 Ma) as the maximum exposure. Higher erosion rates would lead to concentrations that plot within the grey area of the plots, where the measured concentrations could not be reached, due to increased rejuvenation by critical erosion rate.

### 3.3 Fault morphology

Three distinct fault scarps were identified using remote-sensing techniques and analyzed in detail. The three studied faults are well expressed by clear morphological signatures in the landscape (Figure 18). These include a well-defined, N-S-oriented structure of approximately 30-40 km length at the eastern foothills of the Sierra de Escaya that is associated with the Pumahuasi Fault and two 10 (Sama West) to 13-km-long (Sama East), range parallel structures in the eastern and western foothills of the Cordillera de Sama. Due to the selected illumination direction and angle, east-facing escarpments appear darker, west facing escarpments on the other hand, appear brighter than their surroundings. These structures cut through the alluvial deposits of the piedmonts. Besides these major faults, no secondary splay faults can be identified in the vicinity of the structures. Additionally, a clear pattern of changing incision associated with channels on the alluvial fans clearly coincides with these faults. For example, channel depths are greater, and incision seems to be more effective on the distal sections of the faulted alluvial fans, reflected by a stronger topographic effect on the hillshade. Similar observations can be made on the slope maps. Low-slope areas are colored in red to yellow and mark the areas of the low-gradient alluvial fan surfaces. Distinct breaks in slope coincide with the location of the faults. Moreover, the distal surfaces are more dissected by channels and show a stronger overprint of fluvial incision, whereas the proximal surfaces are very gently inclined with slopes of less than 5°.

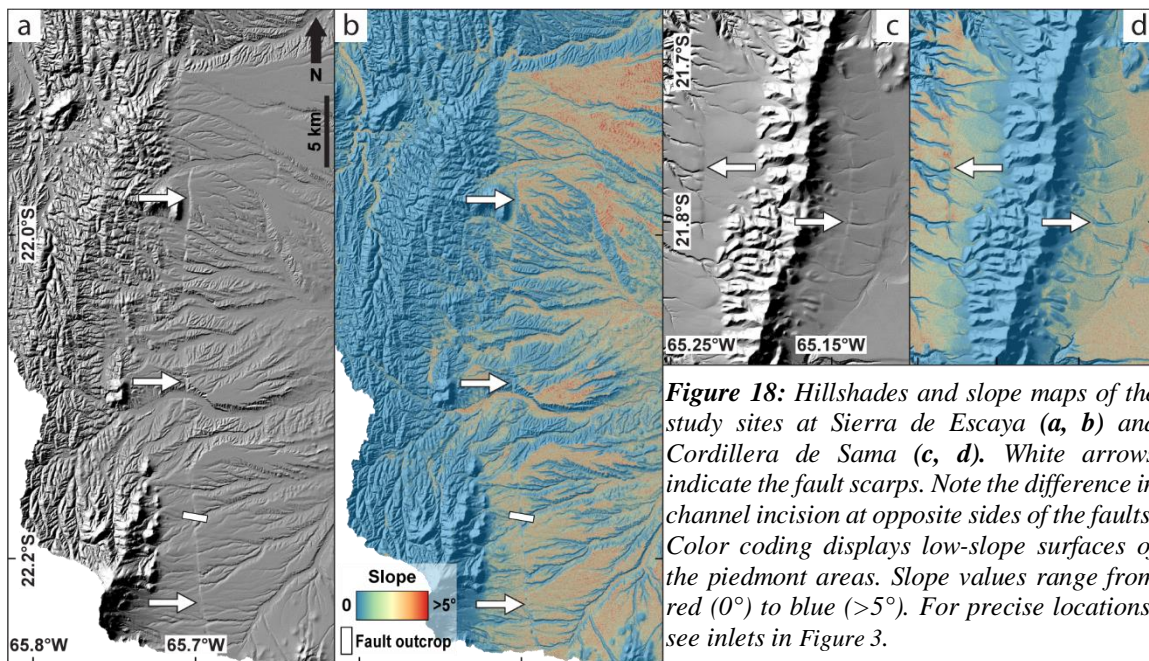


**Figure 18:** Hillshades and slope maps of the study sites at Sierra de Escaya (a, b) and Cordillera de Sama (c, d). White arrows indicate the fault scarps. Note the difference in channel incision at opposite sides of the faults. Color coding displays low-slope surfaces of the piedmont areas. Slope values range from red (0°) to blue (>5°). For precise locations, see inlets in Figure 3.

## 3.4 Drainage-basin morphometries

### 3.4.1 Stream network

The fault-crossing streams, feeding the alluvial fans in the piedmonts of the two different ranges, show pronounced changes in drainage patterns and morphological features coinciding with the faults. The drainage pattern is dendritic to parallel associated to the horizontally layered sediments and elongated and sloping surface of the alluvial fans, respectively. Where the drainage network interacts with the resistant ridges formed by the fault scarps, the drainage pattern resembles a trellis drainage pattern (Schumm *et al.*, 2000). Channels bend, merge, and are occasionally disconnected from the drainage network in the proximal to central parts of the alluvial fans. At the Sierra de Escaya, channels were partly cut off by faulting that caused damming and deposition of fine-grained material in small ponds at the base of the fault scarp. Some channels however, were forced to merge at the

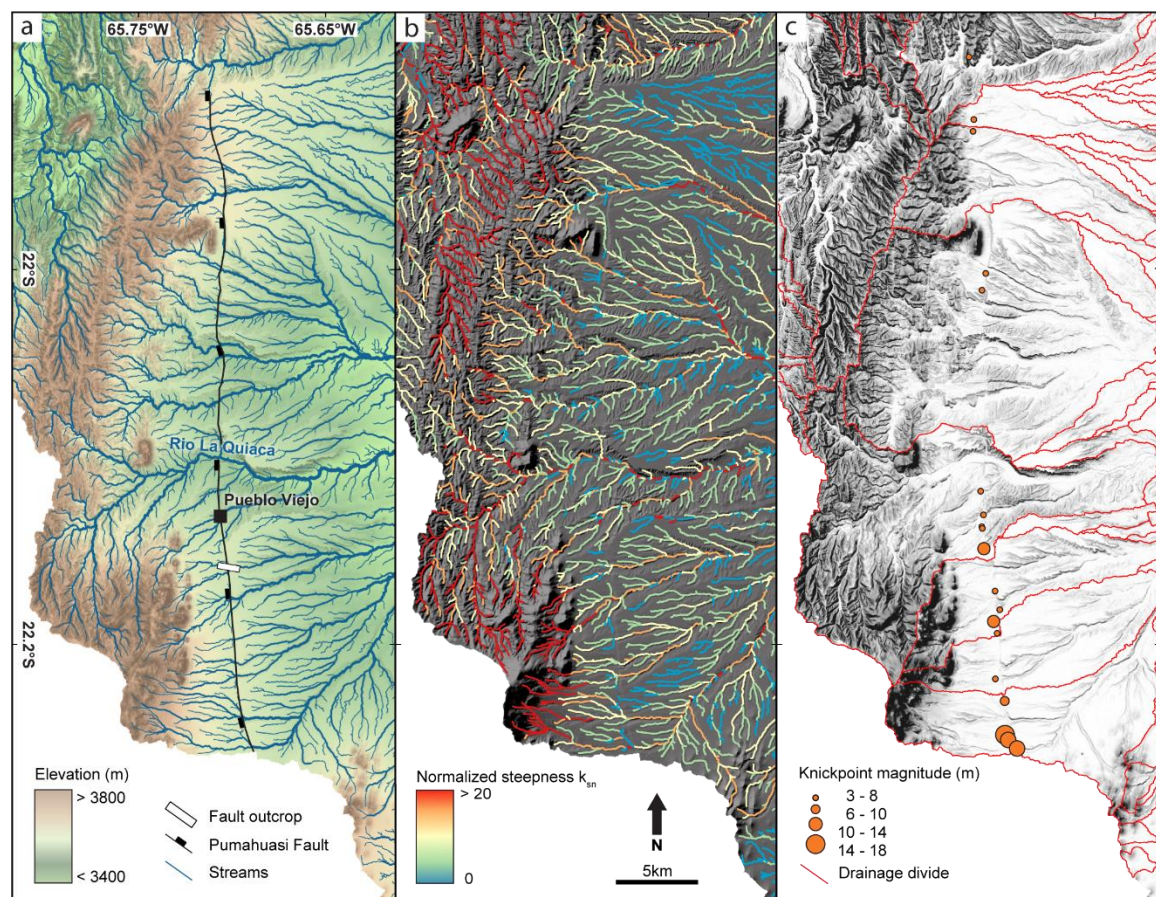


**Figure 19:** Drainage basin morphometric analysis of the Pumahuasi fault. **a)** Elevation (gradient), stream network (blue), flow accumulation (stroke width of streams) and fault (black). Drainage system and flow accumulation shows anomalies, coinciding with the fault. **b)** Normalized River steepness indices. High steepness in warm, low steepness in colder colors. Note the abrupt change in steepness at the intersection of the fault. **c)** Knickpoints (orange) and drainage divides (red). Knickpoints and laterally displaced drainage divides indicate vertical and lateral displacement along the fault.

fault scarp in order to create greater width and erosional power that enabled a maintenance of the drainage across the structure (Figure 19a and Figure 20a). Others seem to re-source at the highest elevated parts of the footwall and drain towards east, where they join the main drainage.

### 3.4.2 Normalized river-steepness index

Normalized river-steepness values, extracted from the stream networks of the two study sites, were draped over the hillshade and color-coded with a spectral color scheme. Reddish colors indicate high steepness, yellow denotes intermediate steepness, and blue marks low steepness.

In the Argentinean sector of the Pumahuasi Fault, variations in steepness indices match the location of the fault and the changes in fluvial channel morphology. Steepness decreases with increasing distance from the range, but abruptly increases as the channels approach the fault scarp. From this point westward, values steadily decrease again (Figure 19b).

The normalized river-steepness values at the Cordillera de Sama in Bolivia exhibit a comparable pattern. At the western flank of the range, a drastic increase in steepness values can be observed that coincides with the location of the fault. This behavior is less pronounced at the eastern flank. However, in this context it should be pointed out that the

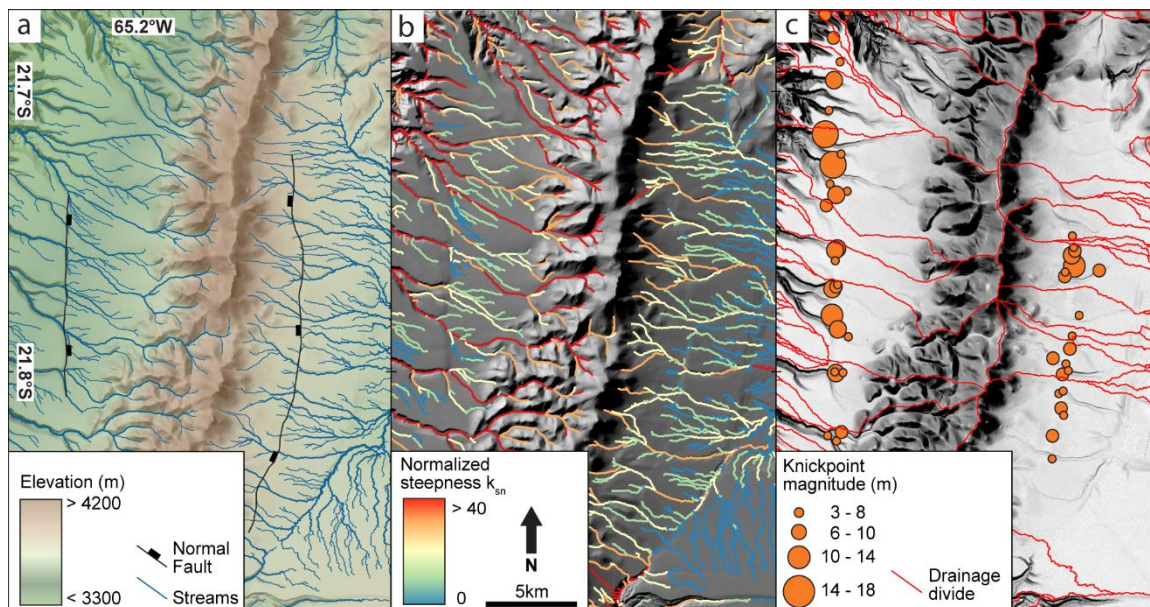


**Figure 20:** Drainage-basin morphometric analysis of the faults at Cordillera de Sama. **a)** Elevation (gradient), stream network (blue), flow accumulation (stroke width of streams) and fault (black). Drainage system and flow accumulation shows anomalies, coinciding with the fault. **b)** Normalized River steepness indices. High steepness in warm, low steepness in colder colors. Note the abrupt change in steepness at the intersection of the fault. **c)** Knickpoints (orange) and drainage divides (red). Knickpoints indicate vertical displacement along the fault. In contrast to the Pumahuasi Fault, lateral displacement is not expressed along the drainage divides.

streams of the western flank are bordered by a steep canyon that drains the high elevation surfaces in this area, whose erosive power might have a non-negligible influence on the channel slopes of the hanging wall. The eastern flank however drains into the endorheic ‘Laguna Grande Salar’, an flat plain of low hillslope gradients (Figure 20b).

### ***3.4.3 Drainage divides***

The analysis of drainage divides, in the area of the Sierra de Escaya provided a set of seven sub-basins that cross the Pumahuasi Fault and partly show lateral displacements where the drainage divides intersect the fault scarp (Figure 19c). Displacement values of the drainage divides are inconsistent along the fault and decrease from the center towards the tips. As such, offset values decrease from a maximum of ~1000 m in the central regions towards the southern tip of the structure to ~450 m. The central to northern section of the structure consists of less sub-basins, therefore less drainage divides, and hence less displacement is displayed. Drainage divides primarily show a sinistral sense of displacement. The drainage divides at the Cordillera de Sama do not show evidence of lateral displacements (Figure 20c).

### ***3.4.4 Knickpoints***

Knickpoint calculations revealed a large amount of knickpoints, distributed throughout the study area. Knickpoints that are not associated with the identified and validated tectonic structures are neither displayed nor discussed here. The majority of knickpoint magnitudes at the Pumahuasi Fault range between 3 and 6 m, only a small amount exceeds a magnitude of 10 m; these are the knickpoints that are closest to the laterally displaced drainage divides (Figure 19c). As observed in the case of the drainage divides, most data points are clustered around the southern sector of the fault.

Knickpoints at the Cordillera de Sama exhibit a comparable pattern, but with greater magnitudes at the western structure. Here, magnitudes tend to be in a range between 6 and 14 m. In contrast, on the eastern flank, magnitudes are smaller and range between 3 and 6 m (Figure 20c).

## **3.5 Fault scarp profiling**

Vertical separation and fault-scarp width values were measured for 39 selected profiles at the Pumahuasi Fault, for 15 profiles west of the Cordillera de Sama, and 11 profiles east of it. Coordinates and displacement values are listed in tables 1 to 3. Vertical displacement

values range between 2.7 and 43.5 m at the Pumahuasi Fault, 9.3 to 30.6 m at the western, and 4.9 to 26.5 m at the eastern side of the Cordillera de Sama. Several profiles show discontinuities at the base of the fault scarp that impacted the linear fit of the alluvial fan surfaces and thus lead to an overestimate of the vertical separation. Fault-scarp width is in the order of 53.2 to 262.4 m at the Pumahuasi Fault, 87.9-277.9 m at the western alluvial fans of the Cordillera de Sama and 4.9-26.5 m on the eastern alluvial fans. Profiles are numbered for each individual fan and site separately according to the alluvial fan numbering scheme in Figure 9. The average measured displacement value at the Pumahuasi Fault is 19.12 m with an exceptionally high standard deviation of 8.8 m. At the Cordillera de Sama West, the average displacement is around 18.9 m with a standard deviation of 6.5 m. On the eastern side of the Cordillera da Sama, the average displacement measured is 14.7 m, with a standard deviation of 6 m. In contrast, if displayed in boxplots, 75% of the data from the Pumahuasi Fault are between 12.9-26 m, with a median of 17.5 m, 75% of the data from the eastern side of the Cordillera de Sama range from 9.9-16.5 m with a median of 13.1 m and on the western side from 13.9-22.9 m with a median of 18.8 m (Figure 21).

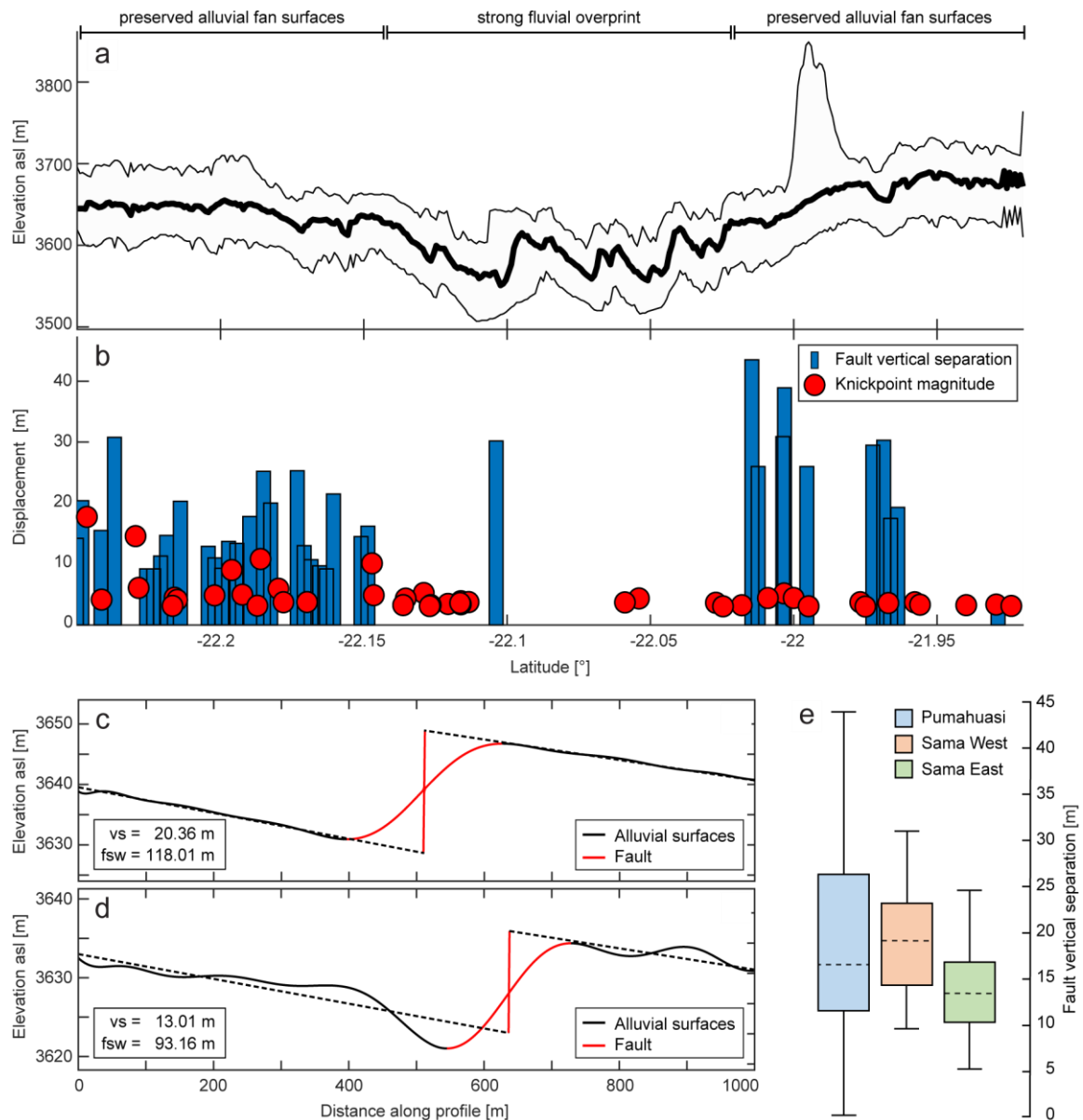


**Figure 21:** Data compilation from the fault-scarp measurements along the different faults. **a**) N-S directed swath profile along the Pumahuasi Fault crossing the different alluvial fan levels in the footwall. While the northern and southern sectors do show almost continuous elevations, the central sectors are incised by the drainage network. **b**) Vertical separation values of the alluvial fan surfaces (blue bars) and knickpoints (red circles) within the drainage network. Note the absence of knickpoints and useful vertical separation measurements in the central sectors coincide with the sectors of enhanced erosion by the major rivers. **c**) Exemplary ideal elevation profile for measuring the vertical separation (vs) and fault-scarp width (fsw) of the individual fan surfaces. **d**) Exemplary elevation profile resulting in overestimated vertical separation values due to fault-parallel incision of range draining river channels. Note how the linear fit (black dashed line) is diverted by the incision of the channel. **e**) Boxplot of the different vertical separation measurements along the three different faults. The values for the Pumahuasi Fault (blue boxplot) range between 12.9 and 26 m, with a median of 17.5 m, for the fault west of Cordillera de Sama (orange boxplot) from 13.9-22.9 m with a median of 18.8 m, and for the fault east of the Cordillera de Sama (green boxplot) from 9.9-16.5 m, with a median of 13.1 m. Notice that the 75% quartiles of the three different faults agree within error.

### 3.6 Pumahuasi Fault

This section summarizes the field observations made along the Pumahuasi Fault. Due to the abundance of ore deposits associated with the fault, mining around the central sectors of the fault generated open pits, enabling access to various vertical cuts perpendicular to the strike of the fault. Unfortunately, much of the ore-hosting fault plane was removed during the mining operations. The remaining outcrops that contain kinematic information are described here. In order to quantify the amount of displacement generated within said outcrops, a brief stratigraphic description is necessary to define viable piercing points for the offset measurements.

#### *3.6.1 Fault outcrop - Quebrada Cusco Ara*

A key outcrop along the main branch of the Pumahuasi Fault was found at its central section (for precise location, see Figure 19a), containing critical information about the kinematics of the structure (Figure 22).

##### *Debris flow deposits*

The lowermost unit exposed in the footwall comprises rhyolitic and andesitic clasts, deposited within a sandy matrix. Clasts vary in size from cm- to dm-scale, are of angular to sub-angular shape and poorly sorted. The overall appearance resembles a fanglomerate, formed by debris flows and subsequent fluvial transport processes. This unit is only exposed on the footwall of the faulted strata and pinches out towards the main fault F1.

##### *Flood plain deposits 1*

The coarse units at the base are followed by a beige to whitish, pervasively fractured, fine-grained sediment body that is comprised of sand, silt and clay. Insignificant amounts of mica can be found, and no signs of a volcanoclastic input exist. In contrast to the previous deposit, this unit stretches horizontally over the whole exposure of the outcrop and can be well-distinguished from the other units, therefore making it useful as displacement marker. It is vertically offset for a cumulative count of about  $100 \pm 10$  cm along F1 and F2. More precise offset estimates are difficult due to an erosional contact with the overlying unit. This undulating contact also displays various signs of soft-sediment deformation, such as load casts and clastic dikes. A prominent clastic dike is well expressed along F1, where associated deposits emerge sub-vertically toward the topsoil. Parallel, vertical shear planes can be recognized but due to the friable character of the material, no slickensides for

kinematic analysis were found. A zone of conglomerates and finer-grained deposits overlies this unit on the hanging-wall block, whereas on the footwall, superimposed with finer-grained sediments and thin conglomeratic lenses form a more pronounced and better-established contact. Due to the fine-grained character and beige color of these deposits, they resemble what has been described as the Tafna Formation, but, at this location, with a neglectable to non-existent amount of volcanoclastic input. As of these similarities, the depositional environment must have been a low-energy, fluvial environment, such as a flood plain.

### ***Conglomerates***

A two- to three-meter-thick layer of conglomeratic material with interbedded sand and silt layers covers the flood plain deposits in the hanging wall. On the footwall, these deposits are limited to thin lenses of 10-30 cm thickness. These matrix-supported conglomerates are built by poorly sorted sub-angular to angular clasts, that only show weak signs of imbrication. Clast sizes vary between 1 and 30 cm in diameter, larger components are mainly of igneous origin, while smaller components were derived from metapelitic sources. The lenses in the footwall contain smaller clasts with a more continuous grain-size distribution. The sudden increase in grain size and hence available transport energy compared to the deposits of the fluvial silt deposits indicate an environmental change in the source area, facilitating the deposition of these conglomerates.

### ***Flood plain deposits 2***

The flood plain deposits 2 resemble the flood plain deposits 1 but show a more distinct bedding due to grain-size variations. In addition, a slightly darker color and the effect of traversing joints create a different overall appearance. On the hanging wall, these deposits form lenses that are intercalated in the surrounding layers but become more continuous towards the fault zone. On the footwall the flood plain deposits 2 constitute a major part of the whole succession and only thin lenses of conglomerates are sub-horizontally intercalated into these deposits. Soft-sediment deformation in form of diapiric structures along F1 and F2 connect flood plain deposits 1 and 2. The top of this unit is well-defined by a transition to overlying alluvial fan deposits and serve as piercing points for offset measurements.

#### *Alluvial fan deposits*

Flat, angular metapelitic gravels of Acoite Formation in clast sizes of up to 10 cm and sporadically distributed larger igneous and quartzitic clasts of the Faja Eruptiva de la Puna Oriental dominate the youngest deposits underneath the topsoil. Since these formations are cropping out at the Sierra de Escaya, they must be derived from the West. Sorting of the material increases from west to east, from quite chaotic in the western section, to a fining-upward sequence atop the units close to F1. Along F1 this unit is offset for about 80 cm and additionally for 20-30 cm along F2. It pinches out towards the flood plain deposits 2 at the eastern border of the exposure. Due to their angular shape and comparably larger size, the components of these deposits appear to have traveled less than the conglomerates but must have been transported in a fluvial environment. They are part of alluvial fan deposits, sourced from the Sierra de Escaya.

#### *Colluvium*

A well-stratified sandy layer of less than 2 m width is located in the central section of the exposure, just underneath the topsoil, close to F1. The sands are horizontally discontinuous and appear to have filled a small depression in the stratigraphic column. Bioturbation features are present in the form of two burrow holes. This deposit could have been deposited within a pond that was formed due to fault activity that generated vertical displacement, hence it forms the colluvium of the fault scarp.

#### *F1*

The main fault zone F1 consists of a 30 to 40-cm-thick fault gouge of disaggregated sediments of the flood plain deposits 1 and 2 that extends from the lowest part of the exposure to the topsoil. Parallel, subvertical 'bedding' with an orientation of 304/83 (dip direction/dip angle) marks a steep westward dip of the almost N-S-striking fault. Except the topsoil, all units are offset along this fault, with the greatest offset of about 80 cm measured in the flood plain deposits 2.

#### *F2*

F2 is a synthetic fault to the main fault F1, separating the flood plain deposits 1 and 2 with a cumulative offset of 40-60 cm. The fault is less linear compared to the main fault, but dips westward and probably roots in the fault plane of F1. Above the unit of the flood plain deposits 1 the fault splays into three smaller branches, surrounding wedges of fault gouge. Splays propagate up to the topsoil.

***F?***

A possible secondary fault may exist two meters west of F1. No clear offsets, however, were identified at this branch, but sediment of the flood plain deposits 1 propagates upward through the conglomerates, where a small depression is situated that is also visible in the alluvial fan deposits. It is important to note that all exposed faults in the outcrop must be secondary synthetic structures with respect to a west-dipping normal fault with much greater offset. However, the fault scarp has been obliterated by degradation and the remaining structure is a fault-line scarp.

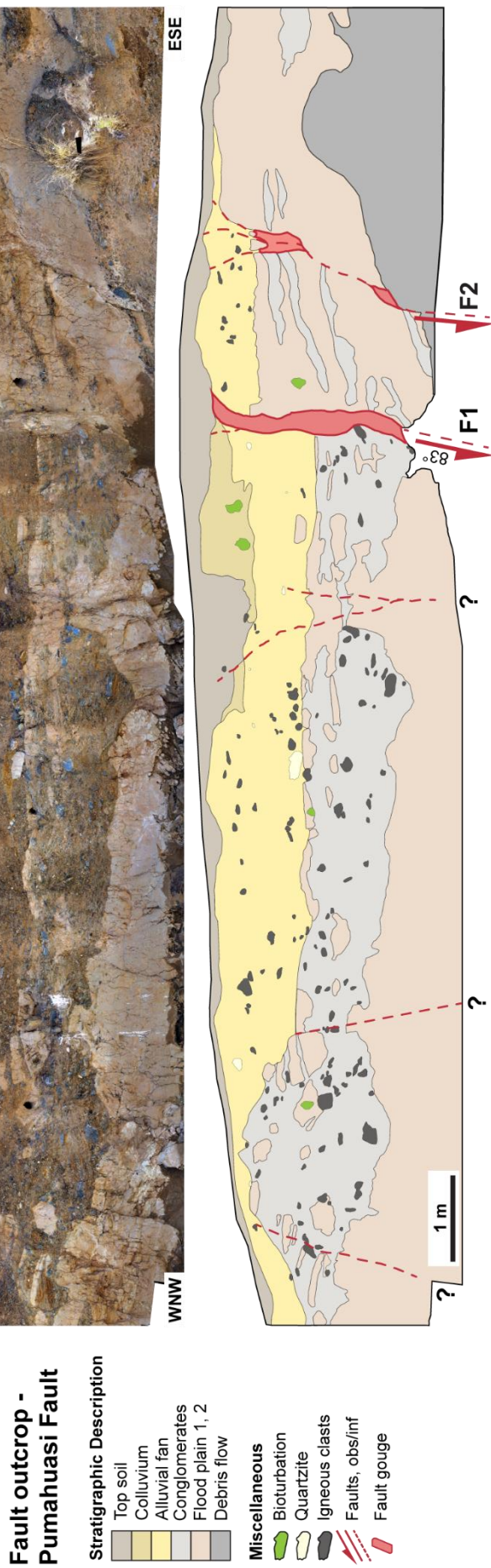


**Figure 22:** Photomosaic (upper Figure) and graphic log (lower figure) of a key outcrop at the Pumahuasi Fault. The outcrop stretches over a distance of approximately 14 m in WNW ESE direction and vertically for around 4 m. Vertical displacement was identified in the central to ESE part of the outcrop along two steeply westward-dipping faults (F1 and F2). Along the major fault F1, displacement values are on the order of 80-90 cm, as measured along the offset lacustrine deposits. Displacement along the synthetic fault F2 is on the order of 20-30 cm, measured within the same unit. The faults cut through the entire sedimentary succession, except for the topsoil. The outcrop can be subdivided into hanging wall (WNW part) and footwall (ENE part) along the major fault F1. While the footwall comprises a relatively continuous succession of sedimentary deposits, the hanging-wall deposits appear to have been overprinted by fluvial processes and display load casts, leading to the formation of a mixed zone between the lake deposits and the conglomerates. The contact between the two layers seems to be of erosive nature and parts of the lake deposits were subsequently injected into the conglomerates. The same process was observed along the main fault F1, where a 20-cm-thick layer sandy to silty deposits vertically injected into the sediment succession. Fractures indicated with a stippled line and question mark could be part of the fault activity. The major faults F1 and F2 are probably connected at depth as their dip points to the same origin. The principal fault responsible for the scarp must have been obliterated by scarp degradation and all visible faults in the outcrop must constitute synthetic secondary faults

### 3.6.2 Fault outcrop - La Cienega

Additional outcrops along the Pumahuasi Fault were found close to the settlement of Pueblo Viejo (Figure 19a). Evidence for faulting exists immediately along a roadcut, where an outcrop exposes vertically displaced local strata. A set of westward-dipping faults offsets the Tafna Formation for about 30-40 cm. The contact with the overlying alluvial deposits is erosional (Figure 23).

North of the road outcrop, many open pits from the mining operations along the Pumahuasi Fault were found. The main accumulation of the mined iron- and manganese-ore deposits coincides with the surface expression of the fault. Mining was carried out in hand-dug holes and trenches, which are still open today. Although these mining pits allow direct access to many cuts crossing the fault scarp, unambiguous signs of faulting are scarce in these pits because of the removal of ores. However, in some of these outcrops, dense sheets of ore

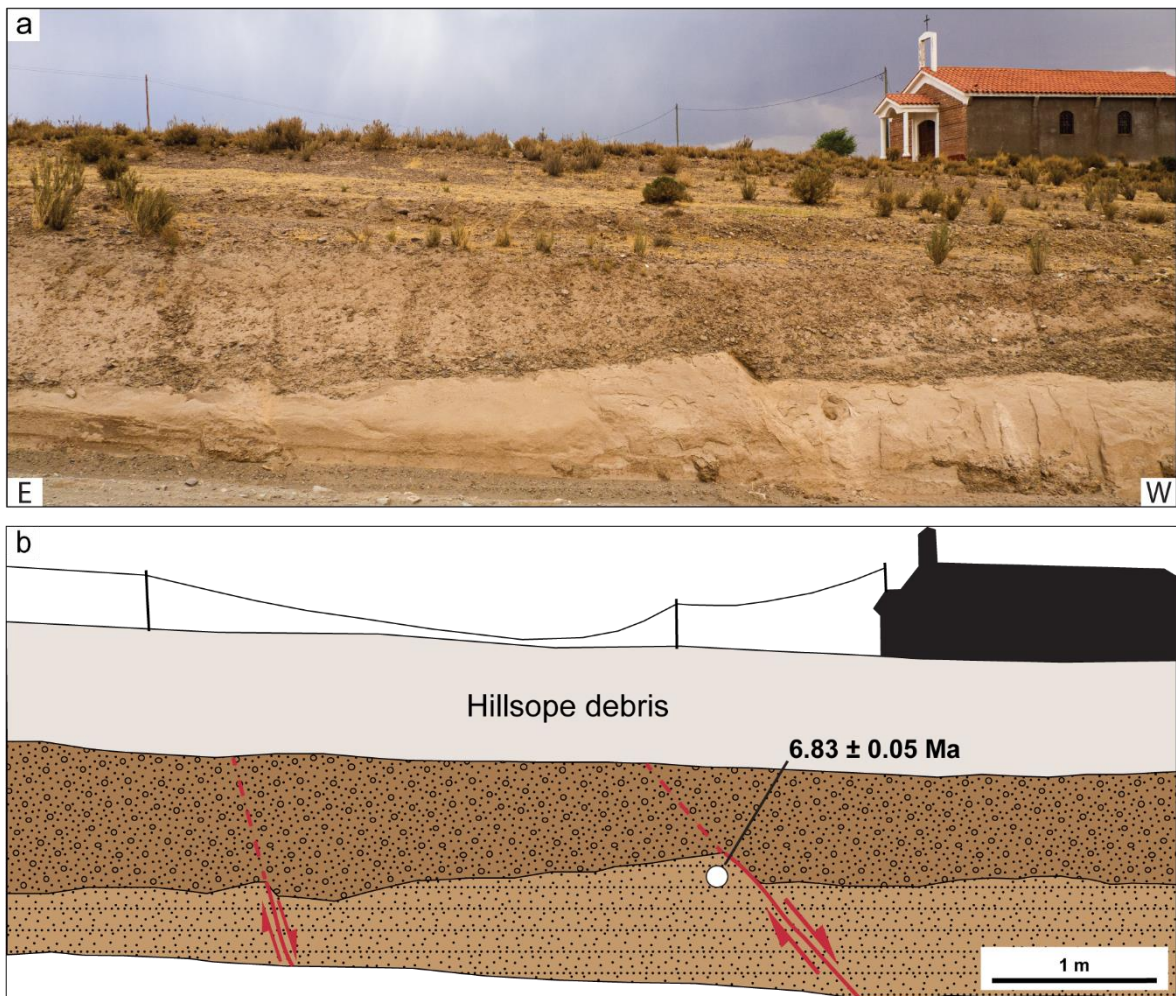


**Figure 23:** Road outcrop image (a) and sketch (b) close to the settlement of La Cienega, central section of the Pumahuasi Fault. Alluvial gravels cover fine-grained Tafna Formation deposits. Both units are faulted along two minor faults, steeply dipping westwards. The Tafna Formation at this section was dated at 6.83 Ma.

mineralization were found. Farther north, close to the Río La Quiaca, meter-thick, steeply westward dipping sheets of ore enriched sediment layers are exposed at subsurface level within the pits (Figure 24). The same material also crops out at the alluvial fan surface in form of hardened strips that follow a N-S trend (Figure 25a, b). These sheets comprise well-rounded to angular clasts of the surrounding alluvial fan gravels, cemented by an ore-bearing matrix. Structural measurements from the fault planes themselves presented in Figure 22 and Figure 23 are in good agreement with data of conjugated joints taken at the mineralized strips seen in Figure 25 and Figure 25b. As displayed in the stereoplot in Figure 24, all measured planes dip with around 80-90° towards WNW; the fault planes have a steeper dip angle than the indirect measurements of the secondary fault features expressed by the ore-bearing sediment sheets.



**Figure 24:** Subvertical and horizontal sheets of sediment layers cemented by ores. The subvertical layers mark the orientation of the fault plane. Dip directions and dips are plotted in equal area, lower hemisphere stereoplot, red lines denote measured fault planes as seen in Figure 23 and Figure 24, black lines show measurements taken at the ore-cemented sediment sheets and hardened strips cropping out at the surface of the alluvial fan deposits.

From aerial views it is noticeable that the ore-bearing sectors along the fault zone are accompanied by color variations at the surface. Deep brown to yellowish patches can be observed within the rust-brown alluvial fan deposits. Besides these fault-bounded sheet-like deposits in the upper alluvial fan strata, ore deposits were also found within the layers of the lacustrine to tuffaceous Tafna Formation. In the latter scenario, thin veins and nodules of apparently pure, dark ore mineralization stand out from the brighter surrounding deposits. The nodules have a radius of 10-20 cm, show a radial structure and columnar growth (Figure 25c). It should also be mentioned here that the clasts of the alluvial deposits have developed a coating of ore minerals. The concentration of these elements increases with depth and reaches a maximum where the Tafna Formation and the alluvial fan gravels meet. This contact is marked by a zone of high ore concentration that penetrates several centimeters into the finer grained deposits (Figure 25d). Ore concentrations decrease with

increasing distance from the fault and the river. A former kaolinite mine is located 3 km farther West on the hanging wall, close to the settlement of Tafna. This mine comprises a large open pit, where the contact of the Tafna Formation and the overlying alluvial fan deposits can be observed (Figure 25d, e). The contact between the two units shows a long-wavelength undulating erosional contact. The thickness of the Tafna Formation is in a range of 20-40 m (Figure 25e). The bedding of the layers within the formation is horizontal and does not show any signs of tilting. It should be noted that the concentration of the ore minerals is difficult to recognize at this point. Rust-colored alteration of the alluvial deposits and precipitates related to these zones can be observed close to the contact of the

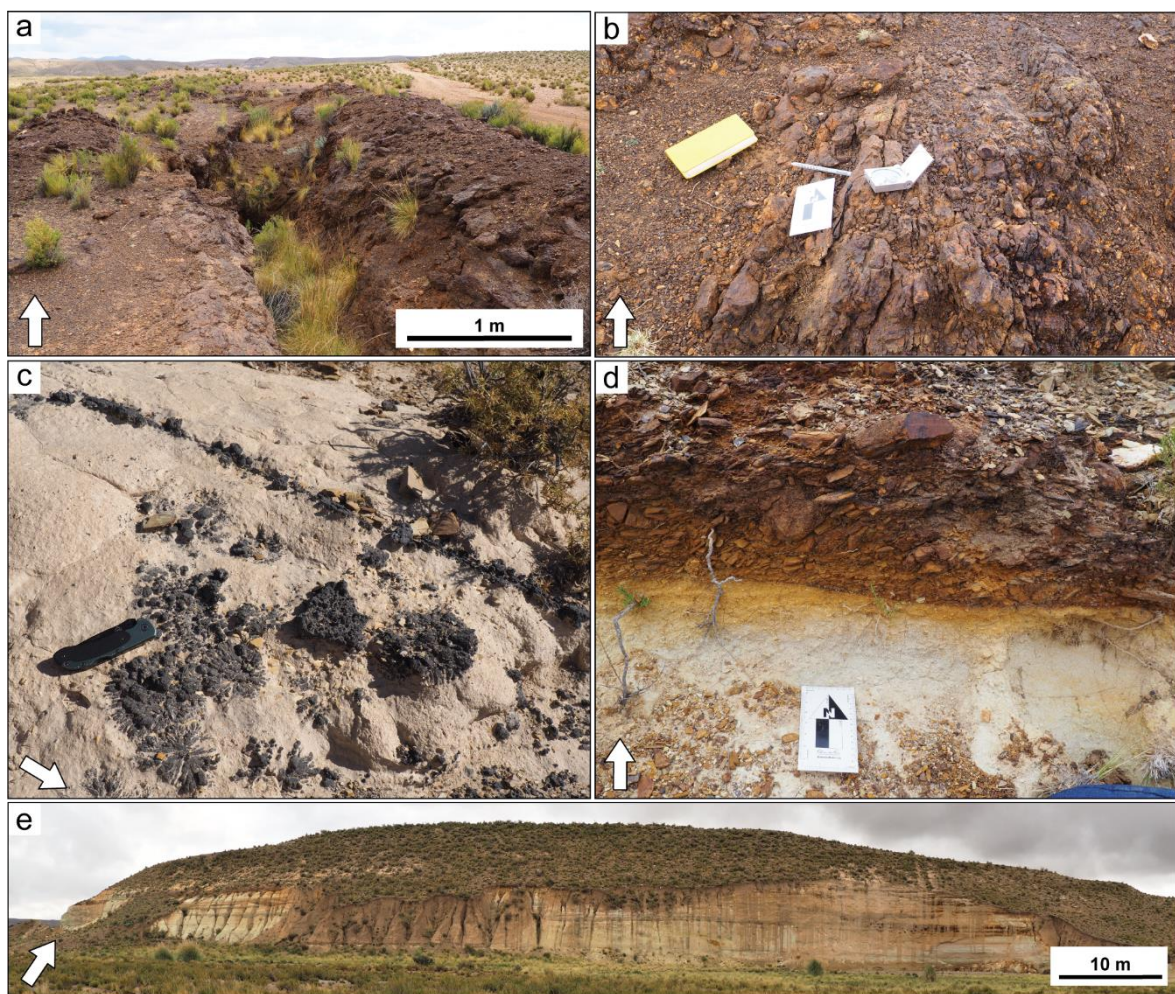


**Figure 25:** Outcrops of the manganese and iron-ore deposits of the former mines along the Pumahuasi Fault: **a)** open trench of former manganese mine. **b)** Alluvial fan surface with N-S-striking hardened strips of ore-cemented sediments. **c)** Ore nodules and veins within the Tafna Formation. Nodules show botryoidal texture and vary from spherical to prolate shapes. The buried parts appear rougher and denser. N-S-oriented veins are filled with the same material (knife for scale). **d)** Close-up of contact between the Tafna Formation and the alluvial deposits. Note the yellow coloration in the upper parts of the Tafna Formation, indicating Fe mobilization from the alluvial deposits and re-precipitation. **e)** Panorama view of the mined sediments at the Tafna quarry on the hanging wall of the fault. This formation comprises sands and tuffaceous layers of about 20-30 m thickness, overlain by alluvial fan gravels. The contact between the two units differs depending on location but can often be observed as an erosional contact.

two layers. Concretions, such as those found along the fault are absent. The great abundance of kaolinite within this formation is apparently closely related to an accumulation of volcanic ashes and subsequent chemical alteration.

### **3.7 Yavi Fault**

Unlike the other studied faults described above, the normal fault east of the village of Yavi does not show any prominent morphological surface features that indicate recent tectonic activity. Neither has this structure a measurable influence on the drainage system. The fault is expressed by distinct stratigraphic discontinuities exposed along a road outcrop below the surface of the upper surface level S1. Additional outcrops with exposures of normal faults affecting the same unit were found to the north and south of this site.

#### ***3.7.1 Yavi – Surface outcrop***

Following the road from Yavi eastward, just before reaching the top of the upper paleo-surface, a several hundred-meter-wide outcrop exposes the upper strata of the valley fill, which is pervasively fractured and affected by normal faults (Figure 26). The outcrop can be subdivided along a steeply westward-dipping normal fault into a western hanging wall and eastern footwall (Figure 26a, e , f). On the footwall, the lower section of the outcrop comprises beige to brownish sands of homogeneous grain size. Those deposits are overlain by another thin layer of light brownish to orange-colored sands. This prominent color contrast is useful as a piercing point for measuring vertical offsets. An approximately 1-m-thick, dark-brown conglomerate superimposes the sands, followed by a beige to pink-colored layer of conglomerates that onlap the darker conglomerates and that defines the top of the succession in the northern section of the outcrop. This layer strikingly resembles the deposits that were sampled for surface-exposure dating (chapter 2.1.4). A lens of volcanoclastics within this layer was dated at 3.05 Ma (Arg21-Ash05, see Table 1 and Figure 4). Prominent white patches are zones of CaCO<sub>3</sub> cementation and constitute pedogenic K-horizons. On the hanging wall, the succession is discontinuous: A compact dark grey deposit of finer grain size is deposited on top of the offset beige to brownish and orange-colored sands. The overall appearance of this layer resembles the upper outcrop at Sansana (see chapter 3.1.1). The brownish and skin-tone-colored conglomerates found on the footwall are missing.

The major displacement at this site can be found in the light brownish to orange-colored sands that are offset for approximately 5 m along a steeply westward-dipping fault zone in

the friable alluvial material (Figure 26a, e, f). Two additional minor offsets can be found around 5 m north of it, where the same deposits are step-wisely faulted with around 2 m of displacement along at least two faults that create an impression of a down-ward bending of the strata. South of the major fault, on the associated hanging wall, pervasive cracks and transgranular extension fractures in individual clasts are well expressed. One major extensional crack, with an opening width of around 10-20 cm, was found in the central section of the outcrop (Figure 26a, d, f), though this feature was not traceable into the subordinate layers. Moreover, two steeply westward dipping faults with small displacement values of only 10-30 cm were found in the southern section of the outcrop in the beige sand layers (Figure 26a, b, c, f).

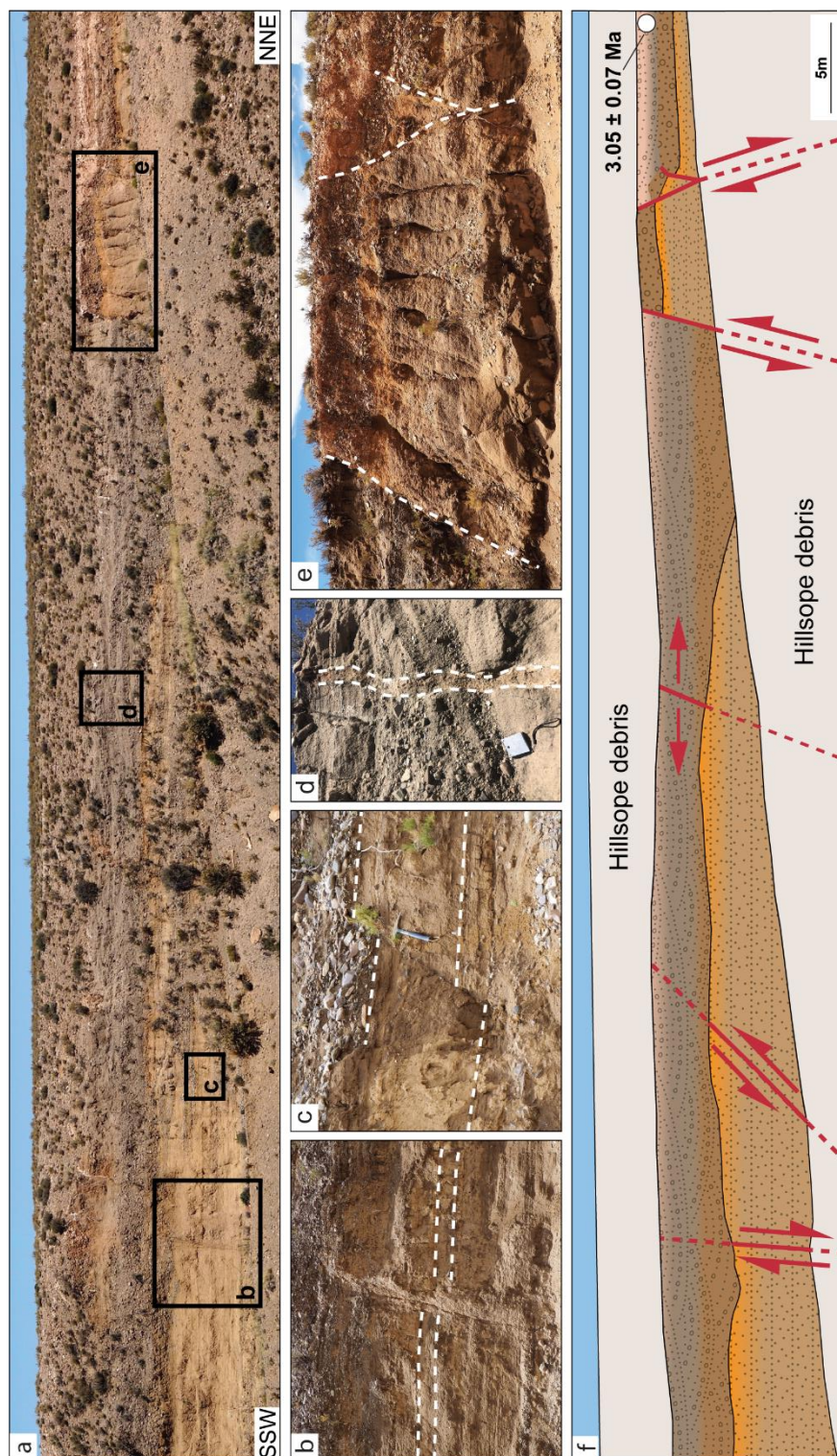


**Figure 26:** Fault outcrop of the road cut exposure east of Yavi. **a)** Panoramic view of the outcrop with the major westward-dipping normal fault in the NNE of the picture separating grey silt layers from brown sandy layers. Inlets marking the position of **b), c), d) and e),** Minor normal faults offsetting the beige to brownish sands in the southern section of the outcrop. **c)** Sediment-filled extensional joint in e dark silt and conglomerate layers. **d)** Main fault, offsetting orange to brownish sandy layers against dark grey silty layers step-wisely offsetting the sandy layers in the East. **f)** Simplified sketch of the outcrop exposing basin fill deposits (light brown layers), that are offset along several steeply westward dipping and one eastward-dipping normal fault in centimeter- to meter-scale. Superimposed layers differ on hanging wall (left in figure, SSW) and footwall (right in figure, NNE). The former exhibit dark grey layers which consist of an alternation of silty sands and conglomerates, well lithified and jointed, whereas the latter consist of skin-tone-colored conglomerates with accumulations of K-horizons.

### 3.7.2 Yavi - Sand pit

Around 700 meters south of the previous outcrop, a 50-m-deep gorge offers more detailed insights into the faulted stratigraphy. The exposed sediments mainly comprise sands in different tones of beige color with sporadically distributed intercalated thin beds of conglomerates and silts. The diagenesis of the sediments is weak and thus easily eroded. The fine-grained silt layers show closely spaced pervasive conjugated fracturing throughout the exposure. Well-defined faults exist midway through the stratigraphic

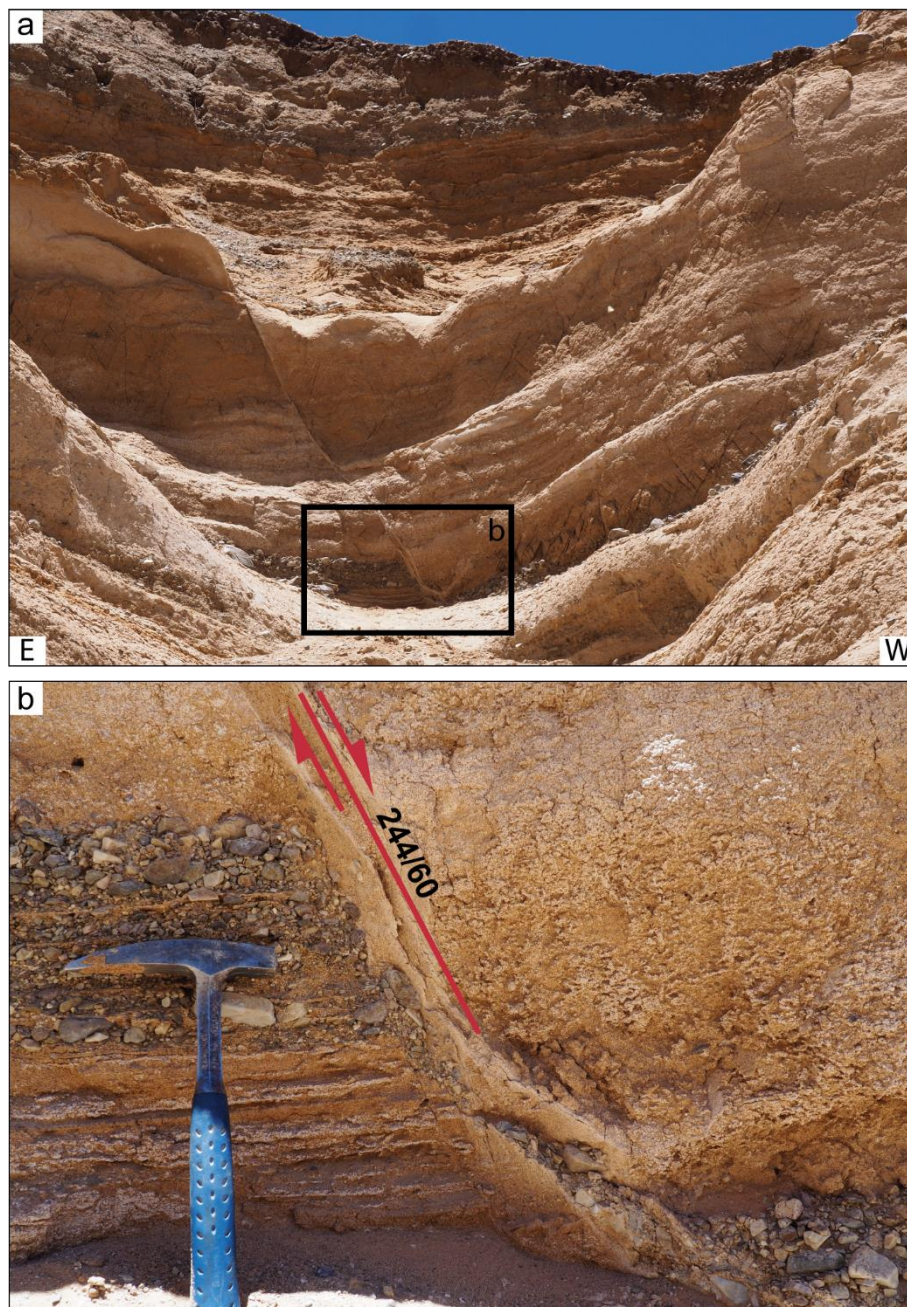


**Figure 27:** Faulted layers at the sand pit east of Yavi. **a)** Westward dipping fault offsetting sand and conglomerate layers. **b)** Inlet box in **a)** showing detailed and scaled offset conglomerate layer. Displacement value is approximately 40cm.

column, vertically displacing the sand deposits. One of these structures offsets a thin layer of conglomerate for approximately 40 cm along a steeply westward dipping plane that comprises a 2 to 3-cm-thick fault gouge (Figure 27). Approximately 5 m west of it, an antithetic fault dips steeply eastward and offsets the sediments a few centimeters.

Farther to the west, close to the entrance of the gorge, an eastward-dipping fault offsets reddish-brown sand layers and juxtaposes them against brown to grey-colored conglomerates. Displacement values must exceed the 5 m high exposure of the outcrop as no marker horizon could be traced across the fault (Figure 28).

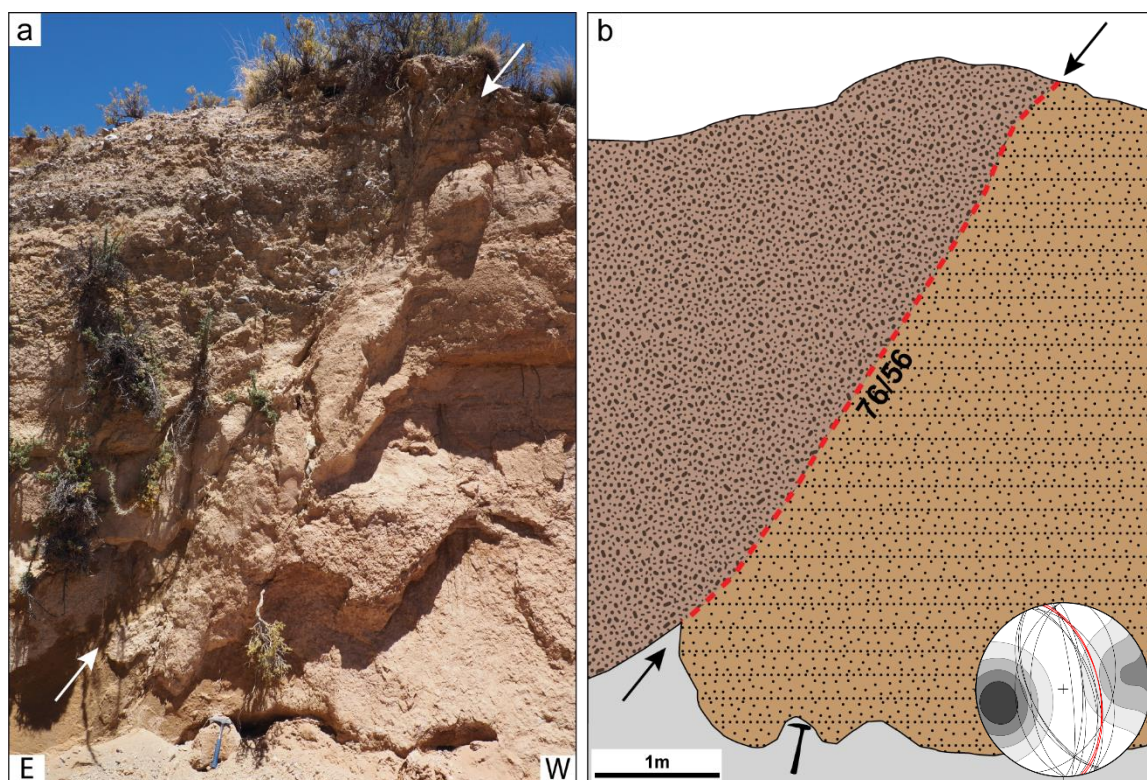


**Figure 28:** Major displacement at the southern outcrop at the sand pit East of Yavi. Conglomerates in the East are offset along a E-dipping fault plane for a cumulative count of at least 5 m. **a)** Outcrop picture, fault plane indicated by white arrows. **b)** Graphic interpretation of the outcrop, fault plane displayed by black arrows, hammer for scale.

### 3.7.3 Yavi Chico

Approximately 4 km NNE of the previous outcrops, a tributary river channel of the main river next to the settlement of Yavi Chico provides an additional outcrop of faulted strata. Although this outcrop does not match the N-S directed lineament connecting the previous two outcrops, the features observed here are worth mentioning in the context of tensional crustal stresses. The outcrop is situated at the confluence of two smaller channels. Much of the wall was covered by vegetation and needed to be cleaned before offering direct view

on the complex fault patterns. The deformed strata incorporate white sands with conglomerates at their base and intercalated sheets of finer grained brownish sand and silt layers (Figure 29). The top of the succession is built by an alternation of several cm-thick paleosols, sands and silts. A complex set of small, conjugated faults dissects the whole outcrop, offsetting the sediment layers in different cm-ranges. This is best observed along the brownish silt and clay layers and the paleosols in the upper section of the outcrops. Like the previously observed structures, these faults are oriented in N-S direction and dip steeply towards East and West. The planes of the faults are marked by thin white lines, along which

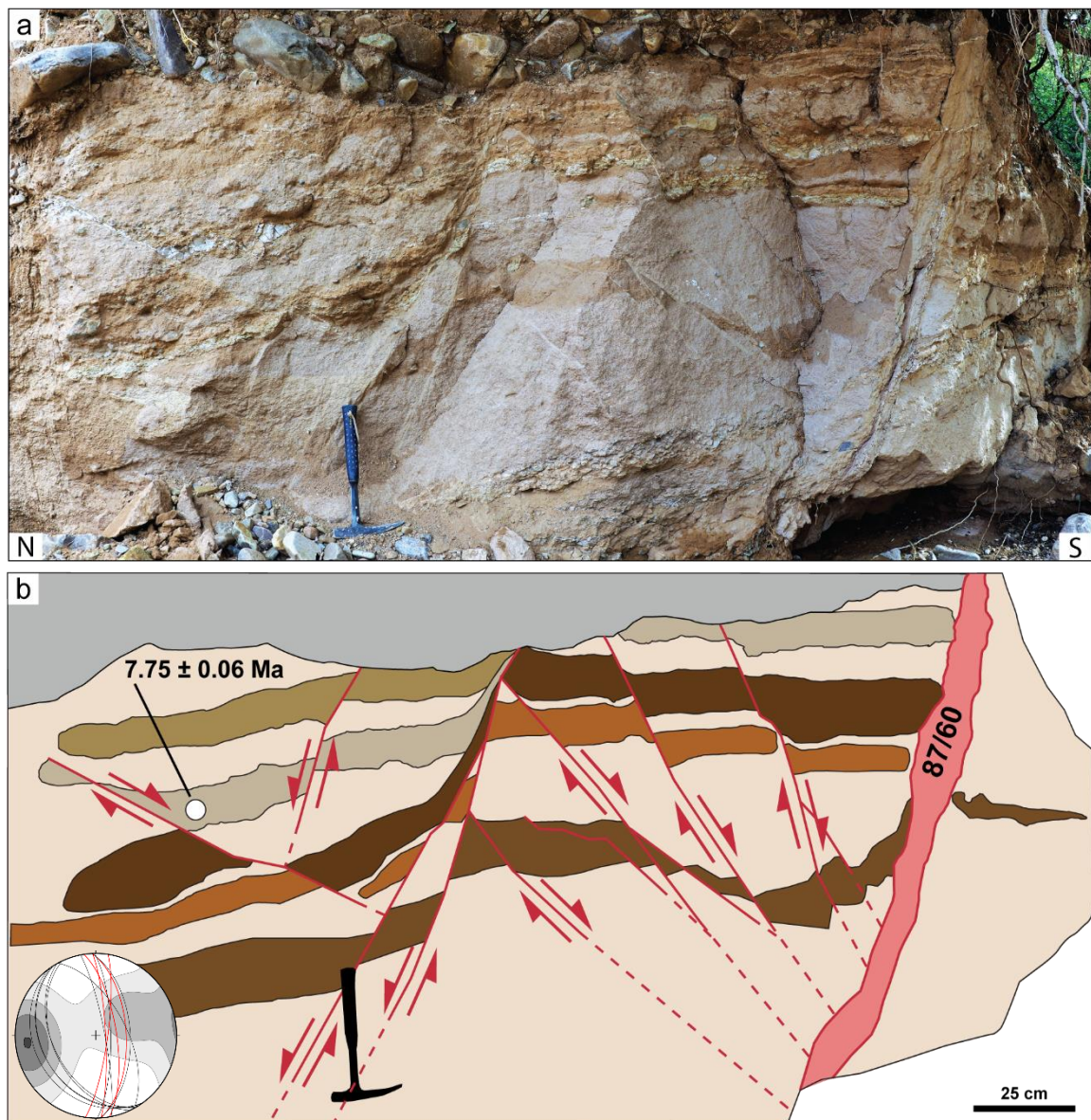


**Figure 29:** Fault outcrop east of Yavi chico. **a)** Photomosaic of fault outcrop and **b)** graphical outcrop interpretation. Major fault marked by a 15 cm wide fault gouge, steeply dipping towards East, indicated by a red line in the sketch, offsets base conglomerates. Secondary synthetic and antithetic faults show complex normal faulting of the different sediment layers with varying displacement values in cm-range (central to northern part) and major fault with 15cm gouge (southern termination). White horizon at northernmost fault was sampled for U-Pb dating.

the sediment layers are offset and/or dragged. Especially within the paleosols, displacement is developed in a rather dragging manor. At the very southern part of the outcrop, a 15 cm thick fault gouge marks the major fault. This fault dips steeply towards East and as the other faults, strikes N-S. At the base of this fault, an approximately 10 cm thick layer of matrix supported conglomerate is dragged for about 20 cm. The overall impression of the whole outcrops tends to be a product of E-W directed tensional stresses. In the upper northern section of the outcrop, a thin layer of white volcanoclastic material is dragged along a minor fault. This layer was sampled for U-Pb age determination, resulting in an age of  $7.75 \pm 0.06$  Ma (Sample Arg21-Ash07, Table 1). The top of the outcrop is covered by conglomerates, which often mark the ultimate sediment cover of the fill units.

### **3.8 Joint measurements**

In addition to the direct implications of deformation along the major fault zones, the stresses acting on the sedimentary fill units of the basin resulted in the formation of extensional joints. The orientation of joints was measured at seven different sites along an E-W directed profile (for location see Figure 12). Joints were developed in different strata and at some points, a refraction in dip angles was observed as they cross beds of varying sediment type. Since only the strike of these joints was measured, this behavior is not reflected in the data presented below.

The measured orientations of the joints are plotted in rose diagrams. At five of the seven measuring sites, a clear trend of NE-SW to NNE-SSW oriented joints is presented within the sediments (Tafna Formation, Sansana, Gruta Señor de Quillacas, Road Quiaca-Yavi and Yavi Fault). Secondary joints are mainly oriented in perpendicular to sub-perpendicular, i.e. NW-SE to WNW-ESE direction and less abundant. At the two sites with less pronounced main orientations, data scatters between the previously described major and secondary directions (Pueblo Viejo, lower surface level S2). Extensional stress, responsible for the formation of the measured joints, is oriented perpendicularly to the main joint orientation and hence follows a NW-SE to E-W direction.

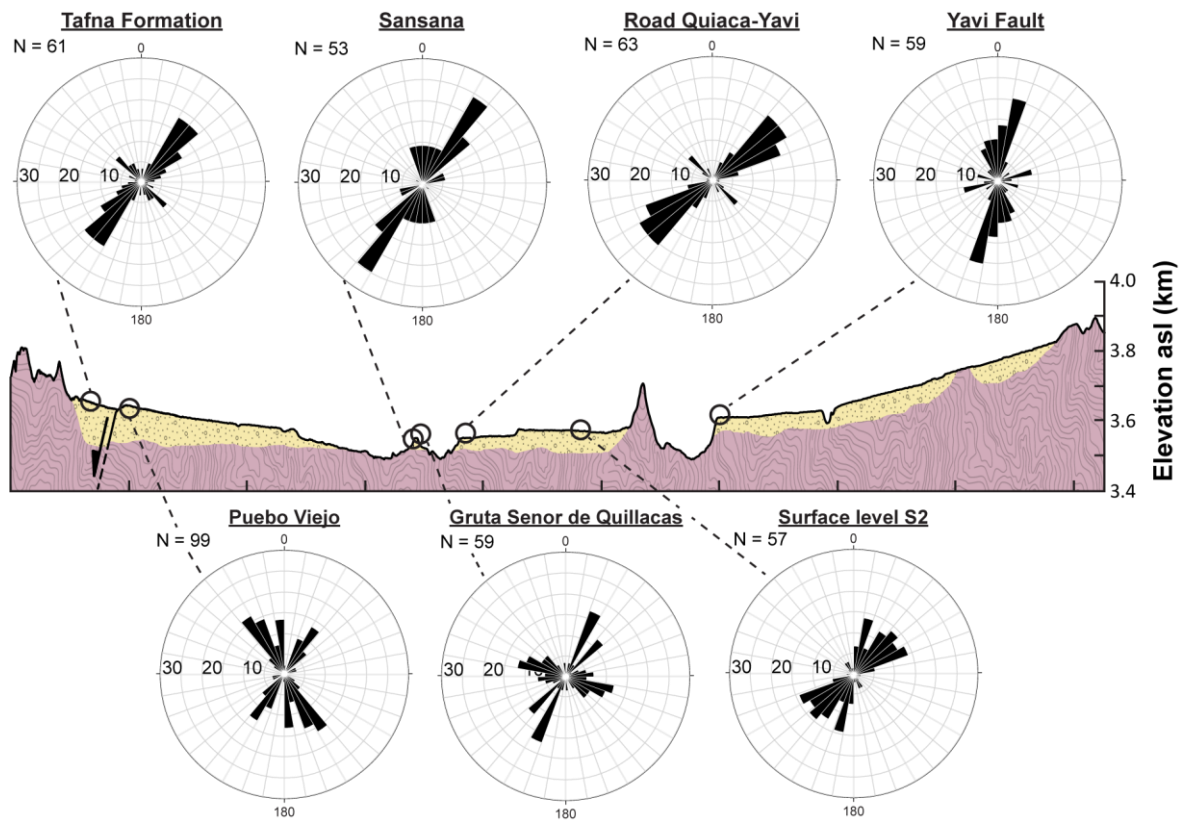


**Figure 30:** Rose diagrams of joint orientations at different sites along an E-W profile crossing the basin (for location see Figure 2). Main orientation of the joints is NE-SW to NNW-SSE. A small amount of secondary joints was measured in (sub-)perpendicular direction. Tensional stress is inferred to be oriented NW-SE to E-W perpendicular to the orientation of the joints.

## **4 Interpretation & Discussion**

The primary goal of this study was to firstly decipher the timing and magnitude of extensional tectonic activity that has affected the northern sector of the Argentinean Puna Plateau; secondly, geochronological and structural information was used to elucidate the basin-fill and subsequent erosion history of the intermontane basins that comprise the north-eastern Puna Plateau. This required a refinement of the local stratigraphic relationships in the context of regional-scale processes and the establishment of a geochronological database to enable a proper temporal integration of the mapped normal faults into the spatiotemporal characteristics of the Cenozoic Andean orogeny. Consequently, intercalated volcanic ashes and surface samples of the tectonically overprinted basin-fill strata were radiometrically dated for their depositional and exposure ages, respectively. Thirdly, the style of tectonic activity was characterized and displacement values were quantified by a combined analysis of remote-sensing techniques and field observations. The influence of the deformation processes was furthermore assessed by determining the tectonic forcing of the local drainage system and the evolution of coalesced alluvial-fan surfaces.

This chapter first focuses on the landscape evolution of the north-eastern Puna Plateau, based on the integration of synthesized and newly acquired stratigraphic and geomorphic information, which was combined with new depositional and exposure ages of the exposed basin-fill units. The concluding interpretation is done in light of existing models that have been proposed for this part of the orogen. In addition, the observed structures and inferred deformation mechanisms are categorized and put into context with respect to the regional stress field, interpreted from structural data collected within the deformed basin-fill sediments. The results from the analysis of fault morphology and morphometry, as well as the obtained radiometric ages are used as indicators for the age and the latest activity of faulting, respectively. This part of the analysis also involved the critical assessment of the amount of measured fault-length and displacement values that were compared to empirical fault parameters in order to provide estimates on paleo-magnitudes of historic earthquakes that generated cumulative fault scarps. Finally, these findings are discussed in the context of a gravitationally driven orogenic collapse of the Andean Plateau.

## **4.1 Landscape evolution of the central sector of the north-eastern Puna Plateau**

### ***4.1.1 Depositional environment and ages of the sediment fill units***

The exposed stratigraphic units in the study area range from late Cambrian-Ordovician rocks to unconsolidated Quaternary sedimentary deposits. The ubiquitous valley-fill units whose youngest strata also constitute the Quaternary conglomerates of coalesced piedmont fans cover a paleo-topography of deformed and eroded basement and sedimentary strata (see chapter 3.1.1). These fill units, which are cut by faults and a dense network of tectonic joints are partly incised and dissected by deep canyons that expose the thalwegs of paleo-rivers, responsible for a drainage system within this part of the present-day Puna Plateau. The valley-fill units are thus strain markers and are crucial elements for a better understanding of the character of the youngest tectonic activity and the ultimate stages of relief formation in the central sectors of the north-eastern Puna Plateau.

The stratigraphic analysis of the sediment-fill units revealed a succession of mainly medium- to fine-grained sands and silts including intercalated conglomerates and volcanoclastics in the form of areally limited layers and lenses. The thickness of the sedimentary succession varies considerably from almost 150 m at Yavi Chico in the east, to only several tens of meters at the location of Tafna in the west as a result of the paleo-topographic highs and lows formed by the basement rocks. Primary sedimentary characteristics such as the grain-size distribution, cross-stratification, imbrication in the conglomerate lenses, as well as load casts point toward a medium- to low-energy deposition by fluvial-, alluvial- and rarely lacustrine processes, supporting the notion of a terrestrial, fluvially dominated depositional environment. U-Pb data of the intercalated tuffs provide maximum depositional ages and range between 8.3 Ma at Yavi Chico and 3.05 Ma in the upper section of the basin fill, below the surface of the 'upper surface level S1' east of Yavi. An even younger age of 2.83 Ma was determined for a tuff layer in the distal part of an alluvial-fan surface west of the city of La Quiaca. However, the oldest age of 8.3 Ma was not extracted from samples at the lowest position within the sedimentary succession and must therefore be considered a minimum age for the onset of deposition. Combining the observation that many of the river cuts in the area form their thalweg as the riverbed reaches basement rocks, and the fact that the oldest sample was taken more than 50 m above the closest riverbed, it can be assumed that the underlying sediments are older and that the

depositional processes must have already been active prior to 8.3 Ma. Neglecting the erosional unconformities within the sediment column and assuming a short transient time between erosional contacts, as well as a constant sediment supply over time, sedimentation rates can be approximated by simply dividing the thickness of the sediment fill between two sampled layers with the difference in age, leading to sedimentation-rate estimates of 10 to 20 m/Ma. Despite the potential errors in this oversimplification, when compared to the derived burial rates of 1-10 m/Ma from the cosmogenic nuclide measurements (chapter 3.2.2) of the upper conglomerate cover, as well as Quaternary sedimentation rates of the hyperarid Atacama desert to the far west, which were estimated to be less than 5 m/Ma (Placzek *et al.*, 2009), the U-Pb based sedimentation-rate estimates appear reasonable. Under the assumption that the calculated rates were constant over the whole timespan of sediment deposition, the age for the lowest deposits within the thickest sediment column of 145 m observed at Yavi Chico must have been deposited within a timeframe between 7.5 and 15 Ma. As the sample closest to the surface in the vicinity of Yavi, where the most continuous sediment column was found, was dated at 3.05 Ma, the deposition of the fill units must have started sometime between 18.05 and 10.55 Ma.

In most places, the succession of the fill units is mantled by conglomeratic gravels that are occasionally found in direct contact with basement rocks forming an integral part of the coalesced alluvial fans. According to their appearance, stratigraphic position and depositional age (as inferred from the geochronology results), these deposits resemble the ubiquitous ‘Punaschotter’ (Penck, 1920), a prominent conglomerate sequence widely distributed in the southern plateau-bounding basins of Argentina. The Punaschotter were described to reflect an abrupt change from various environmental settings, such as ephemeral braided streams, meandering channels and wetlands to alluvial fans (Carrapa *et al.*, 2008; Bywater-Reyes *et al.*, 2010). More recent studies on the formation of these conglomerates attributed their deposition to the combined effect of more local tectonic and superposed climatic forcing (Schoenbohm *et al.*, 2015). However, these coarse-grained, angular to subangular deposits in the study area contrast with the finer-grained, well-rounded clasts and sands of the underlying sequences. While the contact with the latter is marked by a disconformity due to erosion of the sediment-fill units, the contact with the folded basement rocks is marked by an angular unconformity. At the surface, the deposits comprise angular to sub-angular gravels composed of Ordovician rocks dispersed in a sandy matrix forming a matrix-supported conglomerate, while in river cuts it can be seen

that most of the sandy component changes toward a larger amount of gravel, forming a clast-supported conglomerate. This contrast in surface and subsurface characteristics indicates that much of the sand found at the surface was either deposited by sediment inflation due to the arid climate and efficient eolian transport, or that the clasts on the surface have been gradually disintegrated by eolian abrasion as well as chemical and physical weathering. In order for these processes to work efficiently, a persistent surface stability is required.

The coalesced alluvial fans east of the Sierra de Escaya stretch eastward and northward to the city of La Quiaca. The topographic difference between the alluvial-fan surfaces and the present-day base level of the northward-flowing tributary of the Río La Quiaca clearly suggests that these fans were once adjusted to a topographically higher drainage system that subsequently incised into the fans as a consequence of a lowered base level, thus abandoning the fans as transportation surfaces whose dynamics were determined by the behavior of the base level of the Río Pilcomayo. A sample of a primary volcanic ash layer taken from underneath the surface of the distal section of an abandoned alluvial fan close to the city of La Quiaca was dated at 2.83 Ma (see chapter 3.2.1 – sample Arg19\_Ash01 and Figure 4c), indicating that aggradation in this fan system must have been active at least until then. This part of the alluvial-fan history marks an important turning point in the landscape evolution of the north-eastern Puna that clearly predates the regional incision and destruction of the alluvial-fan sequences in the area. Moreover, as the Pumahuasi Fault cuts through the alluvial fan in its proximal section, this dated surface could also be an important strain marker for the assessment of tectonic activity in this region, as the vertical displacement along the fault could also have been a potential driver for the dismemberment and abandonment of the fan, thus diminishing its function as a transportation surface.

The cover units west of the Sierra de Santa Victoria and east of the N-S-trending tributary of the Río La Quiaca form less-incised, overall contiguous surfaces (Figure 12). These exposed sediments characterize the alluvial fans between the city of La Quiaca and the adjacent regions towards the east of Yavi; they are composed of well-rounded pebbles and sands. In places, these conglomerates reach a thickness of up to ten meters, are moderately sorted and, especially in their upper section, cemented by bedding-parallel carbonate K-horizons and calcite fillings of subvertical joints, suggesting protracted post-depositional surface stability (Zamanian *et al.*, 2016). A lens of volcanic ashes, east of the village of Yavi, below the upper surface level S1 was dated at 3.05 Ma. Surface-exposure dating of

the same surface some hundred meters farther east, resulted in an exposure age of 2.55-2.94 Ma. Although the U-Pb age is based on a single zircon grain and the exposure age is based solely on the concentration of  $^{10}\text{Be}$ , the result of these two independent dating approaches support a late Pliocene age for this unit. Due to the relatively short transient time between deposition and exposure, it can be assumed that the surface was not covered by additional material after its deposition. In contrast to the alluvial-fan surfaces in the west, the fans in the east constitute gentler, less fluvially dissected, almost uninterrupted, extensive surfaces (Figure 12). A striking observation on these surfaces is the existence of multiple N-S-oriented breaks in the gentle surface slopes, such as east of the settlement of Sansana as well as close to and east of the village of Yavi (see chapter 3.1.2 and Figure 12). Natural erosional cuts along these lineaments did not provide geological evidence that would imply an unambiguous tectonic origin of these features as proposed by Cladouhos *et al.*, (1993). An alternative explanation for the formation of these structures involves fluvially driven processes: As these linear features trend with the N-oriented courses of the Río Sansana and southern tributary of the Río La Quiaca, they could as well be witnesses of former fluvial incision and therefore be terrace risers adjusted to the N-draining river systems. If this is true, they would reflect a past base-level drop of the principal drainage system. In contrast, smaller rivers such as the Río de Lecho, Río de Yavi and Río de Casti cut these lineaments sub-perpendicularly (Figure 12) and speak either against the theory of fluvial formation of the structures or they incised into the surfaces after the base level had already been lowered to the present-day level, and therefore dissect these lineaments. Arguments presented in the following chapter further support this hypothesis, as the surfaces were formed i.e., exposed at different times in the past, which would not be the case if the lineaments were fault scarps, and the surfaces had once been a contiguous and coherent geomorphic feature.

### ***4.1.2 Surface exposure ages and drainage capture***

In total, three gently inclined geomorphic levels were identified in the eastern piedmonts of the study area, separated by the N-S-trending, slope-breaking lineaments mentioned above. Two of the three surface levels were sampled in order to determine their exposure ages using paired cosmogenic radionuclides. The main target of surface-exposure dating was to bracket the timing of surface deformation that affected the alluvial fans in the west as part of the same fill process, but the data also provide information on a possible fluvial formation of the N-S-oriented lineaments and surfaces, respectively. The analysis involved

sampling cobbles and gravels from the conglomerate cover of the alluvial fans and measuring the concentration of cosmogenic  $^{10}\text{Be}$ -,  $^{21}\text{Ne}$ - and  $^{26}\text{Al}$ -nuclides. Due to its stratigraphic context, geomorphic relationships, and the recent state of the drainage network, the surface-conglomerate layer was identified as being the youngest deposit that was formed prior to the abandonment of the surfaces. Consequently, the obtained exposure ages of the conglomerate layer reflect the final phase of fluvial activity and the abandonment of the respective surfaces. Under the assumption that the drainage network experienced different episodes of base-level lowering during which the piedmont streams adjusted themselves, the exposure ages of the staircase-like surfaces should decrease with elevation. The upper surface level S1 provides an uncorrected exposure age of  $2.94 \pm 0.15$  Ma, which is in good agreement with the depositional age of a volcanic ash lens ( $3.05 \pm 0.07$  Ma), intercalated in the same conglomerate layer. Unfortunately, only the  $^{10}\text{Be}$  data was used for the calculations of the exposure age, as the  $^{26}\text{Al}$  fraction was lost during the isotope-separation process in the laboratory, and the overall amount of available sample material did not suffice for an additional  $^{21}\text{Ne}$ -analysis; consequently, there is no direct benchmark of that age using other nuclide systems. Further analysis using analytical tools for calculating exposure ages resulted in variable ages, where the youngest would be  $1.56 \pm 0.05$  Ma (CRONUS Earth calculator, lm scaling scheme, no erosion) and the oldest  $4.43 \pm 0.58$  Ma (CRONUS Earth calculator, st-scaling scheme, erosion of 0.1 m/Ma). The latter value is unrealistically high, as the exposure age of the surface cannot be older than the depositional age of the underlying sediments nearby. This error could be associated with the chosen scaling scheme, an overestimated erosion rate or an intrinsic miscalculation in the code that cannot be further evaluated here. The application of other calculators confirms the proposed, uncorrected exposure age of  $2.94 \pm 0.15$  Ma, as the age of the surface was dated at  $2.69\text{-}2.39 \pm 0.06$  Ma with an erosion rate of  $0.11\text{-}0.13 \pm 0.02$  m/Ma (CosmoCalc), and  $2.39 \pm 0.06$  Ma with an erosion rate of  $0.13 \pm 0.02$  m/Ma (CREp). These ages are more reasonable compared to the ages derived from the CRONUS Earth calculator, because they are closer to the depositional age provided by U-Pb-dating of the intercalated volcanic ash. However, as erosion rates were neglected during the calculation of these ages, the surface exposure could still be older and close to the 3.05 Ma old, dated zircon extracted from the subsurface. In conclusion, the exposure age of the upper surface level must be in the range between the late Pliocene (3.05 Ma) and the early Pleistocene (2.39 Ma).

Surface level S2 provided a younger uncorrected exposure age between 1.5 and 1.7 Ma based on all three measured nuclides. In comparison, when using the same calculators and settings as discussed above, the ages range from  $1.04 \pm 0.03$  Ma (CRONUS Earth calculator, lm-scaling scheme, no erosion) to  $1.74 \pm 0.08$  Ma (CRONUS Earth calculator, st-scaling scheme, erosion of 0.1 m/Ma). Uncorrected nuclide-concentration ratios have shown that the surface and near-surface sample did not experience burial, indicating a single deposition-exposure history (see chapter 3.2.2 and Figure 13 and Figure 14). In light of these facts and when compared to the upper surface levels' nuclide concentration, it can be concluded that the sampled material on both surfaces was deposited with a time lag of approximately 1-1.5 Ma. This observation suggests fluvially driven incision of the upper surface S1, formation of an active transportation surface at a lower elevation, followed by abandonment and accompanying incision of surface S2. This timing is also reflected by the different grade of K-horizon development on the respective surfaces, which is more pronounced on the conglomerates mantling S1 and less developed on S2. These observations further support the notion that the incision into the fill units and the terracing must have taken place in a stepwise, episodic manner, most probably triggered by base-level changes of the trunk stream or a combination of protracted incision and superposed climatically controlled changes in the transport and erosion regime; the latter scenario has been previously documented in the intermontane Toro basin of the southern Argentine Eastern Cordillera (Tofelde *et al.*, 2017). Ultimately, a 4.47-m.y.-old layer of volcanoclastics just below the surface at an outcrop close to the settlement of Sansana further supports the theory of erosional removal of the younger, superimposed sandy layers found farther east, forming the higher elevated surfaces at the foothills of the Sierra de Santa Victoria and in the vicinity of Yavi.

The measured CRN concentrations and associated exposure ages discussed above were not corrected for a potentially inherited concentration, accumulated during pre-exposure of the sediments. The common approach of sampling along a depth profile did not provide results as expected. Although the measured concentrations decrease with depth, they do not follow a modeled depth profile calculated with empirical parameters. This was further established by a malfunction of a state-of-the-art tool for modeling depth profiles (Hidy *et al.*, 2010) using the measured CRN data. A non-uniform distribution of nuclide concentrations at depth hinders a precise calculation of an inherited concentration, generally resulting in overestimated values of exposure ages. Such issues within sampled depth profiles were

already described in other studies (Le Dortz *et al.*, 2012; Kounov *et al.*, 2015) and can be associated to i) cryo- and bioturbation, leading to post-depositional mixing of the strata (Darvill *et al.*, 2015); ii) inconsistent sedimentation rates between the sampled layers, including possible phases of erosion (Nivière *et al.*, 2016); and iii) differing inherited concentrations due to source-rock variations. An explanation for varying inheritance and nuclide concentrations, respectively, was proposed by Le Dortz *et al.*, (2012), who suggested a process of alluvial ‘cannibalism’ for the endorheic Iranian Plateau, a viable process which could also affect other, generally endorheic, arid regions, such as the alluvial-fan environments of the Altiplano-Puna Plateau. This process was described as being driven by low denudation rates and weak incision, feeding alluvial fans with material that was reworked from older, alluvial-fan deposits located at higher elevations, thus contaminating the deposits with nuclide concentrations derived from previous episodes of surface exposure. However, measured concentrations in the profile analyzed from the alluvial fans of the Puna decrease with depth and do not scatter as much as the data published by Le Dortz *et al.*, (2012). Hence, a simpler scenario might explain the measured depth variations. For example, several erosional unconformities were identified within the sampled depth profile. At the time of sampling, it was assumed that the timespan between erosion and deposition was short enough to not have had a significant impact on the distribution of CRNs at depth. According to the nature of the deposits, it is possible that more than one erosional phase could have interrupted the deposition of the conglomeratic strata; however, this was not detected during the sampling. Based on the data provided, none of the previously described processes can be directly inferred. As a consequence, inheritance-corrected age estimates were calculated under the assumption that the  $^{21}\text{Ne}$  concentration of the deepest sample represents the inherited concentration, as this nuclide series is not affected by decay and, at the sampled depth, should be completely shielded from cosmic rays. In order to determine the inheritance of the other two nuclide series, the  $^{21}\text{Ne}$  concentration of the deepest sample was scaled to  $^{10}\text{Be}$  and  $^{26}\text{Al}$  using production-rate ratios. As these calculated concentrations would be the initial, pre-decayed concentrations, a decay-correction was applied for the time of uncorrected surface exposure of the samples. The resulting ages are  $1.16 \pm 0.14$  Ma for  $^{21}\text{Ne}$ ,  $1.21 \pm 0.08$  Ma for  $^{10}\text{Be}$  and  $1.25 \pm 0.1$  Ma for  $^{26}\text{Al}$ , all agreeing within error bounds. Assuming a similar inherited concentration for the upper surface level S1 resulted in an exposure age of  $2.55 \pm 0.20$  Ma. As this approach is not based on a proper calculation, but rather on a rough estimate of inherited nuclide concentrations, the ratios of the corrected concentrations do not plot properly within the

exposure and burial zones of the two-isotope plots; at least the surface samples would plot within the so-called forbidden zone, indicating that the applied correction is wrong, and the resulting concentrations therefore show unrealistic ratios. Finally, to reduce the assumptions made for the calculations, the most trustworthy approach on exposure ages is to work with the uncorrected ages as initial exposure ages that could still be younger when corrected for inheritance or slightly older, when corrected for erosion. Despite these uncertainties, this novel data generated in this study is useful in order to estimate the timing of fluvial abandonment of the sampled geomorphic surfaces, the corresponding prior drop in base level of the trunk stream, and hence the stepwise progression of incision processes, obliterating the plateau morphology and excavating the sedimentary fill units in the north-eastern Puna.

### **4.1.3 Synthesis**

Thus far, a rigorous assessment of the late Cenozoic development of the central sector of the eastern Andean Plateau has been hampered by the lack of reliable geochronological data. In addition, most of the previous studies analyzing the Neogene to Quaternary tectonic, geomorphic, and sedimentary processes in the Central Andes have been carried out in Bolivia and Peru (Gubbels *et al.*, 1993; Kennan *et al.*, 1995; Kennan *et al.*, 1997; Lamb *et al.*, 1997; Barke & Lamb, 2006; Quade *et al.*, 2007; Leier *et al.*, 2013). In contrast, this study presents for the first time a catalogue of absolute age data from NW-Argentina, where the most coherent parts of the well-studied, eastern paleo-surface remnants are located within the Andean Plateau. This data allows to determine the timing of previously suggested processes, whose chronological order was mainly based on relative age relationships. Accordingly, the late Cenozoic landscape evolution of this part of the Andean Plateau can be broadly separated into three distinct phases that can be constrained by the results of the two different geochronological approaches.

**Phase 1** involves the formation of topographic relief and hence, the generation of accommodation space needed for the subsequent storage of the sediment-fill units. In order to create this space, a drainage system was required to erode material from the mountain front. This drainage network must have been connected to a distal foreland basin, as no detritus associated to this widespread erosion was reported within the interior of the mountain range (Kennan *et al.*, 1997). Although neither this observation nor the data presented in this study imply a discrete age for the onset of initial incision, it can be assumed that it was directly coupled to the uplift of the Central Andes, as the formation of

topographic gradients is commonly accompanied by reinforced erosion (Ruddiman & Kutzbach, 1991; Einsele, 2000). The uplift of the Andes was proposed to have initiated in the Western Cordillera during late Oligocene to early Miocene (~28-20 Ma), as inferred from crustal thickening that led to magmatic-arc activity and from the formation of a foreland basin at the location of the present-day Andean Plateau (Coira *et al.*, 1993; Kay *et al.*, 1995; Allmendinger *et al.*, 1997). Paleocene- to early Eocene marine rock formations found in the Altiplano and Eastern Cordillera must predate the uplift of these morphotectonic provinces (Horton & DeCelles, 2001; Carlotto, 2013). Subsequent east-migrating deformation led to initial uplift in the Eastern Cordillera during early Miocene (24-17 Ma), as inferred from recent stable-isotope-based studies (Leier *et al.*, 2013), although, surface uplift was proposed to have occurred as early as Eocene to early Miocene (45-20 Ma) with elevations only reaching up to 1000 m (Gubbels *et al.*, 1993; Garzione *et al.*, 2017). More recent studies along the transition zone of the Puna Plateau and Eastern Cordillera support these early uplift pulses by proposing even older onsets of deformation of pre-middle Eocene age, derived from angular and intraformational unconformities (Montero-López *et al.*, 2020). When comparing these findings with the age of the dated terrestrial sediments in this study, their deposition must postdate the initial range uplift and the formation of an erosional topography, and it can be deduced that the creation of accommodation space is the result of deformation and uplift prior to 8.3 Ma. As no detritus older than the sampled and dated strata was found in the study area, the depocenter for sediments removed during this phase must be located farther east as suggested by Kennan *et al.*, (1997). Early to mid-Miocene sedimentary sequences, as old as 22 Ma, were described in the foreland fold-and-thrust-belt and Chaco foreland region, which have provenance signals of recycled Paleozoic sedimentary units that also form the uplifted basement of the Andean ranges in the Eastern Cordillera. According to paleo-current analysis, these deposits were derived from western source rocks (Tineo *et al.*, 2022). Moreover, the lack of pre-Miocene deposits in this area is most probably related to the absence of high topography in the west and hence implies a direct correlation between Miocene Andean uplift as proposed by Leier *et al.*, (2013) and the onset of deposition of the foreland-basin strata mentioned above. In conclusion, the accommodation space within the study area must have existed by at least 8.3 Ma, the age of the oldest exposed valley-fill unit, which postdates the starting point for the formation of the sedimentary valley fills in the north-eastern Puna.

**Phase 2** is defined by the formation of the sediment-fill units found within the internal, high-altitude sectors of the mountain range. Following the depositional ages of the sampled sedimentary strata, the onset of sediment accumulation started eventually prior to but was certainly active at around 8.3 Ma (Yavi Chico) and was time-transgressive to around 3 Ma (Yavi - upper surface level S1). As the oldest sample does not cover the deepest section within the sedimentary column, deposition must already have initiated earlier. Radiometrically determined  $^{40}\text{K}/^{40}\text{Ar}$  age data published by MacFadden et al. (1990) of the Quebrada Honda Formation in Bolivia provided ages between 11.96 and 12.83 Ma. In the light of this data and the stratigraphic as well as morphologic similarity of those deposits and the ones in Argentina, the extrapolated, estimated ages for onset of deposition of 18-10 Ma for the sedimentary column at Yavi Chico (chapter 4.1.1) appear reasonable. In other places (sample from Salitre, Bolivia, see Gubbels *et al.*, 1993), 8.78 Ma old, undeformed tuffs that superimpose reverse faults, were interpreted to mark the onset of deposition and the cessation of compressional deformation in the area close to the national border of Argentina and Bolivia (Cladouhos *et al.*, 1994). After the onset of deposition, successive sediment accumulation must have led to an uphill-migration of the erosional front and the piedmont areas expanded due to pedimentation processes but were eventually buried up to the intersection between the alluvial fans and the bedrock outcrops. These cut-and-fill processes, as described by Gubbels *et al.*, (1993) in Bolivia, must be responsible for the formation of the sedimentary fill units that ultimately resulted in the gently inclined San Juan de Oro Surface. However, the onset of deposition of proximal sediments within the internally drained areas of the orogen contrasts the earlier depocenter in the former foreland areas. This change in transport distances and hence, depositional environments requires a modification of the principal drainage system.

Two end-member models for the type of drainage network modification could lead to comparable results regarding sedimentary basin fills; both scenarios are based on the concept that the eastward-migrating Andean deformation front and the associated development of topography are linked with the onset of tectonic activity in the Subandean thin-skinned foreland fold-and-thrust belt. In such a setting deformation and uplift in the westernmost Subandean ranges triggered the changeover of depositional loci and disturbed the fluvial connectivity between the orogen interior and the foreland. One end-member model suggests a severed fluvial network and complete hydrologic isolation of the study area due to rapid uplift and the formation of an orographic barrier in the East, leading to a

changeover from externally to internally drained basin conditions. Such a model has been proposed for other basins associated with orogenic plateaus, such as the Tarim and Quaidan basins in Central Asia (Sobel *et al.*, 2003) or the Iranian Plateau (Heidarzadeh *et al.*, 2017). Under these aspects, it is interesting to see that the ages of the sedimentary fill units postdate the proposed waning of deformation in the Eastern Cordillera around 10 Ma (Jordan & Alonso, 1987; Gubbels *et al.*, 1993; Schmitz & Kley, 1997) and that their onset of deposition is approximately coeval with the onset of deformation in the Subandean ranges as proposed by Echavarría *et al.*, (2003) at around 9 to 8.5 Ma. Taken together, these correlations may point toward a potential hydrologic isolation of the drainage system through the formation of a topographic barrier by accelerated uplift rates, terminating the evacuation of sediment from the internal parts of the evolving Andes. This scenario was also proposed by Kennan *et al.*, (1993), who pointed towards the similarity between the processes in the study area and the ones within the internally drained areas of the plateau realm. An example of this topographic-isolation mechanism was recently inferred from geochronological and sediment provenance studies on foreland basin deposits in the Río Iruya catchment of the Eastern Cordillera, south of the study area (~23°S), where a changeover from distal to more proximal western sediment sources of foreland deposits occurred between 12 to 7 Ma (Rahl *et al.*, 2018), contemporaneous with uplift pulses in the Eastern Cordillera and the onset of deposition of the valley-fill units at around 12-8 Ma (MacFadden *et al.*, 1990; Gubbels *et al.*, 1993). This mechanism could have also affected the study area and facilitated the deposition of the sediment fill units. However, several facts speak against a complete isolation of the drainage system such as the continuous deposition of Mio- to Pliocene basement-derived sediments within the foreland sectors of the fold-and-thrust belt and Chaco plains (Tineo *et al.*, 2022), the fluvial characteristics of the sediment fill units and most importantly, the lack of larger lacustrine and evaporitic sequences in the study area, which are typically formed under endorheic conditions and found in the internally drained regions of the plateau area in Argentina and Bolivia (Alonso *et al.*, 1991).

The second model suggests that the drainage network was never completely disconnected from the foreland, but rather severed by a reduction in stream gradients and a decrease in stream power following the onset and/or acceleration of uplift in the Eastern Cordillera and Subandes, which resulted in a more proximal aggradation of sediment (Kennan *et al.*, 1997). This theory was further developed by Barke & Lamb, (2006), who pointed out that

several facts argue against a complete hydrologic isolation of the drainage system; this includes the lack of recent evidence for the formation of a topographic barrier between the Eastern Cordillera and the Subandes, less conglomerate deposits as expected from the planation of the Eastern Cordillera, and finally, an increase in deposition of sediments in the foreland by 9 Ma. Due to the observations made in here, including the lack of evaporitic and lacustrine deposits close to the present-day northern Puna outlet, this model is feasible. However, this conclusion does not explain the present-day shape of the drainage system, especially the difference in altitude between the study area and the foreland basin, which accounts for up to 3000 m elevation depending on location. Accordingly, and in light of the longitudinal profile of the Río Pilcomayo not being in a steady-state condition (Figure 31), the drainage system and the associated sediment deposits must have been uplifted without internally deforming or tilting the horizontally layered fill units. The issue on the amount and timing of that uplift was addressed in several studies focusing on paleo-elevations of the Andes by analyzing the remnants of paleo-surfaces, longitudinal river profiles and associated knickpoints as indicators of Neogene tectonism. Kennan *et al.*, (1997) pointed out, based on stream gradients of the present-day river profile, that around 2000-2500 m surface uplift relative to the foreland must have occurred since 10 Ma. Barke and Lamb (2006) refined this approach by adding three different methods (upstream profiles, downstream profiles and knickpoints) that delivered surface uplift estimates of  $1705 \pm 695$  m since 12-9 Ma (Figure 31). These findings indicate rapid Neogene surface uplift, which is backed by studies on paleo-elevations and uplift estimates for the northern Altiplano and Eastern Cordillera regions, derived from i) stable isotope measurements proposing paleo-elevations of ~2500 m by mid Miocene (Garzzone *et al.*, 2006; Leier *et al.*, 2013); ii) paleo-botany data proposing 2000-3500 m of surface uplift of the central Altiplano since the late Miocene (Gregory-Wodzicki, 2000; Croft, 2007); and iii) paleontological data retrieved from the Quebrada Honda Formation in the Eastern Cordillera leading to a surface uplift of ~2000 m since its deposition at around 12 Ma (Gibert *et al.*, 2020).

Whilst agreeing on the existence of rapid Neogene surface uplift, two opposing schools of thought are arguing on the underlying uplift mechanisms: mantle driven processes vs. bulk crustal shortening (summarized in e.g., Garzzone *et al.*, 2008; Garzzone *et al.*, 2017). As the uplift did not deform the sediment-fill units in the study area and was a widespread phenomenon, coevally affecting plateau areas in the west (Schildgen *et al.*, 2007; Schildgen

*et al.*, 2009) and east (Hoke & Garzzone, 2008), the latest phase of uplift was associated with ‘wholesale’ uplift, guided by deep-seated processes such as lower crustal flow, magmatic addition and lithospheric delamination (see summary by Garzzone *et al.*, 2017). This argumentation is also based on the difficulty to use balanced cross-sections to account for the measured surface uplift of the plateau realm during the last 10 Ma, because shortening rates four times greater than the observed rates would have been necessary over the course of the last 40 Ma (Garzzone *et al.*, 2008; Garzzone *et al.*, 2017).

Although the arguments for wholesale uplift by mantle-driven processes do seem plausible at first glance, when viewed at a regional tectonic scale, this mechanism cannot be used to explain a well-pronounced knickpoint along the course of the Pilcomayo drainage system, located at the transition between the Eastern Cordillera and the Subandean ranges (Figure 31). This knickpoint marks the position where the elevation of the riverbed is offset by more than 1500 m with respect to the foreland and thus suggesting the location of a major crustal structure accommodating uplift of the Eastern Cordillera. Such a localized, sharp knickpoint is difficult to reconcile with a model involving a regional wholesale uplift driven by mantle processes that are expected to have influenced a much wider region, with knickpoints at the transition between the uplifted and warped sections of the orogen and adjacent undeformed areas. Instead, the pronounced knickpoint and its location at the boundary between two morphotectonic provinces are indicative of structurally controlled uplift of the Eastern Cordillera, which furthermore triggered the onset of deformation in the Subandean foreland fold-and-thrust belt. This interpretation follows uplift models that involve major west-dipping décollements that are linked with a footwall ramp and structures bounding the Eastern Cordillera (Mon *et al.*, 1996; Rodríguez-Fernández *et al.*, 1999; Allmendinger & Zapata, 2000; Elger *et al.*, 2005; Ege *et al.*, 2007). Motion along such a ramp structure could have enabled regional uplift, without strong internal deformation of sedimentary units located in intermontane basins in the hanging wall. New crustal-scale forward-modelling approaches further support this theory of uplift along sequentially-activated décollements, acting as main drivers for lateral plateau growth by the successive foreland-directed development of new décollements and deactivation of older ones associated with decreasing contrast between upper low-strength and lower high-strength layers (Giambiagi *et al.*, 2022). Indeed, at ~23°S thermochronological data indicates rapid, mid to late Miocene exhumation in the Eastern Cordillera that is compatible with such a model (van Kooten *et al.*, 2022). Finally, another recent model suggested

(Armijo *et al.*, 2015) that the ultimate, rapid uplift of the Andes and the onset of deformation within the Subandean belt at about 10 Ma might be explained by the trenchward growth of the Andes that resulted from the onset of westward subduction of the Brazilian Shield underneath the orogen. With respect to the sediments in the orogen interior and the evolution of topography, it is conceivable that such a mechanism involving forces impacting both flanks of the orogen could have had similar effects as a mantle-driven wholesale uplift.

**Phase 3** is defined by the incision of the regional drainage network into the sediment-fill units of the Andean Plateau region. The depositional processes that led to the aggradation of the fill units were replaced by widespread incision and abandonment of the coalesced fan surfaces that defined the youngest fill units that are generally much coarser and characterized by internal erosional unconformities. The several meter-thick fill conglomerates that mantle the finer-grained older fill units reflect a change in energetic conditions of the fluvial processes in the present-day plateau. Based on the morphometric analysis of the different fan surfaces that were sculpted into the basin-fill units at successively lower elevations it can be concluded that incision did not advance in a continuous, but rather in a stepwise episodic manner that followed a base-level lowering of the trunk river, stabilization and formation of a new transport surface at lower elevation and renewed regional incision and abandonment of the geomorphic surfaces. The first base-level lowering occurred 3-2.5 Ma ago, when the oldest and highest geomorphic surface level S1 was abandoned and surface S2 was developed at a lower elevation. Subsequently, a renewed regional base-level lowering occurred 1.7-1 Ma ago, when surface level S2 was incised and abandoned, while the drainage system incised deeper into the fill units, ultimately forming another, quasi-stable transport surface above the valley-fill units.

The timing of the changeover from deposition to incision elaborated in this study agrees with the proposed ages of surface formation and abandonment in the Bolivian Altiplano at about 3 Ma (Kennan *et al.*, 1997) and 1.5 Ma (Gubbels *et al.*, 1993), which were based on regional stratigraphic relationships. Although Barke & Lamb (2006) suggested canyon formation in Bolivia as early as 6.5 Ma ago, the CRN surface-exposure ages and U-Pb-dating of volcanic ashes within the valley fills and the deposits of the different geomorphic surfaces provide for the first time a trustworthy tool and temporal constraint to shed light on the processes of landscape evolution in the eastern sector of the Central Andes. Importantly, as the production rate of CRNs scales with altitude, lower elevations would

correlate with decreased production rates and would ultimately lead to older exposure ages. Since the calculated exposure age of surface S1 is close to the depositional age of the closest U-Pb sample, the final fluvial activity affecting the valley fills and the different Plio-Pleistocene geomorphic surfaces must have occurred at the current altitude. A lower production rate at a lower elevation would have produced exposure ages significantly older than the depositional age. Consequently, the abandonment of the surfaces and the incision into the valley fills must have occurred as the Andes had already reached their current elevation after the most recent uplift.

Despite these findings, it could be well possible that incision into the Andean Plateau was diachronous and disparate in space and fills farther downstream could have been incised prior to the surfaces that are located further upstream, and thus result in different ages regarding the abandonment of terrace surfaces. In consideration of the now incised, yet very well-preserved piedmont terraces in the field area it is suggested that headward erosion and drainage capturing along the courses of the Río Pilcomayo and the Río San Juan de Oro are important processes that record an upstream-migrating wave of incision and resulting foreland connectivity that has reached the La Quiaca and Yavi areas of the Puna Plateau.

A comparative study on canyon incision of the north-eastern and central border of the Andean Plateau based on radiometric and thermo-chronologic data, was published by Lease & Ehlers (2013) and supports the notion of late Pliocene to early Pleistocene onset of incision. Their argumentation implies that widespread incision along the eastern border of the Andes started at about 3 Ma, based on a comparison of incision ages of the Río San Gaban in Peru with incision ages of the Río La Paz in northern Bolivia and the Río San Juan de Oro/Río Pilcomayo in Bolivia/Argentina. According to their study, Pliocene incision into the eastern Andean Plateau is a regional phenomenon, and since it affected regions of different tectonic, geodynamic and hydrologic characteristics, it must have been decoupled from active deformation and tectonic structures, respectively. Following these findings, enhanced moisture flux toward the plateau flanks and its interior must have driven the rapid incision at the eastern margin of the Andes, possibly enhanced by the onset of glaciations (Roberts *et al.*, 2017) and resulting increase in stream power (Kennan *et al.*, 1997). Interestingly, this timing agrees with an increase in foreland-deposition rates by Echavarría *et al.*, (2003), the deposition of the 'Punaschotter' (Bywater-Reyes *et al.*, 2010),

as well as a global increase in sedimentation rates due to a more erosive climate between 4 and 2 Ma (Zhang *et al.*, 2001; Molnar, 2004).

#### 4.1 Landscape evolution of the central sector of the north-eastern Puna Plateau

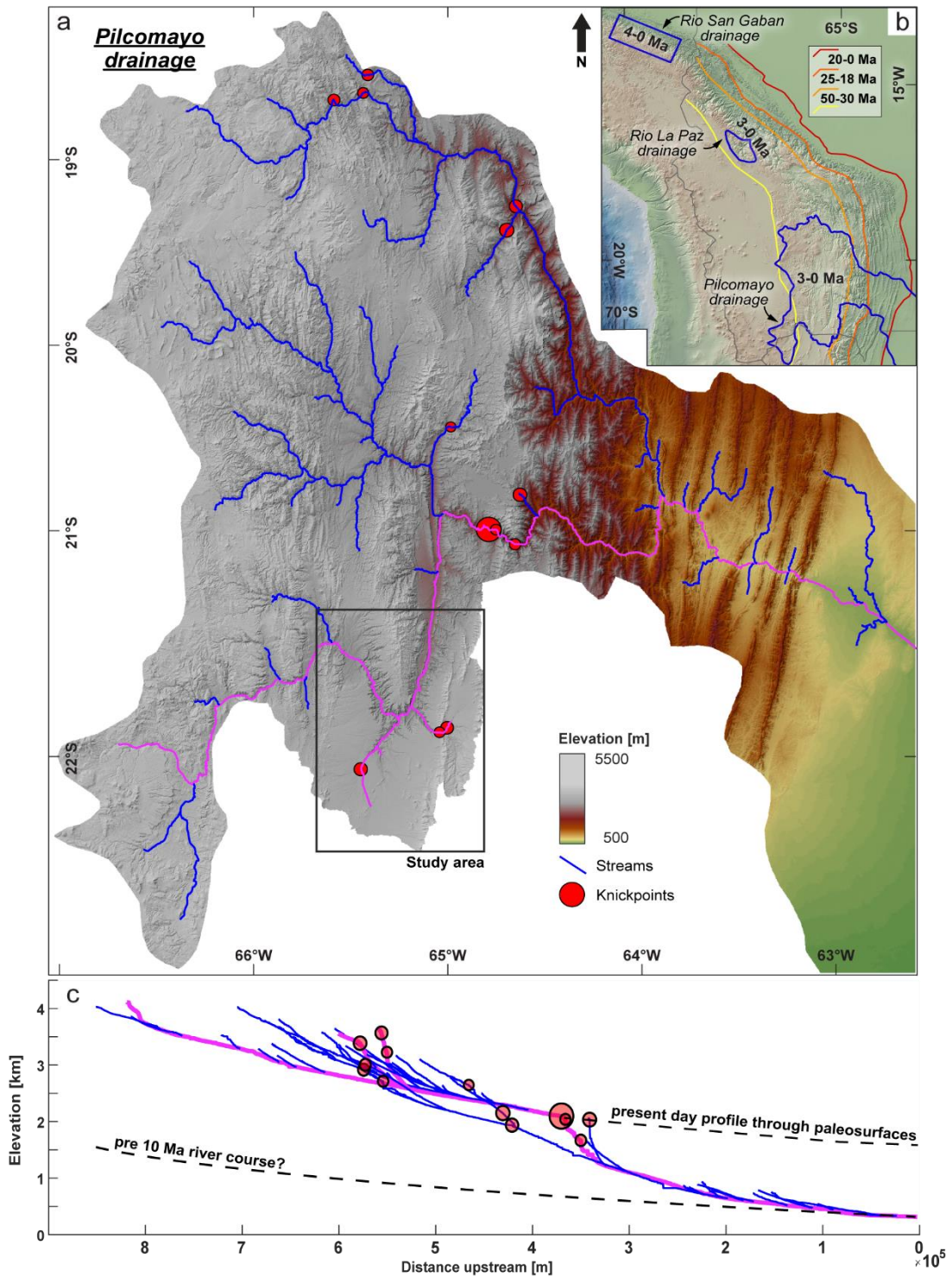


**Figure 31:** Pilcomayo drainage system and knickpoints. **a)** Digital elevation model of the Río Pilcomayo drainage basin (for location see Figure 3) with stream network (blue), selected streams and tributaries of the Río San Juan de Oro (magenta) as part of the southern Río Pilcomayo drainage basin and knickpoints (red dots). **b)** Overview map of the central Andes showing the different range-draining river catchments (blue lines) with onset ages of drainage development in black. Eastward-migrating onset of deformation is displayed in different colored lines. (Modified after Lease & Ehlers 2013). **c)** Longitudinal river profile of the drainage network from source to sink, traversing the Eastern Cordillera and foreland fold-and-thrust belt. Note the major knickpoint where the river crosses the border of the Eastern Cordillera. Upstream areas associated to the surface remnants found in the study area would have been adjusted to a foreland at around 2000 m a.s.l., as inferred from the upper dashed line. Projecting the present-day foreland slope uphill would result in a source area at elevations around 1500 m a.s.l. Elevation change is due in the order of 2000 m to 2500 m. (modified after Kennan et al., 1997).

In conclusion, from the observations made in this study it can be confirmed that widespread tectonic deformation and erosion processes must have influenced the region of the present-day plateau in north-western Argentina, but these processes were superseded by the deposition of sediment-fill units that characterize all Puna basins. These sedimentary fill units and associated paleo-surfaces in the study area, as stated by others, were not formed under endorheic conditions and neither are, nor were they associated to the internally drained basins of the Altiplano-Puna Plateau. They are rather remnants of a foreland basin that got successively incorporated in the Andean mountains by progressive east-directed migration of the deformation front and widespread surface uplift. As such, the incision into these surfaces does not directly imply a hydrological demise of the internally drained plateau area but rather reflects the long-term adaptation of a drainage system that is, and was, under the influence of tectonic modifications. However, hydrologically-driven processes of plateau demise were recently proposed to possibly affect the border of the central Andean Plateau in the future (Seagren & Schoenbohm, 2021), when ongoing headward erosion, stream capturing and drainage-divide migration could potentially lead to the tapping of the internally drained areas of the central plateau as already described along the northeastern border of the Andes (Zeilinger & Schlunegger, 2007; McQuarrie *et al.*, 2008; Lease & Ehlers, 2013), which could ultimately lead to widespread incision as observed on other examples such as the Iranian Plateau (Heidarzadeh *et al.*, 2017), the Colorado Plateau (Schmidt, 1988; Meek & Douglass, 2006) or even in the area of the northern Altiplano (Gérard *et al.*, 2021). Due to its large catchment area and associated erosive capacity, the Pilcomayo drainage system would be a potential initiator of such processes and should therefore be considered a major target for further analytical approaches on hydrologically-driven plateau destruction. Despite the tectonic modifications expressed by the regional uplift of the drainage system, as inferred from proposed lower paleo-elevations, the sedimentary-fill strata have not been modulated by compressional deformation since at least 8.3 Ma; moreover, the deposition of these voluminous fills apparently postdate the proposed onset of deformation and uplift in the Subandean Ranges to the east (Kley & Reinhardt, 1994; Echavarría *et al.*, 2003; Uba *et al.*, 2005). However, in light of the geological conditions associated with the formation of the basin fills in the orogen interior, the structural relationships and the geomorphic characteristics, regional uplift affecting the plateau must have been active in the last 10 Ma; this uplift appears to have been determined by a complex interaction of mantle-driven and structurally controlled processes that were accompanied by the combined effects of

subduction of the Brazilian Shield beneath the Andes and the subduction of the Nazca Plate at the convergent South American margin, which culminated in regional surface uplift, as initially proposed by Isacks (1988).

## **4.2 Extensional tectonic activity**

Based on the geochronological results, the landscape-evolution model, remote-sensing data, and stratigraphic relationships of the basin-fill units, the timing and extent of the extensional deformation of the north-eastern Puna Plateau can be assessed more precisely than previously. In this sub-chapter, remotely sensed information is used in a first step to infer the principal kinematic character of deformation; in this context the relative recency of deformation will also be addressed by inspecting the degree of re-adjustment of the drainage system with respect to the tectonic perturbations in the north-eastern Puna. In a second step, topographic profiles are used to determine absolute displacement values obtained from offsets affecting the gently inclined surfaces of the alluvial fans. In a third step, fault-plane orientations are put into context with the overall deformation characteristics and the tectonic stress field within the north-eastern Puna. In this context conjugated extensional joints are used to approximate slip vectors for the identified Quaternary tectonic structures. In addition, magnitudes of paleo-earthquakes are estimated from single-event displacement values that were retrieved from outcrop data. Finally, possible recurrence intervals of paleo-earthquakes are proposed based on a comparative analysis of the absolute and single-event displacement values with respect to the timing of deformation.

### ***4.2.1 Remotely sensed characterization of fault mechanisms***

The main purpose of the remote-sensing analysis was to identify the principal styles of faulting that governed the motion along the tectonic structures first described by Cladouhos *et al.*, (1994). These authors categorized the faults of the central eastern Puna Plateau as being dominated by strike-slip motion, with a minor component of normal faulting. In order to re-evaluate this assessment in the context of the regional deformation characteristics involving numerous normal faults and pervasively fractured basin-fill units, remotely-sensed data was used to determine and distinguish the style of faulting. The remote-sensing analysis of the present-day fault scarps and drainage anomalies conducted in this study adds valuable information regarding the tectonic overprint of the basin-fill strata. The data reveals that a component of vertical motion must have been of greater magnitude than

previously thought and it probably even exceeded the lateral component of motion, thus characterizing the study area as a region dominated by extension. The following section summarizes the key observations and discusses the rationale that lead to this conclusion.

The analyzed tectonic structures are expressed remarkably well by N-S-striking linear fault segments, with uphill-facing scarps that dissect the valley-fill units; these scarps form a stark contrast with the gentle slopes of the gravel-covered piedmont east of the Sierra de Escaya and the Cordillera de Sama. The linear character of these structures and the lack of secondary splay faults (Figure 18a, c) implies either a dominant component of vertical motion along the faults (Nash, 2013) or a recurring activity of transfer faulting because strike-slip fault zones usually tend to initiate as sets of subparallel segments that grow and merge into larger structures by linkage of smaller segments as deformation progresses over time (Joussineau *et al.*, 2007; Morley, 2017). Hence, if the structures were indeed primarily governed by strike-slip motion, the observed geometries would reflect fairly evolved fault segments in a strike-slip system. However, the general absence of distinct, offset channels, an emblematic of strike-slip fault zones (Wallace, 1968), suggests only a minor lateral component and dominant dip-slip motion to have occurred along these structures. The observed small-scale channel displacement could as well be guided by drainage reorganization due to the formation of a topographic barrier, initiated by dip-slip motion along the faults, blocking individual channels and forcing them to change course and merge with others. This would furthermore explain, why channels are redirected in both, a northern and a southern direction, instead of following a common, dominant pattern. In addition, the reliability of channels as offset markers has been questioned recently. For example, numerical modeling has shown that such offsets, if measured individually, exhibit large uncertainties of up to 30% and displacement values strongly depend on pre-deformation channel spacing and post-deformational surface processes (Reitman *et al.*, 2019). Drainage patterns taken by themselves are therefore not strong, unambiguous indicators of lateral motion. The only unambiguous indicator of potentially lateral displacement found in this study exists with respect to the offset of the drainage divides at the Pumahuasi Fault. Peak-displacement values of up to 1000 m (Figure 19c) were measured at the central section of the fault, decreasing toward the tips, as predicted by McCalpin, 2009 and Morley, 2017, thus suggesting a tectonic origin of these features. The displacement direction of the drainage divides indicates a component of left-lateral shear (Figure 19c), contradicting the interpretation of dextral kinematics as postulated by

Cladouhos *et al.*, (1994), which was primarily based on measured fault striae. In conclusion, either the fault-slip data was geometrically misinterpreted or the offset drainage divides formed as a consequence of other processes which cannot be further tested based on the existing data.

The probability of finding offset drainage divides in the same location as a mapped fault is not considered to be coincidental, and a structural context is most likely. If true, and regardless of the sense of shear, the large amount of displacement along the drainage divides could have only accumulated through episodically recurring fault activity, as no single rupturing event would be capable of creating such large amounts of displacement along a structure of that scale (Wells & Coppersmith, 1994). Interestingly, a striking contradiction arises from such a scenario and it has to be questioned why offsets are well pronounced in the drainage divides, but less so within the channel network and the individual streams, respectively. This phenomenon could be due to the nature of both features: while the channels undergo continuous erosion and reshaping by fluvial overprinting, the drainage divides at the topographic highs of the alluvial-fan surfaces are in a more stable position and less prone to post-seismic alteration by fluvial processes. Although the study area is located in a semi-arid to arid climate (Weischet & Endlicher, 1996; Castino *et al.*, 2017), in case of protracted tectonic quiescence, fluvial processes could have overprinted the tectonic features within the channels, while the drainage divides remained unaltered by erosion. The result of such processes could be akin to the geomorphic features observed here. Nevertheless, offset drainage divides are not found along the faults east and west of the Cordillera de Sama in Bolivia, indicating either more efficient surface-regrading processes or a complete absence of lateral components of motion along these two faults. A more precise evaluation concerning a lateral component of motion along the Pumahuasi Fault is currently impossible and seems far-fetched. In contrast, indicators of vertical motion are numerous and will be discussed in detail below.

The geomorphic information that can be extracted from the DEM-derived hillshades provides various indicators of vertical displacement. Due to the chosen illumination in the model, inclined, west-facing surfaces appear in lighter color with respect to the surrounding surfaces, as seen in the hillshade maps of the Pumahuasi Fault and the eastern flank of the Cordillera de Sama; conversely, inclined, east-facing surfaces appear darker with respect to their surrounding surfaces, as seen at the western flank of the Cordillera de Sama (Figure 18a, b). This relationship allows one to identify the direction of the free-face of the fault

scarp and implies that the more distal areas of the alluvial fans are higher-elevated with respect to the proximal parts, because the shading would be opposite for downhill-facing surfaces. Supporting observations were made by comparing the apparent depths of the channels that have incised the alluvial fans over time. The contrast at the edges of the channels is more developed in the distal areas of the fans, implying stronger and/or more efficient incision compared to the more proximal surfaces, where the edges are less pronounced (Figure 18a, b). Continuous channels that connect both sides of the faults, i.e., they are adjusted to the same base level, should not show strong gradients in discharge or incision, as this effect can only be achieved in the context of different surface elevations. The higher-elevated surfaces must show a stronger imprint of incision to adjust themselves with respect to the base level of the drainage system. This results in an overall impression of a more deeply dissected surface morphology in the distal areas of the fans. The distribution of low-slope surfaces around the tectonic structures agrees with the previous interpretations. Accordingly, proximal parts show more coherent low-slope surfaces, which are less dissected compared to the distal sectors. Linear anomalies that interfere with the low-slope surfaces are the faults and their pronounced vertical component of motion. The west-facing scarps have steeper slopes with respect to their surrounding areas and are therefore highlighted by blue colors in the slope maps (Figure 18b). On the other hand, the east-facing scarp to the east of the Cordillera de Sama has lower slope values than the far-field slopes of the affected alluvial fans and is highlighted by more yellow to reddish color coding on the slope maps (Figure 18d). Again, these well-pronounced, sharply defined escarpments point towards a prominent vertical component of fault motion.

Geomorphic features indicative of more pronounced dip-slip motion along these faults are also reflected by the local drainage network, which is affected by, and has already partly adjusted to the topographic disturbances. For example, the number of drainage channels drastically decreases as the fluvial networks approach the faults. This is due to the topographic barrier formed by the fault scarps, leading to the impoundment, redirecting, and beheading of channels. In addition, at the lines of intersection, small channels are forced to merge with other channels in order to maintain erosive capacity that enables the incision into the topographic barrier constituted by the hanging wall of the faults. Other channels were completely cut off from the drainage network, creating small ponds in the hanging wall at the foot of the fault scarps, previously described as sag ponds (Cladouhos *et al.*, 1994).

Finally, changes in the amount of discharge and erosivity must have led to disequilibria expressed in longitudinal river profiles; this is indicated by the variations in river steepness. For example, at first glance an increased steepness of river channels against a topographic barrier might seem difficult to explain, but to maintain flow across a topographic barrier, the river's erosional capacity had to increase, in this case by merging streams of the redirected channels. Furthermore, similar processes must have resulted in the creation of knickpoints along the fault, which are additional indicators of repeated vertical displacement. Unfortunately, the knickpoint magnitudes are neither spatially nor temporally consistent (Figure 19 and Figure 21), which renders them not useful for the quantification of displacement. Despite their usefulness in assessing the general characteristics of drainages in tectonically active regions to first order, knickpoints and variations in river steepness should therefore be interpreted with caution, as they could also result from a change in the mechanical strength of the substrate at the base of the channels (Pavano *et al.*, 2016). At isolated locations along the Pumahuasi Fault, outcropping basement rocks were mapped (Turner, 1964b), but they are not associated with all perturbations found along the streams draining the fault zone. As such, the possibility of changing substrate conditions in the channel beds potentially exists, but field observations did not support such an influence.

After the identification of vertical displacement along the studied faults, estimates of displacement values need to be brought into context with the age of the faulted strata, to better understand the period and frequency of tectonic activity. In order to quantify the component of dip-slip displacement, vertical separation was measured along elevation profiles crossing the alluvial-fan surfaces in areas not disturbed by fluvial overprint (chapter 2.2.5). The resulting data scatters over a wide range due to the measurements carried out on different alluvial fans that were probably active at different times in the past and frequently regraded; accordingly, they only record separate events in the tectonic processes (Figure 9). However, as the measured amounts of vertical displacement range between 13 and 26 m, it can be concluded that this must result from repeated fault motion as such high values are atypical for faults of this size and in this type of geodynamic environment (Wells & Coppersmith, 1994); this is further corroborated by the rather low, instrumentally recorded earthquake magnitudes in the orogen interior of the Central Andes (Doser, 1987; Cabrera *et al.*, 1991; Holtkamp *et al.*, 2011; Devlin *et al.*, 2012; Wimpenny *et al.*, 2018; Aguirre *et al.*, 2021).

The topographic and geomorphic analysis of the elevation profiles across the faults was performed on continuous surfaces that are isolated from the local drainage system and the mountain front; these features can only be explained by linear vertical motion as no range-parallel rivers exist in this environment that could have carved linear, asymmetric fluvial terraces. The age relationships between the different geomorphic surfaces and the degree of degradation of the escarpments suggests that fault scarps must have been active during or after the alluvial transportation surface containing the 2.86 Ma volcanic ash (Table 1 – Arg19-Ash01) was abandoned. A Pleistocene age of normal faulting is therefore viable.

### ***4.2.2 Faults, stress-field orientation and earthquake paleo-magnitudes***

In this study the faults analyzed by Cladouhos *et al.* (1994) were revisited in the field, and displacement values and fault-plane orientations were documented. Apart from the Pumahuasi Fault, the most notable expression of neotectonic surface deformation in the area, is the combination of pervasive joints and normal faults without prominent surface expression in the vicinity of Yavi (see chapter 3.7). These structures are overlain by the Quaternary alluvial-fan gravels that characterize the eastern piedmont of the study area. The exposed fractures and faults found in the sedimentary fill enabled a first-order assessment of the tectonic stress field during the late Tertiary to Quaternary.

#### ***Pumahuasi Fault***

The Pumahuasi Fault is characterized by a W-directed, uphill-facing fault scarp and forms an almost 40-km-long, N-S-striking linear structure that dissects alluvial-fan deposits in the piedmont of the Sierra de Escaya (Figure 3, Figure 19). Fault-scarp profiling shows that vertical displacement values of the alluvial-fan surfaces range from 13-26 m across a total fault-zone width of 50-250 m. The new field observations show that displacement is distributed over a set of fault branches, adding up to less cumulative displacement as recorded by the topography. A key outcrop in the central sector of the fault (Figure 22, chapter 3.6.1) records rupture along three fault branches; the steeply W-dipping (83°) main branch offsets the alluvial-fan strata 80-100 cm, whereas two minor, antithetic and synthetic branches offset the strata only by several centimeters. The trace of the main fault is marked by a 20 to 30-cm-thick fault gouge of beige to whitish clays and silts. Displacement of the sediment layers clearly identifies this structure as a normal fault. The overall arrangement of principal and secondary structures suggests that this fault may be part of a negative flower structure (Harding, 1985). The existence of several fault branches

in combination with the wide fault scarp indicates that the Pumahuasi Fault is an integral part of a linked fault system rather than a single-strand fault as described by Cladouhos *et al.*, (1994). Slip-partitioning over a set of additional faults within the subsurface would explain why the fault forms a wide deformation zone, instead of a narrow, but steeper fault scarp. Such additional faults were found close to the settlement of La Cienega, where the Tafna Formation and superseding alluvial-fan gravels are cut by two steeply westward-dipping normal faults. As these faults only accrue small displacement values, it is assumed that the main fault is not exposed at this outcrop. From the observations made along the Pumahuasi Fault, coseismic displacement of a single event along this structure is in a range of approximately 0.8-1 m and affected the whole sedimentary column, including the alluvial-fan gravels. Importantly, according to the structural observations made in the field, it can be concluded that the exposed faults of the Pumahuasi Fault zone are associated with an important component of normal dip-slip motion that caused vertical displacement in a cm- to m-range, but due to the fact that the main fault zone has been obliterated by erosion, these must be considered minimum values and the principal fault is inferred to have had more pronounced offsets (see chapter 3.6).

Another striking observation along the Pumahuasi Fault is the abundant exposure of the tuffaceous Tafna Formation. Although other deposits incorporating volcanoclastics can be found in the Central Andean Plateau, the large tuff-content and bright white color makes the Tafna Formation a remarkable deposit within the study area and a former target of kaolinite extraction (Kröger, 1956). In a structural context it is interesting that the Tafna Formation is exclusively found in the hanging wall of the Pumahuasi Fault, where it is limited to its central section surrounding the Río La Quiaca. The deposition of the Tafna Formation was thus coupled with motion on the fault and severance of the drainage system in the past. Turner (1964b) suggested that the Tafna Formation was deposited in local depressions and bodies of stagnant water associated with lacustrine episodes. Accordingly, during low-energy episodes of fluvial activity, volcanic ashes and eolian sediments were deposited in the hanging wall of the Pumahuasi Fault. The impoundment of the E-directed drainage system is therefore a viable mechanism that motion along the Pumahuasi Fault resulted in the deposition of the Tafna Formation within the tectonically formed depressions of its hanging wall (Figure 33); in this context, the large amount of pyroclastics can be explained by the trapping of volcanic ash within the formed bodies of stagnant water. This process must have been ongoing until the deposits in the hanging wall ultimately

reached the elevation of the footwall and overspilled the fault-controlled depocenter, thus leading to a reconnection with the regional drainage system, which was superseded by the deposition of alluvial-fan strata.

The interpretation that motion of the Pumahuasi Fault created a topographic barrier and accommodation space for sediments is thus a feasible scenario, which may partly explain possibly correlative sedimentary deposits that yield late Miocene to early Pliocene mammalian fossils (Quiñones *et al.*, 2019). This age range agrees well with the depositional ages of 6.83 Ma to 2.86 Ma based on volcanic ashes in the vicinity of the fault and west of La Quiaca (See chapter 3.2.1). In light of the regional pinch-outs and the areal extent of the Tafna Formation, including the topographically higher Pozuelos Basin in the west, a former connectivity of the paleo-drainage network and an overflow of the Pozuelos Basin (Figure 3) with resulting eastward flow and sediment transport appears to be viable. In contrast, Camacho *et al.*, (2015) have interpreted the Tafna Formation to be mainly of eolian origin, but this depositional model is difficult to reconcile with the observed facies character and distribution, which includes conglomeratic intercalations within the re-transported pyroclastic deposits. In any case, despite uncertainties regarding the tenuous correlation between outcrops of the Tafna Formation exposed at the Pumahuasi Fault and within the Pozuelos Basin, it can be concluded that the deposition of this unit was intimately associated with tectonic activity along the Pumahuasi Fault, and that the onset of faulting can be constrained to late Miocene time. Subsequently, the fault must have been active until at least 2.86 Ma, as this age corresponds to a volcanic ash sample from beneath the surface layer of a distal part of an alluvial-fan sequence that covers the Tafna Formation, and which is dissected in its proximal section by the Pumahuasi Fault. As these youngest deposits of the alluvial fans are part of a surface that records the complete cumulative displacement that was determined by the topographic profiles, it can be inferred that displacement was accrued after the material had been deposited at 2.86 Ma.

Another, but rather indirect indicator of extensional tectonism and fault-controlled hydrological connectivity along the Pumahuasi Fault can be inferred from the abundance of the ore mineral deposits in the fault zone. Although interpreted as a product of weathering by Cladouhos *et al.*, (1994), the density of mineral accumulation found in direct contact with the normal-faulted sectors and the steep westward dip of the deposits suggests a co-genetic origin. The fault zone was probably used as an upward pathway by hydrothermal fluids that carried high concentrations of dissolved manganese and iron that

were precipitated in form of several-meter-thick ore sheets. Such fault-bound manganese- and iron-ores are a common feature associated with extensional structures (Kuleshov, 2017) and were also described in a tectonic context in the United States (Chan *et al.*, 2000), Greece (Lykakis & Kiliyas, 2010), and Australia (Jones *et al.*, 2013; Jones, 2017). A fault-hosted precipitation can be further supported by the decrease of ore concentration in horizontally-layered sheets away from the fault.

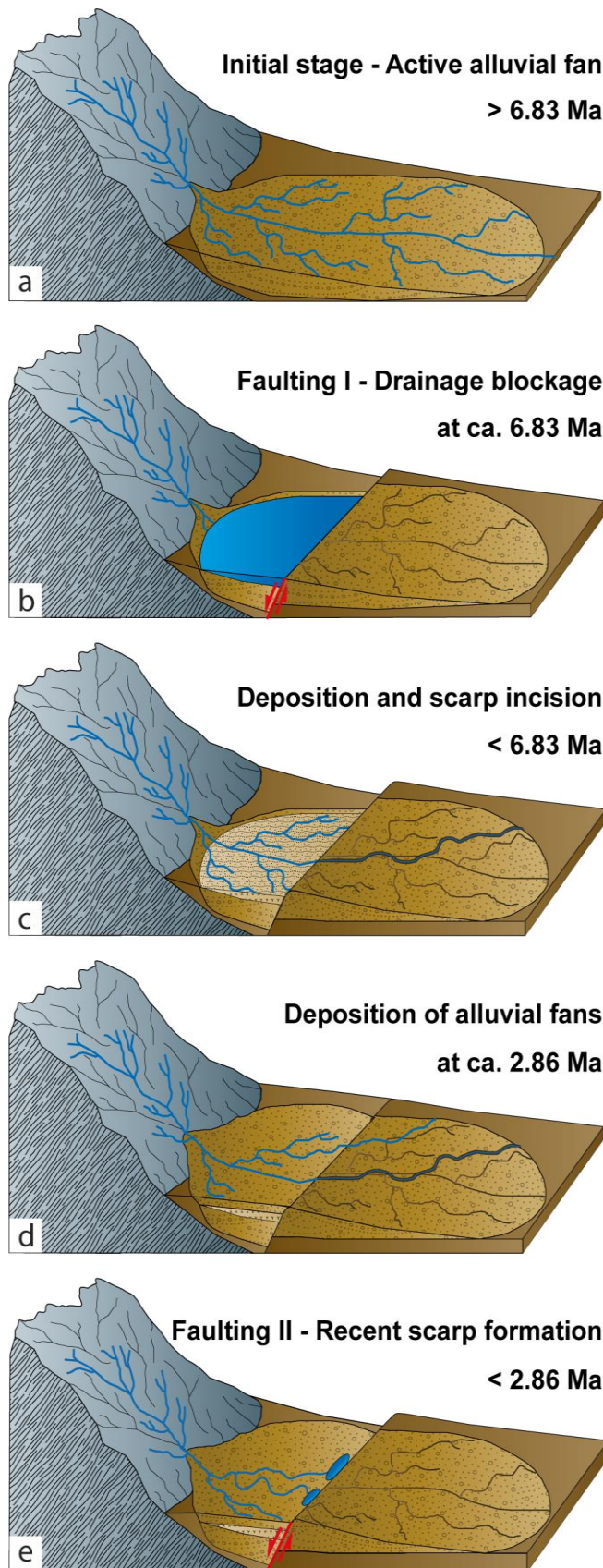


**Figure 32:** Late Miocene to Quaternary landscape-evolution model for the eastern piedmont of the Sierra de Escaya, activity of the Pumahuasi Fault, and the deposition of the Tafna Formation.

*a)* Initial stage prior to 6.83 Ma defined by the deposition of undisturbed alluvial-fan sequences.

*b)* Normal faulting along the Pumahuasi Fault, dissection of the alluvial fans in the footwall, and drainage impoundment. Streams on the footwall of the fault were disconnected and abandoned.

*c)* Some streams eventually cut through the footwall and re-connected drainage network. Deposition in the fault-related accommodation space in the hanging wall block against the free face of the fault scarp results in the fluvial strata of the Tafna Formation (beige unit). Volcaniclastics were also trapped within the fault-bounded depression. The depositional age of the Tafna Formation is 6.83 Ma and it thus postdates the activity of the Pumahuasi Fault.

*d)* Continued deposition of alluvial-fan sediments filled the depression, thus obliterating the scarp morphology and providing connectivity with lower sectors of the piedmont. Volcaniclastics dated at 2.86 Ma and interbedded within the distal section of this alluvial-fan sequence, predates the formation of the present-day fault scarp and the renewed severed drainage conditions.

*e)* Repeated tectonic activity of the Pumahuasi Fault since then accumulated vertical displacements between 13 and 26 m by repeated faulting since then. While streams on the footwall were again abandoned, sag ponds formed on the hanging wall. The fault scarp eventually degraded to its present-day morphology. Simultaneously, the drainage system partly re-incised into the scarp leading to partial connectivity with the areas to the east.

*Yavi fault(s)*

Despite not showing a prominent surface expression, the faults east of the village of Yavi record unambiguous extensional deformation that affected the fill units. Faults exposed in a roadcut immediately east of the Río de Yavi and below the ‘upper surface level S1’ is the most remarkable example. A striking feature of this outcrop is a steeply westward-dipping fault that offsets basin-fill strata, although the exact amount cannot be measured due to the lack of piercing points (Figure 26). From a distance however, it can be recognized that a brown to orange-colored sand horizon stands out in the upper section of the footwall and this horizon re-appears farther SSW in the hanging wall, around 5 m below the footwall, where it is overlain by brown to greyish sands and conglomerates. There, the brown to orange sands are covered by a dark-brown to skin-colored, strongly carbonate-cemented conglomerate of one meter thickness that is similar to the sediments that were sampled for exposure dating of Surface S1 (see chapter 2.1.4). The stratigraphic difference between footwall and hanging wall implies that the block on the SSW side of the outcrop had moved along the westward-dipping normal fault by about 5 m. Accordingly, the superseding layers on the hanging-wall block are not present on the footwall block where they were eroded or not deposited (Figure 33).

Additional fault branches exist farther NNE along the footwall block, where two minor, eastward and westward-dipping faults offset the sedimentary succession by up to 2 m. A clockwise-rotated (45°) wedge appears to fill the opening between the two faults, suggesting that the layers may have been warped instead of faulted. The skin-colored, carbonate-cemented conglomerate forming the top of the footwall is 3.05 m.y. old (Table 1, sample Arg21-Ash05) and pinches out toward the SSW, limiting it to only a thin layer on the hanging wall. As this conglomerate layer was moved along the fault for about 5 m, the timing of faulting is consequently younger than 3.05 Ma. A sand-filled joint of approximately 20 cm width in the upper conglomerate layer of the hanging wall, along with the large number of joints within the strata, is a direct result of extensional strain. Together, the deformation along the opposing faults forms a horst-and-graben structure, typical for extensional environments (Fuller & Waters, 1929; Valdiya, 2016). Additional westward-dipping faults with minor displacement (cm-range) were found at the SSW section of the outcrop (Figure 26). Due to their small offsets and the nature of the overlying conglomerates, the faults cannot be traced further into the upper layers. Nonetheless, they

must be the result of similar processes and could either be formed during an earlier or the same episode of extension that generated the major fault in the NNE section.

Farther south more evidence of normal faulting affecting the sedimentary fill units was identified along the walls of a narrow gorge. Two faults of opposing dip offset the fill units vertically, whereas one of the faults generated a displacement of approximately 40 cm (Figure 27), the opposing fault only generated a minor offset involving 5 cm. Similar to the larger structures described above these opposing faults also form a half-graben structure. Unfortunately, due to the friable nature of the deformed sediments it was not possible to identify potential continuations toward the top or the bottom of the gorge. Farther west however, and closer to the entrance of the gorge, a major structure was found that offsets conglomerates against sand layers along a steeply eastward-dipping fault plane. As no piercing points were found, offsets must be greater than the vertical extent of the outcrop. As at the other outcrops, multiple sets of conjugated joints could be identified at this locality as well.

Finally, close to Yavi Chico, an outcrop of complexly faulted strata was found at the valley flanks of the northward-draining Río Casti. Although this outcrop cannot be connected with the two previously discussed N-S-striking fault zones, the fault zone follows the overall trend of the other structures with a major, steeply west-dipping fault, while a set of a synthetic and antithetic faults root in this major structure. The main fault is characterized by a 10 to 20-cm-thick fault gouge. As in the previously discussed cases, most of the faults in this outcrop are highlighted by a cm-thick-layer of white sands that form a pronounced contrast with the surrounding darker-colored sediments. Lenses of volcanic ashes were also sheared along sub-horizontal fault planes, that were dated at  $7.75 \pm 0.06$  Ma (Table 1, sample Arg21-Ash07), thus setting a maximum age of deformation at this site. However, as the site is of lower elevation and thus within a section of older stratigraphy as the discussed section earlier, the deformation could have been possibly associated with the same episode of extension that generated the other faults, which must have started after 3.05 Ma.

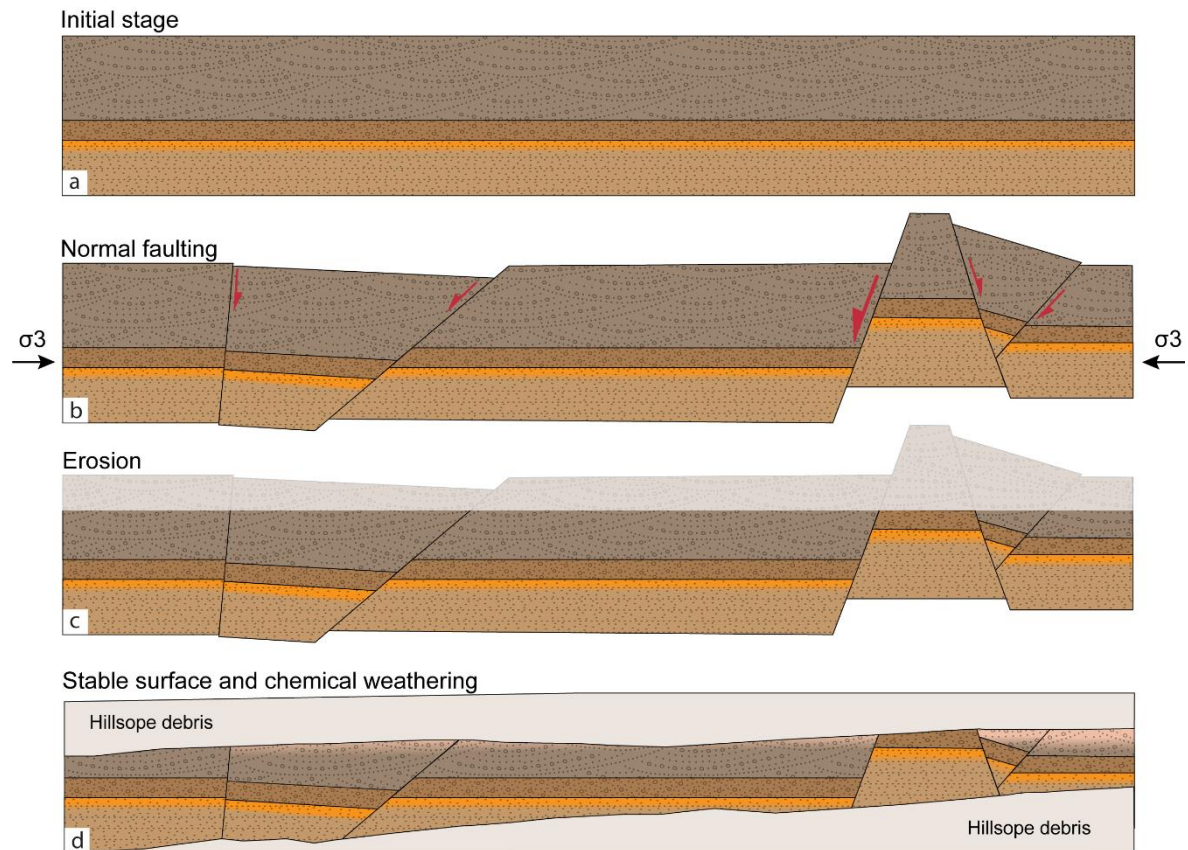


**Figure 33:** Tectonic overprint of sedimentary fill units observed in and along a road cut east of the village of Yavi - compare to photo a in (Figure 23). **a)** Initial condition of horizontally layered strata of the upper fill units. **b)** Normal faulting along several fault branches has created a horst-and-graben structure. The most reliable piercing point is marked by the boundaries of the orange to brown-colored units that stand out from the other sediments and that mark the transition from sand to conglomerates. The least horizontal stress  $S_{hmin}$  ( $\sigma_3$ ) is inferred to have been oriented approximately E-W. **c)** Erosion of the upper layers of the deposit beveled the deformed surface. **d)** Protracted surface stability resulted in weathering and the formation of calcic soil horizons, leading to a color change in the upper conglomerate horizon.

### Conjugated joints

The orientations of the ubiquitous conjugated extensional joints within the sedimentary fill units were measured with the aim to support the interpretation on the principal axes of the stress field that caused the pervasive fracturing and faulting. In contrast to the orientation of the faults, whose geometry and orientation could be biased by pre-existing, basement-associated, crustal heterogeneities (Hongn *et al.*, 2007; Cook & Royden, 2008), the joints found within the sediment layers reflect the unperturbed orientation of the regional shallow crustal stress field (Whitaker & Engelder, 2005; DeGuidi *et al.*, 2013). A compilation of all measured joint orientations is displayed in Figure 35a. Although variability in joint orientations exists, a primary trend in NE-SW orientation and a secondary trend in NW-SE direction can be deduced (Figure 35a). Applying a quantitative inversion technique on this

data allows to infer the causative tectonic stress tensor (Caputo & Caputo, 1989). The resulting strike-perpendicular vector represents the opening direction of the joints and thus, the applied least horizontal stress  $S_{\text{hmin}} (\sigma_3)$ , displayed by the Kamb-contour plot in Figure 35b. This results in a WNW-ESE orientation for the least horizontal stress  $S_{\text{hmin}}$  (Figure 35c). However, this method only allows to infer  $S_{\text{hmin}} (\sigma_3)$  - the orientation and magnitude of the principal horizontal stress ( $S_{\text{Hmax}}$ ) and the vertical stress ( $S_{\text{V}}$ ) can only be estimated from the joint orientations. The major principal stress ( $\sigma_1$ ), capable of forming the observed extensional joints of the measured orientations could have acted in a vertical, or a horizontal position, parallel to the strike of the joints. Both possibilities are feasible to create the observed deformation. However, the fact that the joint orientations and the strikes of the analyzed normal faults are overall similar and broadly compatible with an ESE-WNW-to NW-SE-oriented tensional stress field suggests that an extensional deformation regime has been responsible for deformation processes in the north-eastern Puna during the Quaternary.

### ***Fault kinematics***

Additional information on the orientation of the major principal stress ( $\sigma_1$ ) can be made regarding the orientations and mechanics of the faults documented in this study. The measured fault-plane orientations of all structures are displayed in Figure 35d. The majority of the structures strike N-S (average of all data  $89.4^\circ$  direction with a standard deviation of  $20^\circ$ ) and dip with intermediate to high angles in E- and W-direction (Figure 35d). When combining the structural measurements and the observed mechanisms of faulting along these structures, an approximately E-W-oriented extension direction can be derived from the measurements (Figure 35e). As this result does not directly correlate with, but is rather oblique to the opening direction inferred from the joints, the structural relation between these two tectonic features allows to indirectly derive the direction of the major principal stress axes. Interestingly, when the extension direction derived from the joint orientations is considered, then the tectonic regime affecting the sedimentary fill should have been characterized by transtensional motion along the N-S oriented fault planes by partitioning the slip vector into N-S-directed, right-lateral shear, and an E-W-oriented extensional component (Figure 35f). This observation is the key element to determine the orientation of the major principal stress,  $\sigma_1$ .

As stated above,  $\sigma_1$  could either be oriented horizontally in NE-SW direction or vertically in the z-direction. Although the former would generally agree with measured, recent

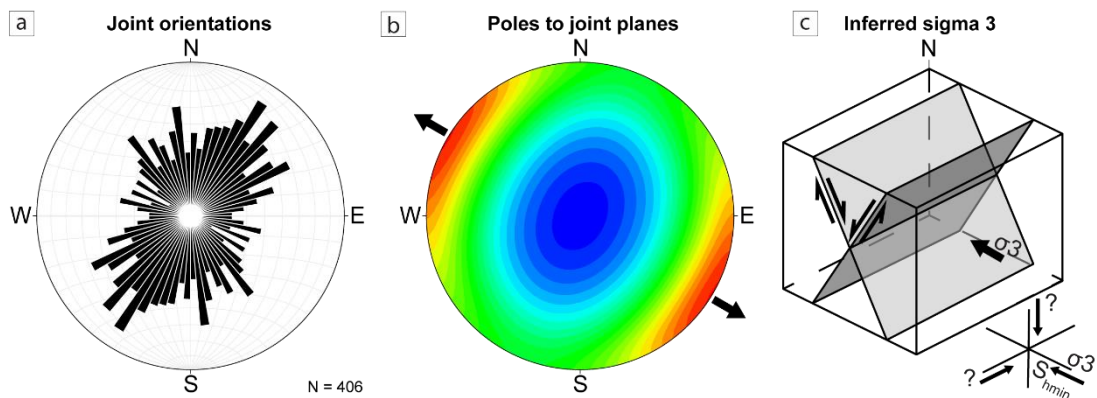
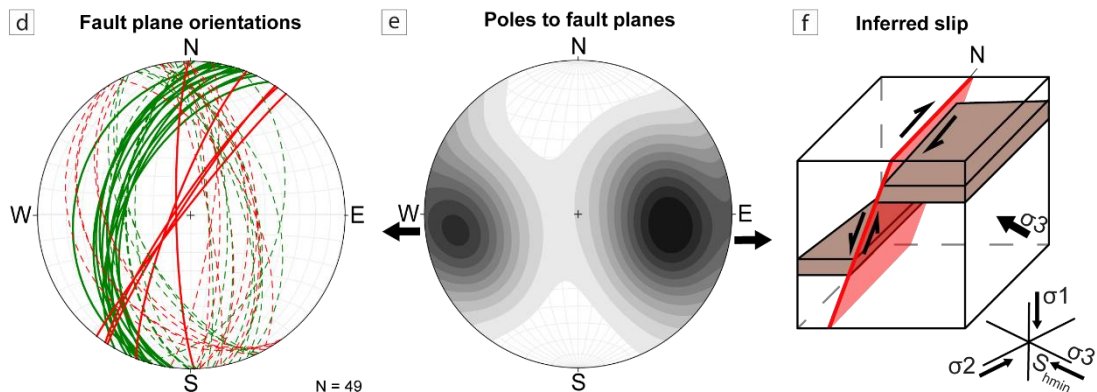
regional shortening directions provided by GPS measurements (McFarland *et al.*, 2017; Figueroa *et al.*, 2021), it would generate compressional and transpressional deformation, respectively. This type of deformation contradicts the observed kinematics in the field and the fault categorization by Cladouhos *et al.*, (1994) who suggested right-lateral fault motion. As such, a horizontal principal stress direction cannot reconcile the deformation patterns that have affected the sedimentary fill. Instead, a vertical position of the principal stress and a horizontal intermediate stress tensor would be needed to result in the observed normal faulting and minor strike-slip faulting, a scenario which is compatible with the observed deformation structures.

Intriguingly, the resulting right-lateral shear supports the mechanical interpretation for the Pumahuasi Fault proposed by Cladouhos *et al.*, (1994) and contradicts the left-lateral displacement derived from the displaced drainage divides (see chapter 3.4.3). As the former is based on geological and geo-mechanical evidence from field data, the latter was extracted from remotely sensed surface data, which may be biased by post-tectonic, erosion and deposition processes, the field-based observations are considered to be more trustworthy and the structural context of faults and joints confirms the interpretation from Cladouhos *et al.*, (1994). Finally, the observed deviation in orientation between the faults and the joints allows to suggest the two following conclusion: First, if the faults and joints were formed under the influence of the same stress field, which appears to be plausible since both structural features affect the entire sedimentary-fill succession, the faults must in fact have hosted transfer motion during their time of activity. In addition, the obliquity of the faults with respect to the stress field suggests that the fault orientations might be associated with inherited crustal heterogeneities that were reactivated during this phase of extensional tectonism. The reactivation of faults is mechanically and energetically often favored over the creation of new structures and has been described in a variety of settings (e.g. Sibson, 1985). Although the faults described here are found in young sediments and show intermediate to steep dip angles as expected from normal faults, the existence of basement rocks at shallow depths and the basement ranges in the vicinity point towards a possibility that their position and strike may have been influenced by pre-existing heterogeneities in the bedrock underlying the intermontane fill units. Moreover, the measured strike of the faults follows the N-S-oriented trends of the basement ranges and intervening basins that originally resulted from regional shortening of the crust and potentially compressive reactivation of former normal faults (e.g. Carrera & Muñoz, 2008 among others). It is thus

conceivable that the deformation of the sediment-fill units may be guided along reactivated structures that had been formed during the compressive tectonic pulses that deformed the Andes prior to the regional extension.

In a regional context, these observations proof the concept of earlier works that focused on the tectono-mechanical development of the Central Andes and the sectors of the Altiplano-Puna plateau. Allemendinger *et al.*, (1986) showed the existence of young normal faults and strike-slip faults along the southeastern margin of the Puna Plateau. Although missing precise age data, the presence of deformed, widespread Punaschotter – whose descriptions appears to resemble the conglomerate cover described in this study – allowed to infer a Quaternary age (between ~3 Ma and present) of deformation. Hence, these structures must have formed after a change in regional dynamics and tectonics of the mountain building has occurred (Allmendinger, 1986). A Late Neogene onset of young extensional deformation was further emphasized by Marrett *et al.*, (1994) who found normal and strike faults, independent of elevation in different sectors of the mountain range between 28° and 20° S. This evidence allowed these authors to favor a regional cause for the change in dynamics and the onset of extensional deformation instead of a process that was driven by local body forces (Marrett *et al.*, 1994). Proof for the widely distributed occurrence of such extensional structures can be drawn from works that were carried out in the Central Altiplano Plateau of Peru, where recent normal-faulting was described (Dalmayrac & Molnar, 1981; Mercier *et al.*, 1991; Wimpenny *et al.*, 2018). As already stated by Schoenbohm *et al.*, (2009) and Montero Lopez *et al.*, (2010), extensional deformation of not just the Puna but the whole Andean Plateau appears to be widespread yet spatially disparate and therefore, the structures analyzed in this work must be part of such a phenomenon.

Within this reference frame, the observations from all analyzed outcrops, involving the Yavi and Pumahuasi faults, as well as the joint measurements and the inverted orientation of the principal stress components, a distinct pattern of transtensional deformation emerges for the eastern Central Andean Plateau.

**Joints****Faults**

**Figure 34:** Structural data compilation of the conjugated joints and the two different faults identified in the study area. **a)** Rose diagram showing the orientation of the 406 measured joint orientations. The majority of joints shows a NE-SW trend, whereas the minority is oriented perpendicularly in NW-SE direction. **b)** Kamb-contour plot of the inverted poles of the joint planes. High density of poles is indicated by warm, small density in cooler colors. Inferred NW-SE opening direction of the joints is indicated by black arrows. **c)** Block scheme of exemplary conjugated joints and applied minor principal stress ( $\sigma_3$ ) perpendicular to the opening direction of the joints. Major principal stress ( $\sigma_1$ ) could possibly be applied parallel to the joint-plane orientation or vertically. **d)** Stereoplot of the measured major fault planes in solid lines and minor, as well as partly anithetic faults in dashed lines (Pumahuasi in red and Yavi in green). Faults strike approximately N-S ( $89.4^\circ \pm 20^\circ$ ) with intermediate to steep dip angles. **e)** Contour plot of the fault plane poles. High density is indicated by dark colors, low density in light colors. The majority of the poles is oriented in E-W direction. **f)** Schematic block of an exemplary N-S striking fault with E-W directed extension along steeply dipping normal fault (red plane). Following the joint orientations, the minor principal stress is applied in NW-SE direction. The major principal stress must be applied vertically to create extensional strain as a horizontally applied major principal stress would result in thrust faulting. Accordingly, the intermediate principal stress ( $\sigma_2$ ) is applied horizontally in NE-SW direction. The resulting slip vector along the faults is split into E-W oriented extensional and N-S oriented transfer motion, hence transtensional faulting.

**Estimated magnitudes of past earthquakes associated with the Pumahuasi Fault**

The surface-rupture length of the faults and the apparent single-event coseismic displacement values derived from the Pumahuasi Fault (see chapter 3.6.1) were compared with empirical fault data to gain more insight into the seismogenic behavior of this fault. A global catalog of empirical data on fault length, fault displacement, and earthquake magnitude compiled by Wells & Coppersmith (1994) is commonly used to view fault-zone data into a semi-quantitative seismogenic context. By using regression-derived equations

of the catalogues data, moment magnitudes associated with the surface-rupture length of the Pumahuasi Fault (35-45 km) can be calculated, which results in paleo-earthquake magnitudes of approximately  $M_w = 6.9 \pm 0.8$ . In the hypothetical case that the fault had been primarily characterized by strike-slip motion, the corresponding moment magnitudes would have been  $M_w = 6.9 \pm 0.3$  (Figure 35a). Both values are comparable in size and agree within error. When using an average displacement of about 0.6-1 m as observed at the different fault branches, a paleo-magnitude of  $M_w = 6.5 \pm 0.2$  would be compatible for this amount of displacement (Figure 35c). Thus, the calculated paleo-magnitudes for events along the Pumahuasi Fault may have ranged between  $M_w = 6.1$  and  $7.7$  (Figure 35). It should be noted that the result of the displacement-based magnitude determination solely relies on the measured vertical displacement, neglecting displacement associated with a possible lateral component of motion, because the measured displacement along the offset drainage divides contrasts the previously interpreted fault kinematics. If the Pumahuasi Fault did indeed accommodate some lateral motion during its latest activity, the derived magnitudes of paleo-earthquakes may have been even higher.

For the faults at the Cordillera de Sama, Bolivia, only the surface-rupture length can be used to infer paleo-magnitudes, due to the lack of robust field data. As such, the paleo-magnitudes for the 10 to 13-km-long scarps at the flanks of the Cordillera de Sama would be in the range of  $M_w = 6.3 \pm 0.7$  for a normal faulting mechanism, and  $M_w = 6.3 \pm 0.3$  for strike-slip earthquakes (Figure 35b).

Unfortunately, the same approach cannot be used for the faults close to Yavi, due to the absence of a clear surface expression of the fault and the lack of precise, single-event displacement measurements. Nevertheless, in light of the observed 5 m of dip-slip offsets, it can be inferred that this fault must have been repeatedly active in the past.

### ***Recurrent fault activity***

An intriguing question concerning the Pumahuasi site exists as to how the measured cumulative displacement can be explained in light of recurrent, individual earthquakes. Using a simple approach to determine the number of events that occurred along the Pumahuasi Fault, cumulative displacement as recorded by the offset alluvial-fan surfaces involving 13 to 26 m can be divided by the amount of single-event displacement values as recorded by the obtained outcrop data of approximately 1 m vertical offsets, which is also a realistic amount for a fault of 40 km length as shown by empirical data compiled by Wells

& Coppersmith (1994). This, however, is based on the assumption, that earthquakes produced by such a fault follow a characteristic behavior, i.e., the events had always a comparable size. According to this approach, between about 13 and 32 earthquakes could have ruptured the Pumahuasi Fault since its onset of motion.

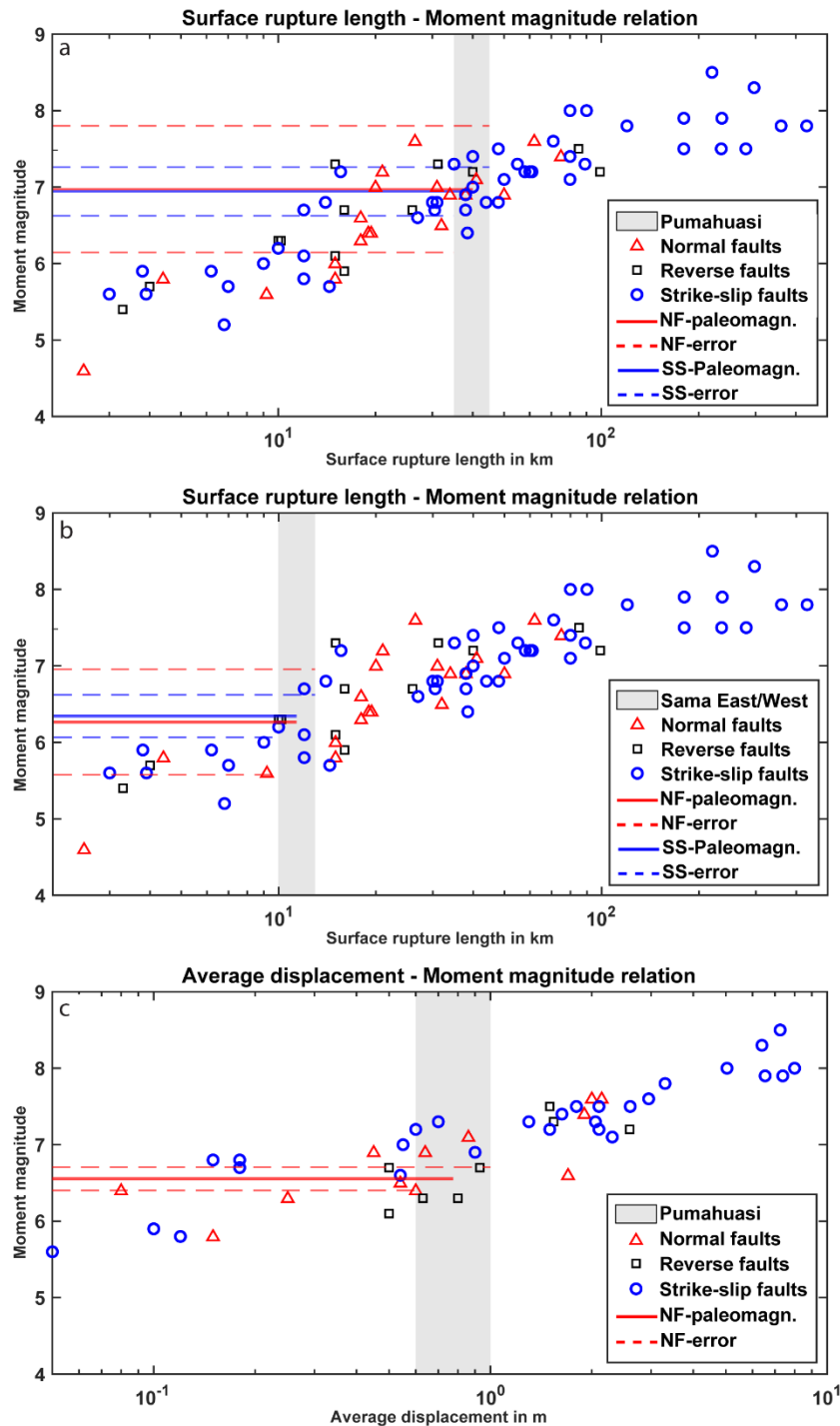


**Figure 35:** Magnitudes of possible paleo-earthquake events that formed the scarps and generated the coseismic displacement, as recorded by the offset sediments, in relation to the empirical dataset compiled by Wells & Coppersmith (1994). The empirical data is highlighted by the designated markers as shown in the legend. The fault data, surface-rupture length and average displacement, from this study is shown in grey bars. The calculated magnitudes are plotted as solid lines, the associated errors in dashed lines and color-coded as the empirical data. **a)** Surface-rupture length - Moment-magnitude relation plot and calculated paleo-magnitudes for the Pumahuasi Fault with the assumption of a 35 to 45-km-long fault scarp and surface rupture length, respectively. Magnitudes are between  $M_w = 6.1$  and  $7.7$ . **b)** Surface-rupture length - Moment-magnitude relation plot and calculated paleo-magnitudes for the faults east and west of the Cordillera the Sama, assuming a 10 to 13-km-long fault scarp and surface-rupture length, respectively. Magnitudes are between  $M_w = 5.6$  and  $7.0$ . **c)** Average displacement - Moment-magnitude relation plot and calculated paleo-magnitudes for the Pumahuasi Fault assuming a 0.8-1 m displacement. Magnitudes are between  $M_w = 6.1$ - $7.7$ . Although based on different approaches for paleo-magnitude calculations, the results provide comparably sized earthquake magnitudes.

### 4.2.3 Timing of tectonic activity

A first-order constraint for the timing of deformation can be defined by the depositional ages of the tectonically affected intermontane-basin strata. According to the U-Pb dating of the intercalated volcanic ashes, the deposition of the sediments was time transgressive from at least  $8.23 \pm 0.05$  Ma to  $2.86 \pm 0.02$  Ma. As all described faults, except for the partly inaccessible ones around the area of Yavi (see chapter 3.7.2 and chapter 3.7.3), affect the surface of the dated sediments, active tectonism along these structures must postdate the youngest depositional ages of 2.86 Ma. This age therefore provides the maximum age of faulting. Indicators of older tectonic activity, for example structures and growth strata that terminate before reaching the surface, were not found in the field. The sole, yet also hypothetical indicator of syn-sedimentary deformation proposed in this study was associated with late Miocene motion along the Pumahuasi Fault and was considered a possible trigger mechanism for the deposition of the Tafna Formation (see chapter 4.2.1). If true, the tectonic activity along the Pumahuasi Fault would predate the depositional ages of the incorporated ashes and hence exceed the age of 6.59 Ma of the oldest dated sample taken from the Tafna Formation. This timing would furthermore coincide with the proposed onset of extensional deformation in the southern Puna (Montero-López *et al.*, 2010) and magmatic manifestations associated with normal faulting in the Salar de Antofalla region (Risse *et al.*, 2008), the Cerro Galán area (Kay & Coira, 2009), and in the area of Antofagasta de la Sierra (Kraemer *et al.*, 1999; Zhou *et al.*, 2013; Filipovich *et al.*, 2019). In the context of the overall spatiotemporal geodynamic setting of the study area, this timing would also postdate the eastward migration of the deformation front towards the foreland fold-and-thrust belt between approximately 10 and 8 Ma (Gubbels *et al.*, 1993; Allmendinger & Zapata, 2000; Echavarría *et al.*, 2003). However, the displacement that is reflected by the scarp of the Pumahuasi Fault must have been accumulated after the alluvial-fan strata were deposited. As such, the entire strain recorded by the alluvial-fan surfaces was accumulated after 2.86 Ma. Possible older surface deformation was obliterated by erosion and regrading of the surfaces prior to the deposition of the last alluvial-fan sequences.

More detailed age determinations are provided by surface-exposure ages and the observed deformation around the village of Yavi. As for the Pumahuasi Fault, the structures penetrate the surface and thus must have been active after the deposition of the youngest deposits at approximately 3.05 Ma. However, the tectonic features in the vicinity of Yavi, which are

now covered by the gravels of the 'upper surface level S1', were apparently beveled between 2.39 and 2.9 Ma after extensional deformation had taken place, as none of the structures shows evidence for having caused renewed surface deformation. Based on these facts, the timing of extensional tectonism can be further constrained and a late Plio- to early Pleistocene episode of extensional tectonism can be deduced. Due to the lack of single-event displacement values for the faults around Yavi, further paleoseismological analysis has to be restricted to the Pumahuasi Fault.

With the assumption that the proposed timeframe of extensional tectonism is also valid for the Pumahuasi Fault, and that paleo-earthquakes followed a characteristic behavior (Schwartz & Coppersmith, 1984), recurrence-interval estimates can be calculated by dividing the time of deformation by the amount of earthquake events that was inferred from the relation between cumulative and single-event displacement. According to this simplification, faulting along the Pumahuasi Fault occurred over a timeframe of 150-660 ka, with hypothetical recurrence intervals on the order of 4.7 to 50.7 ka, but faulting did apparently not continue into the Holocene. An additional approach of determining the age of these scarps via fault scarp degradation modeling (Wallace, 1977) could not be carried out as the scarps form uphill-facing instead of downhill-facing free faces, a geometry that breaches the limitations of the diffusion equation (Hanks, 2000).

### 4.3 Implications for an orogenic collapse

According to van Bemmelen, (1965) “*All geodynamic processes should be explained by the fundamental principle of the strive for gravitational equilibrium*”. Based on this statement, the geodynamic implication of the results from this study are discussed with respect to the concept of an orogenic collapse that affected the Puna Plateau, because the study region is characterized by a changeover in kinematics from widely distributed shortening and uplift to extension, which reflects profound changes in the tectonic stresses that might eventually cause the collapse of the orogen.

The tectonic collapse of mountain ranges and associated orogenic plateaus is generally driven by the synergistic interaction of two main factors: erosion and gravitation (Jadamec *et al.*, 2007). Despite the fact that these processes constitute an integral part of orogenic processes and are closely linked with the build-up of topography through crustal shortening that might furthermore be coupled with mantle delamination and ensuing isostatic uplift, the combined elevation and mass of the orogen will ultimately exert a gravitational force that counteracts the plate-tectonic forces that drive shortening and uplift and thus cause the maintenance of the plateau at high elevation (Sébrier *et al.*, 1988; Mercier *et al.*, 1991). Gravitation will induce crustal thinning and tectonic denudation by extensional faulting (Molnar *et al.*, 1993). This process thus releases potential energy, eventually reduces topography and it may be accompanied by areally widespread erosional processes that help downwearing the topography. The erosion of the plateau region may be more pronounced at this stage, because the previous uplift-induced, localized downcutting along a few rivers draining the plateau flanks will be substituted by knickpoint migration toward the plateau interior and more pronounced lateral erosion. Such a scenario exists in the upper reaches of the upper Río Pilcomayo drainage, the Río Consata, and Río Grande. The combination of structural and geomorphological observations thus points toward the existence of an important geodynamic process that has impacted the high sectors of the Central Andes.

In light of these observations the thrust-fault bounded ranges and the normal faults and ubiquitous joints within the sedimentary intermontane basin strata of the north-eastern Puna constitute unambiguous evidence for a transition from a compressional to a tensional, perhaps transtensional state of crustal stresses that was established during the late Miocene to Pliocene. In contrast, a protracted compressional stress field continued to affect the topographically lower plateau flanks and foreland sectors, and still causes deformation

associated with thrust faulting until the present day. This is comparable to the evolution of the tectonic stress field in the Peruvian and Bolivian Altiplano (Sébrier *et al.*, 1988; Mercier *et al.*, 1991; Wimpenny *et al.*, 2020), the southern Puna (Allmendinger, 1986; Schoenbohm & Strecker, 2009; Montero-López *et al.*, 2010), and other Cenozoic plateaus (Armijo *et al.*, 1986; Molnar *et al.*, 1993). The observed fault patterns in the intermontane basins of the Puna are thus not a local structural anomaly, but they rather represent manifestations of expected tectonic processes in the orogen's interior, where the plateau must have reached an elevation threshold that was not conducive for further crustal shortening.

Although not synchronous with the onset of normal faulting in the high plateau, it appears likely that compressional deformation migrated eastward and triggered deformation in the Subandean fold-and-thrust belt (e.g., Echavarría *et al.*, 2003), when the critical plateau elevation had been attained. According to the depositional and exposure ages of the sampled strata in the alluvial-fans of the north-eastern Puna, the extensional episode affecting these areas must have lasted at least from late Pliocene to early Pleistocene, but in case of the Pumahuasi Fault it may have started as early as 6.59 Ma. Importantly, normal faulting must have terminated in this part of the plateau by 2.39 Ma, a conclusion which is supported by the lack of present-day surface deformation and seismicity. Despite these observations, the most recent normal-faulting earthquake in the Eastern Cordillera to the southeast clearly indicates that the tensional stress field associated with the highest sectors of the Andes is still responsible for local extensional deformation, which, when it is viewed at the scale of the entire plateau, is highly disparate in space and time.

## 5. Conclusion

The results of this study contribute to a better understanding of the late Tertiary to Quaternary tectonic and sedimentary evolution of basins in the southern Central Andes of northwestern Argentina. This region includes the Andean Plateau (Altiplano-Puna Plateau), the second-highest orogenic plateau on Earth, which is a high-elevation, low-relief region in the interior of the orogen. The plateau is characterized by a low degree of active tectonism and seismicity, and for the most part, it is internally drained. In Argentina, however, the plateau has a fluvial outlet in its northeastern part – the area of this study –, which is connected with the Río Pilcomayo that drains toward the foreland. For the first time, the timing of the late Cenozoic sedimentary, erosional, and tectonic processes within the northeastern Puna Plateau could be quantified by combining radiometric and cosmogenic nuclide dating, structural, geomorphic and sedimentary analysis.

The first part of the thesis sheds light on the landscape evolution of the central-eastern Andean plateau, where the headwaters of the Pilcomayo drainage system are currently incising into thick sedimentary fill deposits; this has formed a landscape of alternating basins and ranges, gently inclined, sequences of abandoned alluvial-fan surfaces at high elevation, and deeply incised canyons. After the Andes rose to a primary altitude, deposition of these sediment units took place from at least 8.78 Ma until approximately 2.86 Ma, with sedimentation rates of 10-20 m/Ma, which are reasonable rates in the environmental context of the semi-arid climate of the study area. According to the observed facies, the depositional environment was characterized by a braided river system. As such, the deposits exposed in the study were not part of the internally drained basins of the Central Andean Plateau, where lacustrine and evaporitic deposits are common features. Instead, the strata rather reflect part of a former foreland basin that was uplifted and incorporated into the Andean orogen by the eastward-progressing migration of the deformation front. This assessment is corroborated by the existence of a well-pronounced knickpoint along the eastward-directed course of the Río Pilcomayo, confirming that the drainage system was modified by a rapid, late Miocene regional uplift of the Andes that also shifted the depositional loci from distal to more proximally located areas. This process is inferred to have been driven by uplift along a major décollement that drove uplift of the Eastern Cordillera, but which must have also enabled the onset of deposition of the sediment-fill

units within the plateau realm by late Miocene time. The new radiometric ages of volcanic ashes intercalated within the fill units and cosmogenic nuclide dating of unconformably overlying gravelly cover units document that deposition of the sediment fill units took place from ~ 8 Ma to 3 Ma and that the incision into these units started at approximately 3 Ma. As the exposure ages of the abandoned alluvial-fan surfaces and their topographic position indicate, this process progressed in a stepwise manner over a timespan of around 2 Ma, forming several generations of gently inclined fan surfaces at successively lower elevations that were once adjusted to higher base levels of the trunk streams. Although paleoclimatic data for the study region are not available, in light of regional paleoclimatic data the changeover from deposition to incision in the northern Puna basins may have been associated with climate oscillations that caused episodic changes in runoff, sediment transport and erosivity of the fluvial system. Due to the size and erosive capacity of the Pilcomayo drainage system and assuming that headward erosion of the Río Pilcomayo will progress farther into the orogen with time, it may be hypothesized that adjacent sedimentary basins in the Puna Plateau will ultimately be breached in the future, thus causing further destruction of plateau morphology and sedimentary unloading.

The structural and tectono-geomorphic analyses presented in the second part of the thesis have provided novel data on the timing, kinematics, and displacement of extensional deformation in the Central-Eastern Andean Plateau after regional shortening and uplift had ceased. Extensional faulting occurred along approximately N-S-striking faults between 3.05 and 2.39 Ma, but may have started even earlier at about 6.59 Ma. Slip occurred along principal faults and subsidiary synthetic normal faults. The kinematic relation between the opening direction of associated ubiquitous, well-expressed joints and the strike of faults suggests that the kinematics were of transtensional character. The observed oblique motion, and the associated tectonic stress field suggest that the N-S-striking faults may be linked with crustal heterogeneities that were reactivated during extension. The relationship between inferred coseismic motion of these faults, single-event displacement, and cumulative displacement, as inferred from outcrop data and from topographic measurements, respectively, indicates that this episode of tectonic activity must have lasted for 13 to 26 earthquake cycles. Under the assumption of a characteristic earthquake behavior, this would correspond to recurrence intervals of 4.7-50.7 ka for the individual faulting events. According to empirical fault geometry and moment-magnitude relations, the magnitudes of paleo-earthquakes along the analyzed structures must have been in a

range of  $M_w = 6.0-7.5$ . Importantly, the absence of fault or fold-related deformation features on a 2.39 to 2.94-m.y.-old former alluvial-fan surface suggests tectonic quiescence during the Quaternary, which is compatible with the absence of instrumentally recorded seismic activity in the area. Similar to other sectors of the Andean Plateau the driving factor of the transtensional motion along the faults in the northern Puna is interpreted to be related to a gravitational collapse of the tectonically thickened crust, which is manifested by a disparate spatiotemporal distribution of normal faulting in the core region of the Andes, while shortening continues to govern the peripheral sectors of the eastern flanks of the Andean orogenic wedge.

## 6. References

Adams, C.J., Miller, H., Aceñolaza, F.G., Toselli, A.J., and Griffin, W.L., 2011, The Pacific Gondwana margin in the late Neoproterozoic–early Paleozoic: Detrital zircon U–Pb ages from metasediments in northwest Argentina reveal their maximum age, provenance and tectonic setting: *Gondwana Research*, v. 19, no. 1, p. 71–83, doi: 10.1016/j.gr.2010.05.002.

Aguirre, E., Benavente, C., Audin, L., Wimpenny, S., Baize, S., Rosell, L., Delgado, F., García, B., and Palomino, A., 2021, Earthquake surface ruptures on the altiplano and geomorphological evidence of normal faulting in the December 2016 ( $M_w$  6.1) Parina earthquake, Peru: *Journal of South American Earth Sciences*, v. 106, p. 103098, doi: 10.1016/j.jsames.2020.103098.

Allen, M.B., Saville, C., Blanc, E.J.-P., Talebian, M., and Nissen, E., 2013, Orogenic plateau growth: Expansion of the Turkish-Iranian Plateau across the Zagros fold-and-thrust belt: *Tectonics*, v. 32, no. 2, p. 171–190, doi: 10.1002/tect.20025.

Allen, P.A., 2017, *Sediment routing systems: The fate of sediment from source to sink*: Cambridge, New York, NY, Port Melbourne, Cambridge University Press, 407 p.

Allmendinger, R.W., 1986, Tectonic development, southeastern border of the Puna Plateau, northwestern Argentine Andes: *Geological Society of America Bulletin*, v. 97, no. 9, p. 1070, doi: 10.1130/0016-7606(1986)97<1070:TDSBOT>2.0.CO;2.

Allmendinger, R.W., Cardozo, N., and Fisher, D., 2020, Stereonet 11.

## 6. References

---

- Allmendinger, R.W., and Gubbels, T., 1996, Pure and simple shear plateau uplift, Altiplano-Puna, Argentina and Bolivia: *Tectonophysics*, v. 259, p. 1–13.
- Allmendinger, R.W., Jordan, T.E., Kay, S.M., and Isacks, B.L., 1997, The evolution of the Altiplano-Puna Plateau of the Central Andes: *Annual Review of Earth and Planetary Sciences*, v. 25, p. 139–174.
- Allmendinger, R.W., Strecker, M.R., Eremchuk, J.E., and Francis, P., 1989, Neotectonic deformation of the southern Puna Plateau, northwestern Argentina: *Journal of South American Earth Sciences*, v. 2, no. 2, p. 111–130.
- Allmendinger, R.W., and Zapata, T.R., 2000, The footwall ramp of the Subandean decollement, northernmost Argentina, from extended correlation of seismic reflection data: *Tectonophysics*, v. 321, no. 1, p. 37–55, doi: 10.1016/S0040-1951(00)00077-9.
- Alonso, R.N., Bookhagen, B., Carrapa, B., Coutand, I., Haschke, M., Hilley, G.E., Schoenbohm, L., Sobel, E.R., Strecker, M.R., Trauth, M.H., and Villanueva, A., 2006, Tectonics, Climate, and Landscape Evolution of the Southern Central Andes: the Argentine Puna Plateau and Adjacent Regions between 22 and 30°S, in Oncken, O., Chong, G., et al., eds., *The Andes*, Springer Berlin Heidelberg. *Frontiers in Earth Sciences*, p. 265–283.
- Alonso, R.N., Jordan, T.E., Tabbutt, K.T., and Vandervoort, D.S., 1991, Giant evaporite belts of the Neogene central Andes: *Geology*, v. 19, no. 4, p. 401, doi: 10.1130/0091-7613(1991)019<0401:GEBOTN>2.3.CO;2.
- Alonso, R.N., and Viramonte, J.G., 1987, *Geología y Metalogenia de la Puna: Estudios Geológicos*, v. 43, 5-6, doi: 10.3989/egeol.87435-6610.
- Amidon, W.H., Fisher, G.B., Burbank, D.W., Ciccioli, P.L., Alonso, R.N., Gorin, A.L., Silverhart, P.H., Kylander-Clark, A.R.C., and Christoffersen, M.S., 2017, Mio-Pliocene aridity in the south-central Andes associated with Southern Hemisphere cold periods: *Proceedings of the National Academy of Sciences of the United States of America*, v. 114, no. 25, p. 6474–6479, doi: 10.1073/pnas.1700327114.
- Andersen, T., 2002, Correction of common lead in U–Pb analyses that do not report <sup>204</sup>Pb: *Chemical Geology*, v. 192, no. 1, p. 59–79, doi: 10.1016/S0009-2541(02)00195-X.
- Anderson, R.S., Repka, J.L., and Dick, Gregory, S., 1996, Explicit treatment of inheritance in dating depositional surfaces using in situ <sup>10</sup>Be and <sup>26</sup>Al: *Geology*, v. 24, no. 1, p. 47–51.

- 
- Argand, E., 1922, La tectonique de l'Asie, in 13th International Geological Congress: Brussels, p. 171–372.
- Armijo, R., Lacassin, R., Coudurier-Curveur, A., and Carrizo, D., 2015, Coupled tectonic evolution of Andean orogeny and global climate, Volume 143.
- Armijo, R., Tapponnier, P., Mercier, J.L., and Han T.-L., 1986, Quaternary extension in southern Tibet: Field observations and tectonic implications: *Journal of Geophysical Research*, v. 91, B14, p. 13803–13872.
- Arnous, A., Zeckra, M., Venerdini, A., Alvarado, P., Arrowsmith, R., Guillemoteau, J., Landgraf, A., Gutiérrez, A., and Strecker, M.R., 2020, Neotectonic Activity in the Low-Strain Broken Foreland (Santa Bárbara System) of the North-Western Argentinean Andes (26°S): *Lithosphere*, v. 2020, no. 1, doi: 10.2113/2020/8888588.
- Astini, R.A., Vigliocco, A.C., and Gomez, F.J., 2020, Una cuña marina dominada por mareas en la base de la Formación Lecho en el extremo noroeste argentino: *Revista de la Asociación Geológica Argentina*, v. 77, no. 2, p. 272–295.
- Audin, L., David, C., Hall, S., Farber, D., and Hérail, G., 2006, Geomorphic evidences of recent tectonic activity in the forearc, southern Peru: *Revista de la Asociación Geológica Argentina*, v. 61, no. 4, p. 545–554.
- Avouac, J.-P., 2015, Mountain Building: From Earthquakes to Geologic Deformation, in Schubert, G., ed., *Treatise on Geophysics*, 2nd ed (Online-Ausg.) ed.: Burlington, Elsevier Science, p. 381–432.
- Avouac, J.-P., and Tapponnier, P., 1993, Kinematic model of active deformation in central Asia: *Geophysical Research Letters*, v. 20, no. 10, p. 895–898, doi: 10.1029/93GL00128.
- Babaei, S., Dehbozorgi, M., Hosseiniasl, A., and Hakimi Asiabar, S., 2020, New insights into the effect of the quaternary fault activity on river knickpoints in the Central Alborz (Iran): *Quaternary International*, v. 562, no. 1, p. 104–120, doi: 10.1016/j.quaint.2020.09.025.
- Baby, P., Rochat, P., Mascle, G., and Hérail, G., 1997, Neogene shortening contribution to crustal thickening in the back arc of the Central Andes: *Geology*, v. 25, no. 10, p. 883, doi: 10.1130/0091-7613(1997)025<0883:NSCTCT>2.3.CO;2.

## 6. References

---

- Bahlburg, H., Berndt, J., and Gerdes, A., 2016, The ages and tectonic setting of the Faja Eruptiva de la Puna Oriental, Ordovician, NW Argentina: *Lithos*, 256-257, p. 41–54, doi: 10.1016/j.lithos.2016.03.018.
- Bahlburg, H., Breitzkreuz, C., Maletz, J., Moya, M.C., and Salfity, J.A., 1990, The Ordovician sedimentary rocks in the northern Puna of Argentina and Chile: New stratigraphical data based on graptolites: *Newsletters on Stratigraphy*, v. 23, no. 2, p. 69–89, doi: 10.1127/nos/23/1990/69.
- Bai-ping, Z., Xiao-dong, C., Bao-lin, L., and Yong-hui, Y., 2002, Biodiversity and conservation in the Tibetan Plateau: *Journal of Geographical Sciences*, v. 12, no. 2, p. 135–143, doi: 10.1007/BF02837467.
- Balco, G., 2006, Converting Al and Be isotope ratio measurements to nuclide concentrations in quartz: [https://hess.ess.washington.edu/math/docs/common/ams\\_data\\_reduction.pdf](https://hess.ess.washington.edu/math/docs/common/ams_data_reduction.pdf) (January 2022).
- Balco, G., and Shuster, D.L., 2009,  $^{26}\text{Al}$ – $^{10}\text{Be}$ – $^{21}\text{Ne}$  burial dating: *Earth and Planetary Science letters*, v. 286, 3-4, p. 570–575, doi: 10.1016/j.epsl.2009.07.025.
- Balco, G., Stone, J.O., Lifton, N.A., and Dunai, T.J., 2008, A complete and easily accessible means of calculating surface exposure ages or erosion rates from  $^{10}\text{Be}$  and  $^{26}\text{Al}$  measurements: *Quaternary Geochronology*, v. 3, no. 3, p. 174–195, doi: 10.1016/j.quageo.2007.12.001.
- Ballato, P., Brune, S., and Strecker, M.R., 2019, Sedimentary loading–unloading cycles and faulting in intermontane basins: Insights from numerical modeling and field observations in the NW Argentine Andes: *Earth and Planetary Science letters*, v. 506, p. 388–396, doi: 10.1016/j.epsl.2018.10.043.
- Barke, R., and Lamb, S., 2006, Late Cenozoic uplift of the Eastern Cordillera, Bolivian Andes: *Earth and Planetary Science letters*, v. 249, 3-4, p. 350–367, doi: 10.1016/j.epsl.2006.07.012.
- Barnes, J.B., 2008, Deformation and erosion of the central Andean fold-thrust belt and plateau [Dissertation]: Michigan, USA, University of Michigan, 257 p.
- Beck, S.L., and Zandt, G., 2002, The nature of orogenic crust in the central Andes: *Journal of Geophysical Research*, v. 107, B10, ESE 7-1-ESE 7-16, doi: 10.1029/2000JB000124.

- 
- Berlin, M.M., and Anderson, R.S., 2007, Modeling of knickpoint retreat on the Roan Plateau, western Colorado: *Journal of Geophysical Research*, v. 112, F3, p. 273, doi: 10.1029/2006JF000553.
- Best, M.G., Barr, D.L., Christiansen, E.H., Gromme, S., Deino, A.L., and Tingey, D.G., 2009, The Great Basin Altiplano during the middle Cenozoic ignimbrite flareup: insights from volcanic rocks: *International Geology Review*, v. 51, 7-8, p. 589–633, doi: 10.1080/00206810902867690.
- Bhosle, B., Parkash, B., Awasthi, A.K., and Pati, P., 2009, Use of digital elevation models and drainage patterns for locating active faults in the Upper Gangetic Plain, India: *International Journal of Remote Sensing*, v. 30, no. 3, p. 673–691, doi: 10.1080/01431160802392604.
- Bird, P., 1979, Continental Delamination and the Colorado plateau: *Journal of Geophysical Research*, v. 84, B13, p. 7561–7571.
- Borchers, B., Marrero, S., Balco, G., Caffee, M., Goehring, B., Lifton, N., Nishiizumi, K., Phillips, F., Schaefer, J., and Stone, J., 2016, Geological calibration of spallation production rates in the CRONUS-Earth project: *Quaternary Geochronology*, v. 31, p. 188–198, doi: 10.1016/j.quageo.2015.01.009.
- Boulton, S.J., Stokes, M., and Mather, A.E., 2014, Transient fluvial incision as an indicator of active faulting and Plio-Quaternary uplift of the Moroccan High Atlas: *Tectonophysics*, v. 633, no. 4, p. 16–33, doi: 10.1016/j.tecto.2014.06.032.
- Brooks, B.A., Bevis, M., Whipple, K., Ramon Arrowsmith, J., Foster, J., Zapata, T., Kendrick, E., Minaya, E., Echalar, A., Blanco, M., Euillades, P., Sandoval, M., and Smalley, R.J., 2011, Orogenic-wedge deformation and potential for great earthquakes in the central Andean backarc: *Nature Geoscience*, v. 4, no. 6, p. 380–383, doi: 10.1038/ngeo1143.
- Brown, E.T., Raisbeck, G.M., Yiou, F., and Kurz, M.D., 1992, Effective attenuation length of cosmic rays producing  $^{10}\text{Be}$  and  $^{26}\text{Al}$  in Quartz: Implications for exposure age dating: *Geophysical Research Letters*, v. 19, no. 4, p. 369–372.
- Buatois, L.A., Zeballo, F.J., Albanesi, G.L., Ortega, G., Vaccari N. E., and Mangano, M.G., 2006, Depositional environments and stratigraphy of the upper Cambrian - lower Ordovician Santa Rosita Formation at the Alfarcito area, Cordillera Oriental, Argentina:

Integration of biostratigraphic data within a sequence stratigraphic framework: *Latin American Journal of Sedimentology and Basin Analysis*, v. 13, no. 1, p. 1–29.

Burbank, D.W., and Anderson, R.S., 2012, *Tectonic geomorphology*, 2nd ed.: Chichester, Wiley-Blackwell, XIV, 454 str.

Burke, W.B., Laskowski, A.K., Orme, D.A., Sundell, K.E., Taylor, M.H., Guo, X., and Ding, L., 2021, Record of Crustal Thickening and Synconvergent Extension from the Dajiamang Tso Rift, Southern Tibet: *Geosciences*, v. 11, no. 5, p. 209, doi: 10.3390/geosciences11050209.

Bywater-Reyes, S., Carrapa, B., Clementz, M., and Schoenbohm, L., 2010, Effect of late Cenozoic aridification on sedimentation in the Eastern Cordillera of northwest Argentina (Angastaco basin): *Geology*, v. 38, no. 3, p. 235–238, doi: 10.1130/G30532.1.

Cabrera, J., Sébrier, M., and Mercier, J., L., 1991, Plio-Quaternary geodynamic evolution of a segment of the Peruvian Andean Cordillera located above the change in the subduction geometry: The Cuzco region: *Tectonophysics*, no. 190, p. 331–362.

Cadena, E.A., Anaya, F., and Croft, D.A., 2015, Giant fossil tortoise and freshwater chelid turtle remains from the middle Miocene, Quebrada Honda, Bolivia: Evidence for lower paleoelevations for the southern Altiplano: *Journal of South American Earth Sciences*, v. 64, p. 190–198, doi: 10.1016/j.jsames.2015.10.013.

Caffe, P.J., and Coira, B.L., 2002, Chronostratigraphy of the San Juan de Oro basin and its tectonic implications for the northern Puna during the Miocene, 109 p.

Cahill, T., Isacks, B.L., Whitman, D., Chatelain, J.-L., Perez, A., and Chiu, J.M., 1992, Seismicity and tectonics in Jujuy Province, northwestern Argentina: *Tectonics*, v. 11, no. 5, p. 944–959, doi: 10.1029/92TC00215.

Camacho, M., and Kulemeyer, J.J., 2017, The Quaternary of the Laguna de los Pozuelos Basin, Northern Puna, Argentina, in Rabassa, J., ed., *Advances in geomorphology and quaternary studies in Argentina: Proceedings of the Sixth Argentine Geomorphology and Quaternary Studies Congress*: Cham, Switzerland, Springer. *Springer Earth System Sciences*, p. 237–259.

Caputo, M., and Caputo, R., 1989, Estimate of the regional stress field using joint systems = Εκτίμηση του γενικού εντατικού πεδίου με τη χρησιμοποίηση συστημάτων διακλάσεων: *Δελτίον της Ελληνικής Γεωλογικής Εταιρείας*, v. 23, no. 1, p. 101–118.

- Cardozo, N., and Allmendinger, R.W., 2013, Spherical projections with OSXStereonet: *Computers & Geosciences*, v. 51, p. 193–205, doi: 10.1016/j.cageo.2012.07.021.
- Carlotto, V., 2013, Paleogeographic and tectonic controls on the evolution of Cenozoic basins in the Altiplano and Western Cordillera of southern Peru: *Tectonophysics*, v. 589, p. 195–219, doi: 10.1016/j.tecto.2013.01.002.
- Carrapa, B., Hauer, J., Schoenbohm, L., Strecker, M.R., Schmitt, A.K., Villanueva, A., and Sosa Gomez, J., 2008, Dynamics of deformation and sedimentation in the northern Sierras Pampeanas: An integrated study of the Neogene Fiambala basin, NW Argentina: *Geological Society of America Bulletin*, v. 120, 11-12, p. 1518–1543, doi: 10.1130/B26111.1.
- Carrera, N., and Muñoz, J.A., 2008, Thrusting evolution in the southern Cordillera Oriental (northern Argentine Andes): Constraints from growth strata: *Tectonophysics*, v. 459, 1-4, p. 107–122, doi: 10.1016/j.tecto.2007.11.068.
- Castino, F., Bookhagen, B., and Strecker, M.R., 2017, Rainfall variability and trends of the past six decades (1950–2014) in the subtropical NW Argentine Andes: *Climate Dynamics*, v. 48, 3-4, p. 1049–1067, doi: 10.1007/s00382-016-3127-2.
- Catena, A.M., Hembree, D.I., Saylor, B.Z., Anaya, F., and Croft, D.A., 2017, Paleosol and ichnofossil evidence for significant Neotropical habitat variation during the late middle Miocene (Serravallian): *Palaeogeography Palaeoclimatology Palaeoecology*, v. 487, 10A, p. 381–398, doi: 10.1016/j.palaeo.2017.09.024.
- Chan, M.A., Parry, W.T., and Bowman, J.R., 2000, Diagenetic Hematite and Manganese Oxides and Fault-Related Fluid Flow in Jurassic: *AAPG Bulletin*, v. 84, no. 9, p. 1281–1310.
- Cheng, F., Garzzone, C., Jolivet, M., Guo, Z., Zhang, D., and Zhang, C., 2018, A New Sediment Accumulation Model of Cenozoic Depositional Ages From the Qaidam Basin, Tibetan Plateau: *Journal of Geophysical Research: Earth Surface*, v. 123, no. 11, p. 3101–3121, doi: 10.1029/2018JF004645.
- Chevalier, M.-L., Tapponnier, P., Woerd, J., Leloup, P.H., Wang, S., Pan, J., Bai, M., Kali, E., Liu, X., and Li, H., 2020, Late Quaternary Extension Rates Across the Northern Half of the Yadong-Gulu Rift: Implication for East-West Extension in Southern Tibet: *Journal of Geophysical Research: Solid Earth*, v. 125, no. 7, doi: 10.1029/2019JB019106.

## 6. References

---

- Cladouhos, T.T., Allmendinger, R.W., Coira, B., and Farrar, E., 1994, Late cenozoic deformation in the Central Andes: fault kinematics from the northern Puna, northwestern Argentina and southwestern Bolivia: *Journal of South American Earth Sciences*, v. 7, no. 2, p. 209–228, doi: 10.1016/0895-9811(94)90008-6.
- Clark, D., and Leonard, M., 2003, Principal stress orientations from multiple focal-plane solutions: new insight into the Australian intraplate stress field\*, in Hillis, R.R., Müller, R.D., eds., *Evolution and dynamics of the Australian plate*: Boulder, Colo., Geological Society of America. Special paper / Geological Society of America, Volume 372.
- Clark, M.K., Royden, L.H., Whipple, K.X., Burchfiel, B.C., Zhang, X., and Tang, W., 2006, Use of a regional, relict landscape to measure vertical deformation of the eastern Tibetan Plateau: *Journal of Geophysical Research*, v. 111, F3, n/a-n/a, doi: 10.1029/2005JF000294.
- Coira, B., Kay, S.M., and Viramonte, J., 1993, Upper Cenozoic magmatic evolution of the Argentine Puna - A model for changing subduction geometry: *International Geology Review*, v. 35, no. 8, p. 677–720, doi: 10.1080/00206819309465552.
- Coira, B., and Koukharsky, M., editors, 1991, *Lavas en allmohadilla ordovicias en el Cordon de Escaya, Puna Septentrional, Argentina*, 7 p.
- Coira, B.L., 1979, Descripción geológica de la Hoja 3c, Abra Pampa, Provincia de Jujuy: *Carta geológico-económica de la República Argentina, escala 1: 200.000*: Boletín, no. 170.
- Colavitto, B., Blanc, P.A., Olivar, J., Alcacer, J.M., and Perruca, L., 2021, Caracterización del terremoto del 29 de noviembre de 2020 del Noroeste Argentino (límite Salta-Jujuy): *Revista de la Asociación Geológica Argentina*, Vol. 78 (2), p. 338–343.
- Cook, K.L., and Royden, L.H., 2008, The role of crustal strength variations in shaping orogenic plateaus, with application to Tibet: *Journal of Geophysical Research: Solid Earth*, v. 113, B8, p. 450, doi: 10.1029/2007JB005457.
- Cortés, M., and Angelier, J., 2005, Current states of stress in the northern Andes as indicated by focal mechanisms of earthquakes: *Tectonophysics*, v. 403, 1-4, p. 29–58, doi: 10.1016/j.tecto.2005.03.020.
- Costa, C.H., Audemard, A.A., Bezerra, F.H., Lavenu, A., Machette, M.N., and París, G., 2006, AN OVERVIEW OF THE MAIN QUATERNARY DEFORMATION OF SOUTH AMERICA: *Revista de la Asociación Geológica Argentina*, v. 61, no. 4, p. 461–479.

- 
- Cottle, J.M., 2014, In-situ U-Th/Pb geochronology of (urano)thorite: *American Mineralogist*, v. 99, no. 10, p. 1985–1995, doi: 10.2138/am-2014-4920.
- Cottle, J.M., Burrows, A.J., Kylander-Clark, A., Freedman, P.A., and Cohen, R.S., 2013, Enhanced sensitivity in laser ablation multi-collector inductively coupled plasma mass spectrometry: *Journal of Analytical Atomic Spectrometry*, v. 28, no. 11, p. 1700–1706, doi: 10.1039/C3JA50216C.
- Coutand, I., Cobbold, P.R., Urreiztieta, M. de, Gautier, P., Chauvin, A., Gapais, D., Rossello, E.A., and López-Gamundí, O., 2001, Style and history of Andean deformation, Puna plateau, northwestern Argentina: *Tectonics*, v. 20, no. 2, p. 210–234.
- Craddock, W.H., Kirby, E., Harkins, N.W., Zhang, H., Shi, X., and Liu, J., 2010, Rapid fluvial incision along the Yellow River during headward basin integration: *Nature Geoscience*, v. 3, no. 3, p. 209–213, doi: 10.1038/ngeo777.
- Croft, D.A., 2007, The middle Miocene (Levantan) Quebrada Honda fauna, southern Bolivia and a description of its notoungulates: *Paleontology*, no. 50, p. 277–303.
- Crosby, B.T., and Whipple, K.X., 2006, Knickpoint initiation and distribution within fluvial networks: 236 waterfalls in the Waipaoa River, North Island, New Zealand: *Geomorphology*, v. 82, 1-2, p. 16–38, doi: 10.1016/j.geomorph.2005.08.023.
- Crowley, J.L., Schoene, B., and Bowring, S.A., 2007, U-Pb dating of zircon in the Bishop Tuff at the millennial scale: *Geology*, v. 35, no. 12, p. 1123, doi: 10.1130/G24017A.1.
- Dalmayrac, B., and Molnar, P., 1981, Parallel thrust and normal faulting in Peru and constraints on the state of stress: *Earth and Planetary Science letters*, v. 55, no. 3, p. 473–481, doi: 10.1016/0012-821X(81)90174-6.
- D'Arcy, M., Schildgen, T.F., Strecker, M.R., Wittmann, H., Duesing, W., Mey, J., Tofelde, S., Weissmann, P., and Alonso, R.N., 2019, Timing of past glaciation at the Sierra de Aconquija, northwestern Argentina, and throughout the Central Andes: *Quaternary Science Reviews*, v. 204, p. 37–57.
- D'Arcy, M., and Whittaker, A.C., 2014, Geomorphic constraints on landscape sensitivity to climate in tectonically active areas: *Geomorphology*, v. 204, B8, p. 366–381, doi: 10.1016/j.geomorph.2013.08.019.
- Darvill, C.M., Bentley, M.J., Stokes, C.R., Hein, A.S., and Rodés, Á., 2015, Extensive MIS 3 glaciation in southernmost Patagonia revealed by cosmogenic nuclide dating of outwash

## 6. References

---

sediments: *Earth and Planetary Science letters*, v. 429, p. 157–169, doi: 10.1016/j.epsl.2015.07.030.

DeGuidi, G., Caputo, R., and Scudero, S., 2013, Regional and local stress field orientation inferred from quantitative analyses of extension joints: Case study from southern Italy: *Tectonics*, v. 32, no. 2, p. 239–251, doi: 10.1002/tect.20017.

Dehnert, A., Kracht, O., Preusser, F., Akçar, N., Kemna, H.A., Kubik, P.W., and Schlüchter, C., 2011, Cosmogenic isotope burial dating of fluvial sediments from the Lower Rhine Embayment, Germany: *Quaternary Geochronology*, v. 6, 3-4, p. 313–325, doi: 10.1016/j.quageo.2011.03.005.

Devlin, S., Isacks, B.L., Pritchard, M.E., Barnhart, W.D., and Lohman, R.B., 2012, Depths and focal mechanisms of crustal earthquakes in the central Andes determined from teleseismic waveform analysis and InSAR: *Tectonics*, v. 31, no. 2, n/a-n/a, doi: 10.1029/2011TC002914.

Dewey, J.F., 1988, Extensional collapse of orogens: *Tectonics*, v. 7, no. 6, p. 1123–1139, doi: 10.1029/TC007i006p01123.

Dewey, J.F., and Burke, K.C.A., Tibetan, Variscan, and Precambrian Basement Reactivation: Products of Continental Collision.

Dewey, J.F., Ryan, P.D., and Andersen, T.B., 1993, Orogenic uplift and collapse, crustal thickness, fabrics and metamorphic phase changes: the role of eclogites: *Geological Society, London, Special Publications*, v. 76, no. 1, p. 325–343, doi: 10.1144/GSL.SP.1993.076.01.16.

Do Campo, M., Nieto, F., Albanesi, G.L., Ortega, G., and Monaldi, R., 2017, Outlining the thermal postdepositional evolution of the Ordovician successions of northwestern Argentina by clay mineral analysis, chlorite geothermometry and Kübler index: *Andean Geology*, v. 44, no. 2, p. 179, doi: 10.5027/andgeoV44n2-a04.

Do Campo, M., Omarini, R., and Ostersa, H., 1994, Edades K-Ar en fracciones finas de pelitas en la Formación Puncoviscana, Salta, Argentina: *Andean Geology*, v. 21, no. 2, p. 233–240, doi: 10.5027/andgeoV21n2-a06.

Dorbath, C., and Granet, M., 1996, Local earthquake tomography of the Altiplano and the Eastern Cordillera of northern Bolivia: *Tectonophysics*, v. 259, 1-3, p. 117–136, doi: 10.1016/0040-1951(95)00052-6.

- Dorn, F.M., 2021, Changing territorialities in the Argentine Andes: lithium mining at Salar de Olaroz-Cauchari and Salinas Grandes: *Die ERDE*, p. 1–17, doi: 10.12854/erde-2021-515.
- Doser, D.I., 1987, The Ancash, Peru, earthquake of 1946 November 10: evidence for low-angle normal faulting in the high Andes of northern Peru: *Geophysical Journal International*, v. 91, no. 1, p. 57–71, doi: 10.1111/j.1365-246X.1987.tb05213.x.
- Dunai, T.J., 2000, Scaling factors for production rates of in situ produced cosmogenic nuclides: a critical reevaluation: *Earth and Planetary Science letters*, v. 176, no. 1, p. 157–169, doi: 10.1016/S0012-821X(99)00310-6.
- Echavarría, L., Hernández, R., Allmendinger, R., and Reynolds, J., 2003, Subandean thrust and fold belt of northwestern Argentina: Geometry and timing of the Andean evolution: *AAPG Bulletin*, v. 87, no. 6, p. 965–985, doi: 10.1306/01200300196.
- Ege, H., Sobel, E.R., Scheuber, E., and Jacobshagen, V., 2007, Exhumation history of the southern Altiplano plateau (southern Bolivia) constrained by apatite fission track thermochronology: *Tectonics*, v. 26, no. 1, n/a-n/a, doi: 10.1029/2005TC001869.
- Einsele, G., 2000, *Sedimentary basins: Evolution, facies, and sediment budget*, 2., completely rev. and enl. ed.: Berlin, Heidelberg, New York, Barcelona, Hong Kong, London, Milan, Paris, Singapore, Tokyo, Springer, 792 p.
- Elger, K., Oncken, O., and Glodny, J., 2005, Plateau-style accumulation of deformation: Southern Altiplano: *Tectonics*, v. 24, no. 4, n/a-n/a, doi: 10.1029/2004TC001675.
- Elliott, J.R., Walters, R.J., England, P.C., Jackson, J.A., Li, Z., and Parsons, B., 2010, Extension on the Tibetan plateau: recent normal faulting measured by InSAR and body wave seismology: *Geophysical Journal International*, v. 183, no. 2, p. 503–535, doi: 10.1111/j.1365-246X.2010.04754.x.
- Engelder, T., 1985, Loading paths to joint propagation during a tectonic cycle: an example from the Appalachian Plateau, U.S.A: *Journal of Structural Geology*, v. 7, 3-4, p. 459–476, doi: 10.1016/0191-8141(85)90049-5.
- Engelder, T., and Gross, M.R., 1993, Curving cross joints and the lithospheric stress field in eastern North America: *Geology*, no. 21, p. 817–820.
- Engelkemeir, R.M., and Khan, S.D., 2008, Lidar mapping of faults in Houston, Texas, USA: *Geosphere*, v. 4, no. 1, p. 170–182, doi: 10.1130/GES00096.

- Escayola, M.P., van Staal, C.R., and Davis, W.J., 2011, The age and tectonic setting of the Puncoviscana Formation in northwestern Argentina: An accretionary complex related to Early Cambrian closure of the Puncoviscana Ocean and accretion of the Arequipa-Antofalla block: *Journal of South American Earth Sciences*, v. 32, no. 4, p. 438–459, doi: 10.1016/j.jsames.2011.04.013.
- Evans, A.D., Teagle, D.A.H., Craw, D., Henstock, T.J., and Falcon-Suarez, I.H., 2021, Uplift and Exposure of Serpentinized Massifs: Modeling Differential Serpentine Diapirism and Exhumation of the Troodos Mantle Sequence, Cyprus: *Journal of Geophysical Research: Solid Earth*, v. 126, no. 6, doi: 10.1029/2020JB021079.
- Farber, D.L., Mériaux, A.-S., and Finkel, R.C., 2008, Attenuation length for fast nucleon production of  $^{10}\text{Be}$  derived from near-surface production profiles: *Earth and Planetary Science letters*, v. 274, 3-4, p. 295–300, doi: 10.1016/j.epsl.2008.07.015.
- Ferrero, M.E., and Villalba, R., 2019, Interannual and Long-Term Precipitation Variability Along the Subtropical Mountains and Adjacent Chaco (22–29° S) in Argentina: *Frontiers in Earth Science*, v. 7, doi: 10.3389/feart.2019.00148.
- Figueroa, S., Weiss, J.R., Hongn, F., Pingel, H., Escalante, L., Elías, L., Aranda-Viana, R.G., and Strecker, M.R., 2021, Late Pleistocene to Recent Deformation in the Thick-Skinned Fold-and-Thrust Belt of Northwestern Argentina (Central Calchaquí Valley, 26°S): *Tectonics*, v. 40, no. 1, doi: 10.1029/2020TC006394.
- Filipovich, R., Báez, W., Bustos, E., Villagrán, A., Chiodi, A., and Viramonte, J., 2019, Estilos eruptivos asociados al volcanismo monogenético máfico de la región de Pasto Ventura, Puna Austral, Argentina: *Andean Geology*, v. 46, no. 2, p. 300, doi: 10.5027/andgeoV46n2-3091.
- Folguera, A., Bottesi, G., Zapata, T., and Ramos, V.A., 2008, Crustal collapse in the Andean backarc since 2 Ma: Tromen volcanic plateau, Southern Central Andes (36°40'–37°30'S): *Tectonophysics*, v. 459, 1-4, p. 140–160, doi: 10.1016/j.tecto.2007.12.013.
- Franceschinis, P.R., Escayola, M.P., Rapalini, A.E., and Rodríguez Picada, C., 2020, Age constraints on the Cambrian Mesón Group (NW Argentina) based on detrital zircons U–Pb geochronology and magnetic polarity bias: *Journal of South American Earth Sciences*, v. 104, p. 102835, doi: 10.1016/j.jsames.2020.102835.

- Froidevaux, C., and Isacks, B.L., 1984, The mechanical state of the lithosphere in the Altiplano-Puna segment of the Andes: *Earth and Planetary Science letters*, v. 71, p. 305–314.
- Fuller, R.E., and Waters, A.C., 1929, The Nature and Origin of the Horst and Graben Structure of Southern Oregon: *The Journal of Geology*, v. 37, no. 3, p. 204–238, doi: 10.1086/623616.
- Funk, J., Mann, P., McIntosh, K., and Stephens, J., 2009, Cenozoic tectonics of the Nicaraguan depression, Nicaragua, and Median Trough, El Salvador, based on seismic-reflection profiling and remote-sensing data: *Geological Society of America Bulletin*, v. 121, 11-12, p. 1491–1521, doi: 10.1130/B26428.1.
- Gallen, S.F., and Wegmann, K.W., 2017, River profile response to normal fault growth and linkage: an example from the Hellenic forearc of south-central Crete, Greece: *Earth Surf. Dynam. (Earth Surface Dynamics)*, v. 5, no. 1, p. 161–186, doi: 10.5194/esurf-5-161-2017.
- Ganas, A., Pavlides, S., and Karastathis, V., 2005, DEM-based morphometry of range-front escarpments in Attica, central Greece, and its relation to fault slip rates: *Geomorphology*, v. 65, 3-4, p. 301–319, doi: 10.1016/j.geomorph.2004.09.006.
- Gao, Y., Tilmann, F., Herwaarden, D.-P., Thrastarson, S., Fichtner, A., Heit, B., Yuan, X., and Schurr, B., 2021, Full Waveform Inversion Beneath the Central Andes: Insight Into the Dehydration of the Nazca Slab and Delamination of the Back-Arc Lithosphere: *Journal of Geophysical Research: Solid Earth*, v. 126, no. 7, doi: 10.1029/2021JB021984.
- García, V.H., Hongn, F., and Cristallini, E.O., 2013, Late Miocene to recent morphotectonic evolution and potential seismic hazard of the northern Lerma valley: Clues from Lomas de Medeiros, Cordillera Oriental, NW Argentina: *Tectonophysics*, v. 608, p. 1238–1253, doi: 10.1016/j.tecto.2013.06.021.
- Garzzone, C.N., Hoke, G.D., Libarkin, J.C., Withers, S., MacFadden, B., Eiler, J., Ghosh, P., and Mulch, A., 2008, Rise of the Andes: *Science (New York, N.Y.)*, v. 320, no. 5881, 1304 - 1307.
- Garzzone, C.N., McQuarrie, N., Perez, N.D., Ehlers, T.A., Beck, S.L., Kar, N., Eichelberger, N., Chapman, A.D., Ward, K.M., Ducea, M.N., Lease, R.O., Poulsen, C.J., Wagner, L.S., Saylor, J.E., Zandt, G., and Horton, B.K., 2017, Tectonic Evolution of the Central Andean Plateau and Implications for the Growth of Plateaus: *Annual Review of*

## 6. References

---

Earth and Planetary Sciences, v. 45, no. 1, p. 529–559, doi: 10.1146/annurev-earth-063016-020612.

Garziona, C.N., Molnar, P., Libarkin, J.C., and MacFadden, B.J., 2006, Rapid late Miocene rise of the Bolivian Altiplano: Evidence for removal of mantle lithosphere: Earth and Planetary Science letters, v. 241, 3-4, p. 543–556, doi: 10.1016/j.epsl.2005.11.026.

Gérard, B., Audin, L., Robert, X., Gautheron, C., van der Beek, P., Bernet, M., Benavente, C., and Delgado, F., 2021, Pliocene river capture and incision of the northern Altiplano: Machu Picchu, Peru: Journal of the Geological Society, v. 178, no. 2, jgs2020-100, doi: 10.1144/jgs2020-100.

Giambiagi, L., Alvarez, P., and Spagnotto, S., 2016, Temporal variation of the stress field during the construction of the central Andes: Constrains from the volcanic arc region (22–26°S), Western Cordillera, Chile, during the last 20 Ma: Tectonics, v. 35, no. 9, p. 2014–2033, doi: 10.1002/2016TC004201.

Giambiagi, L., Tassara, A., Echaurren, A., Julve, J., Quiroga, R., Barrionuevo, M., Liu, S., Echeverría, I., Mardóñez, D., Suriano, J., Mescua, J., Lossada, A.C., Spagnotto, S., Bertoa, M., and Lothari, L., 2022, Crustal anatomy and evolution of a subduction-related orogenic system: Insights from the Southern Central Andes (22–35°S): Earth-Science Reviews, v. 232, p. 104138, doi: 10.1016/j.earscirev.2022.104138.

Giambiagi, L.B., Alvarez, P., Godoy, E., and Ramos, V.A., 2003, The control of pre-existing extensional structures on the evolution of the southern sector of the Aconcagua fold and thrust belt, southern Andes: Tectonophysics, v. 369, 1-2, p. 1–19, doi: 10.1016/S0040-1951(03)00171-9.

Gibert, L., Deino, A., Valero, L., Anaya, F., Lería, M., Saylor, B., and Croft, D.A., 2020, Chronology of Miocene terrestrial deposits and fossil vertebrates from Quebrada Honda (Bolivia): Palaeogeography, Palaeoclimatology, Palaeoecology, v. 560, p. 110013, doi: 10.1016/j.palaeo.2020.110013.

Giovanni, M.K., Horton, B.K., Garziona, C.N., McNulty, B., and Grove, M., 2010, Extensional basin evolution in the Cordillera Blanca, Peru: Stratigraphic and isotopic records of detachment faulting and orogenic collapse in the Andean hinterland: Tectonics, v. 29, no. 6, n/a-n/a, doi: 10.1029/2010TC002666.

- Goethals, M.M., Hetzel, R., Niedermann, S., Wittmann, H., Fenton, C.R., Kubik, P.W., Christl, M., and Blanckenburg, F. von, 2009, An improved experimental determination of cosmogenic  $^{10}\text{Be}/^{21}\text{Ne}$  and  $^{26}\text{Al}/^{21}\text{Ne}$  production ratios in quartz: *Earth and Planetary Science letters*, v. 284, 1-2, p. 187–198, doi: 10.1016/j.epsl.2009.04.027.
- Göğüş, O.H., and Pysklywec, R.N., 2008, Mantle lithosphere delamination driving plateau uplift and synconvergent extension in eastern Anatolia: *Geology*, v. 36, no. 9, p. 723, doi: 10.1130/G24982A.1.
- González, G., Cembrano, J., Aron, F., Veloso, E.E., and Shyu, J.B.H., 2009, Coeval compressional deformation and volcanism in the central Andes, case studies from northern Chile (23°S-24°S): *Tectonics*, v. 28, no. 6, n/a-n/a, doi: 10.1029/2009TC002538.
- Gosse, J.C., and Phillips, F.M., 2001, Terrestrial in situ cosmogenic nuclides: theory and application: *Quaternary Science Reviews*, v. 20, no. 14, p. 1475–1560, doi: 10.1016/S0277-3791(00)00171-2.
- Granger, D.E., 2006, A review of burial dating methods using  $^{26}\text{Al}$  and  $^{10}\text{Be}$ , in Siame, L.L., Siame, L., et al., eds., *In situ-produced cosmogenic nuclides and quantification of geological processes: Boulder, Colorado, Geological Society of America. Special paper / Geological Society of America, Volume 415*, p. 1–16.
- Granger, D.E., and Muzikar, P.F., 2001, Dating sediment burial with in situ-produced cosmogenic nuclides: theory, techniques, and limitations: *Earth and Planetary Science letters*, v. 188, 1-2, p. 269–281, doi: 10.1016/S0012-821X(01)00309-0.
- Gregory-Wodzicki, K.M., 2000, Uplift history of the Central and Northern Andes: A review: *Geological Society of America Bulletin*, v. 112, no. 7, p. 1091–1105, doi: 10.1130/0016-7606(2000)112<1091:UHOTCA>2.0.CO;2.
- Gubbels, T.L., Isacks, B.L., and Farrar, E., 1993, High-level surfaces, plateau uplift, and foreland development, Bolivian central Andes: *Geology*, v. 21, p. 695–698.
- Gudmundsson, A., 2000, Fracture dimensions, displacements and fluid transport: *Journal of Structural Geology*, v. 22, p. 1221–1231.
- Guo, X., Gao, R., Zhao, J., Xu, X., Lu, Z., Klemperer, S.L., and Liu, H., 2018, Deep-seated lithospheric geometry in revealing collapse of the Tibetan Plateau: *Earth-Science Reviews*, v. 185, p. 751–762, doi: 10.1016/j.earscirev.2018.07.013.

## 6. References

---

- Hain, M.P., Strecker, M.R., Bookhagen, B., Alonso, R.N., Pingel, H., and Schmitt, A.K., 2011, Neogene to Quaternary broken foreland formation and sedimentation dynamics in the Andes of NW Argentina (25°S): *Tectonics*, v. 30, no. 2, n/a-n/a, doi: 10.1029/2010TC002703.
- Hancock, P.L., 1985, Brittle microtectonics: principles and practice: *Journal of Structural Geology*, v. 7, 3-4, p. 437–457, doi: 10.1016/0191-8141(85)90048-3.
- Hanks, T.C., 2000, The Age of Scarplike Landforms From Diffusion-Equation Analysis, in Noller, J.S., Sowers, J.M., et al., eds., *Quaternary geochronology: Methods and applications*: Washington, DC, American Geophysical Union. AGU Reference Shelf, Volume 4, p. 313–338.
- Harding, T.P., 1985, Seismic Characteristics and Identification of Negative Flower Structures, Positive Flower Structures, and Positive Structural Inversion: *AAPG Bulletin*, v. 69, doi: 10.1306/AD462538-16F7-11D7-8645000102C1865D.
- Heidarzadeh, G., Ballato, P., Hassanzadeh, J., Ghassemi, M.R., and Strecker, M.R., 2017, Lake overspill and onset of fluvial incision in the Iranian Plateau: Insights from the Mianeh Basin: *Earth and Planetary Science letters*, v. 469, p. 135–147, doi: 10.1016/j.epsl.2017.04.019.
- Hendrix, M.S., Graham, S.A., Carroll, A.R., Sobel, E.R., McKnight, C.L., Schulein, B.J., and Wang, Z., 1992, Sedimentary record and climatic implications of recurrent deformation in the Tian Shan: Evidence from Mesozoic strata of the north Tarim, south Junggar, and Turpan basins, northwest China: *Geological Society of America Bulletin*, v. 104, no. 1, p. 53–79, doi: 10.1130/0016-7606(1992)104<0053:SRACIO>2.3.CO;2.
- Henríquez, S., DeCelles, P.G., Carrapa, B., Hughes, A.N., Davis, G.H., and Alvarado, P., 2020, Deformation history of the Puna plateau, Central Andes of northwestern Argentina: *Journal of Structural Geology*, v. 140, p. 104133, doi: 10.1016/j.jsg.2020.104133.
- Hidy, A.J., Gosse, J.C., Pederson, J.L., Mattern, J.P., and Finkel, R.C., 2010, A geologically constrained Monte Carlo approach to modeling exposure ages from profiles of cosmogenic nuclides: An example from Lees Ferry, Arizona: *Geochemistry Geophysics Geosystems*, v. 11, doi: 10.1029/2010GC003084.

- 
- Hodge, M., Biggs, J., Fagereng, Å., Elliott, A., Mdala, H., and Mphepo, F., 2019, A semi-automated algorithm to quantify scarp morph morphology (SPARTA): application to normal faults in southern Malawi: *Solid Earth*, v. 10, p. 27–57.
- Hoke, G.D., and Garziona, C.N., 2008, Paleosurfaces, paleoelevation, and the mechanisms for the late Miocene topographic development of the Altiplano plateau: *Earth and Planetary Science letters*, v. 271, 1-4, p. 192–201, doi: 10.1016/j.epsl.2008.04.008.
- Hoke, G.D., Isacks, B.L., Jordan, T.E., Blanco, N., Tomlinson, A.J., and Ramezani, J., 2007, Geomorphic evidence for post-10 Ma uplift of the western flank of the central Andes 18°30'-22°S: *Tectonics*, v. 26, no. 5, n/a-n/a, doi: 10.1029/2006TC002082.
- Hoke, L., Hilton, D.R., Lamb, S.H., Hammerschmidt, K., and Friedrichsen, H., 1994, 3He evidence for a wide zone of active mantle melting beneath the Central Andes: *Earth and Planetary Science letters*, v. 128, 3-4, p. 341–355, doi: 10.1016/0012-821X(94)90155-4.
- Holtkamp, S.G., Pritchard, M.E., and Lohman, R.B., 2011, Earthquake swarms in South America: *Geophysical Journal International*, v. 187, no. 1, p. 128–146, doi: 10.1111/j.1365-246X.2011.05137.x.
- Hongn, F., del Papa, C., Powell, J.W., Petrinovic, I., Mon, R., and Deraco, V., 2007, Middle Eocene deformation and sedimentation in the Puna– Eastern Cordillera transition (23°–26°S): Control by preexisting heterogeneities on the pattern of initial Andean shortening: *Geology*, v. 35, no. 3, p. 271–274.
- Horton, B.K., and DeCelles, P.G., 2001, Modern and ancient fluvial megafans in the foreland basin system of the central Andes, southern Bolivia: implications for drainage network evolution in fold-thrust belts: *Basin Research*, v. 13, no. 1, p. 43–63, doi: 10.1046/j.1365-2117.2001.00137.x.
- Houseman, G.A., McKenzie, D.P., and Molnar, P., 1981, Convective instability of a thickened boundary layer and its relevance for the thermal evolution of continental convergent belts: *Journal of Geophysical Research*, v. 86, B7, p. 6115–6132, doi: 10.1029/JB086iB07p06115.
- Husson, L., and Sempere, T., 2003, Thickening the Altiplano crust by gravity-driven crustal channel flow: *Geophysical Research Letters*, v. 30, no. 5, n/a-n/a, doi: 10.1029/2002GL016877.

## 6. References

---

- Isacks, B.L., 1988, Uplift of the Central Andean Plateau and bending of the Bolivian Orocline: *Journal of Geophysical Research*, v. 93, B4, p. 3211–3231, doi: 10.1029/JB093iB04p03211.
- Jackson, S.E., Pearson, N.J., Griffin, W.L., and Belousova, E.A., 2004, The application of laser ablation-inductively coupled plasma-mass spectrometry to in situ U–Pb zircon geochronology: *Chemical Geology*, v. 211, no. 1, p. 47–69, doi: 10.1016/j.chemgeo.2004.06.017.
- Jadamec, M.A., Turcotte, D.L., and Howell, P., 2007, Analytic models for orogenic collapse: *Tectonophysics*, v. 435, 1-4, p. 1–12, doi: 10.1016/j.tecto.2007.01.007.
- Jones, R.S., Small, D., Cahill, N., Bentley, M.J., and Whitehouse, P.L., 2019, iceTEA: Tools for plotting and analysing cosmogenic-nuclide surface-exposure data from former ice margins: *Quaternary Geochronology*, v. 51, p. 72–86, doi: 10.1016/j.quageo.2019.01.001.
- Jones, S., McNaughton, N.J., and Grguric, B., 2013, Structural controls and timing of fault-hosted manganese at Woodie Woodie, East Pilbara, Western Australia: *Ore Geology Reviews*, v. 50, p. 52–82, doi: 10.1016/j.oregeorev.2012.10.002.
- Jones, S.A., 2017, Geology and geochemistry of fault-hosted hydrothermal and sedimentary manganese deposits in the Oakover Basin, east Pilbara, Western Australia: *Australian Journal of Earth Sciences*, v. 64, no. 1, p. 63–102, doi: 10.1080/08120099.2017.1272492.
- Jordan, T.E., and Alonso, R.N., 1987, Cenozoic Stratigraphy and Basin Tectonics of the Andes Mountains, 20°–28° South Latitude: *AAPG Bulletin*, v. 71, doi: 10.1306/94886D44-1704-11D7-8645000102C1865D.
- Jordan, T.E., Isacks, B.L., Allmendinger, R.W., Brewer, J.A., Ramos, V.A., and C. J. Ando, 1983, Andean tectonics related to geometry of the subducted Nazca plate: *Geological Society of America Bulletin*, v. 94, no. 3, p. 341–361.
- Jordan, T.E., Nester, P.L., Blanco, N., Hoke, G.D., Dávila, F., and Tomlinson, A.J., 2010, Uplift of the Altiplano-Puna plateau: A view from the west: *Tectonics*, v. 29, no. 5, n/a-n/a, doi: 10.1029/2010TC002661.

- Joussineau, G.d., Mutlu, O., Aydin, A., and Pollard, D.D., 2007, Characterization of strike-slip fault–splay relationships in sandstone: *Journal of Structural Geology*, v. 29, no. 11, p. 1831–1842, doi: 10.1016/j.jsg.2007.08.006.
- Kanamori, H., and Brodsky, E.E., 2004, The physics of earthquakes: *Reports on Progress in Physics*, v. 67, no. 8, p. 1429–1496, doi: 10.1088/0034-4885/67/8/R03.
- Kapp, P., Taylor, M., Stockli, D., and Ding, L., 2008, Development of active low-angle normal fault systems during orogenic collapse: Insight from Tibet: *Geology*, v. 36, no. 1, p. 7, doi: 10.1130/G24054A.1.
- Karlstrom, K.E., Wilgus, J., Thacker, J.O., Schmandt, B., Coblenz, D., and Albonico, M., 2022, Tectonics of the Colorado Plateau and Its Margins: *Annual Review of Earth and Planetary Sciences*, v. 50, no. 1, doi: 10.1146/annurev-earth-032320-111432.
- Kay, S.M., Coira, B., and Mpodozis, C., 1995, Neogene magmatic evolution and the shape of the subducting oceanic slab beneath the central Andean arc: IUGG 21th General Assembly, pp. A440. Boulder, CO: Int. Union Geod. Geophys.
- Kay, S.M., and Coira, B.L., 2009, Shallowing and steepening subduction zones, continental lithospheric loss, magmatism, and crustal flow under the Central Andean Altiplano-Puna Plateau, in Mahlburg Kay, S., Kay, S.M., et al., eds., *Backbone of the Americas: Shallow subduction, plateau uplift, and ridge and terrane collision*: Boulder, Colo, Geological Society of America. *Memoir / Geological Society of America*, Volume 204.
- Kelly, M.A., Lowell, T.V., Applegate, P.J., Phillips, F.M., Schaefer, J.M., Smith, C.A., Kim, H., Leonard, K.C., and Hudson, A.M., 2015, A locally calibrated, late glacial  $^{10}\text{Be}$  production rate from a low-latitude, high-altitude site in the Peruvian Andes: *Quaternary Geochronology*, v. 26, p. 70–85, doi: 10.1016/j.quageo.2013.10.007.
- Kennan, L., Lamb, S., and Rundle, C., 1995, K-Ar dates from the Altiplano and Cordillera Oriental of Bolivia: implications for Cenozoic stratigraphy and tectonics: *Journal of South American Earth Sciences*, v. 8, no. 2, p. 163–186.
- Kennan, L., Lamb, S.H., and Hoke, L., 1997, High-altitude palaeosurfaces in the Bolivian Andes: evidence for late Cenozoic surface uplift: Geological Society, London, *Special Publications*, v. 120, no. 1, p. 307–323, doi: 10.1144/GSL.SP.1997.120.01.20.
- Kirby, E., and Whipple, K.X., 2012, Expression of active tectonics in erosional landscapes: *Journal of Structural Geology*, v. 44, p. 54–75, doi: 10.1016/j.jsg.2012.07.009.

- Kleinert, K., and Strecker, M.R., 2001, Climate change in response to orographic barrier uplift: Paleosol and stable isotope evidence from the late Neogene Santa María basin, northwestern Argentina: *Geological Society of America Bulletin*, v. 113, no. 6, p. 728–742, doi: 10.1130/0016-7606(2001)113<0728:CCIRTO>2.0.CO;2.
- Kley, J., and Monaldi, C.R., 1998, Tectonic shortening and crustal thickness in the Central Andes: How good is the correlation?: *Geology*, v. 26, no. 8, p. 723, doi: 10.1130/0091-7613(1998)026<0723:TSACTI>2.3.CO;2.
- Kley, J., and Reinhardt, M., 1994, Geothermal and Tectonic Evolution of the Eastern Cordillera and the Subandean Ranges of Southern Bolivia, in Reutter, K.-J., Scheuber, E., et al., eds., *Tectonics of the Southern Central Andes*: Berlin, Heidelberg, Springer Berlin Heidelberg, p. 155–170.
- Kober, F., Alifimov, V., Ivy-Ochs, S., Kubik, P.W., and Wieler, R., 2011, The cosmogenic  $^{21}\text{Ne}$  production rate in quartz evaluated on a large set of existing  $^{21}\text{Ne}$ – $^{10}\text{Be}$  data: *Earth and Planetary Science letters*, v. 302, 1-2, p. 163–171, doi: 10.1016/j.epsl.2010.12.008.
- Koçyiğit, A., 2013, New field and seismic data about the intraplate strike-slip deformation in Van region, East Anatolian plateau, E. Turkey: *Journal of Asian Earth Sciences*, v. 62, p. 586–605, doi: 10.1016/j.jseaes.2012.11.008.
- Kounov, A., Niedermann, S., WIT, M.J. de, CODILEAN, A.T., VIOLA, G., ANDREOLI, M., and CHRISTL, M., 2015, COSMOGENIC  $^{21}\text{Ne}$  AND  $^{10}\text{Be}$  REVEAL A MORE THAN 2 Ma ALLUVIAL FAN FLANKING THE CAPE MOUNTAINS, SOUTH AFRICA: *South African Journal of Geology*, v. 118, no. 2, p. 129–144, doi: 10.2113/gssajg.118.2.129.
- Kraemer, B., Adelman, D., Alten, M., Schnurr, W., Erpenstein, K., Kiefer, E., van den Bogaard, P., and Görler, K., 1999, Incorporation of the Paleogene foreland into the Neogene Puna plateau: The Salar de Antofalla area, NW Argentina: *Journal of South American Earth Sciences*, v. 12, no. 2, p. 157–182, doi: 10.1016/S0895-9811(99)00012-7.
- Kröger, J., 1956, *Depositos de Manganeso del distrito de Tafna*: Buenos Aires.
- Krystopowicz, N.J., Schoenbohm, L.M., Rimando, J., Brocard, G., and Rojay, B., 2020, Tectonic geomorphology and Plio-Quaternary structural evolution of the Tuzgölü fault zone, Turkey: Implications for deformation in the interior of the Central Anatolian Plateau: *Geosphere*, v. 16, no. 5, p. 1107–1124, doi: 10.1130/GES02175.1.

- 
- Kulemeyer, J.J., 2005, Holozänentwicklung im Einzugsgebiet des Río Yavi (Jujuy / Argentinien) [Doctoral Thesis]: Uni, Universität Bayreuth, 157 p.
- Kuleshov, V., 2017, Genetic Types, Classifications, and Models of Manganese-Ore Formation, in *Isotope Geochemistry*, ELSEVIER, p. 63–352.
- Lague, D., 2014, The stream power river incision model: evidence, theory and beyond: *Earth Surf. Process. Landforms (Earth Surface Processes and Landforms)*, v. 39, no. 1, p. 38–61, doi: 10.1002/esp.3462.
- Lal, D., 1991, Cosmic ray labeling of erosion surfaces: in situ nuclide production rates and erosion models: *Earth and Planetary Science letters*, v. 104, 2-4, p. 424–439, doi: 10.1016/0012-821X(91)90220-C.
- Lal, D., and Peters, B., 1967, Cosmic Ray Produced Radioactivity on the Earth, in Sitte, K., ed., *Kosmische Strahlung II / Cosmic Rays II*: Berlin, Heidelberg, Springer. *Handbuch der Physik / Encyclopedia of Physics*, 9 / 46 / 2, p. 551–612.
- Lamb, S., Hoke, L., Kennan, L., and Dewey, J., 1997, Cenozoic evolution of the Central Andes in Bolivia and northern Chile, in *The Geological Society*, ed., *Orogeny Through Time*: London, p. 237–264.
- Latrubesse, E.M., 2015, Large rivers, megafans and other Quaternary avulsive fluvial systems: A potential "who's who" in the geological record: *Earth-Science Reviews*, v. 146, p. 1–30.
- Le Dortz, K., Meyer, B., Sébrier, M., Braucher, R., Bourlès, D., Benedetti, L., Nazari, H., and Foroutan, M., 2012, Interpreting scattered in-situ produced cosmogenic nuclide depth-profile data: *Quaternary Geochronology*, v. 11, no. 1, p. 98–115, doi: 10.1016/j.quageo.2012.02.020.
- Lease, R.O., and Ehlers, T.A., 2013, Incision into the eastern Andean Plateau during Pliocene cooling: *Science (New York, N.Y.)*, v. 341, no. 6147, p. 774–776, doi: 10.1126/science.1239132.
- Ledesma, J., del Papa, C., and Payrola, P.A., 2019, Revisión de la estratigrafía eocena-pliocena de la cuenca intermontana de San Antonio de los Cobres, Puna Saltena, Argentina: *Latin American Journal of Sedimentology and Basin Analysis*, v. 26, no. 1, p. 57–73.

## 6. References

---

- Leier, A., McQuarrie, N., Garzione, C., and Eiler, J., 2013, Stable isotope evidence for multiple pulses of rapid surface uplift in the Central Andes, Bolivia: *Earth and Planetary Science letters*, 371-372, p. 49–58, doi: 10.1016/j.epsl.2013.04.025.
- Levander, A., and Miller, M.S., 2012, Evolutionary aspects of lithosphere discontinuity structure in the western U.S: *Geochemistry, Geophysics, Geosystems*, v. 13, no. 7, n/a-n/a, doi: 10.1029/2012GC004056.
- Levandowski, W., Jones, C.H., Butcher, L.A., and Mahan, K.H., 2018, Lithospheric density models reveal evidence for Cenozoic uplift of the Colorado Plateau and Great Plains by lower-crustal hydration: *Geosphere*, v. 14, no. 3, p. 1150–1164, doi: 10.1130/GES01619.1.
- Liu, M., 2003, Extensional collapse of the Tibetan Plateau: Results of three-dimensional finite element modeling: *Journal of Geophysical Research*, v. 108, B8, doi: 10.1029/2002JB002248.
- Liu, M., Shen, Y., and Yang, Y., 2000, Gravitational collapse of orogenic crust: A preliminary three-dimensional finite element study: *Journal of Geophysical Research*, v. 105, B2, p. 3159–3173.
- Liu, Z., Zhao, Y., Colin, C., Statterger, K., Wiesner, M.G., Huh, C.-A., Zhang, Y., Li, X., Sompongchaiyakul, P., You, C.-F., Huang, C.-Y., Liu, J.T., Siringan, F.P., Le, K.P., Sathiamurthy, E., Hantoro, W.S., Liu, J., Tuo, S., Zhao, S., Zhou, S., He, Z., Wang, Y., Bunsomboonsakul, S., and Li, Y., 2016, Source-to-sink transport processes of fluvial sediments in the South China Sea: *Earth-Science Reviews*, v. 153, p. 238–273, doi: 10.1016/j.earscirev.2015.08.005.
- Liu-Zeng, J., Tapponnier, P., Gaudemer, Y., and Ding, L., 2008, Quantifying landscape differences across the Tibetan plateau: Implications for topographic relief evolution: *Journal of Geophysical Research*, v. 113, F4, doi: 10.1029/2007JF000897.
- Lork, A., Miller, H., and Kramm, U., 1989, U•Pb zircon and monazite ages of the La Angostura granite and the orogenic history of the northwest Argentine basement: *Journal of South American Earth Sciences*, v. 2, no. 2, p. 147–153, doi: 10.1016/0895-9811(89)90042-4.
- Luna, L.V., Bookhagen, B., Niedermann, S., Rugel, G., Scharf, A., and Merchel, S., 2018, Glacial chronology and production rate cross-calibration of five cosmogenic nuclide and

- mineral systems from the southern Central Andean Plateau: *Earth and Planetary Science letters*, v. 500, p. 242–253, doi: 10.1016/j.epsl.2018.07.034.
- Lykakis, N., and Kiliyas, S.P., editors, 2010, Epithermal Manganese mineralization, Kimolos Island, South Aegean volcanic arc, Greece, 12 p.
- Ma, Y., and Stuart, F.M., 2018, The use of in-situ cosmogenic  $^{21}\text{Ne}$  in studies on long-term landscape development: *Acta Geochimica*, v. 37, no. 2, p. 310–322, doi: 10.1007/s11631-017-0216-9.
- MacFadden, B.J., Anaya, F., Perez, H., Naeser, C.W., Zeitler, P.K., and Campbell, K.E., 1990, Late Cenozoic Paleomagnetism and Chronology of Andean Basins of Bolivia: Evidence for Possible Oroclinal Bending: *The Journal of Geology*, v. 98, no. 4, p. 541–555.
- Madarieta-Txurruka, A., Galindo-Zaldívar, J., González-Castillo, L., Peláez, J.A., Ruiz-Armenteros, A.M., Henares, J., Garrido-Carretero, M.S., Avilés, M., and Gil, A.J., 2021, High- and Low-Angle Normal Fault Activity in a Collisional Orogen: The Northeastern Granada Basin (Betic Cordillera): *Tectonics*, v. 40, no. 7, e2021TC006715, doi: 10.1029/2021TC006715.
- Maloney, K.T., Clarke, G.L., Klepeis, K.A., and Quevedo, L., 2013, The Late Jurassic to present evolution of the Andean margin: Drivers and the geological record: *Tectonics*, v. 32, no. 5, p. 1049–1065, doi: 10.1002/tect.20067.
- Manger, E., 1963, Porosity and bulk density of sedimentary rocks, 60 p.
- Marliyani, G.I., Arrowsmith, J.R., and Whipple, K.X., 2016, Characterization of slow slip rate faults in humid areas: Cimandiri fault zone, Indonesia: *Journal of Geophysical Research: Earth Surface*, v. 121, no. 12, p. 2287–2308, doi: 10.1002/2016JF003846.
- Marquillas, R.A., Del Papa, C., and Sabino, I.F., 2005, Sedimentary aspects and paleoenvironmental evolution of a rift basin: Salta Group (Cretaceous–Paleogene), northwestern Argentina: *International Journal of Earth Sciences*, v. 94, no. 1, p. 94–113, doi: 10.1007/s00531-004-0443-2.
- Marrero, S.M., Phillips, F.M., Borchers, B., Lifton, N., Aumer, R., and Balco, G., 2016, Cosmogenic nuclide systematics and the CRONUScale program: *Quaternary Geochronology*, v. 31, p. 160–187, doi: 10.1016/j.quageo.2015.09.005.
- Marrett, R.A., Allmendinger, R.W., Alonso, R.N., and Drake, R.E., 1994, Late Cenozoic tectonic evolution of the Puna Plateau and adjacent foreland, northwestern Argentine

## 6. References

---

Andes: *Journal of South American Earth Sciences*, v. 7, no. 2, p. 179–207, doi: 10.1016/0895-9811(94)90007-8.

Martin, L., Blard, P.-H., Lavé, J., Braucher, R., Lupker, M., Condom, T., Charreau, J., Mariotti, V., Team, A., and Davy, E., 2015, In situ cosmogenic  $^{10}\text{Be}$  production rate in the High Tropical Andes: *Quaternary Geochronology*, v. 30, p. 54–68, doi: 10.1016/j.quageo.2015.06.012.

Maune, D., 2007, Digital elevation model technologies and applications: The DEM users manual.

Maune, D., Kopp, S., Crawford, C., and Zervas, C., 2001, Digital elevation model technologies and applications: The DEM users manual Chapter 1 Introduction, in *Digital Elevation Modeling Techniques and Applications: The DEM Users Manual*, p. 1–34.

McCalpin, J.P., 2009, *Paleoseismology*, 2. ed.: Amsterdam, Elsevier Acad. Press, International geophysics series, Volume 95.

McFarland, P.K., Bennett, R.A., Alvarado, P., and DeCelles, P.G., 2017, Rapid Geodetic Shortening Across the Eastern Cordillera of NW Argentina Observed by the Puna-Andes GPS Array: *Journal of Geophysical Research: Solid Earth*, v. 122, no. 10, p. 8600–8623, doi: 10.1002/2017JB014739.

McQuarrie, N., and Chase, C.G., 2000, Raising the Colorado Plateau: *Geology*, v. 28, no. 1, p. 91.

McQuarrie, N., Ehlers, T.A., Barnes, J.B., and Meade, B., 2008, Temporal variation in climate and tectonic coupling in the central Andes: *Geology*, v. 36, no. 12, p. 999, doi: 10.1130/G25124A.1.

McQuarrie, N., Horton, B.K., Zandt, G., Beck, S., and DeCelles, P.G., 2005, Lithospheric evolution of the Andean fold–thrust belt, Bolivia, and the origin of the central Andean plateau: *Tectonophysics*, v. 399, 1-4, p. 15–37, doi: 10.1016/j.tecto.2004.12.013.

Meek, N., and Douglass, J., 2001, Lake overflow: an alternative hypothesis for Grand Canyon incision and development of the Colorado River, in Young, R.A., Spamer, E.E., ed., *Colorado River: Origin and Evolution*, Volume 12, p. 199–204.

Meek, N., and Douglass, J., 2006, Lake Overflow An Alternative Hypothesis for Grand Canyon Incision and Development of the Colorado River.

- 
- Mercier, J.L., 1981, Extensional-compressional tectonics associated with the Aegean Arc: comparison with the Andean Cordillera of south Peru - north Bolivia: *Philosophical Transactions of the Royal Society*, no. 300, p. 337–355.
- Mercier, J.L., Carey-Gailhardis, E., and Sébrier, M., 1991, Palaeostress determinations from fault kinematics: application to the neotectonics of the Himalayas-Tibet and the Central Andes: *Philosophical Transactions of the Royal Society of London. Series A: Physical and Engineering Sciences*, v. 337, no. 1645, p. 41–52, doi: 10.1098/rsta.1991.0105.
- Métivier, F., Gaudemer, Y., Tapponnier, P., and Meyer, B., 1998, Northeastward growth of the Tibet plateau deduced from balanced reconstruction of two depositional areas: The Qaidam and Hexi Corridor basins, China: *Tectonics*, v. 17, no. 6, p. 823–842.
- Molnar, P., 2004, Late Cenozoic increase in accumulation rates of terrestrial sediment: How Might Climate Change Have Affected Erosion Rates?: *Annual Review of Earth and Planetary Sciences*, v. 32, no. 1, p. 67–89, doi: 10.1146/annurev.earth.32.091003.143456.
- Molnar, P., England, P., and Martinod, J., 1993, Mantle dynamics, uplift of the Tibetan Plateau, and the Indian Monsoon: *Reviews of Geophysics*, v. 31, no. 4, p. 357, doi: 10.1029/93RG02030.
- Molnar, P., and Lyon-Caen, H., 1988, Some simple physical aspects of the support, structure, and evolution of mountain belts: *Geological Society of America Special Papers*, no. 218, p. 179–208.
- Mon, R., Mena, R., and Amenguel, R., 1996, Plegamiento cenozoico del basamento proterozoico de la Cordillera Oriental del norte Argentino: *Revista de la Asociación Geológica Argentina*, no. 51, p. 213–223.
- Mon, R., Mena, R., Marrett, R.A., and Hongn, F., 1988, Rasgos de neotectónica en la Puna Austral (República Argentina): *V Congreso Geológico Chileno. Acta 1:*, p. 69–83.
- Montero-López, C., Strecker, M.R., Schildgen, T.F., Hongn, F., Guzmán, S., Bookhagen, B., and Sudo, M., 2014, Local high relief at the southern margin of the Andean plateau by 9 Ma: evidence from ignimbritic valley fills and river incision: *Terra Nova*, v. 26, no. 6, p. 454–460, doi: 10.1111/ter.12120.
- Montero-López, M.C., Hongn, F., Strecker, M.R., Marrett, R.A., Seggiaro, R., and Sudo, M., 2010, Late Miocene–early Pliocene onset of N–S extension along the southern margin

of the Central Andean Puna Plateau: Evidence from magmatic, geochronological and structural observations: *Tectonophysics*, no. 494, p. 48–63.

Montero-López, C., Hongn, F., López Steinmetz, R.L., Aramayo, A., Pingel, H., Strecker, M.R., Cottle, J.M., and Bianchi, C., 2020, Development of an incipient Paleogene topography between the present-day Eastern Andean Plateau (Puna) and the Eastern Cordillera, southern Central Andes, NW Argentina: *Basin Research*, v. 74, no. 6, p. 180, doi: 10.1111/bre.12510.

Montero-López, C., Hongn, F., López Steinmetz, R.L., Aramayo, A., Pingel, H., Strecker, M.R., Cottle, J.M., and Bianchi, C., 2021, Development of an incipient Paleogene topography between the present-day Eastern Andean Plateau (Puna) and the Eastern Cordillera, southern Central Andes, NW Argentina: *Basin Research*, v. 33, no. 2, p. 1194–1217, doi: 10.1111/bre.12510.

Moreno, J.A., 1970, Estratigrafía y paleogeografía del Cretácico superior en la cuenca del noroeste argentino, con especial mención de los Subgrupos Balbuena y Santa ...: *Revista de la Asociación Geológica Argentina*, v. 25, p. 9–44.

Morley, C.K., 2017, The impact of multiple extension events, stress rotation and inherited fabrics on normal fault geometries and evolution in the Cenozoic rift basins of Thailand: *Geological Society, London, Special Publications*, v. 439, no. 1, p. 413–445, doi: 10.1144/SP439.3.

Mudd, S.M., Clubb, F.J., Gailleton, B., and Hurst, M.D., 2018, How concave are river channels?: *Earth Surf. Dynam. (Earth Surface Dynamics)*, v. 6, no. 2, p. 505–523, doi: 10.5194/esurf-6-505-2018.

Mulcahy, P., Chen, C., Kay, S.M., Brown, L.D., Isacks, B.L., Sandvol, E., Heit, B., Yuan, X., and Coira, B.L., 2014, Central Andean mantle and crustal seismicity beneath the Southern Puna plateau and the northern margin of the Chilean-Pampean flat slab: *Tectonics*, v. 33, no. 8, p. 1636–1658, doi: 10.1002/2013TC003393.

Mulch, A., and Chamberlain, C.P., 2006, The rise and growth of Tibet: *Nature*, no. 439, p. 670–671.

Murawski, H., Albers, H.J., Bender, P., Berners, H.-P., Dürr, S., Huckriede, R., Kauffmann, G., Kowalczyk, G., Meiburg, P., Müller, R., Muller, A., Ritzkowski, S., Schwab, K., Semmel, A., Stapf, K., Walter, R., Winter, K.-P., and Zankl, H., 1983, Regional Tectonic

- Setting and Geological Structure of the Rhenish Massif, in Fuchs, K., Gehlen, K., et al., eds., *Plateau Uplift: The Rhenish Shield - A Case History*: Berlin, Heidelberg, s.l., Springer Berlin Heidelberg, p. 9–38.
- Mutti, M., Vallati, M., Tomás, S., Galli, C., Bahniuk Rumbelsperger, A.M., Maerz, S., and Coira, B., 2023, Constraining depositional evolution and reservoir compartmentalization in a mixed carbonate-siliciclastic lacustrine system: The Yacoraite formation, Salta Group, NW Argentina: *Marine and Petroleum Geology*, v. 149, p. 106049, doi: 10.1016/j.marpetgeo.2022.106049.
- Myers, S.C., Beck, S., Zandt, G., and Wallace, T., 1998, Lithospheric-scale structure across the Bolivian Andes from tomographic images of velocity and attenuation for <emph type: *Journal of Geophysical Research*, v. 103, B9, p. 21233–21252.
- Nash, D., 2013, 5.10 Tectonic Geomorphology of Normal Fault Scarps, in Shroder, J.F., ed., *Treatise on geomorphology*: Amsterdam, Elsevier/Acad. Press, p. 234–249.
- Niedermann, S., 2002, Cosmic-Ray-Produced Noble Gases in Terrestrial Rocks: Dating Tools for Surface Processes: *Reviews in Mineralogy and Geochemistry*, v. 47, no. 1, p. 731–784, doi: 10.2138/rmg.2002.47.16.
- Nivière, B., Lacan, P., Regard, V., Delmas, M., Calvet, M., Huyghe, D., and Roddaz, B., 2016, Evolution of the Late Pleistocene Aspe River (Western Pyrenees, France). Signature of climatic events and active tectonics: *Comptes Rendus Geoscience*, v. 348, 3-4, p. 203–212, doi: 10.1016/j.crte.2015.07.003.
- Özsayin, E., Çiner, A., Rojay, F., Dirik, R., Melnick, D., Fernández-Blanco, D., Bertotti, G., Schildgen, T., Garcin, Y., and Strecker, M., 2018, Plio-Quaternary extensional tectonics of the Central Anatolian Plateau: a case study from the Tuz Gölü Basin, Turkey, 24 p.
- Paton, C., Woodhead, J.D., Hellstrom, J.C., Hergt, J.M., Greig, A., and Maas, R., 2010, Improved laser ablation U-Pb zircon geochronology through robust downhole fractionation correction: *Geochemistry Geophysics Geosystems*, v. 11, no. 3, n/a-n/a, doi: 10.1029/2009GC002618.
- Pavano, F., Pazzaglia, F.J., and Catalano, S., 2016, Knickpoints as geomorphic markers of active tectonics: A case study from northeastern Sicily (southern Italy): *Lithosphere*, v. 8, no. 6, p. 633–648, doi: 10.1130/L577.1.

- Penck, W., 1920, Der Südrand der Puna de Atacama (NW-Argentinien): Ein Beitrag zur Kenntnis des Andinen Gebirgstypus und der Frage der Gebirgsbildung: *Abhandlungen der Sächsischen Akademie der Wissenschaften*, no. 1, p. 3–420.
- Perkins, J.P., Ward, K.M., Silva, S.L. de, Zandt, G., Beck, S.L., and Finnegan, N.J., 2016, Surface uplift in the Central Andes driven by growth of the Altiplano Puna Magma Body: *Nature communications*, v. 7, p. 13185, doi: 10.1038/ncomms13185.
- Perrigo, A., Hoorn, C., and Antonelli, A., 2020, Why mountains matter for biodiversity: *Journal of Biogeography*, v. 47, no. 2, p. 315–325, doi: 10.1111/jbi.13731.
- Pingel, H., Alonso, R.N., Mulch, A., Rohrmann, A., Sudo, M., and Strecker, M.R., 2014, Pliocene orographic barrier uplift in the southern Central Andes: *Geology*, v. 42, no. 8, p. 691–694, doi: 10.1130/G35538.1.
- Pingel, H., Schildgen, T., Strecker, M.R., and Wittmann, H., 2019, Pliocene–Pleistocene orographic control on denudation in northwest Argentina: *Geology*, v. 47, no. 4, p. 359–362, doi: 10.1130/G45800.1.
- Pingel, H., Strecker, M.R., Mulch, A., Alonso, R.N., Cottle, J., and Rohrmann, A., 2020, Late Cenozoic topographic evolution of the Eastern Cordillera and Puna Plateau margin in the southern Central Andes (NW Argentina): *Earth and Planetary Science letters*, v. 535, p. 116112, doi: 10.1016/j.epsl.2020.116112.
- Placzek, C., Quade, J., Rech, J.A., Patchett, P.J., and Pérez de Arce, C., 2009, Geochemistry, chronology and stratigraphy of Neogene tuffs of the Central Andean region: *Quaternary Geochronology*, v. 4, no. 1, p. 22–36, doi: 10.1016/j.quageo.2008.06.002.
- Pope, D.C., and Willett, S.D., 1998, Thermal-mechanical model for crustal thickening in the central Andes driven by ablative subduction: *Geology*, v. 26, no. 6, p. 511, doi: 10.1130/0091-7613(1998)026<0511:TMMFCT>2.3.CO;2.
- Prezzi, C., Caffè, P.J., and Somoza, R., 2004, New paleomagnetic data from the northern Puna and western Cordillera Oriental, Argentina: a new insight on the timing of rotational deformation: *Journal of Geodynamics*, v. 38, no. 2, p. 93–115, doi: 10.1016/j.jog.2004.05.001.
- Quade, J., Garziona, C., and Eiler, J., 2007, Paleoelevation Reconstruction using Pedogenic Carbonates: *Reviews in Mineralogy and Geochemistry*, v. 66, no. 1, p. 53–87, doi: 10.2138/rmg.2007.66.3.

- 
- Queiroz, G.L., Salamuni, E., and Nascimento, E.R., 2015, Knickpoint finder: A software tool that improves neotectonic analysis: *Computers & Geosciences*, v. 76, p. 80–87, doi: 10.1016/j.cageo.2014.11.004.
- Quiñones, S.I., Miño-Boilini, Á.R., Zurita, A.E., Contreras, S.A., Luna, C.A., Candela, A.M., Camacho, M., Ercoli, M.D., Solís, N., and Brandoni, D., 2019, New records of Neogene Xenarthra (Mammalia) from eastern Puna (Argentina): diversity and biochronology: *Journal of Paleontology*, v. 93, no. 06, p. 1258–1275, doi: 10.1017/jpa.2019.64.
- Rahl, J.M., Harbor, D.J., Galli, C.I., and O'Sullivan, P., 2018, Foreland Basin Record of Uplift and Exhumation of the Eastern Cordillera, Northwest Argentina: *Tectonics*, v. 37, no. 11, p. 4173–4193, doi: 10.1029/2017TC004955.
- Ramasamy, S.M., 2006, Remote sensing and active tectonics of South India: *International Journal of Remote Sensing*, v. 27, no. 20, p. 4397–4431, doi: 10.1080/01431160500502603.
- Ramos, V.A., 2018, Tectonic Evolution of the Central Andes: From Terrane Accretion to Crustal Delamination, *AAPG Special Volumes*, 1 p.
- Ramos, V.A., and McNulty, B., 2002, Flat-slab subduction in the Andes: *Journal of South American Earth Sciences*, v. 15, no. 1, p. 1–2, doi: 10.1016/s0895-9811(02)00011-1.
- Reitman, N.G., Bennett, S.E.K., Gold, R.D., Briggs, R.W., and DuRoss, C.B., 2015, High-Resolution Trench Photomosaics from image-Based Modeling: Workflow and Error Analysis: *Bulletin of the Seismological Society of America*, v. 105, pp.-.
- Reitman, N.G., Mueller, K.J., Tucker, G.E., Gold, R.D., Briggs, R.W., and Barnhart, K.R., 2019, Offset Channels May Not Accurately Record Strike-Slip Fault Displacement: Evidence From Landscape Evolution Models: *Journal of Geophysical Research: Solid Earth*, v. 124, no. 12, p. 13427–13451, doi: 10.1029/2019JB018596.
- Rey, P., Vanderhaeghe, O., and Teyssier, C., 2001, Gravitational collapse of the continental crust: definition, regimes and modes: *Tectonophysics*, v. 342, 3-4, p. 435–449, doi: 10.1016/S0040-1951(01)00174-3.
- Rey, P.F., Teyssier, C., and Whitney, D.L., 2010, Limit of channel flow in orogenic plateaux: *Lithosphere*, v. 2, no. 5, p. 328–332, doi: 10.1130/L114.1.

## 6. References

---

- Risse, A., Trumbull, R.B., Coira, B., Kay, S.M., and van Bogaard, P. den, 2008, 40Ar/39Ar geochronology of mafic volcanism in the back-arc region of the southern Puna plateau, Argentina: *Journal of South American Earth Sciences*, v. 26, no. 1, p. 1–15, doi: 10.1016/j.jsames.2008.03.002.
- Roberts, N.J., Barendregt, R.W., and Clague, J.J., 2017, Multiple tropical Andean glaciations during a period of late Pliocene warmth: *Scientific Reports*, v. 7, no. 1, p. 41878, doi: 10.1038/srep41878.
- Rodríguez-Fernández, L.R., Heredia, N., González, M.A., and Seggiaro, R.E., 1999, Estructura Andina de la Cordillera Oriental en el área de la Quebradade Humahuaca, Provincia de Jujuy, NO de Argentina.): *Trabajos de Geología*, v. 21, no. 21, p. 321–332, doi: 10.17811/tdg.21.1999.321-333.
- Roeder, D., 1988, Andean-age structure of Eastern Cordillera (Province of La Paz, Bolivia): *Tectonics*, v. 7, no. 1, p. 23–39, doi: 10.1029/TC007i001p00023.
- Rohrmann, A., Sachse, D., Mulch, A., Pingel, H., Tofelde, S., Alonso, R.N., and Strecker, M.R., 2016, Miocene orographic uplift forces rapid hydrological change in the southern central Andes: *Scientific Reports*, v. 6, no. 1, p. 35678, doi: 10.1038/srep35678.
- Rothery, D.A., and Drury, S.A., 1984, The neotectonics of the Tibetan Plateau: *Tectonics*, v. 3, no. 1, p. 19–26.
- Rubiolo, D., 2003, Programa Nacional de Cartas Geológicas de la República Argentina: Hoja Geológica 2366-II/2166-IV: Buenos Aires, Boletín N°246, La Quiaca, 123 p.
- Ruddiman, W.F., editor, 1997, *Tectonic Uplift and Climate Change*: Boston, MA, s.l., Springer US, 535 p.
- Ruddiman, W.F., and Kutzbach, J.E., 1991, Plateau Uplift and Climatic Change: *Scientific American*, no. 264, p. 66–75.
- Sánchez, M.C., and Salfity, J.A., 1999, La cuenca cámbrica del Grupo Mesón en el Noroeste Argentino: desarrollo estratigráfico y paleogeográfico: The Cambrian Mesón Group basin (NW Argentina): stratigraphic and paleogeographic development: *ACTA GEOLOGICA HISPANICA*, no. 34, p. 123–139.
- Schildgen, T.F., Cosentino, D., Bookhagen, B., Niedermann, S., Yildirim, C., Echtler, H., Wittmann, H., and Strecker, M.R., 2012, Multi-phased uplift of the southern margin of the

- 
- Central Anatolian plateau, Turkey: A record of tectonic and upper mantle processes: *Earth and Planetary Science letters*, 317-318, p. 85–95, doi: 10.1016/j.epsl.2011.12.003.
- Schildgen, T.F., Ehlers, T.A., Whipp, D.M., van Soest, M.C., Whipple, K.X., and Hodges, K.V., 2009, Quantifying canyon incision and Andean Plateau surface uplift, southwest Peru: A thermochronometer and numerical modeling approach: *Journal of Geophysical Research*, v. 114, F4, doi: 10.1029/2009JF001305.
- Schildgen, T.F., Hodges, K.V., Whipple, K.X., Reiners, P.W., and Pringle, M.S., 2007, Uplift of the western margin of the Andean plateau revealed from canyon incision history, southern Peru: *Geology*, v. 35, no. 6, p. 523, doi: 10.1130/G23532A.1.
- Schlunegger, F., Zeilinger, G., Kounov, A., Kober, F., and Husser, B., 2006, Scale of relief growth in the forearc of the Andes of Northern Chile (Arica latitude, 18oS): *Terra Nova*, v. 18, no. 3, p. 217–223, doi: 10.1111/j.1365-3121.2006.00682.x.
- Schmidt, K.-H., 1988, *Die Reliefentwicklung des Colorado Plateaus*: Berlin, Im Selbstverlag des Institutes für Physische Geographie der Freien Universität Berlin, Berliner geographische Abhandlungen, Heft 49, 183 p.
- Schmitz, M., 1994, A balanced model of the southern Central Andes: *Tectonics*, v. 13, no. 2, p. 484–492, doi: 10.1029/93TC02232.
- Schmitz, M., and Kley, J., 1997, The geometry of the central Andean backarc crust: Joint interpretation of cross-section balancing and seismic refraction data: *Journal of South American Earth Sciences*, v. 10, no. 1, p. 99–110, doi: 10.1016/S0895-9811(97)00009-6.
- Schoenbohm, L., Carrapa, B., McPherson, H.M., Pratt, J., Bywater-Reyes, S., and Mortimer, E., 2015, Climate and tectonics along the southern margin of the Puna Plateau, NW Argentina: Origin of the late Cenozoic Puna Schotter conglomerates: undefined.
- Schoenbohm, L.M., and Strecker, M.R., 2009, Normal faulting along the southern margin of the Puna Plateau, northwest Argentina: *Tectonics*, v. 28, no. 5, n/a-n/a, doi: 10.1029/2008TC002341.
- Schumm, S.A., Dumont, J.F., and Holbrook, J.M., 2000, *Active Tectonics and Alluvial Rivers*: Cambridge, UK, Cambridge University Press.
- Schurr, B., Asch, G., Rietbrock, A., Kind, R., Pardo, M., Heit, B., and Monfret, T., 1999, Seismicity and average velocities beneath the Argentine Puna Plateau: *Geophysical Research Letters*, v. 26, no. 19, p. 3025–3028.

Schurr, B., Rietbrock, A., Asch, G., Kind, R., and Oncken, O., 2006, Evidence for lithospheric detachment in the central Andes from local earthquake tomography: *Tectonophysics*, v. 415, 1-4, p. 203–223, doi: 10.1016/j.tecto.2005.12.007.

Schwab, K., 1973, *Die Stratigraphie in der Umgebung des Salar de Cauchari (NW-Argentinien): Ein Beitrag zur erdgeschichtlichen Entwicklung der Puna ; mit 5 Tabellen:* Stuttgart, Schweizerbart, *Geotektonische Forschungen*, Volume 43, 168 p.

Schwanghart, W., and Kuhn, N.J., 2010, TopoToolbox: A set of Matlab functions for topographic analysis: *Environmental Modelling & Software*, v. 25, no. 6, p. 770–781, doi: 10.1016/j.envsoft.2009.12.002.

Schwanghart, W., and Scherler, D., 2014, Short Communication: TopoToolbox 2 – MATLAB-based software for topographic analysis and modeling in Earth surface sciences: *Earth Surf. Dynam. (Earth Surface Dynamics)*, v. 2, no. 1, p. 1–7, doi: 10.5194/esurf-2-1-2014.

Schwanghart, W., and Scherler, D., 2014, The difference between carving and filling (2): <https://topotoolbox.wordpress.com/2014/05/04/the-difference-between-carving-and-filling-2/> (November 2021).

Schwartz, D.P., and Coppersmith, K.J., 1984, Fault behavior and characteristic earthquakes: Examples from the Wasatch and San Andreas Fault Zones: *Journal of Geophysical Research*, v. 89, B7, p. 5681–5698, doi: 10.1029/JB089iB07p05681.

Seagren, E.G., and Schoenbohm, L.M., 2021, Drainage Reorganization Across the Puna Plateau Margin (NW Argentina): Implications for the Preservation of Orogenic Plateaus: *Journal of Geophysical Research: Earth Surface*, v. 126, no. 8.

Sébrier, M., Mercier, J.L., Macharé, J., Bonnot, D., Cabrera, J., and Blanc, J.L., 1988, The state of stress in an overriding plate situated above a flat slab: The Andes of central Peru: *Tectonics*, v. 7, no. 4, p. 895–928, doi: 10.1029/TC007i004p00895.

Servant, M., Sempere, T., Argollo, J., Bernart, M., Feraud, G., and Lo Bello, P., 1989, Morphogenèse et soulèvement de la Cordillère orientale des Andes de Bolivie au Cénozoïque: *Comptes rendus de l'Académie des sciences Paris, Série II*, no. 309, p. 417–422.

Sibson, R.H., 1985, A note on fault reactivation: *Journal of Structural Geology*, v. 7, no. 6, p. 751–754, doi: 10.1016/0191-8141(85)90150-6.

- 
- Smit, J.H.W., Brun, J.P., and Sokoutis, D., 2003, Deformation of brittle-ductile thrust wedges in experiments and nature: *Journal of Geophysical Research: Solid Earth*, v. 108, B10, p. 3, doi: 10.1029/2002JB002190.
- Smith, A.T., and Foggin, J.M., 1999, The plateau pika (*Ochotona curzoniae*) is a keystone species for biodiversity on the Tibetan plateau: *Animal Conservation*, v. 2, no. 4, p. 235–240, doi: 10.1111/j.1469-1795.1999.tb00069.x.
- Sobel, E.R., Hilley, G.E., and Strecker, M.R., 2003, Formation of internally drained contractional basins by aridity-limited bedrock incision: *Journal of Geophysical Research*, v. 108, B7, doi: 10.1029/2002JB001883.
- Sobel, E.R., and Strecker, M.R., 2003, Uplift, exhumation and precipitation: tectonic and climatic control of Late Cenozoic landscape evolution in the northern Sierras Pampeanas, Argentina: *Basin Research*, v. 15, no. 4, p. 431–451, doi: 10.1046/j.1365-2117.2003.00214.x.
- Soler, M.M., and Coira, B., 2002, Volcanismo oligoceno superior – mioceno inferior en la sierra de Pirurayo, Puna jujeña: estratigrafía y mecanismos eruptivos: *Revista de la Asociación Geológica Argentina*, v. 57, no. 2, p. 160–172.
- Strecker, M.R., Alonso, R., Bookhagen, B., Carrapa, B., Coutand, I., Hain, M.P., Hilley, G.E., Mortimer, E., Schoenbohm, L., and Sobel, E.R., 2009, Does the topographic distribution of the central Andean Puna Plateau result from climatic or geodynamic processes?: *Geology*, v. 37, no. 7, p. 643–646, doi: 10.1130/G25545A.1.
- Strecker, M.R., Alonso, R.N., Bookhagen, B., Carrapa, B., Hilley, G.E., Sobel, E.R., and Trauth, M.H., 2007, Tectonics and Climate of the Southern Central Andes: *Annual Review of Earth and Planetary Sciences*, v. 35, no. 1, p. 747–787, doi: 10.1146/annurev.earth.35.031306.140158.
- Strecker, M.R., Alonso, R.N., Bookhagen, B., and Pingel, H., 2016, Neotectonics and Landscape Evolution in the south central andes of NW Argentina, 53 p.
- Such, P., Buatois, L.A., and Mangano, M.G., 2007, Estratigrafía, ambientes deposicionales e icnología del Paleozoico inferior en el área de Azul Pampa, provincia de Jujuy: *Revista de la Asociación Geológica Argentina*, v. 62, no. 3, p. 331–344.

- Tao, W.C., and O'Connell, R.J., 1992, Ablative subduction: A two-sided alternative to the conventional subduction model: *Journal of Geophysical Research*, v. 97, B6, p. 8877, doi: 10.1029/91JB02422.
- Tapia, J., Murray, J., Ormachea, M., Tirado, N., and Nordstrom, D.K., 2019, Origin, distribution, and geochemistry of arsenic in the Altiplano-Puna plateau of Argentina, Bolivia, Chile, and Perú: *The Science of the total environment*, v. 678, p. 309–325, doi: 10.1016/j.scitotenv.2019.04.084.
- Thomas, F., Rizza, M., Bellier, O., Billant, J., Dussouillez, P., Fleury, J., Delanghe, D., Ollivier, V., Godard, V., and Talon, B., 2021, Assessing post-pliocene deformation in a context of slow tectonic deformation: insights from paleoseismology, remote sensing and shallow geophysics in Provence, France: *Natural Hazards*, v. 105, no. 2, p. 1453–1490, doi: 10.1007/s11069-020-04362-5.
- Tibaldi, A., and Bonali, F.L., 2018, Contemporary recent extension and compression in the central Andes: *Journal of Structural Geology*, v. 107, p. 73–92, doi: 10.1016/j.jsg.2017.12.004.
- Tineo, D.E., Moyano-Paz, D., Varela, A.N., and Poiré, D.G., 2022, Onset of the Miocene Chaco foreland basin: depositional conditions, provenance and paleogeographic implications of the Tranquitas Formation (Argentina): *International Journal of Earth Sciences*, v. 111, no. 6, p. 1739–1771, doi: 10.1007/s00531-022-02203-3.
- Tofelde, S., Duesing, W., Schildgen, T.F., Wickert, A.D., Wittmann, H., Alonso, R.N., and Strecker, M.R., 2018, Effects of deep-seated versus shallow hillslope processes on cosmogenic  $^{10}\text{Be}$  concentrations in fluvial sand and gravel: *Earth Surf. Process. Landforms (Earth Surface Processes and Landforms)*, v. 43, p. 3086–3098.
- Tofelde, S., Schildgen, T.F., Savi, S., Pingel, H., Wickert, A.D., Bookhagen, B., Wittmann, H., Alonso, R.N., Cottle, J., and Strecker, M.R., 2017, 100 kyr fluvial cut-and-fill terrace cycles since the Middle Pleistocene in the southern Central Andes, NW Argentina: *Earth and Planetary Science letters*, v. 473, p. 141–153, doi: 10.1016/j.epsl.2017.06.001.
- Turner, J.C.M., 1964b, Descripción geológica de la Hoja 2c, Santa Victoria (Provincias Salta y Jujuy): Instituto Nacional de la Geología y Minería: Boletín, no. 104.
- Turner, J.C.M., 1975, Geología del sector oriental de los departamentos de Santa Victoria e Iruya, provincia de Salta, República Argentina: *Bol. Acad. Nac. Cien.*, no. 51, p. 11–24.

- 
- Uba, C.E., Heubeck, C., and Hulka, C., 2005, Facies analysis and basin architecture of the Neogene Subandean synorogenic wedge, southern Bolivia: *Sedimentary Geology*, v. 180, 3-4, p. 91–123, doi: 10.1016/j.sedgeo.2005.06.013.
- Vacek, F., and Žák, J., 2019, A lifetime of the Variscan orogenic plateau from uplift to collapse as recorded by the Prague Basin, Bohemian Massif: *Geological Magazine*, v. 156, no. 3, p. 485–509, doi: 10.1017/S0016756817000875.
- Valdiya, K.S., 2016, *The Making of India: Geodynamic Evolution*, 2nd ed. 2016: Cham, Springer, SpringerLink Bücher, 924 p.
- van Kooten, W.S., Sobel, E.R., Del Papa, C., Payrola, P., Starck, D., and Bande, A., 2022, Constraining the formation of the fault-bound Cianzo basin, NW Argentina using low-temperature thermochronology.
- Vanderhaeghe, O., and Teyssier, C., 2001, Crustal-scale rheological transitions during late-orogenic collapse: *Tectonophysics*, v. 335, 1-2, p. 211–228, doi: 10.1016/S0040-1951(01)00053-1.
- Vermeesch, P., 2007, CosmoCalc: An Excel add-in for cosmogenic nuclide calculations: *Geochemistry, Geophysics, Geosystems*, v. 8, no. 8, n/a-n/a, doi: 10.1029/2006GC001530.
- Victor, P., Oncken, O., and Glodny, J., 2004, Uplift of the western Altiplano plateau: Evidence from the Precordillera between 20° and 21°S (northern Chile): *Tectonics*, v. 23, no. 4, n/a-n/a, doi: 10.1029/2003TC001519.
- Walker, F., and Allen, M.B., 2012, Offset rivers, drainage spacing and the record of strike-slip faulting: The Kuh Banan Fault, Iran: *Tectonophysics*, 530-531, S1, p. 251–263, doi: 10.1016/j.tecto.2012.01.001.
- Wallace, R.E., 1968, Notes on channels offset by the San Andreas Fault, Southern Coast Ranges, California.
- Wallace, R.E., 1977, Profiles and ages of young fault scarps, north-central Nevada: undefined.
- Wang, H., Currie, C.A., and DeCelles, P.G., 2021, Coupling Between Lithosphere Removal and Mantle Flow in the Central Andes: *Geophysical Research Letters*, v. 48, no. 16, doi: 10.1029/2021GL095075.

## 6. References

---

- Weischet, W., and Endlicher, W., 1996, *Regionale Klimatologie*. 1. Die neue Welt: Amerika, Neuseeland, Australien; mit 38 Tabellen: Stuttgart, Teubner.
- Wells, D.L., and Coppersmith, K.J., 1994, New Empirical Relationships among Magnitude Ruptur Length, Rupture Width, Rupture Area and Surface Displacement: *Bulletin of the Seismological Society of America*, v. 84, no. 4, p. 974–1002.
- Westoby, M.J., Brasington, J., Glasser, N.F., Hambrey, M.J., and Reynolds, J.M., 2012, ‘Structure-from-Motion’ photogrammetry: A low-cost, effective tool for geoscience applications: *Geomorphology*, v. 179, p. 300–314, doi: 10.1016/j.geomorph.2012.08.021.
- Whipple, K.X., Shirzaei, M., Hodges, K.V., and Ramon Arrowsmith, J., 2016, Active shortening within the Himalayan orogenic wedge implied by the 2015 Gorkha earthquake: *Nature Geoscience*, v. 9, no. 9, p. 711–716, doi: 10.1038/ngeo2797.
- Whitaker, A.E., and Engelder, T., 2005, Characterizing stress fields in the upper crust using joint orientation distributions: *Journal of Structural Geology*, v. 27, no. 10, p. 1778–1787, doi: 10.1016/j.jsg.2005.05.016.
- Whittaker, A.C., and Boulton, S.J., 2012, Tectonic and climatic controls on knickpoint retreat rates and landscape response times: *Journal of Geophysical Research: Earth Surface*, v. 117, F2, n/a-n/a, doi: 10.1029/2011JF002157.
- Wigger, P.J., Schmitz, M., Araneda, M., Asch, G., Baldzuhn, S., Giese, P., Heinsohn, W.-D., Martínez, E., Ricaldi, E., Röwer, P., and Viramonte, J., 1994, Variation in the Crustal Structure of the Southern Central Andes Deduced from Seismic Refraction Investigations, in Reutter, K.-J., Scheuber, E., et al., eds., *Tectonics of the Southern Central Andes*: Berlin, Heidelberg, Springer Berlin Heidelberg, p. 23–48.
- Willett, S.D., 2006, *Tectonics, climate, and landscape evolution*: Boulder Colo., Geological Society of America, Special paper, Volume 398, xi, 447.
- Willis, B., 1893, *Mechanics of Appalachian Structure*: US Geological Survey Annual Report, v. 13, in Thirteenth Annual report of the United States Geological Survey to the Secretary of the Interior, 1891-1892: Part 2.
- Wimpenny, S., Benavente, C., Copley, A., Garcia, B., Rosell, L., O’Kane, A., and Aguirre, E., 2020, Observations and dynamical implications of active normal faulting in South Peru: *Geophysical Journal International*, v. 222, no. 1, p. 27–53, doi: 10.1093/gji/ggaa144.

- Wimpenny, S., Copley, A., Benavente, C., and Aguirre, E., 2018, Extension and Dynamics of the Andes Inferred From the 2016 Parina (Huarichancara) Earthquake: *Journal of Geophysical Research: Solid Earth*, v. 123, no. 9, p. 8198–8228, doi: 10.1029/2018JB015588.
- Wüthrich, L., Brändli, C., Braucher, R., Veit, H., Haghypour, N., Terrizzano, C., Christl, M., Gnägi, C., and Zech, R., 2017, <sup>10</sup>Be depth profiles in glacial sediments on the Swiss Plateau: deposition age, denudation and (pseudo-) inheritance: *E&G Quaternary Science Journal*, v. 66, no. 2, p. 57–68, doi: 10.5194/egqsj-66-57-2017.
- Xu, Q., Li, Z., Wolff, R., Tan, X., Hetzel, R., Yue, Y., and Tang, X., 2021, Two-phase Himalayan extension recorded in the Late Miocene-Pleistocene Gyirong Basin, south Tibet: *Sedimentary Geology*, v. 417, p. 105892, doi: 10.1016/j.sedgeo.2021.105892.
- Zamanian, K., Pustovoytov, K., and Kuzyakov, Y., 2016, Pedogenic carbonates: Forms and formation processes: *Earth-Science Reviews*, v. 157, p. 1–17, doi: 10.1016/j.earscirev.2016.03.003.
- Zámolyi, A., Székely, B., Draganits, E., and Timár, G., 2010, Neotectonic control on river sinuosity at the western margin of the Little Hungarian Plain: *Geomorphology*, v. 122, 3–4, p. 231–243, doi: 10.1016/j.geomorph.2009.06.028.
- Zandt, G., Myers, S.C., and Wallace, T.C., 1995, Crust and mantle structure across the Basin and Range-Colorado Plateau boundary at 37°N latitude and implications for Cenozoic extensional mechanism: *Journal of Geophysical Research*, v. 100, B6, p. 10529–10548, doi: 10.1029/94JB03063.
- Zeilinger, G., and Schlunegger, F., 2007, Possible flexural accommodation on the eastern edge of the Altiplano in relation to focussed erosion in the Rio La Paz drainage system: *Terra Nova*, v. 19, no. 5, p. 373–380, doi: 10.1111/j.1365-3121.2007.00762.x.
- Zhang, P., Molnar, P., and Downs, W.R., 2001, Increased sedimentation rates and grain sizes 2–4 Myr ago due to the influence of climate change on erosion rates: *Nature*, v. 410, no. 6831, p. 891–897, doi: 10.1038/35073504.
- Zheng, B., Schwieger, V., and Kosmann, D., 2010, Evaluierung des TanDEM-X Geländemodells mittels kinematischem GPS, in DVW e. V. - Gesellschaft für Geodäsie, Geoinformation und Landmanagement, ed., GNSS 2010 – Vermessung und Navigation im 21. Jahrhundert: Beiträge zum 100. DVW-Seminar am 4. und 5. Oktober in Köln. GNSS

## 6. References

---

2010 – Vermessung und Navigation im 21. Jahrhundert, Cologne. 10.4.20120 - 10.5.2010, Volume 63: Augsburg, Wißner-Verlag GmbH & Co. KG.

Zhou, R., Schoenbohm, L.M., and Cosca, M., 2013, Recent, slow normal and strike-slip faulting in the Pasto Ventura region of the southern Puna Plateau, NW Argentina: *Tectonics*, v. 32, no. 1, p. 19–33, doi: 10.1029/2012TC003189.

Zhou, R., Schoenbohm, L.M., Sobel, E.R., Carrapa, B., and Davis, D.W., 2016, Sedimentary record of regional deformation and dynamics of the thick-skinned southern Puna Plateau, central Andes (26–27°S): *Earth and Planetary Science letters*, v. 433, p. 317–325, doi: 10.1016/j.epsl.2015.11.012.

Zhu, L., Wang, C., Zheng, H., Xiang, F., Yi, H., and Liu, D., 2006, Tectonic and sedimentary evolution of basins in the northeast of Qinghai-Tibet Plateau and their implication for the northward growth of the Plateau: *Palaeogeography, Palaeoclimatology, Palaeoecology*, v. 241, no. 1, p. 49–60, doi: 10.1016/j.palaeo.2006.06.019.

Zuza, A.V., 2016, *Tectonic Evolution of the Northeastern Tibetan Plateau*: LA, California, USA, University of California, 522 p.

## 7. Appendix

## Data Tables

## U-Pb measurements

## Arg19 samples

Table 1: Isotope measurements of the U, Pb and Th for the samples Arg19-xx

Sample / grain	Concentrations (ppm)		Th / U <sub>anom</sub>	<sup>207</sup> Pb/ <sup>206</sup> Pb	2σ (%)	Isotope ratios		<sup>206</sup> Pb/ <sup>238</sup> U	2σ (%)	Rho <sup>ρ</sup>	Isotopic age (Ma)		2σ (abs.)	w.m.	±1s	±2s	MSWD	n
	Pb	U				Th	Th/ <sup>232</sup> Th				2σ (%)	<sup>206</sup> Pb/ <sup>238</sup> U						
ARG19-1_030	1.9	461	1310	2.763	0.23700	13.96	0.02303	14.44	0.00071	3.68	0.26	3.47	0.10					3.54
ARG19-1_009	3.8	721	849	1.152	0.08580	9.03	0.00689	9.32	0.00058	2.29	0.25	3.52	0.23					0.04
ARG19-1_033	3.0	634	1726	2.695	0.07500	21.36	0.00661	21.66	0.00061	3.59	0.17	3.60	0.10					0.09
ARG19-1_034	0.2	239	117	0.480	0.07200	6.19	0.00604	6.74	0.00061	2.66	0.39	3.88	0.16					1.78
ARG19-1_014	2.3	1232	1086	0.867	0.17000	14.15	0.01635	14.63	0.00070	3.72	0.25	3.88	0.11					3.40
ARG19-1_018	0.5	157	117	0.722	0.06580	8.87	0.00551	9.22	0.00061	2.51	0.27	3.88	0.20					
ARG19-1_037	1.1	710	473	0.663	0.17400	6.97	0.01715	7.52	0.00072	2.84	0.38	3.91	0.11					
ARG19-1_038	1.4	400	266	0.653	0.08320	11.94	0.00733	12.51	0.00064	3.74	0.30	3.95	0.14					
ARG19-1_022	0.5	215	214	0.970	0.12700	9.50	0.01192	9.77	0.00068	2.29	0.23	4.01	0.16					
ARG19-1_016	0.7	278	211	0.752	0.05930	5.82	0.00517	6.49	0.00063	2.87	0.44	4.03	0.12					
ARG19-1_023	0.8	905	397	0.432	0.07130	7.92	0.00632	8.16	0.00064	1.98	0.24	4.10	0.12					
ARG19-1_013	1.1	879	522	0.579	0.06050	8.98	0.00529	9.27	0.00064	2.28	0.25	4.10	0.09					
ARG19-1_032	0.7	572	339	0.587	0.06940	5.99	0.00616	6.23	0.00064	1.69	0.27	4.11	0.10					
ARG19-1_035	1.1	918	417	0.442	0.18500	8.71	0.01963	9.44	0.00077	3.65	0.39	4.12	0.08					
ARG19-1_007	1.5	373	348	0.919	0.05870	6.72	0.00537	6.99	0.00066	1.94	0.28	4.17	0.18					
ARG19-1_019	0.9	1356	363	0.265	0.07280	10.49	0.00685	10.76	0.00068	2.41	0.22	4.31	0.09					
ARG19-1_002	1.4	1971	269	0.133	0.05670	7.30	0.00531	7.65	0.00068	2.29	0.30	4.36	0.12					
ARG19-1_028	0.7	526	318	0.598	0.08150	11.82	0.00839	12.08	0.00075	2.49	0.21	4.41	0.11					
ARG19-1_036	0.7	626	117	0.189	0.05350	6.99	0.00618	7.20	0.00084	1.75	0.24	4.70	0.13					
ARG19-1_040	0.9	576	381	0.647	0.07550	6.30	0.00901	6.61	0.00087	2.00	0.30	5.44	0.10					
ARG19-1_005	1.9	1998	335	0.165	0.05010	2.97	0.00588	3.65	0.00085	2.13	0.58	5.48	0.12					
ARG19-1_031	0.6	3045	208	0.067	0.05370	2.97	0.00641	3.42	0.00087	1.71	0.50	5.57	0.12					
ARG19-1_004	1.4	1500	554	0.363	0.04890	5.01	0.00601	5.45	0.00089	2.15	0.39	5.63	0.10					
ARG19-1_006	1.1	1032	446	0.424	0.04970	4.73	0.00638	5.34	0.00093	2.47	0.46	5.82	0.13					
ARG19-1_027	1.4	932	475	0.501	0.04950	4.75	0.00646	5.30	0.00095	2.34	0.44	6.07	0.15					
ARG19-1_001	0.8	817	272	0.330	0.05800	11.08	0.00844	11.35	0.00106	2.48	0.22	6.18	0.15					
ARG19-1_026	0.4	583	79	0.134	0.06350	10.91	0.00943	11.35	0.00108	3.13	0.28	6.81	0.18					
ARG19-1_039	0.5	272	127	0.476	0.04749	1.36	0.00706	2.19	0.00108	1.71	0.78	6.88	0.22					
ARG19-1_012	0.8	8410	267	0.031	0.04940	3.39	0.00743	4.16	0.00109	2.42	0.58	7.05	0.13					
ARG19-3_013	0.2	257	240	0.894	0.29100	32.66	0.00353	33.68	0.00019	8.23	0.24	0.48	0.09					0.48
ARG19-3_021	0.2	1039	379	0.352	0.09200	17.42	0.00122	17.69	0.00010	3.08	0.17	0.68	0.05					0.04
ARG19-3_009	0.2	591	338	0.571	0.09200	26.11	0.00126	26.40	0.00010	3.94	0.15	0.70	0.05					0.09
ARG19-3_029	1.8	533	322	0.584	0.046600	9.07	0.01869	10.01	0.00029	4.24	0.42	0.97	0.11					
ARG19-3_037	0.3	468	233	0.482	0.07300	16.47	0.00327	16.64	0.00032	2.40	0.14	2.12	0.07					1.40
ARG19-3_036	0.6	1763	520	0.289	0.05420	5.99	0.00245	6.23	0.00033	1.72	0.28	2.20	0.05					
ARG19-3_025	0.7	764	490	0.625	0.06900	17.42	0.00359	17.69	0.00038	3.08	0.17	2.46	0.09					
ARG19-3_035	0.2	286	160	0.543	0.06400	17.22	0.00349	17.35	0.00040	2.15	0.12	2.58	0.08					
ARG19-3_008	1.2	1316	658	0.501	0.05120	4.60	0.00409	4.91	0.00058	1.72	0.35	3.80	0.18					
ARG19-3_033	1.1	472	495	1.038	0.06830	10.15	0.00580	10.42	0.00062	2.34	0.22	3.94	0.10					

7. Appendix

Sample / grain	Concentrations (ppm)			Isotope ratios			Isotopic age (Ma)			2σ (abs.)			
	Pb	Th	Th/U <sub>non</sub>	<sup>207</sup> Pb/ <sup>206</sup> Pb	2σ (%)	<sup>206</sup> Pb/ <sup>238</sup> U	2σ (%)	Rho <sup>δ</sup>	<sup>207</sup> Pb and <sup>230</sup> Th-corrected <sup>206</sup> Pb/ <sup>238</sup> U age				
ARG19-3_034	0.3	455	0.306	0.05600	10.23	0.00506	10.39	0.00066	1.82	0.18	4.27	0.09	†
ARG19-3_019	0.6	528	0.547	0.05190	7.58	0.00507	7.83	0.00071	1.97	0.25	4.63	0.10	†
ARG19-3_012	1.2	436	0.652	0.09910	6.93	0.01233	7.15	0.00090	1.75	0.25	5.52	0.11	†
ARG19-3_024	1.8	302	0.428	0.23600	8.11	0.03636	8.69	0.00112	3.12	0.36	5.57	0.25	†
ARG19-3_010	1.8	1163	0.567	0.04910	7.20	0.00580	7.33	0.00086	1.41	0.19	5.60	0.09	†
ARG19-3_016	0.6	656	0.321	0.05130	6.32	0.00609	6.55	0.00087	1.71	0.26	5.62	0.11	†
ARG19-3_003	1.8	1057	0.623	0.04920	4.58	0.00589	4.76	0.00087	1.29	0.27	5.66	0.08	†
ARG19-3_023	0.6	1021	0.181	0.05080	4.83	0.00671	5.09	0.00096	1.60	0.31	6.25	0.11	†
ARG19-3_015	0.5	324	0.439	0.05370	9.55	0.00752	9.67	0.00102	1.55	0.16	6.58	0.12	†
ARG19-3_051	0.6	1424	0.131	0.05010	3.35	0.00698	3.61	0.00101	1.35	0.37	6.59	0.10	†
ARG19-3_027	1.0	453	0.402	0.08150	7.79	0.01195	8.06	0.00106	2.05	0.25	6.65	0.15	†
ARG19-3_020	0.5	541	0.278	0.04940	5.96	0.00695	6.19	0.00102	1.70	0.27	6.65	0.12	†
ARG19-3_040	0.9	268	0.580	0.09440	6.54	0.01617	6.91	0.00124	2.25	0.32	7.61	0.18	†
ARG19-3_030	1.5	884	0.371	0.05830	9.66	0.01003	9.80	0.00125	1.69	0.17	8.02	0.15	†
ARG19-3_007	1.1	727	0.278	0.03800	5.95	0.01025	6.36	0.00128	2.26	0.36	8.24	0.19	†
ARG19-3_004	0.6	373	0.357	0.05020	6.26	0.00881	6.46	0.00127	1.61	0.25	8.26	0.14	†
ARG19-3_032	0.6	411	0.370	0.05180	5.12	0.00926	5.38	0.00130	1.65	0.31	8.39	0.15	†
ARG19-3_002	1.2	707	0.373	0.05040	3.52	0.00930	3.83	0.00134	1.50	0.39	8.68	0.14	†
ARG19-3_001	1.5	1080	0.359	0.04930	3.20	0.00908	3.59	0.00134	1.62	0.45	8.68	0.15	†
ARG19-3_059	1.2	767	0.284	0.05400	8.21	0.01011	8.41	0.00136	1.84	0.22	8.76	0.17	†
ARG19-3_017	0.7	400	0.282	0.06750	9.98	0.01293	10.17	0.00139	2.00	0.20	8.81	0.19	†
ARG19-3_018	1.4	1692	0.190	0.04947	1.95	0.00995	2.39	0.00146	1.39	0.58	9.46	0.14	†
ARG19-3_038	1.2	1653	0.163	0.04790	2.31	0.00966	2.75	0.00146	1.48	0.54	9.51	0.15	†
ARG19-3_014	2.1	404	1.225	0.05060	5.04	0.01031	5.25	0.00148	1.47	0.28	9.55	0.15	†
ARG19-3_005	4.5	2386	0.233	0.06570	5.72	0.01379	5.93	0.00152	1.55	0.26	9.67	0.16	†
ARG19-3_028	2.1	429	1.140	0.05480	5.92	0.01149	6.15	0.00152	1.65	0.27	9.78	0.17	†
ARG19-3_011	2.2	2276	0.104	0.05910	2.26	0.01285	2.67	0.00158	1.42	0.53	10.10	0.15	†
ARG19-3_026	1.1	603	0.381	0.04930	3.01	0.01099	3.36	0.00162	1.50	0.45	10.47	0.16	†
ARG19-3_006	0.7	278	0.469	0.05330	5.90	0.01275	6.13	0.00174	1.66	0.27	11.18	0.19	†
ARG19-3_022	1.8	1860	0.184	0.04681	1.85	0.01216	2.25	0.00189	1.28	0.57	12.24	0.16	†
ARG19-4_016	1.4	764	0.621	0.10030	5.87	0.00868	6.16	0.00063	1.87	0.30	3.86	0.09	w.m.
ARG19-4_010	1.1	1091	0.532	0.04980	4.92	0.00423	5.20	0.00062	1.66	0.32	4.05	0.08	±1σ
ARG19-4_056	0.5	420	0.426	0.06700	20.92	0.00624	21.27	0.00068	3.83	0.18	4.34	0.18	±2σ
ARG19-4_029	3.0	3088	1.220	0.03930	2.66	0.00597	3.03	0.00082	1.45	0.48	5.34	0.09	MSWD
ARG19-4_003	0.6	346	0.597	0.05670	10.10	0.00667	10.27	0.00085	1.82	0.18	5.52	0.11	n
ARG19-4_035	0.6	383	0.502	0.05610	7.91	0.00681	8.20	0.00088	2.17	0.27	5.70	0.13	†
ARG19-4_001	1.1	1276	0.282	0.05160	4.95	0.00625	5.23	0.00088	1.69	0.32	5.73	0.10	†
ARG19-4_024	2.7	2520	0.424	0.04810	3.17	0.00699	3.59	0.00091	1.75	0.41	5.91	0.11	†
ARG19-4_030	1.6	1322	0.479	0.04960	3.19	0.00622	3.59	0.00091	1.65	0.46	5.93	0.11	†
ARG19-4_040	0.7	420	0.540	0.05580	8.48	0.00772	8.67	0.00101	1.79	0.21	6.52	0.13	†
ARG19-4_013	0.8	496	0.533	0.05260	6.92	0.00752	7.10	0.00104	1.60	0.23	6.72	0.12	†
ARG19-4_007	0.6	490	0.336	0.05280	6.70	0.00756	6.93	0.00104	1.76	0.25	6.74	0.13	†
ARG19-4_005	1.4	499	0.707	0.05950	6.13	0.00882	6.46	0.00108	2.03	0.31	6.90	0.15	†
ARG19-4_025	1.4	611	0.422	0.07800	10.05	0.01274	10.17	0.00119	1.55	0.15	7.42	0.14	†
ARG19-4_037	0.6	566	0.256	0.04960	4.94	0.00870	5.26	0.00127	1.80	0.34	8.26	0.15	†
ARG19-4_014	0.4	712	0.145	0.04990	4.72	0.00876	4.94	0.00127	1.49	0.30	8.27	0.13	†
ARG19-4_015	2.3	809	0.750	0.05030	4.29	0.00891	4.56	0.00129	1.54	0.34	8.32	0.13	†
ARG19-4_020	0.8	486	0.351	0.05730	9.13	0.01025	9.33	0.00130	1.90	0.20	8.34	0.17	†
ARG19-4_026	0.6	593	0.278	0.04770	4.72	0.00847	4.95	0.00129	1.48	0.30	8.38	0.13	†
ARG19-4_039	1.4	2880	0.092	0.04997	2.13	0.01054	2.66	0.00153	1.59	0.60	9.92	0.16	†
ARG19-4_021	1.4	428	0.546	0.05490	6.63	0.01438	7.17	0.00190	2.72	0.38	12.20	0.34	†
ARG19-4_051	2.3	391	0.257	0.04820	2.49	0.01255	2.85	0.00189	1.38	0.48	12.24	0.17	†
ARG19-4_022	1.5	421	0.581	0.05100	4.81	0.01392	5.11	0.00198	1.73	0.34	12.77	0.23	†
ARG19-4_027	1.7	831	0.365	0.04820	3.27	0.01323	3.61	0.00199	1.53	0.42	12.90	0.20	†
ARG19-4_034	0.2	747	0.041	0.04910	3.60	0.01357	4.01	0.00201	1.76	0.44	12.97	0.23	†
ARG19-4_006	4.0	1513	0.425	0.04827	2.01	0.01376	2.52	0.00207	1.53	0.61	13.39	0.21	†
ARG19-4_019	1.0	254	0.641	0.05310	7.60	0.01532	7.77	0.00209	1.63	0.21	13.46	0.23	†
ARG19-4_028	2.1	958	0.383	0.04610	2.59	0.01321	2.95	0.00208	1.42	0.48	13.49	0.20	†
ARG19-4_017	4.4	2081	0.352	0.04738	2.28	0.01408	2.70	0.00209	1.45	0.54	13.49	0.20	†
ARG19-4_033	1.4	992	0.218	0.04890	2.84	0.01408	3.22	0.00209	1.52	0.47	13.51	0.21	†
ARG19-4_023	2.0	228	1.515	0.05000	7.67	0.01457	7.88	0.00211	1.81	0.23	13.62	0.26	†
ARG19-4_004	2.5	816	0.468	0.04825	2.10	0.01402	2.70	0.00211	1.70	0.63	13.64	0.23	†
ARG19-4_012	3.0	1211	0.380	0.04822	1.80	0.01424	2.35	0.00212	1.51	0.64	13.68	0.21	†

Sample / grain	Concentrations (ppm)				Isotope ratios				Isotopic age (Ma)				2σ (abs.)	2σ (abs.)
	Pb	U	Th	Th/U <sub>non</sub>	<sup>207</sup> Pb/ <sup>206</sup> Pb	<sup>207</sup> Pb/ <sup>235</sup> U	2σ (%)	<sup>206</sup> Pb/ <sup>238</sup> U	2σ (%)	Rho <sup>δ</sup>	<sup>207</sup> Pb and <sup>230</sup> Th-corrected <sup>206</sup> Pb/ <sup>238</sup> U age	2σ (abs.)		
ARG19-4_011	1.6	443	236	0.525	0.05100	4.24	4.66	0.00212	1.93	0.41	13.69	0.27	†	
ARG19-4_052	2.7	925	394	0.421	0.05100	3.86	4.23	0.00213	1.73	0.45	13.70	0.24	†	
ARG19-4_058	1.8	497	289	0.571	0.04800	3.08	3.45	0.00214	1.54	0.45	13.86	0.22	†	
ARG19-4_008	4.7	1482	734	0.485	0.04731	2.06	2.61	0.00214	1.61	0.62	13.88	0.23	†	
ARG19-4_018	2.8	1275	449	0.341	0.04836	2.09	2.60	0.00215	1.53	0.59	13.91	0.22	†	
ARG19-4_009	0.4	114	37	0.314	0.05370	14.37	14.56	0.00224	2.30	0.16	20.75	0.52	†	
ARG19-4_002	18	116	83	0.697	0.05738	1.43	2.23	0.00255	1.37	0.77	492.29	8.24	†	
ARG19-5_027	4.1	2325	1681	0.734	0.05110	3.29	3.56	0.00087	1.71	0.39	5.67	0.09	w.m.	
ARG19-5_024	2.3	1335	668	0.505	0.07000	5.24	5.69	0.00091	2.22	0.32	5.76	0.13	±1s	
ARG19-5_052	1.6	1041	419	0.405	0.07210	4.96	5.22	0.00092	1.65	0.32	5.81	0.11	±2s	
ARG19-5_023	5.6	1890	610	0.330	0.12270	5.39	5.74	0.00100	1.98	0.34	5.89	0.13	MSWD	
ARG19-5_006	0.9	985	369	0.315	0.04950	3.77	4.16	0.00091	1.75	0.42	5.91	0.11	n	
ARG19-5_022	0.9	815	249	0.309	0.06090	7.78	7.95	0.00092	1.64	0.21	5.92	0.11	†	
ARG19-5_028	1.6	1145	594	0.524	0.05230	4.14	4.52	0.00093	1.55	0.35	6.02	0.10	†	
ARG19-5_059	1.8	1475	619	0.421	0.05070	3.50	4.03	0.00093	2.00	0.50	6.03	0.13	†	
ARG19-5_050	4.4	2540	1485	0.590	0.05350	4.78	5.52	0.00093	2.77	0.50	6.04	0.17	†	
ARG19-5_008	0.9	604	170	0.282	0.08100	24.71	24.93	0.00097	3.27	0.13	6.04	0.25	†	
ARG19-5_038	3.5	1892	1260	0.656	0.04990	5.70	6.04	0.00093	1.99	0.33	6.06	0.13	†	
ARG19-5_007	1.1	756	346	0.462	0.05010	7.25	7.55	0.00093	2.08	0.28	6.06	0.12	†	
ARG19-5_001	0.8	831	265	0.314	0.05050	5.24	5.55	0.00093	1.80	0.33	6.08	0.12	†	
ARG19-5_025	1.2	960	412	0.430	0.05040	4.28	4.53	0.00094	1.46	0.32	6.15	0.10	†	
ARG19-5_013	1.4	1373	475	0.346	0.04890	3.03	3.52	0.00094	1.79	0.51	6.15	0.12	†	
ARG19-5_019	1.3	962	440	0.468	0.04960	4.15	4.56	0.00095	1.88	0.41	6.16	0.12	†	
ARG19-5_014	2.5	1762	920	0.526	0.04900	2.25	2.77	0.00095	1.62	0.58	6.16	0.11	†	
ARG19-5_003	1.2	1022	358	0.352	0.05070	5.03	5.51	0.00095	2.24	0.41	6.17	0.14	†	
ARG19-5_009	1.0	1137	347	0.307	0.04990	3.55	3.84	0.00095	1.45	0.38	6.19	0.10	†	
ARG19-5_011	1.0	713	329	0.467	0.05070	4.26	4.53	0.00096	1.53	0.34	6.21	0.10	†	
ARG19-5_018	1.8	1616	616	0.383	0.04780	3.09	3.45	0.00096	1.53	0.44	6.24	0.10	†	
ARG19-5_005	0.9	796	287	0.360	0.04810	4.89	5.29	0.00096	2.03	0.38	6.29	0.13	†	
ARG19-5_031	0.9	334	284	0.852	0.04990	10.07	10.32	0.00105	2.24	0.22	6.82	0.16	†	
ARG19-5_017	0.9	887	269	0.307	0.05140	3.64	4.14	0.00106	1.98	0.48	6.85	0.14	†	
ARG19-5_037	1.9	2380	568	0.240	0.04950	2.44	3.03	0.00107	1.80	0.59	6.98	0.13	†	
ARG19-5_040	0.8	391	140	0.364	0.07230	9.32	10.12	0.00122	2.28	0.24	7.69	0.19	†	
ARG19-5_010	1.7	1922	432	0.225	0.04801	2.27	2.78	0.00128	1.60	0.58	8.35	0.14	†	
ARG19-5_015	1.8	1385	412	0.300	0.04880	2.85	3.38	0.00131	1.83	0.54	8.48	0.16	†	
ARG19-5_036	3.2	1407	583	0.418	0.04830	2.11	2.99	0.00188	2.12	0.71	12.14	0.26	†	
ARG19-5_017	2.2	894	348	0.389	0.04950	3.77	4.07	0.00201	1.52	0.37	12.96	0.20	†	
ARG19-5_026	0.7	232	65	0.279	0.06940	10.71	10.99	0.00209	2.46	0.22	13.16	0.25	†	
ARG19-5_016	1.5	874	253	0.290	0.04860	3.44	4.02	0.00204	2.07	0.52	13.19	0.28	†	
ARG19-5_021	1.7	1193	264	0.226	0.04764	1.97	2.60	0.00205	1.69	0.65	13.26	0.23	†	
ARG19-5_055	1.8	2272	278	0.121	0.04657	1.79	2.36	0.00205	1.54	0.65	13.27	0.21	†	
ARG19-5_034	3.0	1241	495	0.403	0.04760	2.52	2.93	0.00205	1.50	0.51	13.30	0.20	†	
ARG19-5_033	2.1	1202	319	0.268	0.05030	3.53	4.14	0.00208	1.68	0.45	13.42	0.23	†	
ARG19-5_020	1.2	5650	1950	0.350	0.04732	1.27	2.23	0.00207	1.84	0.82	13.43	0.25	†	
ARG19-5_002	3.8	1400	571	0.400	0.04850	2.48	3.09	0.00208	1.84	0.60	13.44	0.25	†	
ARG19-5_004	0.9	337	139	0.408	0.05040	6.43	6.73	0.00210	1.98	0.29	13.56	0.28	†	
ARG19-5_029	1.5	983	209	0.215	0.04730	3.12	3.41	0.00255	1.37	0.40	16.48	0.23	†	
ARG19-6_038	3.6	2550	731	0.288	0.07120	4.33	4.75	0.00102	1.95	0.41	6.44	0.13	w.m.	
ARG19-6_035	0.9	368	195	0.528	0.08020	7.55	7.99	0.00103	2.62	0.33	6.46	0.18	±1s	
ARG19-6_037	0.6	1664	149	0.089	0.05230	3.40	3.89	0.00100	1.89	0.48	6.51	0.13	±2s	
ARG19-6_031	4.7	4900	1349	0.277	0.05030	2.40	3.35	0.00100	2.33	0.70	6.51	0.15	MSWD	
ARG19-6_001	1.0	900	278	0.306	0.04900	5.60	6.06	0.00101	2.31	0.38	6.58	0.16	n	
ARG19-6_022	1.5	2580	482	0.189	0.04673	2.09	2.93	0.00101	2.05	0.70	6.59	0.14	w.m.	
ARG19-6_032	0.8	859	233	0.272	0.05180	3.99	4.47	0.00103	2.02	0.45	6.66	0.14	†	
ARG19-6_005	2.4	2859	419	0.149	0.06660	7.13	7.90	0.00105	3.40	0.43	6.68	0.23	†	
ARG19-6_007	1.2	1065	272	0.258	0.05380	7.13	7.33	0.00104	1.68	0.23	6.71	0.12	†	
ARG19-6_003	1.4	3420	129	0.037	0.05810	2.77	3.51	0.00104	2.16	0.62	6.72	0.15	†	
ARG19-6_021	1.9	1676	554	0.333	0.04860	2.86	3.32	0.00103	1.68	0.51	6.73	0.12	†	
ARG19-6_023	0.7	628	147	0.236	0.06090	6.64	6.96	0.00105	2.07	0.30	6.73	0.15	†	
ARG19-6_017	0.9	4268	271	0.064	0.04761	1.90	2.77	0.00103	2.01	0.73	6.75	0.14	†	
ARG19-6_004	4.7	2235	1160	0.490	0.05160	2.89	3.56	0.00104	2.08	0.58	6.78	0.14	†	
ARG19-6_015	3.0	1834	397	0.218	0.08600	13.99	14.31	0.00109	3.01	0.21	6.78	0.23	†	

7. Appendix

Sample / grain	Concentrations (ppm)				Isotope ratios				Isotopic age (Ma)				2σ (abs.)
	Pb	U	Th	Th/U <sub>zircon</sub>	<sup>207</sup> Pb/ <sup>206</sup> Pb	2σ (%)	<sup>207</sup> Pb/ <sup>235</sup> U	2σ (%)	Rho <sup>δ</sup>	<sup>207</sup> Pb and <sup>230</sup> Th-corrected <sup>206</sup> Pb/ <sup>238</sup> U age	2σ (abs.)		
ARG19-6_029	2.2	3421	320	0.095	0.06050	2.67	0.00883	1.73	0.54	681	0.12	†	
ARG19-6_056	0.6	816	190	0.235	0.05210	3.41	0.00756	2.40	0.58	684	0.17	†	
ARG19-6_006	1.0	539	272	0.512	0.04770	5.54	0.00694	2.06	0.35	688	0.15	†	
ARG19-6_050	1.2	1810	259	0.141	0.05380	4.75	0.00795	1.80	0.35	694	0.13	†	
ARG19-6_028	2.3	3884	388	0.100	0.06170	1.90	0.00927	2.83	0.74	699	0.15	†	
ARG19-6_008	0.6	343	118	0.339	0.06410	8.64	0.00971	2.74	0.30	702	0.20	†	
ARG19-6_012	0.4	344	125	0.372	0.05580	6.40	0.00808	2.59	0.37	705	0.19	†	
ARG19-6_016	0.5	1075	145	0.136	0.05050	3.89	0.00774	1.61	0.38	723	0.12	†	
ARG19-6_013	3.2	1433	886	0.628	0.04683	2.28	0.00737	2.02	0.66	744	0.15	†	
ARG19-6_020	0.7	652	164	0.253	0.05270	6.53	0.00845	1.70	0.25	754	0.14	†	
ARG19-6_002	2.1	784	497	0.638	0.05570	6.36	0.00901	2.59	0.38	756	0.20	†	
ARG19-6_025	0.9	704	230	0.332	0.04750	4.74	0.00766	2.44	0.46	762	0.19	†	
ARG19-6_011	1.1	1034	231	0.229	0.05180	4.36	0.00902	1.61	0.35	818	0.14	†	
ARG19-6_010	1.4	1349	314	0.233	0.04850	2.29	0.00911	2.15	0.68	826	0.19	†	
ARG19-6_024	1.2	966	265	0.276	0.04910	2.83	0.00928	1.89	0.56	891	0.17	†	
ARG19-6_009	10	1120	698	0.627	0.15740	3.09	0.04660	2.79	0.67	1198	0.34	†	
ARG19-6_018	2.5	930	358	0.389	0.05008	2.42	0.01441	3.28	0.74	1348	0.33	†	
ARG19-6_039	3.5	1538	597	0.386	0.04590	2.40	0.01329	1.35	0.49	1363	0.19	†	
ARG19-6_027	0.9	229	139	0.606	0.05310	5.55	0.01536	5.89	0.33	1366	0.27	†	
ARG19-6_034	2.9	1001	387	0.385	0.05220	3.96	0.01529	2.09	0.47	1369	0.29	†	
ARG19-6_014	4.8	1390	636	0.455	0.05130	2.91	0.01524	3.57	0.58	1389	0.29	†	
ARG19-6_019	0.8	545	85	0.152	0.04820	3.47	0.02166	4.08	0.53	2105	0.45	†	
ARG19-6_033	29	13	9	0.729	0.82230	1.22	13.11202	2.82	0.90	5574	84.9	†	
ARG19-6_040	28	7	5	0.697	0.81940	1.16	22.52915	2.56	0.91	15112	13.19	†	
ARG19-6_026	50	214	190	0.864	0.06424	1.65	0.79238	1.76	0.73	548.93	94.6	†	
Ash01_024	2.7	2928	1688	0.566	0.06890	7.61	0.00417	2.32	0.29	284	0.08	2.86	
Ash01_012	2.3	5760	1399	0.241	0.05580	5.64	0.00334	6.11	0.38	286	0.08	0.01	
Ash01_013	0.7	1048	407	0.387	0.06350	7.94	0.00385	2.48	0.30	287	0.07	0.02	
Ash01_022	1.2	1155	814	0.714	0.05230	5.45	0.00330	1.83	0.32	302	0.08	0.16	
Ash01_006	1.7	1330	780	0.569	0.08100	13.62	0.00536	2.50	0.18	305	0.09	3.40	
Ash01_023	3.7	2771	1580	0.560	0.09560	4.70	0.00631	5.02	0.35	306	0.07	†	
Ash01_016	2.6	2654	1456	0.539	0.07510	5.42	0.00501	5.82	0.36	310	0.08	†	
Ash01_020	1.1	1920	750	0.356	0.05140	4.59	0.00334	2.21	0.43	312	0.10	†	
Ash01_034	0.6	1142	343	0.298	0.05030	6.64	0.00340	3.03	0.41	324	0.08	†	
Ash01_026	0.8	1543	508	0.319	0.04910	4.99	0.00334	5.25	0.31	327	0.07	†	
Ash01_025	0.7	160	246	1.525	0.11700	17.12	0.01398	17.41	0.0087	515	0.22	†	
Ash01_011	1.0	727	249	0.343	0.06930	8.14	0.00821	8.34	0.22	548	0.11	†	
Ash01_031	4.0	1198	577	0.474	0.12400	8.93	0.01721	9.32	0.29	594	0.13	†	
Ash01_040	0.7	689	214	0.310	0.05200	4.72	0.00669	2.08	0.40	607	0.19	†	
Ash01_015	0.9	604	162	0.267	0.07090	8.80	0.01009	2.71	0.29	655	0.19	†	
Ash01_038	3.8	1686	589	0.346	0.04838	2.20	0.01382	2.95	0.67	655	0.26	†	
Ash01_008	6.0	790	848	1.071	0.05110	3.85	0.01473	4.59	0.55	1341	0.26	†	
Ash01_003	35	2483	5020	2.004	0.05006	1.80	0.01450	2.50	0.55	1347	0.34	†	
Ash01_017	4.6	600	720	1.179	0.04970	4.54	0.01447	2.87	0.78	1352	0.30	†	
Ash01_032	1.1	1880	1705	0.902	0.04761	2.05	0.01386	2.96	0.36	1362	0.25	†	
Ash01_018	4.0	948	540	0.564	0.05750	2.63	0.01697	3.21	0.72	1366	0.29	†	
Ash01_039	1.1	296	169	0.567	0.05060	6.21	0.01482	1.93	0.30	1369	0.25	†	
Ash01_010	2.9	1003	467	0.465	0.04730	2.92	0.01381	3.62	0.59	1370	0.27	†	
Ash01_029	2.4	898	367	0.401	0.04790	2.70	0.01401	3.18	0.59	1372	0.29	†	
Ash01_004	2.5	818	332	0.403	0.05160	3.82	0.01519	1.69	0.53	1374	0.24	†	
Ash01_001	3.5	1171	485	0.402	0.04610	2.33	0.01349	1.96	0.46	1376	0.27	†	
Ash01_009	2.5	527	358	0.672	0.06080	4.07	0.01815	2.43	0.72	1378	0.33	†	
Ash01_028	1.2	438	161	0.362	0.05130	6.32	0.01515	2.02	0.44	1378	0.28	†	
Ash01_037	4.5	1210	616	0.500	0.05170	4.00	0.01528	2.37	0.35	1381	0.33	†	
Ash01_036	2.1	716	271	0.369	0.05400	3.48	0.01601	2.16	0.48	1381	0.30	†	
Ash01_019	3.3	1091	456	0.417	0.05190	3.80	0.01536	2.19	0.53	1382	0.31	†	
Ash01_002	2.9	931	387	0.410	0.04771	2.15	0.01536	1.91	0.45	1383	0.27	†	
Ash01_030	2.8	1132	400	0.349	0.04820	2.49	0.01421	1.96	0.67	1383	0.27	†	
Ash01_007	3.9	501	549	1.089	0.04900	3.41	0.01423	2.41	0.70	1384	0.33	†	
Ash01_014	4.1	2035	603	0.289	0.04818	1.99	0.01423	2.75	0.63	1384	0.33	†	
Ash01_027	2.9	784	477	0.623	0.04780	3.90	0.01414	2.41	0.47	1387	0.33	†	
Ash01_035	4.3	1004	576	0.568	0.05050	3.51	0.01414	2.07	0.47	1388	0.29	†	
Ash01_005	2.8	571	357	0.623	0.05130	6.90	0.01533	2.91	0.64	1391	0.41	†	
								2.10	0.62	1396	0.30	†	

Sample / grain	Concentrations (ppm)				Isotope ratios				Isotopic age (Ma)				2σ (abs.)	w.m. ±1s ±2s MSWD n
	Pb	U	Th	<sup>230</sup> Th/ <sup>232</sup> Th <sub>non</sub>	<sup>207</sup> Pb/ <sup>206</sup> Pb	2σ (%)	<sup>207</sup> Pb/ <sup>235</sup> U	2σ (%)	<sup>206</sup> Pb/ <sup>238</sup> U	2σ (%)	Rho <sup>ρ</sup>	<sup>207</sup> Pb and <sup>230</sup> Th-corrected <sup>206</sup> Pb/ <sup>238</sup> U age		
Ash01_021	2.1	221	190	0.840	0.09720	7.27	0.03889	7.66	0.00290	2.42	0.32	17.57	0.46	†
Ash01_033	0.5	73	47	0.615	0.05240	11.30	0.02448	11.73	0.00339	3.11	0.27	21.74	0.69	†
Carb01_015	2.7	964	854	0.882	0.05150	4.77	0.00703	5.16	0.00099	1.99	0.38	6.43	0.13	†
Carb01_035	2.6	1509	788	0.517	0.04890	2.84	0.00689	3.31	0.00102	1.69	0.51	6.66	0.12	†
Carb01_021	1.5	680	454	0.664	0.05300	6.87	0.00757	7.18	0.00104	2.09	0.29	6.71	0.15	†
Carb01_024	1.0	559	307	0.545	0.04950	5.74	0.00705	6.28	0.00103	2.53	0.40	6.73	0.17	†
Carb01_031	0.5	467	145	0.312	0.05160	6.47	0.00741	6.91	0.00104	2.42	0.35	6.77	0.17	†
Carb01_039	1.3	812	388	0.468	0.04750	4.53	0.00680	4.99	0.00104	2.08	0.42	6.78	0.15	†
Carb01_010	2.0	532	552	1.030	0.05130	7.47	0.00740	7.91	0.00105	2.59	0.33	6.78	0.18	†
Carb01_011	0.8	484	94	0.190	0.08470	7.15	0.01275	7.48	0.00109	2.17	0.29	6.80	0.16	†
Carb01_018	0.5	611	140	0.224	0.05150	5.15	0.00742	5.61	0.00105	2.24	0.40	6.80	0.16	†
Carb01_016	3.7	797	157	0.196	0.18350	4.15	0.03194	4.68	0.00126	2.15	0.46	6.83	0.17	†
Carb01_003	0.5	807	139	0.169	0.05140	5.35	0.00746	5.65	0.00105	1.82	0.32	6.84	0.13	†
Carb01_007	0.9	521	178	0.336	0.06990	7.81	0.01046	8.19	0.00109	2.59	0.33	6.89	0.19	†
Carb01_034	1.1	280	339	1.212	0.04780	7.80	0.00699	8.19	0.00106	2.47	0.30	6.90	0.18	†
Carb01_013	1.2	740	367	0.498	0.04990	4.91	0.00730	5.43	0.00106	2.30	0.42	6.90	0.16	†
Carb01_020	3.6	467	101	0.215	0.24600	5.78	0.04807	7.27	0.00142	4.42	0.61	6.93	0.35	†
Carb01_014	1.1	1176	177	0.149	0.06280	5.98	0.00937	6.42	0.00108	2.35	0.37	6.94	0.17	†
Carb01_005	0.8	515	144	0.278	0.06040	8.17	0.01105	8.48	0.00133	2.27	0.27	7.02	0.20	†
Carb01_022	1.9	1708	443	0.260	0.04660	3.37	0.00866	4.05	0.00135	2.24	0.55	8.78	0.20	†
Carb01_036	0.5	1389	274	0.195	0.07330	2.91	0.01118	3.32	0.00111	1.61	0.49	6.95	0.12	†
Carb01_040	1.0	762	279	0.362	0.04940	4.37	0.00749	5.02	0.00110	2.48	0.49	7.16	0.18	†
Carb01_029	0.9	475	216	0.458	0.06510	6.83	0.01016	7.20	0.00113	2.26	0.31	7.21	0.17	†
Carb01_004	0.7	576	184	0.314	0.05260	4.86	0.00843	5.63	0.00116	2.85	0.51	7.53	0.22	†
Carb01_012	1.4	737	340	0.459	0.05330	4.61	0.00879	5.43	0.00120	2.86	0.53	7.73	0.22	†
Carb01_005	0.8	515	144	0.278	0.06040	8.17	0.01105	8.48	0.00133	2.27	0.27	8.50	0.20	†
Carb01_002	1.1	717	250	0.349	0.04910	4.59	0.00918	5.33	0.00136	2.70	0.51	8.80	0.24	†
Carb01_037	1.6	303	130	0.427	0.11580	5.36	0.03039	5.99	0.00190	2.66	0.44	11.28	0.32	†
Carb01_008	1.3	493	198	0.400	0.05710	5.35	0.01432	5.74	0.00182	2.07	0.36	11.66	0.25	†
Carb01_038	1.9	844	288	0.336	0.04700	2.94	0.01314	3.55	0.00203	1.99	0.56	13.15	0.26	†
Carb01_001	1.3	652	174	0.262	0.04960	2.81	0.01437	3.53	0.00210	2.15	0.61	13.58	0.29	†
Carb01_017	0.5	387	69	0.179	0.05500	15.85	0.01607	16.41	0.00212	4.27	0.26	13.61	0.60	†
Carb01_025	2.1	824	340	0.413	0.04840	2.48	0.01409	3.17	0.00211	1.98	0.62	13.67	0.27	†
Carb01_019	2.5	1144	392	0.340	0.04830	2.49	0.01407	3.34	0.00211	2.22	0.67	13.68	0.31	†
Carb01_027	1.5	376	230	0.604	0.04810	5.70	0.01403	6.22	0.00212	2.48	0.40	13.69	0.34	†
Carb01_033	2.0	1518	2955	1.927	0.06650	8.18	0.03005	8.46	0.00219	2.16	0.26	13.79	0.31	†
Carb01_028	7.9	1162	1230	1.068	0.04722	2.13	0.01399	2.74	0.00215	1.72	0.63	13.91	0.24	†
Carb01_006	1.5	373	205	0.545	0.04990	4.13	0.01512	4.70	0.00220	2.24	0.48	14.19	0.32	†
Carb01_026	5.2	979	443	0.453	0.09900	3.67	0.03247	4.08	0.00238	1.78	0.44	14.40	0.27	†
Carb01_030	4.5	584	71	0.121	0.05520	2.73	0.03134	3.94	0.00412	2.85	0.72	26.32	0.75	†
Carb01_032	17	624	80	0.129	0.05606	1.24	0.14417	3.30	0.01866	3.06	0.93	118.14	3.59	†
Carb01_009	48	569	208	0.361	0.05676	1.16	0.15151	2.38	0.06590	2.08	0.87	410.61	8.37	†
ARG19-1_030	1.9	461	1310	2.763	0.23700	13.96	0.02303	14.44	0.00071	3.68	0.26	3.47	0.10	w.m.
ARG19-1_009	3.8	721	849	1.152	0.08580	9.03	0.00689	9.32	0.00058	2.29	0.25	3.52	0.23	±1s
ARG19-1_053	3.0	634	1726	2.695	0.07500	21.36	0.00629	21.66	0.00061	3.59	0.17	3.60	0.10	±2s
ARG19-1_054	0.2	239	117	0.480	0.07200	6.19	0.00604	6.74	0.00061	2.66	0.39	3.88	0.16	MSWD
ARG19-1_014	2.3	1232	1086	0.867	0.17000	14.15	0.01635	14.63	0.00070	3.72	0.25	3.88	0.11	n
ARG19-1_018	0.5	157	117	0.722	0.06580	8.87	0.00551	9.22	0.00061	2.51	0.27	3.88	0.20	†
ARG19-1_057	1.1	710	473	0.663	0.17400	6.97	0.01715	7.52	0.00072	2.84	0.38	3.91	0.11	†
ARG19-1_058	1.4	400	266	0.653	0.08320	11.94	0.00733	12.51	0.00064	3.74	0.23	3.95	0.14	†
ARG19-1_022	0.5	215	214	0.970	0.12700	9.50	0.01192	10.77	0.00068	2.29	0.30	4.01	0.16	†
ARG19-1_016	0.7	278	211	0.752	0.05930	5.82	0.00517	6.49	0.00063	2.87	0.44	4.03	0.12	†
ARG19-1_023	0.8	905	397	0.432	0.07130	7.92	0.00632	8.16	0.00064	1.98	0.24	4.10	0.12	†
ARG19-1_013	1.1	879	522	0.579	0.06650	8.98	0.00529	9.27	0.00064	2.28	0.25	4.10	0.09	†
ARG19-1_052	0.7	572	339	0.587	0.06940	5.99	0.00616	6.23	0.00064	1.69	0.27	4.11	0.10	†
ARG19-1_035	1.1	918	417	0.442	0.18500	8.71	0.01963	9.44	0.00077	3.65	0.39	4.12	0.08	†
ARG19-1_007	1.5	373	348	0.919	0.05870	6.72	0.00537	7.29	0.00066	1.94	0.28	4.17	0.18	†
ARG19-1_019	0.9	1356	363	0.265	0.07280	10.49	0.00685	10.76	0.00068	2.41	0.22	4.31	0.09	†
ARG19-1_002	1.4	1971	269	1.133	0.05670	7.30	0.00531	7.65	0.00068	2.29	0.30	4.36	0.12	†
ARG19-1_028	0.7	526	318	0.598	0.08150	11.82	0.00839	12.08	0.00075	2.49	0.21	4.41	0.11	†
ARG19-1_056	0.7	626	117	0.189	0.05350	6.99	0.00618	7.20	0.00084	1.75	0.24	4.70	0.13	†
ARG19-1_040	0.9	576	381	0.647	0.07550	6.30	0.00901	6.61	0.00087	2.00	0.30	5.44	0.10	†

7. Appendix

Concentrations (ppm)				Isotope ratios				Isotopic age (Ma)				
Sample / grain	Ph	U	Th	Th/U <sub>zircon</sub>	<sup>207</sup> Pb/ <sup>235</sup> U	2σ (%)	<sup>206</sup> Pb/ <sup>238</sup> U	2σ (%)	Rho <sup>δ</sup>	<sup>207</sup> Pb and <sup>230</sup> Th-corrected <sup>206</sup> Pb/ <sup>238</sup> U age	2σ (abs.)	
ARG19-1_005	19	1998	335	0.165	0.05010	2.97	0.00588	2.13	0.58	5.48	0.12	†
ARG19-1_051	0.6	3045	208	0.067	0.05370	2.97	0.00641	3.42	0.50	5.63	0.12	†
ARG19-1_004	1.4	1500	554	0.363	0.04890	5.01	0.00601	5.45	0.39	5.63	0.10	†
ARG19-1_006	1.1	1032	446	0.424	0.04970	4.73	0.00638	5.34	0.46	5.82	0.13	†
ARG19-1_027	1.4	932	475	0.501	0.04950	4.75	0.00646	5.30	0.44	6.07	0.15	†
ARG19-1_001	0.8	817	272	0.330	0.05800	11.08	0.00844	11.35	0.22	6.18	0.15	†
ARG19-1_026	0.4	583	79	0.134	0.06350	10.91	0.00943	11.35	0.28	6.81	0.18	†
ARG19-1_059	0.5	272	127	0.476	0.04749	1.36	0.00706	1.71	0.78	6.88	0.22	†
ARG19-1_012	0.8	8410	267	0.031	0.04940	3.29	0.00743	4.16	0.58	7.05	0.13	†
ARG19-3_013	0.2	257	240	0.894	0.02910	32.66	0.00353	33.68	0.24	0.48	0.09	w.m.
ARG19-3_021	0.2	1039	379	0.352	0.09200	17.42	0.00122	17.69	0.010	0.68	0.05	±1s
ARG19-3_009	0.2	591	338	0.571	0.06600	26.11	0.0026	26.40	0.15	0.70	0.05	±2s
ARG19-3_029	1.8	533	322	0.584	0.46600	9.07	0.01869	10.01	0.42	0.97	0.11	MSWD
ARG19-3_057	0.3	468	233	0.482	0.07300	16.47	0.00327	16.64	0.14	0.97	0.07	n
ARG19-3_056	0.6	1763	520	0.289	0.05420	5.99	0.00245	6.23	0.28	2.20	0.05	†
ARG19-3_025	0.7	764	490	0.625	0.06900	17.42	0.00359	17.69	0.17	2.46	0.09	†
ARG19-3_035	0.2	286	160	0.543	0.06400	17.22	0.00349	17.35	0.12	2.58	0.08	†
ARG19-3_008	1.2	1316	638	0.501	0.05120	4.60	0.00409	4.91	0.35	3.80	0.08	†
ARG19-3_033	1.1	472	495	1.038	0.06830	10.15	0.00580	10.42	0.22	3.94	0.10	†
ARG19-3_034	0.3	455	143	0.306	0.05600	10.23	0.00506	10.39	0.18	4.27	0.09	†
ARG19-3_019	0.6	528	289	0.547	0.05190	7.58	0.00507	7.83	0.25	4.63	0.10	†
ARG19-3_012	1.2	436	289	0.652	0.09910	6.93	0.01233	7.15	0.25	5.52	0.11	†
ARG19-3_024	1.8	302	134	0.428	0.23600	8.11	0.03636	8.69	0.36	5.57	0.25	†
ARG19-3_010	1.8	1163	655	0.567	0.04910	7.20	0.00580	7.33	0.19	5.60	0.09	†
ARG19-3_016	0.6	656	217	0.321	0.05300	6.32	0.00609	6.55	0.26	5.62	0.11	†
ARG19-3_003	1.8	1057	642	0.623	0.04920	4.88	0.00581	4.76	0.27	5.66	0.08	†
ARG19-3_023	0.6	1021	194	0.181	0.05080	4.83	0.00671	5.09	0.31	6.25	0.11	†
ARG19-3_015	0.5	324	155	0.439	0.05720	9.55	0.00752	9.67	0.16	6.58	0.12	†
ARG19-3_031	0.6	1424	191	0.131	0.05010	3.35	0.00698	3.61	0.37	6.59	0.10	†
ARG19-3_027	1.0	453	189	0.402	0.08150	7.79	0.01195	8.06	0.25	6.65	0.15	†
ARG19-3_020	0.5	541	156	0.278	0.04940	5.96	0.00695	6.19	0.27	6.65	0.12	†
ARG19-3_040	0.9	268	158	0.580	0.09440	6.54	0.01617	6.91	0.32	6.61	0.18	†
ARG19-3_050	1.5	884	339	0.371	0.05830	9.66	0.01003	9.80	0.17	8.02	0.15	†
ARG19-3_007	1.1	727	201	0.278	0.05800	5.95	0.01025	6.36	0.36	8.26	0.19	†
ARG19-3_004	0.6	373	131	0.357	0.05020	6.26	0.00881	6.46	0.25	8.26	0.14	†
ARG19-3_032	0.6	411	158	0.370	0.05180	5.12	0.00926	5.38	0.31	8.39	0.15	†
ARG19-3_002	1.2	707	264	0.373	0.05040	3.52	0.00930	3.83	0.39	8.68	0.14	†
ARG19-3_001	1.5	1080	359	0.339	0.04930	3.20	0.00908	3.59	0.45	8.68	0.15	†
ARG19-3_039	1.2	767	284	0.355	0.05400	8.21	0.01011	8.41	0.22	8.76	0.17	†
ARG19-3_017	0.7	400	116	0.282	0.06750	9.98	0.01293	10.17	0.20	8.81	0.19	†
ARG19-3_018	1.4	1692	331	0.190	0.04947	1.95	0.00995	2.39	0.58	9.46	0.14	†
ARG19-3_038	1.2	1653	278	0.163	0.04790	2.31	0.00966	2.75	0.54	9.51	0.15	†
ARG19-3_014	2.1	404	507	1.225	0.05060	5.04	0.01031	5.25	0.28	9.55	0.15	†
ARG19-3_005	4.5	2386	570	0.233	0.06570	5.72	0.01379	5.93	0.26	9.67	0.16	†
ARG19-3_028	2.1	429	507	1.140	0.05480	5.92	0.01149	6.15	0.27	9.78	0.17	†
ARG19-3_011	2.2	2276	242	0.104	0.05910	2.26	0.01285	2.67	0.53	10.10	0.15	†
ARG19-3_026	1.1	603	239	0.381	0.04930	3.01	0.01099	3.36	0.45	10.47	0.16	†
ARG19-3_006	0.7	278	128	0.469	0.05330	5.90	0.01275	6.13	0.27	11.18	0.19	†
ARG19-3_022	1.8	1860	351	0.184	0.04681	1.85	0.01216	2.25	0.57	12.24	0.16	†
ARG19-4_016	1.4	764	482	0.621	0.10030	5.87	0.00868	6.16	0.30	3.86	0.09	w.m.
ARG19-4_010	1.1	1091	597	0.532	0.04980	4.92	0.00423	5.20	0.32	4.05	0.08	±1s
ARG19-4_056	0.5	420	181	0.426	0.06700	20.92	0.00624	21.27	0.18	4.34	0.18	±2s
ARG19-4_029	3.0	3088	1220	0.393	0.05280	2.66	0.00597	3.03	0.48	5.34	0.09	MSWD
ARG19-4_003	0.6	346	213	0.597	0.05670	10.10	0.00667	10.27	0.18	5.52	0.11	n
ARG19-4_035	0.6	383	194	0.502	0.05610	7.91	0.00681	8.20	0.27	5.70	0.13	†
ARG19-4_001	1.1	1276	369	0.282	0.05160	4.95	0.00625	5.23	0.32	5.73	0.10	†
ARG19-4_024	2.7	2520	1078	0.424	0.04810	3.87	0.00599	4.25	0.41	5.91	0.11	†
ARG19-4_054	1.6	1322	644	0.479	0.04960	3.19	0.00522	3.59	0.46	5.93	0.11	†
ARG19-4_040	0.7	420	230	0.540	0.05580	8.48	0.00771	8.67	0.21	6.52	0.13	†
ARG19-4_013	0.8	496	269	0.533	0.05260	6.92	0.00752	7.10	0.23	6.72	0.12	†
ARG19-4_007	0.6	490	167	0.336	0.05280	6.70	0.00756	6.93	0.25	6.74	0.13	†
ARG19-4_005	1.4	499	365	0.707	0.05950	6.13	0.00882	6.46	0.31	6.90	0.15	†

Sample / grain	Concentrations (ppm)				Isotope ratios				Isotopic age (Ma)				2σ (abs.)	2σ (abs.)	w.m. ±1s ±2s MSWD n
	Pb	U	Th	<sup>238</sup> U/ <sup>232</sup> Th	<sup>207</sup> Pb/ <sup>206</sup> Pb	2σ (%)	<sup>206</sup> Pb/ <sup>238</sup> U	2σ (%)	<sup>207</sup> Pb and <sup>235</sup> Th-corrected <sup>206</sup> Pb/ <sup>238</sup> U age	Rho <sup>2</sup>	2σ (%)	2σ (abs.)			
ARG19-4_025	1.4	611	280	0.422	0.07800	10.05	0.01274	10.17	0.00119	1.55	0.15	7.42	0.14	†	†
ARG19-4_037	0.6	566	147	0.256	0.04960	4.94	0.00870	5.26	0.00127	1.80	0.34	8.26	0.15	†	†
ARG19-4_014	7.12	105	105	0.145	0.04990	4.72	0.00876	4.94	0.00127	1.49	0.30	8.27	0.13	†	†
ARG19-4_015	2.3	809	631	0.750	0.05030	4.29	0.00891	4.56	0.00129	1.54	0.34	8.32	0.13	†	†
ARG19-4_020	0.8	486	173	0.351	0.05730	9.13	0.01025	9.33	0.00130	1.90	0.20	8.34	0.17	†	†
ARG19-4_026	0.6	593	165	0.278	0.04770	4.72	0.00847	4.95	0.00129	1.48	0.30	8.38	0.13	†	†
ARG19-4_039	1.4	2880	269	0.092	0.04997	2.13	0.01054	2.66	0.00153	1.59	0.60	9.92	0.16	†	†
ARG19-4_021	1.4	428	239	0.546	0.05490	6.63	0.01438	7.17	0.00190	2.72	0.38	12.20	0.34	†	†
ARG19-4_051	2.3	391	1512	0.257	0.04820	2.49	0.01255	2.85	0.00189	1.38	0.48	12.24	0.17	†	†
ARG19-4_022	1.5	421	249	0.581	0.05100	4.81	0.01392	5.11	0.00198	1.73	0.34	12.77	0.23	†	†
ARG19-4_027	1.7	831	308	0.365	0.04820	3.27	0.01323	3.61	0.00199	1.53	0.42	12.90	0.20	†	†
ARG19-4_034	0.2	747	31	0.041	0.04910	3.60	0.01357	4.01	0.00201	1.76	0.44	12.97	0.23	†	†
ARG19-4_006	4.0	1513	657	0.425	0.04827	2.01	0.01376	2.52	0.00207	1.53	0.61	13.39	0.21	†	†
ARG19-4_019	1.0	254	166	0.641	0.05310	7.60	0.01532	7.77	0.00209	1.63	0.21	13.46	0.23	†	†
ARG19-4_028	2.1	958	372	0.383	0.04610	2.59	0.01321	2.95	0.00208	1.42	0.48	13.49	0.20	†	†
ARG19-4_017	4.4	2081	740	0.352	0.04738	2.28	0.01360	2.70	0.00208	1.45	0.54	13.49	0.20	†	†
ARG19-4_033	1.4	992	218	0.218	0.04890	2.84	0.01408	3.22	0.00209	1.52	0.47	13.51	0.21	†	†
ARG19-4_023	2.0	228	352	1.515	0.05000	7.67	0.01457	7.88	0.00211	1.81	0.23	13.62	0.26	†	†
ARG19-4_004	2.5	816	392	0.468	0.04825	2.10	0.01402	2.70	0.00211	1.70	0.63	13.64	0.23	†	†
ARG19-4_012	3.0	1211	468	0.380	0.04882	1.80	0.01424	2.35	0.00212	1.51	0.64	13.68	0.21	†	†
ARG19-4_011	1.6	443	236	0.525	0.05100	4.24	0.01493	4.66	0.00212	1.93	0.41	13.69	0.27	†	†
ARG19-4_052	2.7	925	394	0.421	0.05100	3.86	0.01494	4.23	0.00213	1.73	0.41	13.70	0.24	†	†
ARG19-4_038	1.8	497	289	0.571	0.04800	3.08	0.01417	3.45	0.00214	1.54	0.45	13.86	0.22	†	†
ARG19-4_008	4.7	1482	734	0.485	0.04731	2.06	0.01398	2.61	0.00214	1.61	0.62	13.88	0.23	†	†
ARG19-4_018	2.8	1275	449	0.341	0.04836	2.09	0.01433	2.60	0.00215	1.53	0.59	13.91	0.22	†	†
ARG19-4_009	0.4	114	37	0.314	0.05370	14.37	0.02396	14.56	0.00324	2.30	0.16	20.75	0.52	†	†
ARG19-4_002	0.9	116	83	0.697	0.05758	1.43	0.63008	1.43	0.63008	2.23	0.77	49.29	8.24	†	†
ARG19-5_027	4.1	2325	1681	0.734	0.05110	3.29	0.00614	3.56	0.00087	1.37	0.39	5.67	0.09	†	5.73
ARG19-5_024	2.3	1335	668	0.505	0.07000	5.24	0.00874	5.69	0.00091	2.22	0.39	5.76	0.13	†	0.04
ARG19-5_032	1.6	1041	419	0.405	0.07210	4.96	0.00911	5.22	0.00092	1.65	0.32	5.81	0.11	†	0.09
ARG19-5_023	5.6	1890	610	0.330	0.12270	3.77	0.01683	5.74	0.00100	1.98	0.34	5.89	0.13	†	2.13
ARG19-5_006	0.9	985	309	0.315	0.04950	3.79	0.00618	4.16	0.00091	1.75	0.42	5.91	0.11	†	3.40
ARG19-5_022	0.9	815	249	0.309	0.06090	7.78	0.00773	7.95	0.00092	1.64	0.21	5.92	0.11	†	†
ARG19-5_028	1.6	1145	594	0.524	0.05230	4.14	0.00668	4.42	0.00093	1.55	0.35	6.02	0.10	†	†
ARG19-5_059	1.8	1475	619	0.421	0.05070	3.50	0.00647	4.03	0.00093	2.00	0.50	6.03	0.13	†	†
ARG19-5_030	4.4	2540	1485	0.590	0.05350	4.78	0.00686	5.52	0.00093	2.77	0.50	6.04	0.17	†	†
ARG19-5_008	0.9	604	170	0.282	0.08100	24.71	0.01077	24.93	0.00097	3.27	0.13	6.04	0.25	†	†
ARG19-5_038	3.5	1892	1260	0.656	0.04990	5.70	0.00640	6.04	0.00093	1.99	0.33	6.06	0.13	†	†
ARG19-5_007	1.1	756	346	0.462	0.05010	7.25	0.00643	7.55	0.00093	2.08	0.28	6.06	0.13	†	†
ARG19-5_001	0.8	831	265	0.314	0.05050	5.24	0.00649	5.55	0.00093	1.80	0.33	6.08	0.12	†	†
ARG19-5_025	1.2	960	412	0.430	0.05040	4.28	0.00656	4.53	0.00094	1.46	0.32	6.15	0.10	†	†
ARG19-5_013	1.4	1373	475	0.346	0.04890	3.03	0.00636	3.52	0.00094	1.79	0.51	6.15	0.12	†	†
ARG19-5_019	1.3	962	440	0.468	0.04960	4.15	0.00646	4.56	0.00095	1.88	0.41	6.16	0.12	†	†
ARG19-5_014	2.5	1762	920	0.526	0.04900	2.25	0.00638	2.77	0.00095	1.62	0.58	6.16	0.11	†	†
ARG19-5_003	1.2	1022	358	0.352	0.05070	5.03	0.00662	5.51	0.00095	2.24	0.41	6.17	0.14	†	†
ARG19-5_026	1.0	1137	347	0.307	0.04990	3.55	0.00653	3.84	0.00095	1.45	0.38	6.19	0.10	†	†
ARG19-5_011	1.0	713	329	0.467	0.05070	4.26	0.00667	4.53	0.00096	1.53	0.34	6.21	0.10	†	†
ARG19-5_018	1.8	1616	616	0.383	0.04780	3.09	0.00629	3.45	0.00096	1.53	0.44	6.24	0.10	†	†
ARG19-5_005	0.9	796	287	0.360	0.04810	4.89	0.00639	5.29	0.00096	2.03	0.38	6.29	0.13	†	†
ARG19-5_012	0.9	334	284	0.852	0.04990	10.07	0.00722	10.32	0.00105	2.24	0.22	6.82	0.16	†	†
ARG19-5_017	0.9	887	269	0.307	0.05140	3.64	0.00747	4.14	0.00106	1.98	0.48	6.85	0.14	†	†
ARG19-5_057	1.9	2380	568	0.240	0.04950	2.44	0.00731	3.03	0.00107	1.80	0.59	6.98	0.13	†	†
ARG19-5_040	0.8	391	140	0.364	0.07230	9.32	0.01215	9.60	0.00122	2.28	0.24	7.69	0.19	†	†
ARG19-5_010	1.7	1922	432	0.225	0.04801	2.27	0.00849	2.78	0.00128	1.60	0.58	8.35	0.14	†	†
ARG19-5_015	1.8	1385	412	0.300	0.04880	2.85	0.00878	3.38	0.00131	1.83	0.54	8.48	0.16	†	†
ARG19-5_036	5.2	1407	583	0.418	0.04830	2.11	0.01248	2.99	0.00188	2.12	0.71	12.14	0.26	†	†
ARG19-5_017	2.2	894	348	0.389	0.04950	3.77	0.01368	4.07	0.00201	1.52	0.37	12.96	0.20	†	†
ARG19-5_026	0.7	232	65	0.279	0.06940	10.71	0.01998	10.99	0.00209	2.46	0.22	13.16	0.35	†	†
ARG19-5_016	1.5	874	253	0.290	0.04860	3.44	0.01366	4.02	0.00204	2.07	0.52	13.19	0.28	†	†
ARG19-5_021	1.7	1193	264	0.226	0.04764	1.97	0.01343	2.60	0.00205	1.69	0.65	13.26	0.23	†	†
ARG19-5_035	1.8	2272	278	0.121	0.04657	1.79	0.01313	2.56	0.00205	1.54	0.65	13.27	0.21	†	†
ARG19-5_034	5.0	1241	495	0.403	0.04760	2.52	0.01347	2.93	0.00205	1.50	0.51	13.30	0.20	†	†
ARG19-5_033	2.1	1202	319	0.268	0.05030	3.33	0.01441	3.73	0.00208	1.68	0.45	13.42	0.23	†	†

## 7. Appendix

Sample / grain	Concentrations (ppm)			Isotope ratios			Isotopic age (Ma)			2σ (abs.)		
	Pb	U	Th	Th/U <sub>nonm</sub>	<sup>207</sup> Pb/ <sup>206</sup> Pb	2σ (%)	<sup>206</sup> Pb/ <sup>238</sup> U	2σ (%)	Rho <sup>a</sup>		<sup>207</sup> Pb and <sup>232</sup> Th-corrected <sup>206</sup> Pb/ <sup>238</sup> U age	
ARG19-5_020	12	5650	1950	0.350	0.04732	1.27	0.01352	2.23	0.82	13.43	0.25	†
ARG19-5_002	3.8	1400	571	0.400	0.04850	2.48	0.01388	3.09	0.60	13.44	0.25	†
ARG19-5_004	0.9	337	139	0.408	0.05040	6.43	0.01460	6.73	0.29	13.56	0.28	†
ARG19-5_029	1.5	983	209	0.215	0.04730	3.12	0.01660	3.41	0.40	16.48	0.23	†
ARG19-6_038	3.6	2550	731	0.288	0.07120	4.33	0.00997	4.75	0.41	6.44	0.13	w.m.
ARG19-6_035	0.9	368	195	0.528	0.08020	7.55	0.01141	7.99	0.33	6.46	0.18	±1s
ARG19-6_037	0.6	1664	149	0.089	0.05230	3.40	0.00722	3.89	0.48	6.51	0.13	±2s
ARG19-6_031	4.7	4900	1349	0.277	0.05030	2.40	0.00693	3.35	0.70	6.51	0.15	MSWD
ARG19-6_001	1.0	900	278	0.306	0.04900	5.60	0.00682	6.06	0.38	6.58	0.16	n
ARG19-6_022	1.5	2580	482	0.189	0.04673	2.09	0.00649	2.93	0.70	6.59	0.14	w.m.
ARG19-6_032	0.8	859	233	0.272	0.05180	3.99	0.00732	4.47	0.45	6.66	0.14	
ARG19-6_005	2.4	2859	419	0.149	0.06660	7.13	0.00961	7.90	0.43	6.68	0.23	
ARG19-6_007	1.2	1065	272	0.258	0.05380	7.13	0.00768	7.33	0.23	6.71	0.12	
ARG19-6_003	1.4	3420	129	0.037	0.05810	2.77	0.00834	3.51	0.62	6.72	0.15	†
ARG19-6_021	1.9	1676	554	0.333	0.04860	2.86	0.00692	3.32	0.51	6.73	0.12	†
ARG19-6_023	0.7	628	147	0.236	0.06090	6.64	0.00880	6.96	0.30	6.73	0.15	†
ARG19-6_017	0.9	4268	271	0.064	0.04761	1.90	0.00678	2.77	0.73	6.75	0.14	†

2σ — 2σ standard error; Rho — Discordance level = 100 [(<sup>206</sup>Pb/<sup>238</sup>U age) / (<sup>207</sup>Pb/<sup>235</sup>U age)]; † — excluded from mean calculations;

Arg21 samples

Table 2: Isotope measurements of the U, Pb and Th for the samples Arg19-xx

Sample / grain	Concentrations (ppm)			Th/U <sub>corr</sub>	<sup>207</sup> Pb/ <sup>206</sup> Pb	Isotope ratios		<sup>206</sup> Pb/ <sup>238</sup> U	2σ (%)	Rho*	<sup>206</sup> Pb and <sup>207</sup> Pb-corrected <sup>230</sup> Th/ <sup>238</sup> U age	2σ (abs.)	w.m. ±1s ±2s MSWD n
	Pb	U	Th			<sup>206</sup> Pb/ <sup>238</sup> U	2σ (%)						
Ash_01_17	0.44	1609.0	143.00	0.088	0.0481	2.53	0.0065	2.86	1.33	0.47	6.38	0.09	6.45
Ash_01_26	0.47	986.0	147.90	0.149	0.0484	3.33	0.0065	3.42	0.77	0.23	6.41	0.06	0.02
Ash_01_27	0.65	133.8	206.40	1.531	0.0518	11.40	0.0071	11.57	2.02	0.17	6.41	0.14	0.04
Ash_01_28	1.47	556.0	486.30	0.870	0.0519	4.64	0.0071	4.85	1.40	0.29	6.46	0.10	0.04
Ash_01_22	0.76	1080.0	232.00	0.215	0.0524	2.89	0.0072	3.13	1.20	0.38	6.51	0.09	1.53
Ash_01_2	0.34	444.0	107.50	0.239	0.0489	3.70	0.0067	3.89	0.0000	0.00	6.51	0.09	6.50
Ash_01_11	0.65	1074.0	216.10	0.198	0.0475	4.86	0.0066	5.03	0.0001	0.01	6.58	0.09	
Ash_01_18	0.68	1299.0	198.90	0.147	0.0495	2.64	0.0069	3.18	0.0001	0.01	6.60	0.12	
Ash_01_13	0.47	2959.0	144.70	0.055	0.0474	1.39	0.0066	2.03	1.48	0.73	6.63	0.10	
Ash_01_23	0.74	3831.0	235.30	0.061	0.0474	1.31	0.0066	1.97	1.48	0.75	6.64	0.10	
Ash_01_36	0.36	424.0	109.10	0.259	0.0496	5.26	0.0070	5.54	0.0002	0.02	6.66	0.12	
Ash_01_3	0.39	276.8	111.80	0.401	0.0491	5.11	0.0069	5.26	1.27	0.24	6.66	0.09	
Ash_01_40	0.45	495.0	136.10	0.272	0.0488	4.93	0.0069	5.15	1.46	0.28	6.68	0.11	
Ash_01_9	3.05	2387.0	1053.0	0.430	0.0495	1.94	0.0070	2.27	1.17	0.52	6.69	0.09	
Ash_01_21	0.42	556.0	112.90	0.202	0.0511	5.30	0.0072	5.41	1.07	0.20	6.69	0.08	
Ash_01_15	0.31	944.0	93.00	0.097	0.0476	1.99	0.0067	2.42	1.36	0.56	6.70	0.10	
Ash_01_5	0.50	1813.0	154.10	0.083	0.0474	2.77	0.0067	3.09	1.36	0.44	6.73	0.10	
Ash_01_35	0.53	432.5	158.10	0.357	0.0481	3.97	0.0069	4.26	1.55	0.36	6.74	0.11	
Ash_01_7	0.84	745.0	267.00	0.346	0.0478	2.75	0.0068	3.11	1.45	0.47	6.75	0.10	
Ash_01_32	1.70	2582.0	560.00	0.218	0.0477	1.97	0.0068	2.63	1.74	0.66	6.76	0.12	
Ash_01_6	0.41	374.0	112.60	0.297	0.0518	3.31	0.0074	3.69	1.63	0.44	6.77	0.12	
Ash_01_4	0.56	3040.0	161.30	0.051	0.0480	1.63	0.0069	2.06	1.25	0.61	6.77	0.09	
Ash_01_24	0.45	298.9	101.90	0.539	0.0619	8.89	0.0090	8.99	1.32	0.15	6.78	0.11	
Ash_01_44	0.40	529.1	112.00	0.203	0.0504	4.78	0.0072	4.99	1.44	0.29	6.78	0.11	
Ash_01_14	0.53	881.0	163.60	0.176	0.0468	3.44	0.0067	3.70	1.35	0.36	6.79	0.10	
Ash_01_20	0.67	2360.0	178.00	0.074	0.0496	1.73	0.0071	2.08	1.15	0.55	6.80	0.09	
Ash_01_42	0.43	2248.0	128.40	0.057	0.0473	1.14	0.0068	1.75	1.34	0.76	6.83	0.10	
Ash_01_48	0.55	550.0	161.30	0.291	0.0504	3.00	0.0073	3.89	2.47	0.64	6.84	0.17	
Ash_01_43	0.46	3320.0	140.60	0.042	0.0478	1.02	0.0069	1.53	1.15	0.75	6.85	0.09	
Ash_01_31	0.28	2084.0	88.90	0.042	0.0481	1.43	0.0070	1.67	0.87	0.52	6.86	0.07	
Ash_01_50	0.42	3210.0	130.10	0.041	0.0475	0.90	0.0069	1.69	1.43	0.85	6.86	0.10	
Ash_01_16	0.30	412.0	93.10	0.224	0.0486	4.13	0.0071	4.34	1.33	0.31	6.87	0.10	
Ash_01_8	2.11	3026.0	663.80	0.216	0.0477	1.26	0.0069	1.70	1.14	0.67	6.87	0.09	
Ash_01_19	1.12	3401.0	277.70	0.081	0.0505	1.67	0.0074	1.91	0.92	0.48	6.89	0.07	
Ash_01_1	0.48	644.0	150.00	0.232	0.0480	2.74	0.0070	3.13	1.51	0.48	6.90	0.11	
Ash_01_30	0.99	1070.0	307.90	0.285	0.0486	2.50	0.0071	2.62	0.78	0.30	6.92	0.07	
Ash_01_29	0.81	444.1	125.40	0.280	0.0790	12.66	0.0121	12.81	1.89	0.15	6.95	0.16	
Ash_01_41	1.33	3775.0	415.00	0.109	0.0480	1.18	0.0070	1.63	1.13	0.69	6.96	0.09	
Ash_01_37	0.47	281.4	77.50	0.273	0.0799	5.65	0.0123	6.29	2.77	0.44	7.02	0.20	
Ash_01_34	0.84	504.1	209.20	0.411	0.0581	5.52	0.0087	5.71	1.47	0.26	7.02	0.11	
Ash_01_12	0.75	2650.0	222.00	0.074	0.0467	1.14	0.0070	1.53	1.01	0.66	7.10	0.08	
Ash_01_53	0.32	574.0	91.30	0.156	0.0485	3.73	0.0073	4.43	2.38	0.54	7.12	0.17	
Ash_01_10	2.76	382.8	68.80	0.177	0.2330	6.88	0.0463	7.11	1.80	0.25	7.20	0.23	
Ash_01_46	1.14	453.1	140.10	0.310	0.0928	2.40	0.0068	3.04	1.86	0.61	7.61	0.15	
Ash_01_38	0.84	1085.0	214.00	0.196	0.0477	2.03	0.0083	2.35	0.00127	0.00	8.25	0.10	
Ash_01_45	1.91	2470.0	315.00	0.127	0.0474	1.17	0.0134	2.36	2.05	0.87	13.28	0.27	
Ash_01_25	1.82	730.0	291.10	0.397	0.0476	2.97	0.0135	3.19	1.17	0.37	13.34	0.16	
Ash_01_49	1.65	1177.0	254.50	0.216	0.0476	1.20	0.0136	2.15	1.78	0.83	13.44	0.24	
Ash_01_47	0.99	475.6	153.70	0.522	0.0484	1.88	0.0141	2.33	1.38	0.59	13.63	0.19	
Ash_01_39	2.09	917.5	325.60	0.354	0.0474	2.15	0.0140	2.54	1.56	0.53	13.84	0.19	
Ash_02_10	0.66	3340.0	211.70	0.064	0.0479	1.36	0.0065	2.04	1.52	0.75	6.45	0.10	6.71
Ash_02_16	1.48	635.0	494.00	0.782	0.0480	2.12	0.0066	3.27	2.49	0.76	6.54	0.17	0.02
Ash_02_15	0.35	623.0	107.30	0.172	0.0487	3.92	0.0068	4.13	1.28	0.31	6.62	0.09	0.04
Ash_02_22	0.50	400.1	165.70	0.418	0.0474	3.82	0.0066	4.34	2.07	0.48	6.63	0.14	0.04
Ash_02_1	0.27	240.0	81.40	0.343	0.0521	5.20	0.0074	5.68	1.66	0.30	6.65	0.12	1.53
Ash_02_27	0.71	353.5	226.60	0.643	0.0501	5.40	0.0071	5.68	0.00103	0.01	6.67	0.12	12/50
Ash_02_14	0.38	647.0	119.70	0.186	0.0487	3.72	0.0069	3.87	1.07	0.28	6.71	0.08	6.71

7. Appendix

Sample / grain	Concentrations (ppm)				Isotope ratios				Isotopic age (Ma)				2 $\sigma$ (abs.)
	Pb	U	Th	Ti/U <sub>zircon</sub>	<sup>207</sup> Pb/ <sup>206</sup> Pb	2 $\sigma$ (%)	<sup>207</sup> Pb/ <sup>235</sup> U	2 $\sigma$ (%)	<sup>206</sup> Pb/ <sup>238</sup> U	2 $\sigma$ (%)	Rho <sup>2</sup>	<sup>207</sup> Pb and <sup>206</sup> Pb-corrected <sup>206</sup> Pb/ <sup>238</sup> U age	
Ash_02_29	0.21	374.0	61.19	0.164	0.0509	4.93	0.0073	5.19	0.00104	1.64	0.32	6.74	0.12
Ash_02_19	0.90	437.0	283.00	0.585	0.0498	2.84	0.0071	3.33	0.00104	1.74	0.52	6.74	0.12
Ash_02_2	0.90	457.3	188.20	0.413	0.0721	5.15	0.0106	5.39	0.00107	1.59	0.29	6.77	0.12
Ash_02_6	1.19	620.8	387.70	0.618	0.0478	3.16	0.0068	3.48	0.00104	1.44	0.42	6.77	0.11
Ash_02_30	0.75	548.0	234.40	0.434	0.0471	4.27	0.0067	4.64	0.00104	1.83	0.39	6.78	0.13
Ash_02_7	0.37	287.0	115.50	0.403	0.0487	5.97	0.0070	6.21	0.00104	1.73	0.28	6.80	0.12
Ash_02_33	1.10	874.0	328.90	0.378	0.0504	4.58	0.0074	4.79	0.00106	1.41	0.29	6.90	0.11
Ash_02_17	0.24	357.0	71.20	0.200	0.0504	4.78	0.0074	5.01	0.00106	1.51	0.30	6.92	0.11
Ash_02_31	0.40	370.7	124.80	0.339	0.0470	4.06	0.0069	4.30	0.00106	1.41	0.33	6.93	0.11
Ash_02_50	0.62	420.8	115.20	0.277	0.0690	3.79	0.0104	3.86	0.00110	0.75	0.19	6.96	0.07
Ash_02_45	0.54	291.1	164.70	0.576	0.0510	6.48	0.0075	6.80	0.00107	2.05	0.30	6.96	0.15
Ash_02_38	1.32	360.0	166.00	0.460	0.1210	11.58	0.0197	11.67	0.00118	1.44	0.12	6.98	0.15
Ash_02_44	1.70	1715.0	528.00	0.312	0.0472	1.78	0.0070	2.63	0.00108	1.94	0.74	7.08	0.14
Ash_02_41	0.21	441.0	57.00	0.131	0.0483	2.93	0.0072	3.45	0.00109	1.84	0.53	7.10	0.14
Ash_02_5	0.81	2376.0	114.70	0.048	0.0531	2.67	0.0080	3.04	0.00110	1.46	0.48	7.11	0.11
Ash_02_3	0.35	617.0	102.00	0.167	0.0476	3.59	0.0072	4.03	0.00110	1.82	0.45	7.16	0.14
Ash_02_32	0.68	590.0	60.42	0.104	0.0766	4.85	0.0121	4.96	0.00115	1.05	0.21	7.22	0.09
Ash_02_11	0.36	237.1	101.00	0.427	0.0500	6.81	0.0078	7.02	0.00113	1.69	0.24	7.31	0.13
Ash_02_49	0.67	389.0	189.00	0.485	0.0492	3.88	0.0077	4.38	0.00113	2.03	0.46	7.37	0.15
Ash_02_4	0.69	695.1	174.80	0.251	0.0509	2.39	0.0080	2.65	0.00114	1.14	0.43	7.38	0.09
Ash_02_18	0.74	619.0	200.30	0.326	0.0509	2.78	0.0081	3.27	0.00116	1.73	0.53	7.50	0.13
Ash_02_39	0.72	611.3	200.90	0.333	0.0478	2.75	0.0078	3.14	0.00118	1.52	0.48	7.69	0.12
Ash_02_43	0.83	486.0	231.40	0.483	0.0479	3.78	0.0079	4.45	0.00120	2.34	0.53	7.78	0.19
Ash_02_34	1.28	509.0	333.80	0.661	0.0483	2.93	0.0085	3.52	0.00128	1.96	0.56	8.30	0.17
Ash_02_28	1.55	1309.0	367.70	0.283	0.0484	2.10	0.0087	2.30	0.00130	0.92	0.40	8.47	0.09
Ash_02_35	0.54	526.0	132.00	0.249	0.0469	3.36	0.0086	3.76	0.00131	1.68	0.45	8.52	0.15
Ash_02_37	0.30	403.3	71.10	0.177	0.0475	4.11	0.0084	4.21	0.00132	0.91	0.22	8.58	0.09
Ash_02_42	0.49	332.5	122.10	0.369	0.0478	5.66	0.0088	6.15	0.00134	2.40	0.39	8.69	0.21
Ash_02_9	2.83	1244.0	415.10	0.332	0.0514	6.43	0.0139	6.59	0.00197	1.42	0.22	12.70	0.19
Ash_02_24	9.38	3660.0	1571.0	0.434	0.0488	1.31	0.0133	1.89	0.00198	1.36	0.72	12.83	0.18
Ash_02_40	1.95	656.0	269.00	0.463	0.0628	4.95	0.0180	5.85	0.00208	3.12	0.53	13.24	0.41
Ash_02_13	1.43	550.0	222.00	0.340	0.0471	2.14	0.0135	2.48	0.00209	1.25	0.50	13.51	0.17
Ash_02_20	1.51	760.0	238.10	0.315	0.0481	1.47	0.0138	1.81	0.00209	1.05	0.58	13.52	0.15
Ash_02_25	3.70	1720.0	591.00	0.347	0.0473	1.09	0.0136	2.12	0.00209	1.82	0.86	13.52	0.25
Ash_02_12	1.29	627.0	202.30	0.322	0.0481	2.32	0.0139	2.94	0.00210	1.81	0.61	13.59	0.25
Ash_02_8	2.11	598.3	335.20	0.561	0.0475	2.77	0.0137	3.05	0.00210	1.29	0.42	13.60	0.18
Ash_02_21	3.91	1789.0	622.90	0.351	0.0473	1.21	0.0137	1.40	0.00211	0.71	0.51	13.68	0.10
Ash_02_26	3.22	1378.0	473.20	0.347	0.0475	1.49	0.0141	2.42	0.00215	1.91	0.79	13.93	0.27
Ash_02_23	1.66	469.0	255.00	0.551	0.0466	2.16	0.0140	2.72	0.00217	1.66	0.61	14.08	0.24
Ash_02_47	2.30	890.0	351.60	0.401	0.0492	2.07	0.0151	3.22	0.00223	2.46	0.77	14.43	0.36
Ash_02_46	2.32	358.9	231.50	0.653	0.0947	7.51	0.0321	8.00	0.00246	2.77	0.35	14.95	0.44
Ash_02_36	1.72	457.3	178.60	0.396	0.0510	2.19	0.0223	2.78	0.00317	1.70	0.61	20.41	0.35
Ash_02_48	14.9	64.6	26.11	0.407	0.0807	0.55	2.3433	1.48	0.21080	1.38	0.93	1234.30	16.37
Ash_03_4	1.09	1138.0	391.90	0.346	0.0483	2.72	0.0057	3.24	0.00085	1.76	0.54	5.57	0.10
Ash_03_45	1.92	840.0	719.00	0.847	0.0491	2.68	0.0061	3.40	0.00091	2.09	0.62	5.91	0.13
Ash_03_19	1.93	1434.0	713.00	0.498	0.0481	2.12	0.0060	2.82	0.00091	1.86	0.66	5.96	0.12
Ash_03_2	1.03	485.0	370.10	0.773	0.0494	5.08	0.0063	5.44	0.00092	1.95	0.36	6.00	0.12
Ash_03_48	2.00	706.0	724.00	0.996	0.0486	3.52	0.0063	3.62	0.00093	0.85	0.23	6.08	0.07
Ash_03_33	0.56	262.2	204.90	0.776	0.0486	7.42	0.0063	7.66	0.00094	1.92	0.25	6.10	0.13
Ash_03_26	1.40	618.0	509.00	0.824	0.0482	3.76	0.0062	4.17	0.00094	1.82	0.44	6.10	0.12
Ash_03_21	0.95	494.2	339.80	0.686	0.0502	4.00	0.0065	4.35	0.00094	1.70	0.39	6.12	0.11
Ash_03_36	1.08	398.0	351.80	0.877	0.0571	3.53	0.0075	4.46	0.00095	2.73	0.61	6.13	0.17
Ash_03_50	0.49	255.7	161.80	0.617	0.0496	7.67	0.0065	7.90	0.00095	1.89	0.24	6.19	0.13
Ash_03_17	0.31	281.7	97.40	0.345	0.0511	6.27	0.0067	6.62	0.00095	2.10	0.32	6.19	0.14
Ash_03_42	3.88	248.4	172.60	0.682	0.3830	2.64	0.0874	5.30	0.00166	4.59	0.87	6.21	0.31
Ash_03_10	1.59	504.3	342.00	0.681	0.0981	6.03	0.0137	6.31	0.00162	1.87	0.30	6.21	0.13
Ash_03_43	0.84	404.0	260.20	0.629	0.0608	5.28	0.0081	5.47	0.00097	1.44	0.26	6.22	0.10
Ash_03_11	0.73	599.0	254.30	0.422	0.0495	6.07	0.0065	6.30	0.00096	1.67	0.27	6.23	0.11
Ash_03_6	2.18	2116.0	740.00	0.353	0.0476	1.75	0.0063	2.28	0.00096	1.46	0.64	6.26	0.10
Ash_03_24	1.33	939.0	461.90	0.489	0.0475	2.56	0.0063	2.94	0.00096	1.46	0.49	6.28	0.10
Ash_03_47	8.40	1880.0	2480.0	1.285	0.0870	12.65	0.0122	12.82	0.00102	2.06	0.16	6.31	0.16
Ash_03_41	0.20	113.3	60.30	0.519	0.0532	12.79	0.0071	12.97	0.00098	2.15	0.17	6.32	0.15

Sample / grain	Concentrations (ppm)				Isotope ratios				Isotopic age (Ma)				2 $\sigma$ (abs.)		
	Pb	U	Th	Ti/U <sub>zircon</sub>	<sup>207</sup> Pb/ <sup>206</sup> Pb	2 $\sigma$ (%)	<sup>207</sup> Pb/ <sup>235</sup> U	2 $\sigma$ (%)	<sup>206</sup> Pb/ <sup>238</sup> U	2 $\sigma$ (%)	Rho <sup>s</sup>	<sup>207</sup> Pb and <sup>206</sup> Pb/ <sup>238</sup> U age			
Ash_03_25	4.00	188.3	186.00	0.976	0.4330	3.49	0.1132	5.89	0.00190	4.74	0.81	6.32	0.38	†	
Ash_03_39	3.04	461.0	461.00	1.010	0.1819	4.74	0.0294	5.17	0.00117	2.05	0.40	6.34	0.16	†	
Ash_03_49	1.56	652.0	351.00	0.531	0.8000	18.99	0.0112	18.99	0.00102	2.96	0.16	6.35	0.23	†	
Ash_03_1	1.17	650.0	271.40	0.423	0.0729	8.65	0.0101	8.90	0.00101	2.09	0.23	6.36	0.15	†	
Ash_03_12	1.05	363.4	340.00	0.909	0.0541	7.77	0.0074	8.03	0.00099	2.03	0.25	6.37	0.14	†	
Ash_03_40	1.31	1321.0	463.00	0.345	0.0481	2.06	0.0065	2.63	0.00098	1.64	0.62	6.39	0.11	†	
Ash_03_3	1.83	1914.0	623.70	0.333	0.0478	1.99	0.0064	2.64	0.00098	1.74	0.66	6.39	0.12	†	
Ash_03_32	1.16	213.0	238.00	1.022	0.1490	19.47	0.0235	19.78	0.00114	3.50	0.18	6.49	0.35	†	
Ash_03_28	1.22	613.0	403.90	0.657	0.0478	3.16	0.0066	3.85	0.00101	2.19	0.57	6.56	0.15	†	
Ash_03_34	1.12	1338.0	366.20	0.271	0.0478	2.54	0.0067	3.27	0.00102	2.06	0.63	6.67	0.14	†	
Ash_03_23	1.45	1219.0	482.80	0.396	0.0480	2.12	0.0068	2.69	0.00103	1.65	0.61	6.71	0.12	†	
Ash_03_30	0.45	369.0	137.10	0.371	0.0491	5.92	0.0070	6.26	0.00103	2.03	0.32	6.74	0.14	†	
Ash_03_44	0.85	260.6	177.90	0.666	0.0996	5.44	0.0153	5.91	0.00112	2.33	0.39	6.80	0.17	†	
Ash_03_31	1.49	1337.0	477.20	0.353	0.0495	2.66	0.0072	3.11	0.00106	1.61	0.52	6.87	0.12	†	
Ash_03_22	1.33	1669.0	407.10	0.242	0.0491	3.28	0.0072	3.65	0.00106	1.60	0.44	6.93	0.12	†	
Ash_03_18	0.62	689.0	188.60	0.274	0.0482	2.52	0.0073	3.22	0.00110	2.01	0.62	7.15	0.15	†	
Ash_03_46	1.38	348.2	135.30	0.381	0.1230	5.38	0.0214	5.88	0.00126	2.37	0.40	7.45	0.19	†	
Ash_03_9	0.84	496.8	209.30	0.424	0.0494	3.26	0.0087	3.44	0.00128	1.09	0.32	8.32	0.10	†	
Ash_03_7	1.24	1016.0	314.30	0.310	0.0470	2.16	0.0085	2.65	0.00131	1.53	0.58	8.51	0.14	†	
Ash_03_5	0.74	3691.0	143.40	0.038	0.0465	1.31	0.0112	2.06	0.00176	1.60	0.77	11.41	0.18	†	
Ash_03_14	2.42	1167.0	446.10	0.384	0.0477	1.26	0.0123	2.13	0.00186	1.72	0.81	12.08	0.21	†	
Ash_03_16	1.29	571.3	217.80	0.385	0.0484	2.10	0.0132	2.82	0.00198	1.87	0.66	12.80	0.24	†	
Ash_03_8	1.57	561.0	254.80	0.455	0.0481	3.97	0.0134	4.44	0.00202	1.98	0.45	13.09	0.26	†	
Ash_03_29	1.90	377.7	299.80	0.779	0.0532	4.53	0.0153	4.94	0.00209	1.96	0.40	13.43	0.27	†	
Ash_03_27	2.17	309.7	290.50	0.936	0.0712	7.59	0.0210	7.80	0.00214	1.77	0.23	13.45	0.26	†	
Ash_03_38	1.71	603.0	254.40	0.413	0.0539	4.10	0.0156	4.54	0.00210	1.95	0.43	13.51	0.27	†	
Ash_03_37	2.08	520.0	307.90	0.583	0.0522	5.00	0.0154	5.27	0.00214	1.68	0.32	13.75	0.24	†	
Ash_03_35	3.97	790.0	401.00	0.503	0.0823	4.03	0.0253	4.38	0.00223	1.71	0.39	13.78	0.24	†	
Ash_03_15	4.86	1322.0	742.00	0.558	0.0471	1.19	0.0141	1.73	0.00217	1.25	0.72	14.04	0.18	†	
Ash_03_13	1.51	425.3	235.40	0.556	0.0480	3.36	0.0144	3.94	0.00218	2.07	0.52	14.08	0.29	†	
Ash_03_20	0.94	738.0	375.00	0.502	0.0816	11.28	0.0260	11.52	0.00251	2.53	0.20	14.53	0.38	†	
Ash_04_48	0.53	425.9	156.30	0.358	0.0496	3.65	0.0076	3.99	0.00111	1.62	0.41	7.23	0.12	w.m.	7.40
Ash_04_19	1.81	2192.0	550.10	0.244	0.0473	1.79	0.0073	2.41	0.00113	1.62	0.67	7.25	0.15	±1s	0.02
Ash_04_32	1.38	2350.0	271.20	0.113	0.0554	4.35	0.0086	4.81	0.00115	2.04	0.42	7.28	0.15	±2s	0.04
Ash_04_41	0.97	1091.0	285.90	0.256	0.0488	2.69	0.0075	3.23	0.00112	1.79	0.55	7.29	0.14	MSWD	1.80
Ash_04_44	0.65	622.0	186.30	0.293	0.0516	2.93	0.0080	3.48	0.00115	1.86	0.54	7.32	0.14	n	22/50
Ash_04_45	2.79	734.0	768.00	1.016	0.0626	2.11	0.0099	2.85	0.00115	1.92	0.67	7.32	0.14		
Ash_04_34	0.35	419.9	96.40	0.224	0.0483	3.34	0.0075	3.73	0.00113	1.68	0.45	7.39	0.13		
Ash_04_3	0.67	434.4	184.00	0.410	0.0525	4.40	0.0083	5.17	0.00114	2.72	0.53	7.39	0.20		
Ash_04_38	0.55	1214.0	148.00	0.116	0.0474	2.35	0.0074	3.23	0.00113	2.21	0.68	7.39	0.17		
Ash_04_36	0.83	532.9	236.50	0.432	0.0489	4.72	0.0077	4.92	0.00114	1.40	0.28	7.42	0.11		
Ash_04_24	0.55	557.0	159.60	0.277	0.0493	3.87	0.0078	4.54	0.00114	2.37	0.52	7.42	0.18		
Ash_04_35	1.17	2357.0	352.90	0.145	0.0471	1.77	0.0074	2.82	0.00114	2.19	0.78	7.45	0.17		
Ash_04_1	0.50	187.8	113.20	0.589	0.0730	26.03	0.0119	26.40	0.00118	4.40	0.17	7.45	0.37	†	
Ash_04_15	0.99	929.0	289.20	0.303	0.0491	2.88	0.0077	3.41	0.00115	1.83	0.54	7.45	0.14		
Ash_04_18	0.44	282.6	126.00	0.432	0.0528	4.56	0.0084	4.85	0.00115	1.65	0.34	7.45	0.13		
Ash_04_13	0.53	368.3	150.80	0.402	0.0481	5.42	0.0076	5.95	0.00115	2.45	0.41	7.46	0.19		
Ash_04_11	0.72	1300.0	202.30	0.151	0.0475	2.00	0.0075	2.90	0.00114	2.10	0.72	7.46	0.16		
Ash_04_40	0.74	199.9	213.70	1.038	0.0485	8.67	0.0077	8.82	0.00115	1.65	0.19	7.49	0.13		
Ash_04_8	0.33	278.0	90.40	0.319	0.0488	3.10	0.0077	3.78	0.00115	2.17	0.57	7.50	0.17		
Ash_04_14	0.72	439.1	208.60	0.463	0.0488	3.10	0.0078	3.64	0.00115	1.91	0.52	7.50	0.15		
Ash_04_10	0.63	462.7	178.20	0.377	0.0496	3.85	0.0079	4.19	0.00116	1.64	0.39	7.53	0.13		
Ash_04_25	1.25	408.0	360.00	0.727	0.0474	4.66	0.0076	5.21	0.00116	2.33	0.45	7.54	0.18		
Ash_04_46	10.4	4950.0	3011.0	0.597	0.0471	1.08	0.0075	2.57	0.00116	2.33	0.91	7.54	0.18		
Ash_04_33	0.93	921.0	263.70	0.280	0.0488	2.49	0.0078	3.18	0.00116	1.98	0.62	7.56	0.15	†	
Ash_04_39	1.64	507.0	469.00	0.904	0.0476	2.55	0.0076	3.08	0.00116	1.72	0.56	7.56	0.14	†	
Ash_04_21	0.23	296.0	62.90	0.207	0.0484	6.83	0.0077	7.00	0.00116	1.55	0.22	7.56	0.13	†	
Ash_04_28	0.46	423.9	131.10	0.302	0.0480	4.19	0.0077	4.67	0.00116	2.07	0.44	7.56	0.16	†	
Ash_04_20	1.19	564.0	276.00	0.475	0.0606	13.37	0.0099	13.64	0.00118	2.71	0.20	7.57	0.22	†	
Ash_04_47	1.96	725.0	507.00	0.678	0.0581	3.98	0.0094	4.43	0.00118	1.95	0.44	7.57	0.15	†	
Ash_04_2	0.67	369.4	182.60	0.483	0.0510	6.09	0.0082	6.26	0.00117	1.46	0.23	7.57	0.12	†	
Ash_04_4	0.60	424.2	155.60	0.362	0.0504	3.00	0.0081	3.50	0.00117	1.80	0.51	7.58	0.14	†	

# 7. Appendix

Sample / grain	Concentrations (ppm)				Th/U <sub>corr</sub>	<sup>207</sup> Pb/ <sup>206</sup> Pb	Isotope ratios			Isotopic age (Ma)			2σ (abs.)	
	Pb	U	Th	U			2σ (%)	<sup>207</sup> Pb/ <sup>235</sup> U	2σ (%)	<sup>206</sup> Pb/ <sup>238</sup> U	2σ (%)	Rho <sup>2</sup>		<sup>207</sup> Pb and <sup>206</sup> Pb-corrected <sup>206</sup> Pb/ <sup>238</sup> U age
Ash_04_27	0.62	403.2	166.10	0.400	0.0507	6.91	0.0082	7.10	0.00117	1.63	0.23	7.59	0.13	†
Ash_04_16	1.10	406.0	319.00	0.734	0.0488	3.71	0.0079	4.16	0.00117	1.88	0.45	7.61	0.15	†
Ash_04_31	0.94	578.5	259.80	0.436	0.0480	2.33	0.0078	2.70	0.00117	1.36	0.51	7.64	0.11	†
Ash_04_49	1.24	750.0	304.00	0.399	0.0548	4.40	0.0090	5.33	0.00119	3.02	0.57	7.69	0.23	†
Ash_04_29	0.88	666.0	247.00	0.358	0.0477	2.34	0.0078	2.99	0.00119	1.85	0.62	7.73	0.15	†
Ash_04_17	0.83	691.0	230.50	0.324	0.0476	2.14	0.0078	2.78	0.00119	1.77	0.64	7.73	0.14	†
Ash_04_50	1.99	1181.0	554.00	0.461	0.0480	1.96	0.0079	3.12	0.00119	1.85	0.86	7.75	0.19	†
Ash_04_37	1.03	4843.0	307.20	0.061	0.0469	1.10	0.0077	2.15	0.00119	1.85	0.86	7.77	0.15	†
Ash_04_22	0.72	395.9	197.60	0.486	0.0521	4.82	0.0086	5.15	0.00120	1.83	0.36	7.78	0.15	†
Ash_04_9	0.50	269.6	110.50	0.403	0.0628	4.00	0.0106	4.36	0.00122	1.72	0.40	7.79	0.14	†
Ash_04_6	0.91	633.0	249.80	0.384	0.0484	2.51	0.0080	3.27	0.00120	2.09	0.64	7.79	0.17	†
Ash_04_43	0.68	275.0	88.80	0.317	0.0886	9.15	0.0154	9.33	0.00126	1.82	0.20	7.81	0.17	†
Ash_04_42	0.32	428.0	88.30	0.202	0.0464	3.69	0.0077	4.01	0.00121	1.57	0.39	7.89	0.13	†
Ash_04_7	1.88	2041.0	483.00	0.231	0.0477	1.42	0.0083	1.95	0.00127	1.34	0.69	8.25	0.12	†
Ash_04_30	1.55	2070.0	386.40	0.180	0.0484	1.70	0.0086	2.53	0.00128	1.87	0.74	8.35	0.16	†
Ash_04_12	0.44	517.6	108.40	0.203	0.0505	3.24	0.0090	3.24	0.00129	1.62	0.50	8.39	0.14	†
Ash_04_26	5.41	1653.0	1319.0	0.767	0.0553	5.08	0.0101	5.47	0.00133	2.03	0.37	8.56	0.18	†
Ash_04_23	0.41	2337.0	92.80	0.038	0.0470	1.44	0.0094	2.20	0.00145	1.66	0.75	9.43	0.16	†
Ash_04_5	2.03	861.0	326.30	0.371	0.0483	1.76	0.0138	2.54	0.00208	1.83	0.72	13.45	0.25	†
ASH_05_17	0.78	1502.0	551.00	0.360	0.0508	2.01	0.0032	2.79	0.00046	1.93	0.69	3.05	0.07	w.m.
ASH_05_37	0.85	440.0	322.00	0.729	0.0552	3.47	0.0063	4.36	0.00083	2.65	0.61	5.38	0.15	†
ASH_05_2	0.65	774.0	246.50	0.310	0.0486	3.52	0.0058	4.27	0.00087	2.42	0.57	5.68	0.14	†
ASH_05_36	0.84	643.0	222.00	0.348	0.0670	6.28	0.0085	6.80	0.00092	2.61	0.38	5.86	0.16	†
ASH_05_16	0.92	836.0	351.00	0.411	0.0497	2.85	0.0062	4.22	0.00090	3.11	0.74	5.86	0.18	†
ASH_05_34	0.76	468.0	263.80	0.567	0.0511	4.71	0.0065	5.80	0.00092	3.38	0.58	5.96	0.20	†
ASH_05_8	0.39	258.8	128.70	0.491	0.0523	6.70	0.0068	6.97	0.00094	1.92	0.28	6.09	0.12	†
ASH_05_5	1.40	1096.0	471.90	0.423	0.0474	2.35	0.0062	3.08	0.00096	1.99	0.65	6.24	0.13	†
ASH_05_9	0.25	386.8	64.30	0.162	0.0499	2.64	0.0071	3.22	0.00103	1.85	0.57	6.70	0.13	†
ASH_05_15	1.18	895.0	364.70	0.398	0.0477	2.55	0.0071	3.45	0.00108	2.32	0.67	7.02	0.17	†
ASH_05_40	0.91	805.0	235.60	0.289	0.0481	1.81	0.0082	2.42	0.00124	1.61	0.66	8.10	0.13	†
ASH_05_7	2.27	1160.0	475.00	0.396	0.0583	6.87	0.0106	7.26	0.00132	2.35	0.32	8.45	0.21	†
ASH_05_3	0.72	1070.0	174.40	0.160	0.0469	3.22	0.0084	4.00	0.00131	2.38	0.59	8.50	0.20	†
ASH_05_29	3.02	1685.0	495.00	0.292	0.0489	1.62	0.0127	2.63	0.00189	2.06	0.79	12.23	0.25	†
ASH_05_38	1.34	885.0	213.90	0.242	0.0477	2.03	0.0131	2.53	0.00200	1.50	0.59	12.96	0.20	†
ASH_05_47	0.99	447.0	160.90	0.358	0.0487	3.72	0.0137	4.30	0.00204	2.16	0.50	13.17	0.29	†
ASH_05_19	1.18	458.0	156.60	0.338	0.0584	7.37	0.0168	8.03	0.00208	3.17	0.39	13.31	0.43	†
ASH_05_25	1.10	305.8	175.50	0.567	0.0486	3.73	0.0138	4.22	0.00207	1.99	0.47	13.35	0.27	†
ASH_05_4	2.16	423.8	346.60	0.805	0.0477	2.75	0.0136	3.21	0.00207	1.64	0.51	13.39	0.22	†
ASH_05_1	1.65	563.0	275.10	0.469	0.0470	2.79	0.0134	3.32	0.00208	1.78	0.54	13.45	0.24	†
ASH_05_27	3.86	1577.0	618.60	0.387	0.0469	1.42	0.0135	2.35	0.00208	1.87	0.80	13.50	0.25	†
ASH_05_30	1.00	251.8	159.10	0.626	0.0489	4.11	0.0141	4.57	0.00209	2.01	0.44	13.52	0.27	†
ASH_05_13	1.41	646.0	221.00	0.336	0.0478	2.75	0.0138	3.61	0.00209	2.35	0.65	13.52	0.32	†
ASH_05_20	1.50	516.0	240.70	0.458	0.0482	2.73	0.0139	3.10	0.00209	1.48	0.68	13.52	0.20	†
ASH_05_41	1.93	373.8	316.10	0.838	0.0495	2.86	0.0144	3.57	0.00210	2.14	0.40	13.58	0.29	†
ASH_05_28	2.81	949.0	448.30	0.470	0.0467	1.51	0.0135	2.36	0.00210	1.81	0.77	13.59	0.25	†
ASH_05_44	4.23	1113.0	675.10	0.605	0.0472	1.27	0.0137	1.88	0.00210	1.38	0.74	13.61	0.19	†
ASH_05_32	3.51	1194.0	549.00	0.457	0.0475	1.33	0.0138	2.28	0.00211	1.85	0.81	13.66	0.25	†
ASH_05_31	2.94	819.0	449.00	0.542	0.0523	1.77	0.0153	2.69	0.00212	2.02	0.75	13.67	0.28	†
ASH_05_33	2.65	514.8	433.00	0.853	0.0470	2.37	0.0137	3.25	0.00212	2.22	0.68	13.69	0.31	†
ASH_05_21	1.00	320.0	154.70	0.479	0.0480	2.12	0.0140	3.60	0.00212	2.41	0.75	13.70	0.33	†
ASH_05_24	1.35	508.0	208.00	0.404	0.0471	3.00	0.0137	3.60	0.00212	1.98	0.55	13.72	0.27	†
ASH_05_18	1.52	800.0	240.70	0.296	0.0470	2.54	0.0140	3.37	0.00212	2.22	0.66	13.73	0.31	†
ASH_05_10	4.80	1737.0	757.00	0.431	0.0478	1.71	0.0138	2.54	0.00212	1.88	0.74	13.76	0.26	†
ASH_05_48	3.22	1436.0	515.80	0.358	0.0475	1.79	0.0139	2.92	0.00213	2.30	0.79	13.77	0.32	†
ASH_05_26	1.60	724.0	248.70	0.339	0.0475	1.77	0.0140	2.72	0.00213	2.06	0.76	13.82	0.29	†
ASH_05_6	2.46	934.0	398.40	0.416	0.0474	1.53	0.0140	2.72	0.00214	1.22	0.62	13.83	0.17	†
ASH_05_23	3.13	1155.0	494.50	0.422	0.0477	1.75	0.0140	2.59	0.00214	1.92	0.74	13.83	0.27	†
ASH_05_39	1.67	294.7	261.80	0.880	0.0477	4.21	0.0141	4.65	0.00214	1.96	0.42	13.86	0.27	†
ASH_05_50	1.98	959.0	302.10	0.310	0.0444	3.44	0.0144	3.44	0.00215	2.56	0.74	13.91	0.36	†
ASH_05_49	0.84	326.5	133.00	0.404	0.0505	3.00	0.0150	3.57	0.00216	1.95	0.54	13.92	0.27	†
ASH_05_42	0.91	531.0	131.50	0.250	0.0488	3.10	0.0146	3.52	0.00217	1.66	0.47	14.02	0.24	†
ASH_05_12	3.12	1096.0	485.80	0.436	0.0467	1.95	0.0139	3.13	0.00216	2.45	0.78	14.03	0.34	†

Sample / grain	Concentrations (ppm)				Isotope ratios				Isotopic age (Ma)					
	Pb	U	Th	Ti/U <sub>Zircon</sub>	<sup>207</sup> Pb/ <sup>206</sup> Pb	2σ (%)	<sup>207</sup> Pb/ <sup>235</sup> U	2σ (%)	<sup>207</sup> Pb/ <sup>238</sup> U	2σ (%)	Rho <sup>2</sup>	<sup>207</sup> Pb and <sup>206</sup> Pb-corrected <sup>206</sup> Pb/ <sup>238</sup> U age	2σ (abs.)	w.m. ±1σ ±2σ MSWD n
ASH_05_35	0.53	148.3	80.80	0.543	0.0499	7.83	0.0151	8.67	0.00220	3.74	0.43	14.16	0.53	
ASH_05_14	1.07	691.0	160.70	0.393	0.0491	2.28	0.0150	3.05	0.00222	2.03	0.67	14.34	0.29	†
ASH_05_46	1.45	404.0	153.00	0.219	0.0464	1.46	0.0202	2.84	0.00516	2.44	0.86	20.41	0.50	†
ASH_05_22	0.80	145.7	74.00	0.502	0.0576	4.88	0.0255	5.61	0.00522	2.77	0.49	20.50	0.57	†
ASH_05_11	1.75	552.0	179.70	0.318	0.0473	1.94	0.0215	3.13	0.00530	2.46	0.78	21.30	0.52	†
ASH_05_43	5.20	175.0	64.60	0.367	0.0573	0.98	0.1815	3.66	0.02298	3.52	0.96	145.04	5.07	†
ASH_05_45	27.8	447.0	93.00	0.208	0.0611	0.49	0.8564	2.12	0.10170	2.06	0.97	624.07	12.54	†
ASH_06_24	0.67	770.0	178.60	0.233	0.0454	2.89	0.0077	3.36	0.00123	1.71	0.51	8.04	0.14	w.m.
ASH_06_41	0.59	748.0	142.90	0.192	0.0485	1.56	0.0083	1.97	0.00124	1.21	0.61	8.09	0.10	±1σ
ASH_06_45	1.10	403.0	169.30	0.426	0.0804	5.86	0.0144	6.24	0.00130	2.16	0.35	8.10	0.18	±2σ
ASH_06_44	0.62	840.0	159.40	0.190	0.0481	1.75	0.0083	2.66	0.00125	2.00	0.75	8.14	0.17	MSWD
ASH_06_39	0.52	568.0	119.50	0.212	0.0516	4.28	0.0089	4.66	0.00126	1.83	0.39	8.15	0.15	n
ASH_06_21	0.73	934.0	194.10	0.211	0.0473	2.57	0.0082	3.11	0.00125	1.76	0.56	8.16	0.15	
ASH_06_40	0.90	614.0	241.00	0.396	0.0469	3.22	0.0081	3.60	0.00125	1.59	0.44	8.17	0.14	
ASH_06_17	0.76	1108.0	195.70	0.177	0.0475	2.77	0.0082	3.70	0.00126	2.46	0.66	8.20	0.20	
ASH_06_15	0.52	365.0	132.40	0.369	0.0488	4.53	0.0085	5.08	0.00126	2.30	0.45	8.21	0.19	
ASH_06_29	0.59	308.1	113.40	0.378	0.0635	10.87	0.0113	11.17	0.00129	2.56	0.23	8.21	0.22	
ASH_06_49	1.26	398.4	168.90	0.425	0.0942	4.05	0.0174	4.23	0.00134	1.19	0.28	8.22	0.11	
ASH_06_11	1.02	684.0	218.70	0.326	0.0585	6.34	0.0103	7.00	0.00128	2.96	0.42	8.24	0.25	
ASH_06_4	0.52	1157.0	133.40	0.117	0.0473	1.80	0.0082	2.40	0.00126	1.58	0.66	8.24	0.13	
ASH_06_33	1.48	1559.0	385.00	0.247	0.0471	2.06	0.0082	2.79	0.00127	1.89	0.68	8.27	0.16	
ASH_06_22	0.60	541.0	157.20	0.299	0.0481	3.97	0.0085	4.46	0.00128	2.03	0.46	8.33	0.17	
ASH_06_20	0.55	424.8	142.20	0.338	0.0504	3.99	0.0089	4.54	0.00129	2.18	0.48	8.33	0.18	
ASH_06_2	1.84	2728.0	468.40	0.173	0.0475	1.35	0.0084	2.50	0.00128	2.11	0.84	8.34	0.18	
ASH_06_5	1.26	1360.0	279.30	0.207	0.0507	2.21	0.0090	2.74	0.00129	1.63	0.59	8.34	0.14	
ASH_06_10	1.21	1516.0	315.60	0.211	0.0474	1.29	0.0084	2.80	0.00128	2.49	0.89	8.36	0.21	
ASH_06_30	0.77	958.0	193.30	0.203	0.0480	1.80	0.0085	2.82	0.00129	2.18	0.77	8.36	0.18	
ASH_06_8	0.79	561.0	170.80	0.310	0.0543	3.34	0.0097	3.78	0.00130	1.77	0.47	8.36	0.15	
ASH_06_7	0.54	112.1	92.80	0.302	0.0633	8.38	0.0115	8.49	0.00132	1.37	0.16	8.39	0.13	
ASH_06_3	2.52	917.1	354.10	0.390	0.0830	20.49	0.0155	20.64	0.00135	2.52	0.12	8.40	0.28	†
ASH_06_38	0.44	526.4	108.90	0.336	0.0465	4.75	0.0083	4.93	0.00130	1.32	0.27	8.42	0.12	†
ASH_06_34	0.65	579.4	163.60	0.284	0.0478	2.54	0.0085	2.83	0.00130	1.23	0.44	8.44	0.11	†
ASH_06_14	0.78	781.0	192.80	0.248	0.0489	1.75	0.0088	2.77	0.00130	2.15	0.78	8.45	0.18	†
ASH_06_42	2.63	1704.0	483.00	0.289	0.0608	2.18	0.0111	2.83	0.00132	1.82	0.64	8.45	0.16	†
ASH_06_1	1.45	1544.0	363.00	0.236	0.0477	2.03	0.0086	2.85	0.00130	2.00	0.70	8.48	0.17	†
ASH_06_28	0.92	1299.0	227.70	0.176	0.0471	2.01	0.0085	3.18	0.00130	2.46	0.77	8.48	0.21	†
ASH_06_13	1.38	400.2	133.80	0.336	0.1089	6.44	0.0212	6.80	0.00141	2.19	0.32	8.49	0.20	†
ASH_06_6	0.82	1068.0	198.60	0.188	0.0474	2.98	0.0085	3.76	0.00131	2.30	0.61	8.50	0.20	†
ASH_06_26	1.48	596.0	278.70	0.470	0.0694	5.92	0.0129	6.30	0.00135	2.15	0.34	8.52	0.19	†
ASH_06_48	1.17	607.8	314.40	0.523	0.0495	3.66	0.0090	4.09	0.00132	1.82	0.45	8.56	0.16	†
ASH_06_31	2.03	1704.0	514.60	0.303	0.0475	1.49	0.0086	2.18	0.00132	1.59	0.73	8.57	0.14	†
ASH_06_19	1.44	286.9	122.40	0.433	0.1418	4.11	0.0293	4.49	0.00150	1.80	0.40	8.57	0.17	†
ASH_06_12	1.36	709.0	292.90	0.414	0.0584	6.35	0.0108	6.68	0.00138	2.09	0.31	8.58	0.19	†
ASH_06_37	2.02	757.0	338.40	0.454	0.0782	4.49	0.0149	4.93	0.00138	2.03	0.41	8.61	0.18	†
ASH_06_43	1.26	1390.0	308.50	0.224	0.0475	1.73	0.0087	2.45	0.00133	1.73	0.71	8.65	0.15	†
ASH_06_27	1.57	715.0	153.50	0.217	0.0863	2.35	0.0167	2.75	0.00140	1.43	0.52	8.68	0.13	†
ASH_06_46	1.35	346.1	174.70	0.511	0.1087	3.61	0.0217	4.16	0.00145	2.07	0.50	8.70	0.19	†
ASH_06_25	1.87	1273.0	461.00	0.364	0.0489	1.65	0.0090	2.54	0.00134	1.94	0.76	8.70	0.17	†
ASH_06_50	0.55	257.5	110.20	0.431	0.0579	8.13	0.0108	8.32	0.00136	1.77	0.21	8.71	0.17	†
ASH_06_18	1.19	737.0	268.00	0.368	0.0480	5.64	0.0089	5.78	0.00134	1.27	0.22	8.72	0.12	†
ASH_06_36	2.45	1209.0	682.00	0.565	0.0490	1.94	0.0092	2.44	0.00136	1.48	0.61	8.79	0.13	†
ASH_06_16	2.19	498.0	203.10	0.412	0.1330	11.30	0.0258	12.07	0.00151	4.24	0.35	8.86	0.41	†
ASH_06_35	1.67	382.9	146.90	0.390	0.1300	10.01	0.0276	10.39	0.00154	2.79	0.27	8.97	0.30	†
ASH_06_23	2.37	446.0	126.90	0.287	0.1520	6.59	0.0359	7.09	0.00162	2.60	0.37	9.12	0.27	†
ASH_06_32	0.89	510.0	147.60	0.293	0.0628	2.42	0.0125	3.52	0.00145	2.56	0.73	9.21	0.24	†
ASH_06_9	1.92	155.2	78.20	0.507	0.2600	7.32	0.0708	7.79	0.00198	2.68	0.34	9.38	0.40	†
ASH_06_47	0.79	439.2	136.40	0.314	0.0494	2.86	0.0131	3.70	0.00192	2.34	0.63	12.42	0.29	†
ASH_07_29	2.36	324.0	245.00	0.754	0.1810	15.47	0.0348	16.20	0.00140	4.80	0.30	7.55	0.48	w.m.
ASH_07_48	1.14	343.0	227.00	0.656	0.0828	5.21	0.0139	5.73	0.00122	2.39	0.42	7.56	0.19	±1σ
ASH_07_4	0.79	1131.0	175.10	0.156	0.0558	3.37	0.0088	3.77	0.00118	1.69	0.45	7.64	0.13	±2σ
ASH_07_38	1.08	357.4	224.50	0.626	0.0777	9.53	0.0131	9.70	0.00122	1.80	0.19	7.64	0.16	MSWD
ASH_07_24	0.67	197.0	69.19	0.352	0.1120	11.61	0.0198	11.74	0.00128	1.72	0.15	7.67	0.19	n

7. Appendix

Sample / grain	Concentrations (ppm)				Isotope ratios				Isotopic age (Ma)				
	Pb	U	Th	Ti/U <sub>Zircon</sub>	<sup>207</sup> Pb/ <sup>206</sup> Pb	2σ (%)	<sup>207</sup> Pb/ <sup>235</sup> U	2σ (%)	<sup>206</sup> Pb/ <sup>238</sup> U	2σ (%)	Rho <sup>s</sup>	<sup>207</sup> Pb and <sup>206</sup> Pb-corrected <sup>206</sup> Pb/ <sup>238</sup> U age	2σ (abs.)
Ash_07_27	0.79	1696.0	222.20	0.130	0.0482	1.87	0.0078	2.21	0.00118	1.19	0.54	7.69	0.10
Ash_07_31	1.54	843.0	238.20	0.282	0.0745	11.01	0.0126	11.40	0.00123	2.93	0.26	7.74	0.24
Ash_07_22	0.89	414.4	246.50	0.593	0.0476	3.39	0.0079	3.97	0.00120	2.08	0.52	7.82	0.17
Ash_07_18	0.34	555.0	91.70	0.168	0.0485	4.14	0.0080	4.50	0.00120	1.74	0.39	7.84	0.14
Ash_07_43	0.49	381.0	127.00	0.332	0.0503	3.10	0.0084	4.07	0.00121	1.90	0.47	7.85	0.15
Ash_07_49	15.6	643.8	4840.0	6.993	0.0601	3.19	0.0104	3.53	0.00126	1.51	0.43	7.86	0.13
Ash_07_19	1.55	807.0	419.90	0.523	0.0081	2.72	0.0079	3.42	0.00121	2.07	0.60	7.87	0.17
Ash_07_21	0.81	263.0	233.20	0.893	0.0474	5.71	0.0081	6.13	0.00121	2.23	0.36	7.88	0.18
Ash_07_26	1.44	2117.0	294.10	0.139	0.0557	1.27	0.0095	2.00	0.00123	1.54	0.77	7.95	0.13
Ash_07_25	1.86	353.0	86.30	0.245	0.1660	15.07	0.0330	16.20	0.00144	5.97	0.37	7.98	0.56
Ash_07_44	0.97	575.9	253.60	0.436	0.0482	2.11	0.0082	3.60	0.00123	2.92	0.81	8.03	0.23
Ash_07_12	0.35	456.0	88.50	0.193	0.0483	3.75	0.0082	4.22	0.00124	1.94	0.46	8.04	0.16
Ash_07_39	0.95	1342.0	200.60	0.149	0.0526	3.82	0.0091	4.28	0.00125	1.92	0.45	8.09	0.16
Ash_07_10	0.72	413.9	181.50	0.438	0.0515	4.29	0.0089	4.73	0.00126	1.99	0.42	8.14	0.17
Ash_07_16	0.51	539.5	135.60	0.249	0.0476	2.55	0.0082	3.19	0.00125	1.92	0.60	8.16	0.16
Ash_07_32	1.11	421.0	288.00	0.679	0.0499	3.43	0.0087	3.96	0.00126	1.98	0.50	8.19	0.17
Ash_07_14	0.75	2192.0	194.90	0.089	0.0475	1.27	0.0082	2.09	0.00126	1.67	0.80	8.22	0.14
Ash_07_30	1.69	2100.0	349.50	0.168	0.0529	2.49	0.0093	3.37	0.00128	2.27	0.67	8.26	0.19
Ash_07_47	1.55	1543.0	377.00	0.243	0.0493	1.38	0.0086	2.80	0.00127	2.44	0.87	8.27	0.20
Ash_07_1	2.61	312.0	107.70	0.346	0.2233	4.05	0.0503	4.61	0.00164	2.20	0.48	8.27	0.22
Ash_07_3	0.96	429.5	248.00	0.579	0.0474	4.45	0.0083	4.60	0.00127	1.18	0.26	8.28	0.11
Ash_07_6	0.50	264.5	106.20	0.402	0.0579	7.09	0.0103	7.42	0.00129	2.17	0.29	8.30	0.19
Ash_07_13	1.60	1284.0	402.50	0.315	0.0479	2.33	0.0084	3.10	0.00128	2.04	0.66	8.30	0.17
Ash_07_7	0.70	988.0	182.40	0.186	0.0471	2.37	0.0083	3.23	0.00128	2.19	0.68	8.31	0.18
Ash_07_35	0.85	344.0	214.00	0.596	0.0478	4.41	0.0084	4.89	0.00128	2.11	0.43	8.32	0.18
Ash_07_20	0.78	892.0	198.50	0.218	0.0472	1.70	0.0083	2.89	0.00128	2.34	0.81	8.35	0.20
Ash_07_15	0.64	376.8	96.94	0.259	0.0690	7.26	0.0126	7.48	0.00132	1.82	0.24	8.37	0.16
Ash_07_2	1.80	391.4	146.60	0.375	0.1345	4.33	0.0269	4.71	0.00145	1.86	0.39	8.40	0.17
Ash_07_46	0.80	497.4	199.50	0.401	0.0474	2.98	0.0085	3.64	0.00129	2.09	0.57	8.42	0.18
Ash_07_8	0.76	492.0	150.70	0.309	0.0599	8.02	0.0109	8.28	0.00132	2.05	0.25	8.45	0.18
Ash_07_11	0.58	351.9	128.80	0.368	0.0630	9.37	0.0115	9.56	0.00133	1.89	0.20	8.46	0.17
Ash_07_9	0.58	516.8	143.60	0.278	0.0488	3.51	0.0090	3.91	0.00135	1.72	0.44	8.46	0.17
Ash_07_36	1.73	502.9	205.60	0.407	0.0950	11.59	0.0187	11.92	0.00143	2.80	0.23	8.74	0.28
Ash_07_23	1.76	1240.0	290.50	0.235	0.0642	3.60	0.0126	3.87	0.00142	1.41	0.36	9.04	0.13
Ash_07_37	0.60	757.0	112.80	0.150	0.0467	1.74	0.0113	2.69	0.00176	2.05	0.76	11.42	0.24
Ash_07_28	8.64	992.0	1382.0	1.385	0.0472	1.93	0.0137	3.06	0.00210	2.38	0.78	13.59	0.32
Ash_07_40	1.70	391.3	264.40	0.671	0.0494	2.06	0.0145	2.85	0.00213	1.97	0.69	13.77	0.27
Ash_07_17	3.62	1277.0	507.00	0.398	0.0540	2.44	0.0164	3.33	0.00220	2.27	0.68	14.15	0.32
Ash_07_5	2.80	1458.0	181.60	0.127	0.0578	7.10	0.0182	8.00	0.00228	3.69	0.46	14.57	0.54
Ash_07_33	1.32	478.0	185.20	0.387	0.0478	2.34	0.0159	3.38	0.00242	2.44	0.72	15.63	0.38
Ash_07_50	2.62	248.7	92.30	0.369	0.0575	1.53	0.0938	3.41	0.01183	3.04	0.89	74.96	2.27
Ash_07_45	45.8	357.0	207.90	0.581	0.0632	2.10	0.6251	2.39	0.07177	1.14	0.48	442.93	5.01
Ash_07_41	0.73	325.1	1.34	0.004	0.0614	0.56	0.8252	1.83	0.09760	1.74	0.95	599.39	10.17
Ash_07_42	95.6	409.3	114.00	0.280	0.1471	0.74	3.4895	1.84	0.17210	1.69	0.92	936.62	15.22
Ash_07_34	7.19	66.1	15.15	0.230	0.0732	0.61	1.7141	1.81	0.17000	1.71	0.94	1011.93	16.65
Ash_08_35	0.61	2792.0	251.70	0.090	0.0523	2.14	0.0049	2.58	0.00068	1.44	0.56	4.45	0.07
Ash_08_36	0.57	2804.0	204.60	0.073	0.0525	1.95	0.0049	2.72	0.00068	1.90	0.70	4.47	0.09
Ash_08_13	0.29	1894.0	117.40	0.063	0.0497	1.95	0.0047	2.83	0.00068	2.05	0.72	4.49	0.10
Ash_08_12	1.31	328.2	139.90	0.425	0.1890	35.45	0.0221	36.51	0.00085	8.71	0.24	4.58	0.61
Ash_08_33	0.48	1082.0	207.60	0.192	0.0505	2.41	0.0049	3.21	0.00071	2.12	0.66	4.63	0.11
Ash_08_37	0.88	293.0	374.00	1.274	0.0509	7.67	0.0054	7.92	0.00077	1.96	0.25	4.99	0.10
Ash_08_2	2.60	2119.0	918.60	0.434	0.0533	2.47	0.0062	2.91	0.00084	1.54	0.53	5.49	0.09
Ash_08_30	3.37	410.3	1344.0	3.289	0.0507	5.14	0.0061	5.68	0.00087	2.42	0.43	5.59	0.14
Ash_08_19	0.84	976.0	320.70	0.329	0.0481	1.95	0.0057	3.49	0.00087	2.89	0.83	5.66	0.17
Ash_08_7	0.65	3865.0	213.00	0.055	0.0478	0.93	0.0057	1.87	0.00086	1.62	0.87	5.66	0.17
Ash_08_1	0.73	521.0	266.60	0.502	0.0497	3.24	0.0060	3.67	0.00086	1.72	0.47	5.68	0.10
Ash_08_11	0.96	893.0	313.00	0.350	0.0474	2.56	0.0063	3.29	0.00097	2.07	0.63	6.32	0.14
Ash_08_4	0.51	423.0	94.30	0.222	0.0639	5.65	0.0095	6.52	0.00108	3.26	0.50	6.87	0.23
Ash_08_25	1.08	1144.0	258.60	0.227	0.0562	2.17	0.0084	4.06	0.00108	3.43	0.84	6.97	0.24
Ash_08_50	2.30	2135.0	716.00	0.335	0.0481	2.12	0.0072	2.87	0.00109	1.94	0.67	7.07	0.14
Ash_08_45	2.22	629.0	558.00	0.891	0.0507	3.38	0.0095	4.21	0.00136	2.51	0.60	8.76	0.22
Ash_08_3	2.50	700.0	429.00	0.581	0.0481	2.32	0.0126	3.39	0.00191	2.47	0.73	12.34	0.30

Sample / grain	Concentrations (ppm)				Isotope ratios				Isotopic age (Ma)				2 $\sigma$ (abs.)
	Pb	U	Th	Th/U <sub>zircon</sub>	<sup>207</sup> Pb/ <sup>206</sup> Pb	2 $\sigma$ (%)	<sup>207</sup> Pb/ <sup>235</sup> U	2 $\sigma$ (%)	<sup>206</sup> Pb/ <sup>238</sup> U	2 $\sigma$ (%)	Rho <sup>s</sup>	<sup>207</sup> Pb and <sup>206</sup> Pb-corrected <sup>206</sup> Pb/ <sup>238</sup> U age	
Ash_08_29	2.85	846.0	482.30	0.569	0.0470	1.30	0.0129	2.87	0.00200	2.36	0.89	12.93	0.33
Ash_08_48	1.48	455.8	242.10	0.535	0.0491	3.28	0.0139	3.63	0.00205	1.56	0.43	13.26	0.21
Ash_08_47	2.11	956.0	349.80	0.569	0.0480	1.73	0.0135	2.76	0.00205	2.15	0.78	13.26	0.29
Ash_08_27	3.19	754.0	573.00	0.757	0.0496	2.85	0.0141	3.74	0.00206	2.43	0.65	13.29	0.32
Ash_08_49	1.59	2075.0	2673.0	1.295	0.0470	1.28	0.0133	2.25	0.00206	1.85	0.82	13.30	0.25
Ash_08_39	1.35	423.2	222.80	0.529	0.0474	2.56	0.0135	3.40	0.00206	2.23	0.66	13.34	0.30
Ash_08_44	3.05	905.0	493.90	0.547	0.0476	1.95	0.0136	2.85	0.00207	2.08	0.73	13.39	0.28
Ash_08_23	2.31	403.9	355.90	0.885	0.0475	4.12	0.0155	4.67	0.00209	2.20	0.47	13.44	0.30
Ash_08_16	7.52	2032.0	1229.0	0.606	0.0473	1.33	0.0135	2.50	0.00208	2.12	0.85	13.46	0.29
Ash_08_32	1.60	829.0	257.40	0.310	0.0476	1.69	0.0137	2.52	0.00209	1.87	0.74	13.51	0.25
Ash_08_34	2.77	1139.0	448.90	0.391	0.0478	1.44	0.0138	3.08	0.00209	2.73	0.88	13.53	0.37
Ash_08_8	2.83	640.0	454.20	0.700	0.0481	1.73	0.0139	3.35	0.00209	2.87	0.86	13.54	0.39
Ash_08_21	2.56	1365.0	416.10	0.305	0.0480	1.14	0.0132	3.22	0.00209	3.02	0.94	13.55	0.41
Ash_08_18	2.03	648.0	328.60	0.509	0.0475	1.55	0.0137	2.73	0.00210	2.24	0.82	13.56	0.30
Ash_08_28	0.86	205.1	137.80	0.675	0.0475	5.70	0.0137	6.37	0.00210	2.86	0.45	13.59	0.39
Ash_08_22	3.07	598.0	471.00	0.790	0.0520	2.53	0.0152	3.53	0.00211	2.46	0.70	13.60	0.34
Ash_08_40	3.78	1138.0	605.50	0.533	0.0467	1.55	0.0136	2.60	0.00211	2.08	0.80	13.69	0.29
Ash_08_42	1.23	251.0	205.00	0.814	0.0471	1.82	0.0142	2.54	0.00215	1.76	0.70	13.94	0.25
Ash_08_6	1.37	774.0	209.40	0.268	0.0480	1.61	0.0141	2.93	0.00212	2.12	0.61	13.72	0.29
Ash_08_26	1.58	286.9	232.00	0.801	0.0506	4.17	0.0149	4.71	0.00213	2.45	0.83	13.76	0.34
Ash_08_41	2.29	674.0	254.70	0.382	0.0475	1.66	0.0136	11.97	0.00214	2.19	0.47	13.81	0.31
Ash_08_31	1.04	358.0	160.80	0.450	0.0461	3.49	0.0135	4.11	0.00218	2.70	0.23	13.81	0.40
Ash_08_17	0.80	178.7	106.80	0.598	0.0482	10.49	0.0174	10.93	0.00213	2.16	0.53	13.83	0.30
Ash_08_46	2.20	951.0	341.70	0.364	0.0479	1.82	0.0142	2.54	0.00217	3.09	0.28	13.86	0.44
Ash_08_43	4.99	1178.0	683.90	0.581	0.0637	12.09	0.0195	12.38	0.00222	2.66	0.21	14.07	0.40
Ash_08_9	3.01	881.0	462.00	0.478	0.0495	1.55	0.0149	3.04	0.00218	2.61	0.86	14.09	0.37
Ash_08_20	3.76	1231.0	581.90	0.471	0.0475	2.14	0.0143	2.95	0.00218	2.02	0.69	14.09	0.29
Ash_08_5	3.37	1240.0	523.00	0.423	0.0470	1.26	0.0141	2.08	0.00218	1.65	0.80	14.12	0.24
Ash_08_24	3.08	508.4	486.00	0.959	0.0478	2.75	0.0145	3.60	0.00220	2.32	0.64	14.22	0.33
Ash_08_15	2.89	1186.0	427.30	0.362	0.0542	2.43	0.0169	2.96	0.00226	1.68	0.57	14.51	0.25
Ash_08_38	1.28	228.0	119.10	0.519	0.0472	2.78	0.0233	3.90	0.00359	2.73	0.70	23.17	0.63
Ash_08_10	0.51	107.7	42.30	0.392	0.0513	7.22	0.0267	7.69	0.00378	2.65	0.34	24.27	0.65
Ash_08_14	5.20	311.0	129.10	0.415	0.0810	4.89	0.07145	46.85	0.08800	46.59	0.99	48.24	33.35
Ash_09_29	0.55	447.0	171.00	0.389	0.0492	5.10	0.0071	5.59	0.00105	2.29	0.41	6.82	0.16
Ash_09_21	0.86	828.0	270.00	0.292	0.0478	2.75	0.0070	3.39	0.00106	1.99	0.59	6.90	0.14
Ash_09_24	0.32	752.0	92.70	0.122	0.0463	3.91	0.0068	4.60	0.00107	2.43	0.53	6.99	0.12
Ash_09_31	0.47	933.0	141.80	0.152	0.0487	3.11	0.0072	3.53	0.00108	1.68	0.47	7.00	0.12
Ash_09_33	0.28	847.0	77.10	0.091	0.0476	2.35	0.0071	3.64	0.00109	2.78	0.76	7.05	0.20
Ash_09_47	0.93	423.0	264.00	0.633	0.0502	3.81	0.0075	4.59	0.00109	2.57	0.56	7.08	0.18
Ash_09_5	1.53	1852.0	482.00	0.262	0.0483	2.07	0.0072	2.83	0.00109	1.93	0.68	7.09	0.14
Ash_09_39	0.42	1123.0	122.60	0.109	0.0475	2.35	0.0071	2.88	0.00109	1.66	0.58	7.09	0.12
Ash_09_34	1.28	662.0	398.00	0.604	0.0488	3.51	0.0073	4.63	0.00109	3.02	0.65	7.10	0.22
Ash_09_16	0.37	1097.0	110.80	0.102	0.0464	2.40	0.0070	3.14	0.00109	2.02	0.64	7.11	0.15
Ash_09_45	0.40	390.0	125.80	0.322	0.0503	4.00	0.0076	4.36	0.00110	1.74	0.40	7.12	0.13
Ash_09_28	0.41	890.0	115.60	0.130	0.0473	1.94	0.0071	2.93	0.00110	2.19	0.75	7.15	0.16
Ash_09_19	3.79	1198.0	1102.0	0.911	0.0573	3.86	0.0088	4.61	0.00112	2.51	0.55	7.16	0.18
Ash_09_20	0.69	492.0	158.30	0.327	0.0611	8.68	0.0094	9.04	0.00112	2.51	0.28	7.16	0.19
Ash_09_12	0.84	484.0	221.40	0.461	0.0555	5.06	0.0085	5.47	0.00111	2.07	0.38	7.16	0.15
Ash_09_18	1.60	810.0	471.90	0.584	0.0476	2.55	0.0072	4.00	0.00111	3.08	0.77	7.20	0.22
Ash_09_8	0.45	587.8	126.30	0.214	0.0485	4.14	0.0074	4.86	0.00111	2.53	0.52	7.21	0.19
Ash_09_7	0.39	873.0	111.70	0.129	0.0480	2.12	0.0073	2.79	0.00111	1.81	0.65	7.22	0.13
Ash_09_35	0.74	442.0	211.80	0.477	0.0496	3.65	0.0076	4.54	0.00112	2.70	0.59	7.23	0.20
Ash_09_32	1.04	602.0	286.80	0.479	0.0550	13.28	0.0085	13.50	0.00112	2.41	0.18	7.24	0.19
Ash_09_40	0.34	333.2	90.60	0.273	0.0542	4.81	0.0084	5.43	0.00112	2.50	0.46	7.24	0.18
Ash_09_13	0.39	1497.0	115.90	0.078	0.0475	1.98	0.0073	3.27	0.00112	2.61	0.80	7.25	0.19
Ash_09_22	0.46	627.0	127.10	0.203	0.0492	1.98	0.0076	3.79	0.00112	2.69	0.71	7.26	0.20
Ash_09_27	0.35	167.2	100.20	0.606	0.0491	7.14	0.0076	7.51	0.00112	2.32	0.31	7.28	0.17
Ash_09_3	0.44	614.0	127.10	0.206	0.0491	2.28	0.0076	3.51	0.00112	2.68	0.76	7.30	0.20
Ash_09_17	0.38	601.7	107.90	0.178	0.0482	4.58	0.0074	5.31	0.00112	2.68	0.70	7.31	0.20
Ash_09_9	1.46	1454.0	400.00	0.277	0.0497	1.66	0.0077	2.77	0.00113	2.21	0.80	7.34	0.17
Ash_09_38	0.44	133.2	123.30	0.922	0.0514	13.04	0.0080	13.51	0.00113	3.52	0.26	7.35	0.27
Ash_09_36	0.50	1252.0	140.10	0.112	0.0485	1.74	0.0076	2.61	0.00113	1.95	0.75	7.37	0.15

## 7. Appendix

Sample / grain	Concentrations (ppm)				Isotope ratios				Isotopic age (Ma)				
	Pb	U	Th	Ti/U <sub>zircon</sub>	<sup>207</sup> Pb/ <sup>206</sup> Pb	2σ (%)	<sup>207</sup> Pb/ <sup>235</sup> U	2σ (%)	<sup>206</sup> Pb/ <sup>238</sup> U	2σ (%)	Rho <sup>s</sup>	<sup>207</sup> Pb and <sup>206</sup> Pb-corrected <sup>206</sup> Pb/ <sup>238</sup> U age	2σ (abs.)
Ash_09_25	1.86	1078.0	560.00	0.518	0.0483	2.31	0.0075	3.08	0.00113	2.03	0.66	7.38	0.15
Ash_09_2	0.55	402.5	155.50	0.389	0.0498	4.84	0.0078	5.28	0.00114	2.11	0.40	7.38	0.16
Ash_09_10	0.48	1034.0	140.40	0.135	0.0470	1.98	0.0074	3.51	0.00114	2.90	0.83	7.44	0.22
Ash_09_14	1.45	1847.0	427.80	0.230	0.0474	1.75	0.0075	2.94	0.00114	2.36	0.80	7.45	0.18
Ash_09_37	1.15	1301.0	256.00	0.197	0.0585	2.09	0.0094	3.00	0.00116	2.15	0.72	7.47	0.16
Ash_09_46	0.27	577.0	84.80	0.147	0.0484	3.12	0.0077	3.71	0.00115	2.01	0.54	7.47	0.15
Ash_09_4	0.92	1679.0	265.80	0.160	0.0474	1.86	0.0075	3.88	0.00115	3.40	0.88	7.48	0.25
Ash_09_1	2.45	1361.0	694.00	0.512	0.0508	2.98	0.0081	3.54	0.00115	1.91	0.54	7.48	0.15
Ash_09_30	0.99	805.0	280.50	0.352	0.0482	2.93	0.0077	4.14	0.00116	2.92	0.71	7.58	0.22
Ash_09_41	0.41	677.0	98.00	0.146	0.0496	3.85	0.0081	4.57	0.00118	2.46	0.54	7.67	0.19
Ash_09_42	0.66	301.5	154.70	0.514	0.0532	5.28	0.0087	5.82	0.00119	2.44	0.42	7.67	0.19
Ash_09_11	0.39	565.4	111.50	0.198	0.0480	3.77	0.0078	4.50	0.00118	2.45	0.54	7.71	0.19
Ash_09_6	0.80	515.5	215.40	0.419	0.0469	3.65	0.0079	4.40	0.00122	2.45	0.56	7.96	0.20
Ash_09_15	1.29	1120.0	349.10	0.316	0.0470	2.58	0.0080	3.39	0.00123	2.19	0.65	8.03	0.18
Ash_09_48	0.92	1154.0	243.40	0.211	0.0472	2.36	0.0082	3.09	0.00126	1.99	0.64	8.19	0.17
Ash_09_50	0.51	402.0	133.60	0.332	0.0482	3.55	0.0084	3.92	0.00127	1.65	0.42	8.25	0.14
Ash_09_26	0.54	799.0	136.00	0.149	0.0478	2.05	0.0086	3.69	0.00130	3.07	0.83	8.48	0.26
Ash_09_44	0.42	1444.0	113.10	0.079	0.0477	1.85	0.0088	3.37	0.00135	2.83	0.84	8.75	0.25
Ash_09_43	3.21	1696.0	482.00	0.283	0.0469	1.36	0.0133	2.61	0.00207	2.23	0.85	13.39	0.30
Ash_09_23	2.15	600.0	303.80	0.508	0.0496	2.45	0.0157	4.04	0.00230	3.21	0.79	14.86	0.48
Ash_09_49	1.18	575.0	128.40	0.222	0.0468	1.99	0.0191	2.79	0.00296	1.96	0.70	19.13	0.38

2σ — 2σ standard error; Rho — Discordance level = 100 [1 - <sup>206</sup>Pb/<sup>238</sup>U age] / <sup>207</sup>Pb/<sup>235</sup>U age; † — excluded from mean calculations.

***Faults scarp measurements****Table 3: Fault scarp profiling results from the Pumahuasi Fault*

Alluvial fan	Profile	Latitude range (°S)	Longitude range (°E)	Vertical separation	Lateral separation
1	1	22.2525 – 22.2562	65.6843 – 65.6933	19.3	95.2
1	2	22.2503 – 22.2540	65.6852 – 65.6942	14.2	87.7
1	3	22.2484 – 22.2513	65.6860 – 65.6952	20.4	118.0
1	4	22.2417 – 22.2513	65.6880 – 65.6974	15.5	218.0
1	5	22.2370 – 22.2395	65.6892 – 65.6986	30.8	106.0
2	1	22.2258 – 22.2270	65.6913 – 65.7009	9.2	140.3
2	2	22.2233 – 22.2246	65.6916 – 65.7012	9.2	137.2
2	3	22.2209 – 22.2222	65.6919 – 65.7015	11.3	161.4
2	4	22.2188 – 22.2146	65.6921 – 65.7017	14.7	100.4
3	1	22.2140 – 22.2146	65.6924 – 65.7021	20.3	199.1
4	1	22.2043 – 22.2050	65.6930 – 65.7027	12.9	118.9
4	2	22.2020 – 22.2025	65.6932 – 65.7029	11.0	126.5
4	3	22.1996 – 22.2001	65.6933 – 65.7030	9.3	109.0
4	4	22.1972 – 22.1976	65.6934 – 65.7031	13.7	153.7
5	1	22.1943 – 22.1957	65.6937 – 65.7033	13.4	105.5
5	2	22.1898 – 22.1906	65.6942 – 65.7039	17.8	204.7
5	3	22.1850 – 22.1858	65.6947 – 65.6947	25.2	188.7
5	4	22.1825 – 22.1834	65.6949 – 65.7045	20.0	129.1
6	1	22.1732 – 22.1734	65.6956 – 65.7053	25.3	117.6
6	2	22.1708 – 22.1710	65.6957 – 65.7054	13.0	93.2
6	3	22.1684 – 22.1686	65.6957 – 65.7054	10.7	109.3
6	4	22.1654 – 22.1667	65.6960 – 65.7056	9.7	162.9
6	5	22.1630 – 22.1643	65.6963 – 65.7059	9.2	104.1
6	6	22.1606 – 22.1619	65.6966 – 65.7062	21.5	117.3
7	1	22.1510 – 22.1524	65.6980 – 65.7076	14.5	222.6
7	2	22.1486 – 22.1500	65.6983 – 65.7079	16.2	262.4
8	1	22.1038 – 22.1034	65.7015 – 65.7112	30.2	120.7
9	1	22.0146 – 22.0123	65.7019 – 65.7112	43.5	122.8
9	2	22.0124 – 22.0099	65.7013 – 65.7106	26.0	101.5
9	3	22.0038 – 22.0041	65.7015 – 65.7111	30.9	148.9
9	4	22.0032 – 21.9998	65.7018 – 65.7109	38.9	151.4
10	1	21.9954 – 21.9936	65.6999 – 65.7094	26.0	139.3
10	3	21.9724 – 21.9733	65.6989 – 65.7085	29.5	126.6
10	4	21.9700 – 21.9709	65.6991 – 65.7087	26.9	114.7
10	5	21.9686 – 21.9674	65.6993 – 65.7089	30.3	221.3
10	6	21.9662 – 21.9650	65.6987 – 65.7086	17.5	126.5
10	7	21.9637 – 21.9627	65.6987 – 65.7083	19.3	96.6
11	1	21.9287 – 21.9317	65.7046 – 65.7138	2.7	53.2
12	1	21.9134 – 21.9136	65.7063 – 65.7160	15.8	177.6

## 7. Appendix

*Table 4: Fault scarp profiling results from the Cordillera de Sama West*

Alluvial fan	Profile	Latitude range (°S)	Longitude range (°E)	Vertical separation	Lateral separation
1	1	21.8076–21.8084	65.2238 – 65.2334	13.9	87.9
1	2	21.8052 – 21.8060	65.2240 – 65.2336	18.8	87.9
1	3	21.8028 – 21.8036	65.2242 – 65.2338	22.3	158.2
2	1	21.7969 – 21.7999	65.2239 – 65.2331	21.2	196.6
2	2	21.7957 – 21.7963	65.2235 – 65.2332	18.9	185.5
2	3	21.7933 – 21.7939	65.2235 – 65.2332	17.5	168.9
2	4	21.7909 – 21.7915	65.2237 – 65.2333	17.7	174.6
2	5	21.7861 – 21.7867	65.2245 – 65.2341	25.8	108.1
2	6	21.7837 – 21.7843	65.2246 – 65.2343	22.9	94.9
3	1	21.7762 – 21.7774	65.2240 – 65.2336	15.3	118.5
4	1	21.7669 – 21.7676	65.2240 – 65.2236	30.6	228.5
4	2	21.7645 – 21.7651	65.2238 – 65.2335	30.5	277.9
4	3	21.7573 – 21.7578	65.2238 – 65.2334	9.8	101.1
5	1	21.7455 – 21.7455	65.2235 – 65.2331	9.3	147.8
5	2	21.7354 – 21.7363	65.2228 – 65.2324	10.2	101.8

*Table 5: Fault scarp profiling results from the Cordillera de Sama East*

Alluvial fan	Profile	Latitude range (°S)	Longitude range (°E)	Vertical separation	Lateral separation
1	1	21.8062 – 21.8076	65.1364 – 65.1460	16.5	106.9
1	2	21.8038 – 21.8052	65.1361 – 65.1457	12.4	91.1
1	3	21.8014 – 21.8028	65.1357 – 65.1453	4.9	43.7
2	1	21.7990 – 21.8004	65.1354 – 65.1450	24.3	98.4
2	2	21.7966 – 21.7980	65.1350 – 65.1446	9.9	68.3
2	3	21.7942 – 21.7956	65.1347 – 65.1443	11.6	81.4
2	4	21.7902 – 21.7900	65.1341 – 65.1438	13.1	63.9
3	1	21.7425 – 21.7427	65.1376 – 65.1473	26.5	99.7
3		21.7401 – 21.7403	65.1375 – 65.1472	16.5	66.8
4	1	21.7327 – 21.7333	65.1369 – 65.1466	16.2	71.8
4	2	21.7302 – 21.7309	65.1368 – 65.1464	9.8	43.8

*Fault plane measurements*

Table 6: Fault plane measurements from all visited sites

Measurement	Dip direction	Dip angle	Strike
<u>Yavi</u>			
1	244	60	64
2	246	60	66
3	268	60	88
4	244	55	64
5	88	71	88
6	69	60	69
7	84	81	84
8	79	59	79
9	82	70	82
10	269	45	89
11	69	45	69
12	72	63	72
13	76	55	76
14	108	42	108
15	271	55	91
16	76	56	76
17	78	56	78
18	87	60	87
19	98	79	98
<u>Yavi Chico</u>			
20	87	81	87
21	81	70	81
22	89	75	89
23	87	55	87
24	79	81	79
25	62	59	62
26	236	33	56
27	241	46	61
28	238	33	58
29	245	45	65
30	234	25	54
<u>Pumhahuasi</u>			
31	303	84	123
32	304	82	124
33	308	86	128
34	269	82	89
35	291	80	111
36	278	45	98
37	286	55	106
38	293	55	113
39	300	55	120
40	293	55	113
41	280	41	100
42	288	45	108
43	290	40	110
44	290	50	110
45	285	40	105
46	285	25	105
47	281	51	101
48	277	45	97
49	295	52	115
<b>Average</b>	<b>199.6</b>	<b>57.2</b>	<b>89.5</b>
<b>Std (1s)</b>	<b>95.8</b>	<b>15.6</b>	<b>19.9</b>

**Joint measurements***Table 7: Joint measurements from all sites*

Measurement	Strike	Measurement	Strike	Measurement	Strike	Measurement	Strike
	181	63	240	125	214	187	225
2	010	64	133	126	210	188	350
3	014	65	070	127	260	189	100
4	159	66	220	128	223	190	080
5	196	67	053	129	215	191	060
6	175	68	225	130	310	192	271
7	212	69	150	131	208	193	100
8	256	70	008	132	220	194	040
9	150	71	205	133	206	195	172
10	254	72	246	134	217	196	097
11	325	73	190	135	221	197	070
12	070	74	210	136	170	198	085
13	248	75	235	137	213	199	111
14	236	76	237	138	165	200	025
15	083	77	238	139	215	201	100
16	230	78	320	140	170	202	100
17	208	79	148	141	212	203	045
18	189	80	040	142	162	204	025
19	190	81	345	143	214	205	110
20	167	82	238	144	208	206	060
21	190	83	182	145	191	207	027
22	070	84	214	146	214	208	100
23	201	85	063	147	174	209	040
24	350	86	218	148	211	210	080
25	155	87	273	149	174	211	055
26	351	88	028	150	184	212	030
27	276	89	003	151	166	213	100
28	172	90	019	152	172	214	110
29	183	91	212	153	215	215	120
30	165	92	220	154	166	216	095
31	135	93	049	155	221	217	105
32	003	94	067	156	195	218	025
33	006	95	235	157	227	219	110
34	348	96	195	158	193	220	045
35	330	97	204	159	258	221	020
36	018	98	337	160	225	222	045
37	019	99	221	161	183	223	015
38	015	100	011	162	255	224	028
39	186	101	015	163	242	225	122
40	200	102	210	164	197	226	256
41	198	103	030	165	229	227	293
42	108	104	054	166	186	228	140
43	188	105	357	167	188	229	120
44	102	106	010	168	213	230	075
45	198	107	244	169	256	231	020
46	080	108	042	170	226	232	015
47	320	109	074	171	220	233	025
48	310	110	074	172	202	234	130
49	345	111	184	173	215	235	140
50	172	112	243	174	214	236	135
51	102	113	040	175	120	237	130
52	019	114	013	176	213	238	030
53	352	115	014	177	217	239	115
54	077	116	021	178	242	240	125
55	193	117	182	179	241	241	204
56	157	118	029	180	194	242	221
57	001	119	112	181	201	243	085
58	167	120	098	182	160	244	135
59	165	121	101	183	200	245	240
60	031	122	047	184	186	246	060
61	063	123	034	185	170	247	228
62	241	124	214	186	020	248	098

---

Measurement	Strike	Measurement	Strike	Measurement	Strike
249	200	311	030	373	330
250	247	312	040	374	010
251	040	313	160	375	125
252	210	314	040	376	160
253	220	315	040	377	328
254	048	316	150	378	140
255	200	317	140	379	065
256	070	318	170	380	000
257	242	319	135	381	357
258	223	320	140	382	002
259	242	321	148	383	133
260	237	322	150	384	022
261	219	323	155	385	036
262	238	324	140	386	142
263	234	325	040	387	150
264	235	326	160	388	210
265	235	327	090	389	352
266	073	328	135	390	037
267	243	329	130	391	158
268	240	330	030	392	168
269	232	331	120	393	177
270	237	332	040	394	147
271	240	333	140	395	149
272	249	334	030	396	033
273	233	335	050	397	144
274	243	336	035	398	028
275	239	337	030	399	168
276	222	338	170	400	159
277	207	339	060	401	172
278	128	340	070	402	026
279	251	341	110	403	024
280	223	342	170	404	032
281	239	343	035	405	174
282	061	344	040	406	025
283	218	345	038		
284	236	346	020		
285	217	347	025		
286	221	348	040		
287	045	349	075		
288	320	350	138		
289	150	351	065		
290	239	352	142		
291	225	353	209		
292	231	354	150		
293	228	355	166		
294	136	356	152		
295	225	357	155		
296	155	358	171		
297	124	359	177		
298	130	360	141		
299	135	361	175		
300	137	362	160		
301	136	363	172		
302	105	364	152		
303	089	365	155		
304	253	366	141		
305	213	367	120		
306	018	368	140		
307	228	369	027		
308	070	370	178		
309	150	371	143		
310	030	372	332		